1995

Finite Element Analysis Of Geometrically Nonlinear Laminated Composite Shell Structures

Bin Wang

National Library of Canada
Acquisitions and Bibliographic Services Branch
395 Wellington Street
Ottawa, Ontario
K1A 0N4

Bibliothèque nationale du Canada
Direction des acquisitions et des services bibliographiques
395, rue Wellington
Ottawa (Ontario)
K1A 0N4

Your file Votre référence

Our file Notre référence

NOTICE

The quality of this microform is heavily dependent upon the quality of the original thesis submitted for microfilming. Every effort has been made to ensure the highest quality of reproduction possible.

If pages are missing, contact the university which granted the degree.

Some pages may have indistinct print especially if the original pages were typed with a poor typewriter ribbon or if the university sent us an inferior photocopy.

Reproduction in full or in part of this microform is governed by the Canadian Copyright Act, R.S.C. 1970, c. C-30, and subsequent amendments.

AVIS

La qualité de cette microforme dépend grandement de la qualité de la thèse soumise au microfilmage. Nous avons tout fait pour assurer une qualité supérieure de reproduction.

S'il manque des pages, veuillez communiquer avec l'université qui a conféré le grade.

La qualité d'impression de certaines pages peut laisser à désirer, surtout si les pages originales ont été dactylographiées à l'aide d'un ruban usé ou si l'université nous a fait parvenir une photocopie de qualité inférieure.

La reproduction, même partielle, de cette microforme est soumise à la Loi canadienne sur le droit d'auteur, SRC 1970, c. C-30, et ses amendements subséquents.

Canada

FINITE ELEMENT ANALYSIS OF GEOMETRICALLY NONLINEAR LAMINATED COMPOSITE SHELL STRUCTURES

by

Bin Wang

Department of Mechanical Engineering
Faculty of Engineering Science

Submitted in partial fulfilment
of the requirements for the degree of
Doctor of Philosophy

Faculty of Graduate Studies
The University of Western Ontario
London, Ontario, Canada
July 1995

ISBN 0-612-03497-6

Name BIN WANG

Dissertation Abstracts International is arranged by broad, general subject categories. Please select the one subject which most nearly describes the content of your dissertation. Enter the corresponding four-digit code in the spaces provided.

MECHANICAL ENGINEERING — SUBJECT TERM

0548 — SUBJECT CODE

U·M·I

Subject Categories

THE HUMANITIES AND SOCIAL SCIENCES

COMMUNICATIONS AND THE ARTS

Architecture 0729
Art History 0377
Cinema 0900
Dance 0378
Fine Arts 0357
Information Science 0723
Journalism 0391
Library Science 0399
Mass Communications 0708
Music 0413
Speech Communication 0459
Theater 0465

EDUCATION

General 0515
Administration 0514
Adult and Continuing 0516
Agricultural 0517
Art 0273
Bilingual and Multicultural 0282
Business 0688
Community College 0275
Curriculum and Instruction 0727
Early Childhood 0518
Elementary 0524
Finance 0277
Guidance and Counseling 0519
Health 0680
Higher 0745
History of 0520
Home Economics 0278
Industrial 0521
Language and Literature 0279
Mathematics 0280
Music 0522
Philosophy of 0998
Physical 0523
Psychology 0525
Reading 0535
Religious 0527
Sciences 0714
Secondary 0533
Social Sciences 0534
Sociology of 0340
Special 0529
Teacher Training 0530
Technology 0710
Tests and Measurements 0288
Vocational 0747

LANGUAGE, LITERATURE AND LINGUISTICS

Language
- General 0679
- Ancient 0289
- Linguistics 0290
- Modern 0291

Literature
- General 0401
- Classical 0294
- Comparative 0295
- Medieval 0297
- Modern 0298
- African 0316
- American 0591
- Asian 0305
- Canadian (English) 0352
- Canadian (French) 0355
- English 0593
- Germanic 0311
- Latin American 0312
- Middle Eastern 0315
- Romance 0313
- Slavic and East European 0314

PHILOSOPHY, RELIGION AND THEOLOGY

Philosophy 0422
Religion
- General 0318
- Biblical Studies 0321
- Clergy 0319
- History of 0320
- Philosophy of 0322

Theology 0469

SOCIAL SCIENCES

American Studies 0323
Anthropology
- Archaeology 0324
- Cultural 0326
- Physical 0327

Business Administration
- General 0310
- Accounting 0272
- Banking 0770
- Management 0454
- Marketing 0338

Canadian Studies 0385
Economics
- General 0501
- Agricultural 0503
- Commerce-Business 0505
- Finance 0508
- History 0509
- Labor 0510
- Theory 0511

Folklore 0358
Geography 0366
Gerontology 0351
History
- General 0578
- Ancient 0579
- Medieval 0581
- Modern 0582
- Black 0328
- African 0331
- Asia, Australia and Oceania 0332
- Canadian 0334
- European 0335
- Latin American 0336
- Middle Eastern 0333
- United States 0337

History of Science 0585
Law 0398
Political Science
- General 0615
- International Law and Relations 0616
- Public Administration 0617

Recreation 0814
Social Work 0452
Sociology
- General 0626
- Criminology and Penology 0627
- Demography 0938
- Ethnic and Racial Studies 0631
- Individual and Family Studies 0628
- Industrial and Labor Relations 0629
- Public and Social Welfare 0630
- Social Structure and Development 0700
- Theory and Methods 0344

Transportation 0709
Urban and Regional Planning 0999
Women's Studies 0453

THE SCIENCES AND ENGINEERING

BIOLOGICAL SCIENCES

Agriculture
- General 0473
- Agronomy 0285
- Animal Culture and Nutrition 0475
- Animal Pathology 0476
- Food Science and Technology 0359
- Forestry and Wildlife 0478
- Plant Culture 0479
- Plant Pathology 0480
- Plant Physiology 0817
- Range Management 0777
- Wood Technology 0746

Biology
- General 0306
- Anatomy 0287
- Biostatistics 0308
- Botany 0309
- Cell 0379
- Ecology 0329
- Entomology 0353
- Genetics 0369
- Limnology 0793
- Microbiology 0410
- Molecular 0307
- Neuroscience 0317
- Oceanography 0416
- Physiology 0433
- Radiation 0821
- Veterinary Science 0778
- Zoology 0472

Biophysics
- General 0786
- Medical 0760

EARTH SCIENCES

Biogeochemistry 0425
Geochemistry 0996
Geodesy 0370
Geology 0372
Geophysics 0373
Hydrology 0388
Mineralogy 0411
Paleobotany 0345
Paleoecology 0426
Paleontology 0418
Paleozoology 0985
Palynology 0427
Physical Geography 0368
Physical Oceanography 0415

HEALTH AND ENVIRONMENTAL SCIENCES

Environmental Sciences 0768
Health Sciences
- General 0566
- Audiology 0300
- Chemotherapy 0992
- Dentistry 0567
- Education 0350
- Hospital Management 0769
- Human Development 0758
- Immunology 0982
- Medicine and Surgery 0564
- Mental Health 0347
- Nursing 0569
- Nutrition 0570
- Obstetrics and Gynecology 0380
- Occupational Health and Therapy 0354
- Ophthalmology 0381
- Pathology 0571
- Pharmacology 0419
- Pharmacy 0572
- Physical Therapy 0382
- Public Health 0573
- Radiology 0574
- Recreation 0575
- Speech Pathology 0460
- Toxicology 0383

Home Economics 0386

PHYSICAL SCIENCES

Pure Sciences

Chemistry
- General 0485
- Agricultural 0749
- Analytical 0486
- Biochemistry 0487
- Inorganic 0488
- Nuclear 0738
- Organic 0490
- Pharmaceutical 0491
- Physical 0494
- Polymer 0495
- Radiation 0754

Mathematics 0405
Physics
- General 0605
- Acoustics 0986
- Astronomy and Astrophysics 0606
- Atmospheric Science 0608
- Atomic 0748
- Electronics and Electricity 0607
- Elementary Particles and High Energy 0798
- Fluid and Plasma 0759
- Molecular 0609
- Nuclear 0610
- Optics 0752
- Radiation 0756
- Solid State 0611

Statistics 0463

Applied Sciences

Applied Mechanics 0346
Computer Science 0984
Engineering
- General 0537
- Aerospace 0538
- Agricultural 0539
- Automotive 0540
- Biomedical 0541
- Chemical 0542
- Civil 0543
- Electronics and Electrical 0544
- Heat and Thermodynamics 0348
- Hydraulic 0545
- Industrial 0546
- Marine 0547
- Materials Science 0794
- Mechanical 0548
- Metallurgy 0743
- Mining 0551
- Nuclear 0552
- Packaging 0549
- Petroleum 0765
- Sanitary and Municipal 0554
- System Science 0790

Geotechnology 0428
Operations Research 0796
Plastics Technology 0795
Textile Technology 0994

PSYCHOLOGY

General 0621
Behavioral 0384
Clinical 0622
Developmental 0620
Experimental 0623
Industrial 0624
Personality 0625
Physiological 0989
Psychobiology 0349
Psychometrics 0632
Social 0451

ABSTRACT

This thesis is concerned with static and dynamic analysis of linear and geometrically nonlinear laminated composite plate and shell structures by using the finite element method.

The emphasis has been on establishing a sound theoretical basis for the formulation of simple and efficient finite elements for large scale linear and geometrically nonlinear analysis of laminated composite plate and shell structures.

A series of simple three-node, six degree-of-freedom (DOF) per node, hybrid strain based flat laminated composite triangular shell finite elements (HLCTS) for linear analysis were developed. These elements were based on the degenerated three dimensional solid concept. The first order shear deformation theory was adopted. The element which had the best performance was further developed for geometrically nonlinear analysis. In the nonlinear finite element analysis, the updated Lagrangian description was employed. The nonlinear HLCTS element accounts for large deformations of large rotations and finite strains. The "exact" geometrical description of a body during large rotations is realized by using exponential mapping. All the linear and nonlinear elements proposed in this investigation were derived explicitly by using symbolic computer algebra packages, MACSYMA and MAPLE. The explicit element stiffness, mass and loading matrices eliminate the use of numerical inversion and integration.

A relatively large collection of linear and geometrically nonlinear plate and shell problems were solved. Static and dynamic responses of such structures under various

lamination schemes, boundary and loading conditions were evaluated. In the nonlinear analysis, structures were analyzed under the considerations of large deformations of large rotations and finite strains. "Thinning effects" were also examined. The results obtained in the analysis were compared with those analytical or numerical solutions available in the literature. The numerical results have demonstrated the excellent performance of the HLCTS elements in both linear and nonlinear analysis.

The investigation also showed that the HLCTS elements are more accurate and converge faster when compared with other low-order finite elements. No shear-locking phenomenon was detected. The improved formulation of the elements has eliminated the zero energy modes or spurious modes.

ACKNOWLEDGMENTS

The author wishes to express his sincere and deep gratitude to his supervisor, Professor C.W.S. To, for his never ending enthusiastic guidance, instruction, encouragement, support and invaluable advice throughout the course of this work.

Thanks are extended to Professors S.M. Dickinson, Ian Moore and B.J. Vickery for serving as members of the advisory committee.

Thanks are also due to those fellow graduate students who have offered their kind assistance and friendly cooperations.

The Ontario Graduate Scholarship of Ministry of Colleges and Universities of Ontario, Graduate Research Fellowship, Admission Scholarship, Special University Scholarships of The University of Western Ontario received by the author, the Teaching Assistantships provided by the Department of Mechanical Engineering and Faculty of Graduate Studies of The University of Western Ontario, and the Research Assistantships provided through the financial support received by his supervisor from the Natural Sciences and Engineering Research Council of Canada are gratefully acknowledged.

Finally, the author would like to express his sincere thanks to his wife, Hua Pei, and his parents for their encouragement and support. Without these, this work would not have been attempted and completed.

TABLE OF CONTENTS

LIST OF TABLES

LIST OF FIGURES

NOMENCLATURE

Following is a list of the principal symbols and notations used in this thesis. The symbols and notations less frequently used and those that have different meanings in different contexts are defined where they are used.

Roman Letters

a	area of an element
a_{ij}, b_{ij}	geometrical parameters of a triangle
A_{ij}	components of membrane stiffness matrix
$\bar{\mathbf{B}}1$	strain-displacement relation matrix
B_{ij}	components of membrane-bending coupling stiffness matrix
B_m, B_b, B_s	linear strain-displacement relations matrices for membrane, bending and shear components
B_L, B_{NL}	linear and nonlinear strain-displacement matrices
C	material stiffness matrix or elasticity matrix
C_{ijkl}	elasticity tensor
$C^{t+\Delta t}$.	configuration at time "$t+\Delta t$"
D_{ij}	components of bending stiffness matrix
e^{ε}	Almansi strain vector at time t which is accumulated from assumed incremental strains
e^{u}	vector of Almansi strains at time t (due to displacement)

Δe^{ε}	vector of independently assumed incremental updated Green strains
Δe^{u}	vector of incremental updated Green "geometric" strains or incremental Washizu strains
E_{ij}	components of transverse shear stiffness matrix
E, E_1, E_2	Young's moduli
$\bar{f}$	body force vector
f_e	element consistent load vector in local co-ordinate
F	assembled consistent load vector
$F^{t+\Delta t}$	relative deformation gradient from time "t" to "t+Δt"
F_I	pseudo-force vector
F_e	element consistent load vector in global co-ordinate
G_{12}, G_{13}, G_{23}	shear moduli of laminates
$(G_{rs})_k$	in-plane shear modulus for k'th layer
h	total thickness of a laminate
h_k	layer co-ordinate in transverse direction at the bottom of the k'th layer
k_{dh}	element stiffness matrix associated with the drilling degree-of-freedom based on hybrid formulation
k_{dd}	element stiffness matrix associated with the drilling degree-of-freedom based on displacement formulation
k_e	element stiffness matrix in local co-ordinate
k_e^l	element stiffness matrix with linear polynomial used for w
k_e^q	element stiffness matrix with quadratic polynomial used for w
k_L	linear element stiffness matrix

k_{NL}	nonlinear or initial stress element stiffness matrix
K	assembled stiffness matrix
K_e	element stiffness in global co-ordinate
L	linear differential operator
m	consistent element mass matrix
M	vector of bending moment resultant
n	number of layers of a laminate
N	vector of membrane stress resultant
P	matrix of strain distributions
q	element nodal displacement vector in local co-ordinate
q'	element nodal displacement vector in global co-ordinate
Δq	vector of incremental nodal displacements
Q, Q_s	vector of shear stress resultant
Q	assembled displacement vector
Q_{ij}	components of reduced stiffness of laminates
r,s,t	local co-ordinates
$S^{t+\Delta t}$	vector of second Piola-Kirchhoff stress at the deformation state "$t+\Delta t$" measured with respect to the reference configuration C^t
ΔS	vector of incremental second Piola-Kirchhoff stress
$\bar{t}$	vector of prescribed surface traction
T, T_r	transformation matrices
u, v, w	displacements in local co-ordinate directions
u^u	assumed displacement field

Δu	vector of incremental displacement
U, V, W	displacements in global co-ordinate directions
V_e	volume of an element at the current configuration
V_i^t	director of node i at the time "t"
W	work done by external forces
ΔW	work-equivalent term corresponding to prescribed body forces and surface tractions in configuration $C^{t+\Delta t}$.
X,Y,Z	global co-ordinates

Greek Letters

α	strain parameter vector
$\Delta\alpha$	vector of incremental strain parameters
$\Delta\beta$	virtual rotation of director field
γ	transverse shear strain vector
$\Delta\gamma^e$	assumed incremental transverse strain
$\Delta\gamma^u$	incremental transverse strain due to displacement
ε^e	assumed strain field
ε^u	strain calculated from displacement field
$\Delta\varepsilon^u_{ij}$	linear components of incremental Washizu strain Δe^u
ε_m	membrane strain
$\Delta\varepsilon_m{}^e$	assumed incremental membrane strain
$\Delta\varepsilon_m{}^u$	incremental membrane strain due to displacement
ζ	co-ordinate along the director direction

$\Delta\eta^{u}_{ij}$	nonlinear components of incremental Washizu strain Δe^{u}
θ_r, θ_s, θ_t	rotations about local axes r, s and t
$\Delta\theta$	vector of incremental rotations
Θ_x, Θ_y, Θ_z	rotations about global axes X, Y and Z
κ	shear correction factor for isotropic materials
κ_i, κ_j	shear correction factors for laminated composite materials
μ	side length to thickness ratio
ν, ν_{12}, ν_{21}	Poisson's ratios
ξ_1, ξ_2, ξ_3	area co-ordinates
ρ_k	density of k'th layer
σ	vector of Cauchy stress
σ^{e}	stress vector calculated from the assumed strain field
ϕ	displacement shape function matrix
$\Delta\varphi$	virtual displacement at the mid-surface
χ	bending curvature
$\Delta\chi^{e}$	assumed incremental bending curvature
$\Delta\chi^{u}$	incremental bending curvature due to displacement
Ω	frequency parameter

Abbreviations

AT	Allman's triangle
BT	basic triangle
C4	clamped on four sides

CST	constant strain triangle
DDOF	drilling degree-of-freedom
DKT	discrete Kirchhoff triangle
DOF	degree-of-freedom
HLCTS	hybrid strain laminated composite triangular shell finite element
$HLCTS^{ld}$	hybrid strain laminated composite triangular shell finite element with linear transversal displacement interpolation and displacement type formulation for the DDOF
$HLCTS^{lh}$	hybrid strain laminated composite triangular shell finite element with linear transversal displacement interpolation and hybrid type formulation for the DDOF
$HLCTS^{qd}$	hybrid strain laminated composite triangular shell finite element with quadratic transversal displacement interpolation and displacement type formulation for the DDOF
$HLCTS^{qh}$	hybrid strain laminated composite triangular shell finite element with quadratic transversal displacement interpolation and hybrid type formulation for the DDOF
$HLCTS_r^{ld}$	similar to $HLCTS^{ld}$ above, used for dynamic analysis in which rotary inertia in the element consistent mass matrix is considered
$HLCTS_r^{lh}$	similar to $HLCTS^{lh}$ above, used for dynamic analysis in which rotary inertia in the element consistent mass matrix is considered
$HLCTS_r^{qd}$	similar to $HLCTS^{qd}$ above, used for dynamic analysis in which rotary inertia in the element consistent mass matrix is considered

$HLCTS_r^{qh}$	similar to $HLCTS^{qh}$ above, used for dynamic analysis in which rotary inertia in the element consistent mass matrix is considered
$HLCTS_t^{qd}$	similar to $HLCTS^{qd}$ above, used for dynamic analysis in which only the mass corresponding to translational DOF is considered
$HLCTS_t^{qh}$	similar to $HLCTS^{qh}$ above, used for dynamic analysis in which only the mass corresponding to translational DOF is considered
LST	linear strain triangle
S4	simply supported on four sides

CHAPTER 1

INTRODUCTION

Over the years, the demand for materials of high strength-to-weight ratio is dramatically increasing. It is not only the problem of producing durable products and saving energy, but also the problem of success or failure in many modern high-technology engineering projects. Being an important class of these materials, laminated composites are widely used. Laminated composite shell structures are frequently used in mechanical and structural systems. The investigation reported in this thesis is directly devoted to studies of the behaviours of laminated composite shell structures by using the finite element method. The scope of the current research is aimed at static and dynamic response analysis of linear and geometrically nonlinear laminated composite shell structures.

1.1. General

Because of their distinctive mechanical properties, shell structures have been used almost everywhere. In mechanical, civil, chemical, aerospace and marine engineering, shells as components or entire structures are frequently used. The main body of a submarine and marine vessels, and aerospace systems are good examples. They can all be classified as the combination of different type of shells.

In terms of materials employed for these shell structures, apart from the commonly used traditional materials, varieties of composites have played an important role.

Composite materials such as fibre-polymer, glass-epoxy, carbon-epoxy or graphite-epoxy have the properties of easy formability, resistance to corrosion and high damping. The most attractive and valuable properties of composite materials are the high strength-to-weight ratio and high stiffness-to-weight ratio. During World War II, military applications of polymer matrix composites led to large-scale commercial exploitation, especially in marine industry. Today, engineering structures are more dependent on composite materials. Owing to their larger strength-to-weight ratio, composite materials are more important to aerospace engineering. The applications are in the fabrication of aircraft wings, tail planes, helicopter rotor blades, interior panels, fuel tanks and so on. As quite a large number of composite materials have unidirectional properties, these materials are often built and used as laminate. A laminate has multi-layers of orthotropic materials bonded together. The layers may be of different materials or of the same orthotropic material with the principal material directions of each layer oriented at different angles to the reference axes. By selecting proper material and orientation for each layer, the laminate can have the strength and other properties which meet the requirements of different applications. In modern industry, composite materials have fully established themselves as truly workable engineering materials.

In parallel, it has long been the interests of scientists and engineers to explore and understand the behaviours of composite shell structures. The first known investigation of anisotropic shell was reported by Shtayerman [1.1] in 1924. However, before 1940's, majority of the work on anisotropic plates and shells was on applications of wood, crystalline solids and reinforced concrete constructions. In the last three decades the dramatically increased uses of high-performance composite materials in aerospace,

automotive, marine vessel-building, medical, chemical and recreational industries have stimulated the interest in comprehensive studies of anisotropic plates and shells. The literature in this area is overwhelming. The recent survey papers by Bert [1.2, 3], Chia [1.4], Kapania [1.5], Noor and Burton [1.6, 7], Noor [1.8], Reddy [1.9-11] and Reddy and Robbins Jr. [1.12] have listed more than one thousand articles in dealing with anisotropic plates and shells. The mechanics of composite materials is widely covered in the books by Chia [1.13], Jones [1.14], Tsai and Hahn [1.15] and Vinson and Sierkowsaky [1.16].

Because of the nature of laminated composite shell structures, the studies of such structures are more complicated than those of commonly used isotropic materials. The difficulties brought in by laminated composite materials together with complex geometries, loadings, boundary conditions and thermal effects in real life shell structures, make the analysis of response of such structures even more challenging. With such a complex problem analytical techniques can hardly be employed and therefore numerical approaches are logical choices. Owing to its versatile capability, the finite element method is adopted in this investigation. In addition to the aforementioned difficulties, there is the difficulty of including nonlinearities in the analysis. Many composite materials possess the properties which cannot be described by classical linear theories. The nonlinear behaviours of these materials are referred to as material nonlinearity. For highly deformable and flexible structures large deformations and finite rotations of structural members constitute the so-called geometrical nonlinearity. Despite the advances in nonlinear theories of structural and material behaviours, very little amount of quantitative information is available. Only a limited number of exact solutions to specific problems

can be found. This, in turn, calls for application of the finite element method.

Nonlinear finite element analysis of solids and structures has been covered in relative detail in the books by Bathe [1.17], Crisfield [1.18], Kleiber [1.19], Oden [1.20] and Owen and Hinton [1.21]. The available literature has quite a few publications in this subject. However, as can be seen later in Chapter 5 of this thesis, nonlinear static and dynamic finite element analysis of laminated composite plate and shell structures is somewhat limited and the understanding of highly nonlinear dynamic behaviours of laminated composite shell structures, in particular, is far from satisfactory.

1.2 Objectives

Therefore, the objectives of the present investigation are:

(1) to develop element matrices for the linear static and dynamic analysis of laminated composite plate and shell structures,

(2) to investigate and develop a nonlinear theory for the analysis of laminated composite plate and shell structures,

(3) to develop an incremental finite element solution procedure for static and dynamic analysis of geometrically nonlinear laminated composite plate and shell structures that emphasize large deformations of finite strains and finite rotations, and

(4) to implement the derived element matrices in a digital computer program that has the capability of dealing with large scale computation, general loading and boundary conditions.

In order to achieve the above objectives, lower order hybrid strain based three

node triangular shell elements for isotropic materials are natural candidates for extension to dealing with laminated composite materials.

1.3 Organization of the thesis

This thesis consists of seven chapters.

Chapter 1 is a brief introduction to the analysis of laminated composite shell structures. It has three sections. The first section brings about the motivation for the investigation. The second section posts the objectives of the investigation. The third section outlines the organization of this thesis.

Chapter 2 discusses the formulations and presents the derivations of hybrid strain based laminated composite triangular shell elements for linear static analysis. In this chapter, a series of simple three-node, six degree-of-freedom (DOF) per node, hybrid strain based laminated composite triangular shell finite elements for linear analysis are proposed. Their element matrices are obtained explicitly by using a symbolic computer algebra package.

In Chapter 3, the hybrid strain based triangular laminated composite shell elements proposed in Chapter 2 are applied to study representative static problems. Several typical cases are selected to illustrate the performance of the new elements. Both plate and shell problems are included.

In Chapter 4, the elements are adopted for free vibration analysis of laminated composite plate and shell structures. As stiffness matrices of the elements have been derived and obtained explicitly in Chapter 2, here element mass matrices are derived. The studies of geometrical nonlinearity of laminated composite shell structures are performed

in Chapter 5. The theory and formulation of simple and efficient laminated composite shell elements for large scale static and dynamic analysis of geometrically nonlinear laminated composite shell structures are presented. Derivation of the element stiffness and mass matrices for a particular element is made. The emphasis here is on large deformations of finite strains and finite rotations.

To validate the incremental finite element procedure and the element matrices derived in Chapter 5, a number of nonlinear problems are studied and reported in Chapter 6. These problems cover geometrically nonlinear analysis of static and dynamic cases. The latter includes isotropic and laminated composite plate as well as shell structures under different types of static and dynamic loads. As much as possible computed results are compared with analytical and numerical solutions available in the literature.

The final chapter, Chapter 7 is concerned with the conclusions and recommendations for future work. There are three sections in this chapter. The first section is a summary of the work reported in this thesis. The second is the conclusions while the third section includes recommendations for future work.

CHAPTER 2

FORMULATION AND DERIVATION OF HYBRID LAMINATED COMPOSITE TRIANGULAR SHELL ELEMENTS

In finite element analysis of laminated composite structures, the use of accurate and efficient elements is essential. Specially, for large scale linear and non-linear analysis of such structures, simple, accurate and efficient elements are critical to success. In this chapter, a series of simple three-node, six degree-of-freedoms (DOF) per node, hybrid strain based laminated composite triangular shell finite elements for linear analysis are proposed. They are derived explicitly by using symbolic computer algebra packages. The one with the best performance will be further developed for non-linear analysis in Chapter 5.

This chapter consists of five sections. Section 2.1 reviews previous work on isotropic plate and shell elements while Section 2.2 reviews lamination theories and Section 2.3 presents literature survey on laminated composite plate and shell elements. Section 2.4 states the preparations made before deriving element matrices, which includes discussions on variational principle, geometrical description of triangular elements and constitutive equation for laminates. Section 2.5 is concentrated on derivation of element matrices. Section 2.6 discusses drilling DOF's (DDOF's) and their contribution to element stiffness matrices. Section 2.7 is concerned with the closing remarks for this chapter.

2.1 Previous Work on Flat and Low-order Isotropic Plate and Shell Elements

A laminated composite shell element is a general purpose anisotropic shell element capable of handling arbitrarily layered shell problems. In the case of single layer the element is an anisotropic shell element.

Since the concept of using flat element in shell analysis was suggested in 1961 by Greene *et al.* [2.1], the development of flat shell elements has long been investigators' interests. A flat shell element is the combination of a membrane element and a plate bending element by superposition. The membrane element represents stretching behaviour while the plate bending element models bending action. In the review paper by Yang, Saigal and Liaw [2.2] the features of this shell modelling were summarized: (1) it is simple to formulate; (2) it is easy to input data to describe the geometry; (3) it is easy to mix with other types of element; (4) it is capable of modelling rigid body motions without including strains; (5) the requirement of using a relatively large number of elements provides the advantages of convenience in incorporating complex loading and boundary conditions. It was also pointed out that: (1) the element excludes coupling of stretching and bending within the element; such coupling is a major contributor towards load carrying mechanism in shells and other curved members; (2) the restriction to triangular shapes when general shells are to be treated; (3) the difficulty of treating junctions where all elements meeting at a point are coplanar; (4) discontinuity bending moments at element juncture lines, which do not appear in the continuously curved actual structures. However, it should be noted that the stretching and bending coupling exist in the assembled finite element model, though they are missed at the element level. Secondly, the triangular shape is the most flexible shape being used to model complex general shell

geometry with less distortion. Thirdly, if DDOF are added to flat element the singularity problems occurring in the case of several flat elements being coplanar will be excluded. Finally, the discontinued bending moment at elements juncture lines gives no fatal effects in terms of predicting overall response quantities. Only in the extreme case, when bending and stretching are strongly coupled flat elements could give poor results. Reference [2.3] reported that in a free vibration analysis, the results for natural frequencies showed fairly good agreement with those from axisymmetric curved elements [2.4]. The results become less accurate for higher modes. However, it is only the lower modes that are of importance to engineers in most of the practical applications. Flat elements were also shown to be capable of giving practical solutions to shell buckling problems [2.5].

It has been pointed out in reference [2.2] that the use of flat elements in shell analysis has been a major feature in almost all the popular finite element codes, such as ABAQUS [2.6], ADINA [2.7], ANSYS [2.8], MARC [2.9], NASTRAN [2.10] and SAP [2.11].

It is well recognized that the use of low-order or C^0 triangular finite elements is perhaps the most promising approach both from the theoretical and computational viewpoints to improve computation efficiency and general analysis capabilities for linear and non-linear shell problems. Three noded flat triangular C^0 elements were developed at the early stage in finite element history. In 1968 two such elements were proposed by Zienkiewicz, Parikh and King, [2.12] and Clough and Johnson [2.13], respectively. These elements were composed using linear polynomial in in-plane displacement variables and cubic displacement field for the lateral. Both of the two are displacement types and have

5-DOF at each node. In 1972, Dawe [2.14] developed a flat thin shell element which is composed of a constant moment bending element and a constant stress element. Later, in 1977 Argyris, Dunne, Malejannakis and Schelke [2.15] presented an element with the mixed second-order derivative of the lateral displacement added to the nodal DOF. Thus, an element with a total of 18 DOF was formulated.

Since a flat shell element is the result of superposing a membrane and a plate bending element, which represents stretching and bending behaviour, respectively, the efforts of improving the qualities of flat shell elements have focused on developing high performance membrane and bending elements. In 1980 Batoz, Bathe and Ho [2.16] re-examined the earlier work in 1969 by Stricklin, Haisler, Tisdale and Gunderson [2.17], and found that the discrete Kirchhoff triangle (DKT) was still among the best elements for analysis of thin plates. Thus, some three node shell elements were developed by combining the three-node DKT and the constant strain triangle (CST) [2.18, 19].

As a linear C^0 triangular shell element has too few kinematic degrees of freedom to provide desired numbers of nodal parameters for allowing accurate approximation of the unknown field the conventional displacement formulation was found to be rather limited in deriving a more efficient linear C^0 triangular element. For example, a three-node C^0 triangular element which has three translational DOF and two rotational DOF (normal rotational DOF not included) can possibly use only CST as stretch evaluation component. And the CST has been proved to be excessively stiff under in-plane bending [2.20]. Saleeb, Chang and Yingyeunyong [2.21], in 1988 developed a C^0 linear triangular element based on mixed formulation. The element has three translational and three rotational DOF. The edge shear constraints were introduced and element efficiency was

improved. But the assumed displacement field for membrane part was still in analogy to CST.

The important progress on low order plane elasticity element was due to Allman [2.22]. In Allman's triangle (AT), two in-plane translational DOF and one normal rotation DOF, called drilling degree-of-freedom (DDOF), are at each of the three nodes. The edge-tangent displacement is considered linear in the edge tangent co-ordinate. The AT gave much better results than the CST, but less accurate than the linear strain triangle (LST). However, in a large mesh the LST may produce more than twice as many DOF. Later, Cook [2.23] pointed out that AT could be regarded as the result of applying a co-ordinate transformation to an element that has mid-side nodes or LST. In fact the compatible quadratic displacements in AT are incomplete quadratic. It is equivalent to applying edge type constraint at mid-side nodes of LST, and then removing the mid-side nodes. Carpenter, Stolarski and Belytschko [2.24] independently proposed an element having the same nine DOF, which turned out to be identical to AT if it was integrated by one-point quadrature. It has been noticed that AT converges from below [2.22], that is, the element is stiff, the 'one-point' element converges from above [2.24]. Another plane stress element which has the same DOF as AT was suggested by Bergan and Felippa [2.25]. The performance of the element was improved by free formulation [2.26].

Cook [2.27] developed a plane hybrid element with rotational DOF and adjustable stiffness. This element is formed by three subtriangles. For each subtriangle the assumed stress field has five independent parameters. By adjusting a control coefficient in front of a submatrix, the element stiffness matrix can be softened. The macro element is finally formulated by constraining the normal rotation and eliminating the translational DOF at

the fourth node, that is, the node at the centroid of the macro element. The new plane stress element was found more accurate than either of the triangles presented in references [2.22] and [2.25]. But apart from the assembling and static condensation processes in forming the macro element the element has two mechanisms besides the expected mechanism in which all nodal rotations are the same.

Later, in 1991, Cook [2.28] did further investigation on nine-DOF plane triangles and a series of elements were obtained. The strategies used in the formulation options are adjusting the influence of DDOF; adding supplementary stiffness matrices to prevent mechanisms; combining strain-displacement relationships of full and reduced-integration elements, or combining stiffness matrices of full-integration and reduced-integration elements. These elements were subsequently used in forming flat shell elements with DKT. Cook summarized that a membrane element that was good for plane problems was poor for shell and vice versa, and the goal of nine-DOF flat triangular element that works well for both types of problem remained unattained.

The effort made in another direction was due to Carpenter, Stolarski and Belytschko [2.29]. Two membrane formulations for triangular shell element were examined. The first element was based on Marguerre shallow shell theory and a strain projection method which eliminated spurious membrane strain energy (membrane locking). The second element was a flat element. It was based on a linear membrane field governed by normal rotations and reduced quadrature. Numerical examples showed that the second element worked well enough to be competitive with curved elements.

Other types of general shell elements are curved and degenerated shell elements. The curved shell elements are more complicated than flat shell elements. To describe

element geometry, data must be supplied in addition to nodal co-ordinates. In reference [2.30] the formulation of curved, two- and three-dimensional elements was illustrated. For more references the readers are referred to the review paper by Yang, Saigal and Liaw [2.2].

Degenerated shell element was first presented by Ahmad, Irons and Zienkiewicz [2.31, 32]. The assumptions are that original normals to the middle surface of a shell are inextensible and remain straight but not necessarily normal after deformation, and the elastic modulus in the normal direction is considered zero. These assumptions allow transverse shear deformation. Thus, degenerated shell elements are available for thin and thick shells.

The most recent attempt on the development of lower order three-node flat degenerated shell element was made by To and Liu [2.33]. A series of hybrid strain based elements were developed. These elements adopted a set of specially designed strain distributions in the assumed strain field to avoid shear locking. For the assumed displacement field, the bending part is degenerated and isoparametric in nature. The membrane component was built on the basis of CST and AT, while much effort was also directed at the DDOF. The best element among this series was used to carry out linear and nonlinear analysis of shell structures.

2.2 Theories for Laminates

The laminated plate and shell theories can be classified into global approximation theories and discrete-layer theories.

In global approximation theories, global through-the-thickness displacement, strain or stress approximations are introduced. The order of the governing equations is independent of the number of layers.

Discrete-layer theories are based on piece-wise, layer-by-layer approximation of the response quantities in the thickness direction. The number of the governing equations depends on the number of layers of shell. Noor [2.34] identified different groups of discrete-layer theories. They are theories based on purely kinematic hypotheses; theories based on hybrid combination of kinematic and stress hypotheses and theories based on uniform state of stress or strain within each layer. The first group utilizes piece-wise approximation for in-plane displacement, and constant transverse displacement in the thickness direction. The continuity of transverse shear stress is not satisfied at the outer layer interfaces. The second group of discrete-layer theory applies the semi-inverse approach for proper in-plane displacement and satisfies the transverse shear continuity requirement. The third group of discrete-layer theories imposes the continuity of transverse stresses at layer interfaces to reduce the total number of generalized displacement parameters. The fourth group theories are based on subdividing the shell layers into thin layers and assuming a uniform state of stress or strain within each sub-layer. In general, discrete-layer theories provide more local details of the laminates. As displacement parameters were set up for each layer, the response quantities of the layer may be more precisely predicted.

The review papers by Noor and Burton [2.34, 35], Reddy [2.36] and Noor [2.37] had given extensive surveys on the development of lamination theories and computational models. Early work on the study of laminated composite plate and shell structures were based on the classical lamination theory [2.38-42]. The classical lamination theory assumes that the normal of the mid-surface of plates or shells remains straight and normal after deformation. That is, the transversal shear effect is neglected. Although classical lamination theory can be applied to many engineering problems, it is restricted to thin plate or shell problems.

Following the first complete lamination plate theory by Yang, Norris and Stavsky [2.43], considerable attention has been paid to the development of appropriate plate and shell theories that can accurately simulate the effects of shear deformations in laminated plate and shell structures.

The first-order shear deformation theories, draw analogy to Reissner-Mindlin plate theory and are based on the assumption of linear displacement variations through the thickness. That is, the normal to the mid-surface of laminated plates or shells before deformation remains straight, but not necessarily normal to the mid-surface after deformation of the structures. As the use of constant transverse shear stresses through thickness to represent actually nearly hyperbolic distribution, shear correction factors are required [2.44-50]. The choice of shear correction factors will affect the range of validity of first-order shear deformation theory. Nevertheless, the first-order theory with proper shear correction factor is able to predict very accurate gross response characteristics for a wide range of lamination and geometric parameters [2.51].

More accurate approximation of transverse shear effect requires higher-order

polynomials to represent the true transverse shear deformation [2.52-54]. But it is obvious that more computational effort has to be made in applying high-order shear deformation theories. Among the shear deformation theories, the first-order theory seems to provide the best compromise between accuracy and computational efficiency [2.36]. High-order polynomials introduce more independent displacement parameters in some higher-order theory formulations. To simplify the problem, the so-called semi-inverse method was proposed. To conduct this simplification, the in-plane displacements which are nonlinear in the thickness coordinate are obtained by using the constitutive relations. Another type of simplification is based on imposing the transverse shear stress (and strain) conditions at the top and bottom surfaces of the shell [2.54-56].

2.3 Literature Survey on Laminated Composite Plate and Shell Elements

Over the years, many of laminated composite finite element have been developed. Since laminated composite materials are often very flexible in shear, the transverse shear strains must be included if an accurate representation of the behaviour of laminated shells is expected. This has almost ruled out the use of classical Kirchhoff type of lamination shell theories. Earlier laminated composite shell elements were based on classical lamination theory. For examples see references [2.57-67]. To a certain extent in linear elastic analysis, these elements may provide a means for quantitative studies of some problems which are not quite sensitive to transverse shear.

At the beginning of 1980's, the concept of degenerated shells elements was used to represent laminated composite plates and shells. Degenerated elements allow transverse shear deformation and are simpler to formulate than those based on three dimensional

elastic models. Panda and Natarajan [2.68, 69], and Natarajan and Widera [2.70] developed a composite shell element by extending the work of Ahmad, Irons and Zienkiewicz [2.31]. As the integrations were performed for each layer separately using a three-dimensional Gaussian integration scheme it is cumbersome for the analysis of structures with a large number of layers. Milford and Schnobrich [2.71] suggested a linear variation in the thickness co-ordinate for strain components and the determinant of the Jacobian. This approach was used for laminated composite shell element by Yunus, Kohnke and Saigal [2.72].

Reddy [2.73] developed a series of isoparametric elements by using the first-order shear deformation theory. In the study, the four-node, eight-node and nine-node elements were obtained. As the elements were too stiff, reduced integration was employed. Other shear flexible laminated composite plate and shell elements were given by Lakshminarayana and Murthy [2.74], Siede and Chaudhuri [2.75], Kosmatka [2.76], Lardeur and Batoz [2.77] and Kosmatka [2.78]. In addintion, Reddy [2.79] proposed mixed finite element formulations of high-order lamination theory. Wu and Yen [2.80] developed an interlaminar stress mixed finite element based on the local high-order lamination theory. Robbins and Reddy [2.81] applied the layerwise laminate theory to develop a layerwise, two-dimensional displacement based finite element model for laminated composite plates. A piece-wise continuous distribution of the transverse shear strains through the laminate thickness was assumed. The resulting element is capable of representing interlaminar stresses and other localized effects with the same level of accuracy as a conventional three-dimensional finite element model.

Cheung and Kong [2.82] proposed a global-local approach to analyze thick

laminated plates. This approach treats a thick laminated plate as a three-dimensional inhomogeneous anisotropic elastic body. The cross-section of a laminated plate is first discretized into conventional eight-node elements. These elements are used to describe the local behaviour within the cross-section. The nodal displacements within the cross-section are then assumed to follow a pattern of variation which is defined by global functions. Argyris and Tenek [2.83] developed a three-node, six DOF per node, flat triangular element by using the concept of natural mode and matrix displacement method together with decomposition and lumping ideas. Later, they applied similar ideas and constructed another triangular element by assembling three edge-beams to carry transverse shear forces [2.84].

Hybrid and mixed formulations have received considerable attention in the analysis of laminated composite structures. The earlier paper in 1972 by Mau, Tong and Pian [2.85] composed of a quadrilateral multilayered plate element using hybrid stress method. The transverse shear effects were included while in each layer no rotational DOF at each node was considered. In 1977, Noor and Andersen [2.86] presented mixed shear-flexible isoparametric triangular and quadrilateral elements for analysis of laminated composite shallow shells. The hybrid-stress eight-node isoparametric multilayered plate elements by Spilker [2.87], the three-dimensional eight-node hybrid stress element by Liou and Sun [2.88] are notable work published in the 1980's. These two elements used independently assumed stress field for each layer. The stress parameters are as many as fifty five for each layer in reference [2.88]. A nine-node assumed strain element for composite plate and shell structures was formulated by Haas and Lee [2.89]. This element is of the degenerated solid type.

The foregoing survey shows that, the studies on laminated composite shell elements are much less common than shell elements. This is mainly due to the complexities of efficient computational model strategies and advanced laminated theories. Some of the elements based on three dimensional elastic solid models and high-order or layerwise lamination theories are very accurate but they are also very expensive or even infeasible for computing reasons. Simplifications made on lamination theories and computational models compromised accuracy and computing efficiency. However, the elements developed with such compromised efforts may still be costly for large scale linear and non-linear analysis of laminated composite structures. Some very simple elements may possess drawbacks, such as inaccuracy, slow convergence, locking and spurious modes. The understanding of mechanical and structural behaviours of laminated composite plate and shell structures and developing of simple, accurate and efficient finite elements for analyzing such structures is, therefore, far from adequate.

In the current study, a series of three-node flat triangular, hybrid strain based, shear deformable laminated composite shell finite elements is derived. They are accurate, efficient and simple to use for large scale linear and nonlinear analysis of laminated composite shell structures. In deriving these elements, every aspect discussed previously is considered. The elements have three translational and three rotational DOF at each vertex. Thus, these elements are easy to be incorporated into most of the commercial finite element packages. The assumed displacement fields are quadratic for translational DOF and linear for rotational DOF. The DDOF are enhanced by considering in-plane torsional strain energy. The assumed strain field has nine independent strain parameters for the triangular elements before the DDOF are enforced. The elements are compatible

with the first-order shear-deformation theory and is degenerated if only the displacement field is considered. The global response of laminated composite shell structures is the major interest of this investigation, and therefore global approximation theory is adopted in forming element matrices.

2.4 Preparation for the Element Derivation

Before starting the element matrices derivation, the variational principle is introduced. Then, the geometrical description of the triangular elements is presented. The constitutive equation for laminated composite structures is also discussed in this section.

2.4.1 Variational principle

The discussion on the major variational principles used in developing hybrid finite elements were recently presented by Kang [2.90]. The modified Hellinger-Reissner principle is directly applied in the present hybrid strain finite element derivation:

$$\pi_{HR}(u,\varepsilon) = \frac{1}{2}\int_V [-(\sigma^\varepsilon)^T\varepsilon^\varepsilon + 2(\sigma^\varepsilon)^T\varepsilon^u - 2(u^u)^T\bar{f}\,]\,dV - \int_a (u^u)^T\bar{t}\,da \tag{2.1}$$

where,

$u^u = \phi\, q$ is the assumed displacement field;

ϕ is the displacement shape function matrix;

$\varepsilon^\varepsilon = P\,\alpha$ is the assumed strain field;

P is a matrix of strain distributions;

α is the strain parameter vector;

$\varepsilon^u = L\, u^u = \bar{B}\, q$;

L is a linear differential operator;

$\bar{B}$ is the strain-displacement relation matrix;

σ^ε is the stress vector calculated from the assumed strain field;

$\bar{f}$ bar is the body force vector;

$\bar{t}$ bar is the vector of prescribed surface traction;

V is the volume of the body;

a is the surface area of the body;

and

$$q = \{u_1\ v_1\ w_1\ \theta_{r1}\ \theta_{s1}\ \theta_{t1}\ u_2\ \ldots\ \}^T \tag{2.2}$$

is the generalized nodal displacement vector. The superscripts u and ε denote the quantities in the assumed displacement field and strain field, respectively.

In this thesis, the square brackets, [ ] will be used to denote matrix and the parentheses, { } to designate vector if confusion with scalar quantities arises.

Then one can write:

$$\int_V (\sigma^\varepsilon)^T \varepsilon^\varepsilon dV = \int_a (N^T \varepsilon_m^\varepsilon + M^T \chi^\varepsilon + Q^T \gamma^\varepsilon) da \tag{3a}$$

$$\int_V (\sigma^\varepsilon)^T \varepsilon^u dV = \int_a (N^T \varepsilon_m^u + M^T \chi^u + Q^T \gamma^u) da \tag{3b}$$

where N, M and Q are, respectively, the membrane, bending and shear stress resultant vectors; and ε_m, χ and γ are the membrane strain, bending curvature and transverse shear strain vectors respectively.

Equation (2.1) represents the total potential energy within the system. Substituting equations (2.3a,b) into equation (2.1) leads to

$$\pi_{HR}(u,\varepsilon) = \int_a (N^T\varepsilon_m^u + M^T\chi^u + Q^T\gamma^u) \, da$$

$$- \frac{1}{2}\int_a (N^T\varepsilon_m^\varepsilon + M^T\chi^\varepsilon + Q^T\gamma^\varepsilon) \, da \qquad (2.4)$$

$$- \int_V (u^u)^T \bar{f} \, dV - \int_a (u^u)^T \bar{t} \, da \, .$$

This equation will be the basis of deriving the element stiffness matrices and load vectors.

2.4.2 Geometrical description of triangular elements

A series of three-node flat triangular elements are developed in the following section. As emphasis of the current study is on the linear and non-linear gross responses of large scale laminated composite shell structures, the global approximation scheme is applied. Figure 2.1 shows a typical laminated flat triangular shell element. The global and local Cartesian co-ordinate system are represented by (X, Y, Z) and (r, s, t), respectively. The origin of the local frame is attached to node 1 on the shell's middle surface. The r axis is coincided with the element edge 1-2. As all three element nodes are on the shell middle surface, they are on the r-s plane. The r-s plane is also the element middle plane. The t axis is perpendicular to r-s plane, but it is not necessary parallel to the shell surface normal. With such an arrangement of co-ordinate system the derivation of element

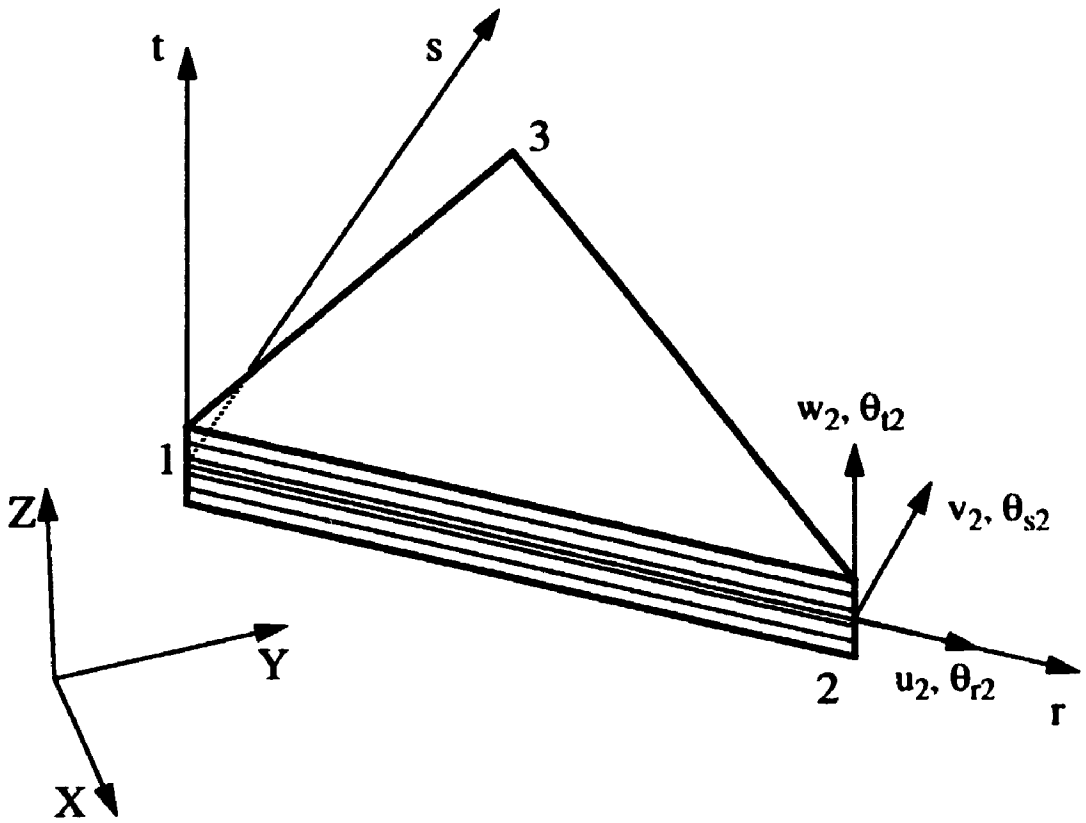

Figure 2.1 A flat laminated composite shell element and its co-ordinate systems

matrices can be simplified.

As indicated in the Figure 2.1, the six nodal variables are u, v, w, θ_r, θ_s, and θ_t, where

u is the displacement in r direction;

v is the displacement in s direction;

w is the displacement in t direction;

θ_r is the rotation about r-axis;

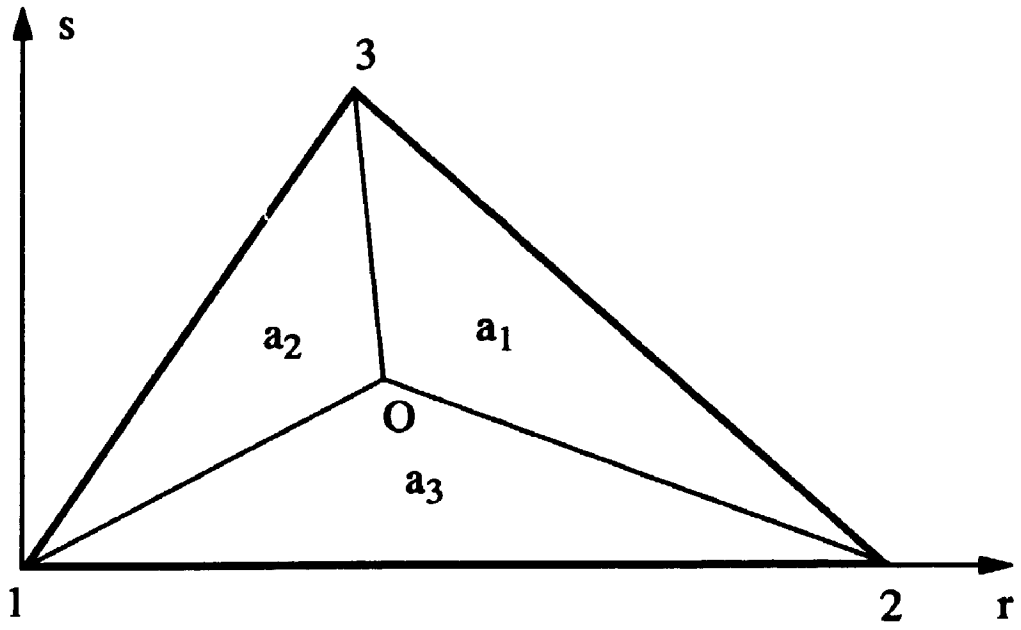

Figure 2.2 Area co-ordinate for a triangular finite element

θ_s is the rotation about s-axis;

θ_t is the rotation about t-axis and it is called the DDOF or normal rotation.

In the derivation, the area co-ordinates are introduced. In Figure 2.2, a triangle with area a is divided into three subtriangles with the areas a_1, a_2 and a_3, by an arbitrarily located point O. Then, the area co-ordinates are defined as the dimensionless quantities

$$\xi_1 = \frac{a_1}{a}, \quad \xi_2 = \frac{a_2}{a}, \quad \xi_3 = \frac{a_3}{a}. \tag{2.5}$$

They satisfy the constraint equation

$$\xi_1 + \xi_2 + \xi_3 = 1 \quad . \tag{2.6}$$

The relations between the local Cartesian and area co-ordinates are

$$\begin{Bmatrix} 1 \\ r \\ s \end{Bmatrix} = [\bar{\Lambda}] \begin{Bmatrix} \xi_1 \\ \xi_2 \\ \xi_3 \end{Bmatrix} \tag{2.7a}$$

or

$$\begin{Bmatrix} \xi_1 \\ \xi_2 \\ \xi_3 \end{Bmatrix} = [\bar{\Lambda}]^{-1} \begin{Bmatrix} 1 \\ r \\ s \end{Bmatrix} \tag{2.7b}$$

where

$$[\bar{\Lambda}] = \begin{bmatrix} 1 & 1 & 1 \\ r_1 & r_2 & r_3 \\ s_1 & s_2 & s_3 \end{bmatrix} \tag{2.7c}$$

$$[\bar{\Lambda}]^{-1} = \frac{1}{2a} \begin{bmatrix} r_2 s_3 - r_3 s_2 & s_{23} & r_{32} \\ r_3 s_1 - r_1 s_3 & s_{31} & r_{13} \\ r_1 s_2 - r_2 s_1 & s_{12} & r_{21} \end{bmatrix} \tag{2.7d}$$

in which

$$r_{ij} = r_i - r_j \qquad s_{ij} = s_i - s_j$$

$$2a = \det[\bar{\Lambda}] = r_{21}s_{31} - r_{31}s_{21} \ .$$

For the co-ordinate system shown in Figure 2.1, one has

$$r_1 = s_1 = s_2 = 0$$

$$[\bar{\Lambda}] = \begin{bmatrix} 1 & 1 & 1 \\ 0 & r_2 & r_3 \\ 0 & 0 & s_3 \end{bmatrix} \tag{2.8a}$$

$$[\bar{\Lambda}]^{-1} = \frac{1}{r_2 s_3} \begin{bmatrix} r_2 s_3 & -s_3 & r_3 - r_2 \\ 0 & s_3 & -r_3 \\ 0 & 0 & r_2 \end{bmatrix} . \tag{2.8b}$$

Later, the formulation of element matrices will require that $\phi(\xi_1\ \xi_2\ \xi_3)$ is differentiated with respect to Cartesian co-ordinates. By applying the chain rule we have

$$\frac{\partial \phi}{\partial r} = \frac{\partial \phi}{\partial \xi_1}\frac{\partial \xi_1}{\partial r} + \frac{\partial \phi}{\partial \xi_2}\frac{\partial \xi_2}{\partial r} + \frac{\partial \phi}{\partial \xi_3}\frac{\partial \xi_3}{\partial r} \tag{2.9a}$$

$$\frac{\partial \phi}{\partial s} = \frac{\partial \phi}{\partial \xi_1}\frac{\partial \xi_1}{\partial s} + \frac{\partial \phi}{\partial \xi_2}\frac{\partial \xi_2}{\partial s} + \frac{\partial \phi}{\partial \xi_3}\frac{\partial \xi_3}{\partial s} \tag{2.9b}$$

where

$$\xi_{1,r} = -\frac{1}{r_2}, \qquad \xi_{1,s} = \frac{r_3 - r_2}{r_2 s_3},$$

$$\xi_{2,r} = \frac{1}{r_2}, \qquad \xi_{2,s} = -\frac{r_3}{r_2 s_3}, \tag{2.10}$$

$$\xi_{3,r} = 0, \qquad \xi_{3,s} = \frac{1}{s_3}.$$

These leads to

$$\begin{Bmatrix} \phi_{,r} \\ \phi_{,s} \end{Bmatrix} = \begin{bmatrix} -\frac{1}{r_1} & \frac{1}{r_2} & 0 \\ \frac{r_{32}}{r_2 s_3} & -\frac{r_3}{r_2 s_3} & \frac{1}{s_3} \end{bmatrix} \begin{Bmatrix} \phi_{,\xi_1} \\ \phi_{,\xi_2} \\ \phi_{,\xi_3} \end{Bmatrix} \tag{2.11}$$

in which ",subscript" denotes partial differentiating with respect to the variables indicated by the subscripts.

Before proceeding further, we define a transformation matrix

$$\begin{Bmatrix} r \\ s \\ t \end{Bmatrix} = [T_r] \begin{Bmatrix} X \\ Y \\ Z \end{Bmatrix} \tag{2.12}$$

where

$$[T_r] = \begin{bmatrix} l_1 & m_1 & n_1 \\ l_2 & m_2 & n_2 \\ l_3 & m_3 & n_3 \end{bmatrix}$$

is the rotation matrix and l_i, m_i, and n_i (i=1,2,3) are the direction cosines. For example, l_1 is the cosine of the angle between X and r axes.

As the element matrices are developed in the local co-ordinate system, they have to be transferred into the global co-ordinate system, where the entire structure is defined and analyzed. For element nodal displacement vectors, one can fined the relation

$$q = T\, q' \tag{2.13}$$

where

$$T = \begin{bmatrix} T_r & & & & & \\ & T_r & & & & \\ & & T_r & & & \\ & & & T_r & & \\ & & & & T_r & \\ & & & & & T_r \end{bmatrix}_{18\times 18}$$

is the transformation matrix, q and q' are the local and global displacement vectors, respectively.

2.4.3 Constitutive equations for laminated composite structures

The general constitutive equation for three dimensional solids is

$$\sigma_{ij} = C_{ijkl}\varepsilon_{kl} \tag{2.14}$$

where Einstein's summation convention for indices has been adopted and i, j, k and l assume values of 1, 2, 3 or x, y, z in the commonly used Cartesian co-ordinate systems;

σ_{ij} is the stress vector;

ε_{kl} is the strain vector;

C_{ijkl} is the elasticity tensor.

Since σ_{ij} and ε_{kl} are second order tensor, they have nine components each. Owing to symmetry

$$\sigma_{ij} = \sigma_{ji} \; ; \quad \varepsilon_{kl} = \varepsilon_{lk}$$

the components are reduced to six. That is

$$\sigma_x, \sigma_y, \sigma_z, \sigma_{yz}\ \sigma_{zx}\ \sigma_{xy} \; ,$$

$$\varepsilon_x, \varepsilon_y, \varepsilon_z, \varepsilon_{yz}\ \varepsilon_{zx}\ \varepsilon_{xy} \; .$$

The elastic tensor C_{ijkl} is a fourth order tensor. It has eighty one components in theory. However, actual materials always have less elastic constants. To study laminated composite materials, we can assume the materials for each layer have three mutually orthogonal planes of elastic symmetry or they can be called orthotropic though the laminates appear to be anisotropic in general. Then, the elastic tensor has only nine elasticity constants left [2.91]. It becomes

$$C_{ij} = \begin{bmatrix} C_{11} & C_{12} & C_{13} & 0 & 0 & 0 \\ C_{12} & C_{22} & C_{23} & 0 & 0 & 0 \\ C_{13} & C_{23} & C_{33} & 0 & 0 & 0 \\ 0 & 0 & 0 & C_{44} & 0 & 0 \\ 0 & 0 & 0 & 0 & C_{55} & 0 \\ 0 & 0 & 0 & 0 & 0 & C_{66} \end{bmatrix} . \tag{2.15}$$

In the case of thin and moderately thick plate and shell problems one would assume that the stress in the thickness direction is zero. Then the basic constitutive equation becomes

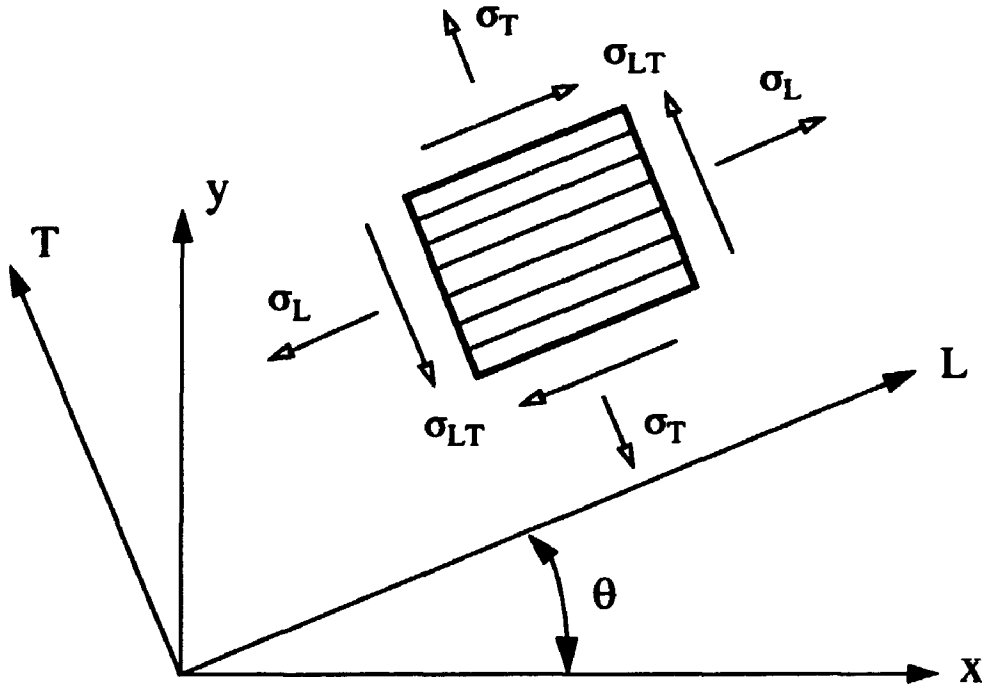

Figure 2.3 Relationship of the material co-ordinate and the global co-ordinate systems

$$\begin{Bmatrix} \sigma_x \\ \sigma_y \\ \sigma_{yz} \\ \sigma_{zx} \\ \sigma_{xy} \end{Bmatrix} = \begin{bmatrix} C_{11} & C_{12} & 0 & 0 & 0 \\ C_{12} & C_{22} & 0 & 0 & 0 \\ 0 & 0 & C_{44} & 0 & 0 \\ 0 & 0 & 0 & C_{55} & 0 \\ 0 & 0 & 0 & 0 & C_{66} \end{bmatrix} \begin{Bmatrix} e_x \\ e_y \\ e_{yz} \\ e_{zx} \\ e_{xy} \end{Bmatrix} \tag{2.16}$$

One can now see that it has six independent elasticity constants. It should be point out that in equation (2.16), the strains are engineering strains rather than those directly from

the strain tensor in equation (2.14). Equation (2.16) represents the material constitutive relations when the axes of Cartesian co-ordinate system are coincided with the principal material axes (or fibre orientation). If we take a piece of such material with constant thickness, let its principal material axes lay arbitrarily in a chosen global Cartesian co-ordinate (x-y-z) system and attach a local or material co-ordinate (L-T-Z) to it, see Figure 2.3, the stresses and strains can be transformed from one of the co-ordinate system to another by the equations below

$$\sigma_l = T_l\, \sigma_g \; ; \qquad \varepsilon_l = T_l\, \varepsilon_g \tag{2.17a,b}$$

and

$$\sigma_g = T_l^{-1}\, \sigma_l \; ; \qquad \varepsilon_g = T_l^{-1}\, \varepsilon_l \tag{2.18a,b}$$

where

$$\begin{aligned} \sigma_l &= \{\, \sigma_L \; \sigma_T \; \sigma_{TZ} \; \sigma_{ZL} \; \sigma_{LT} \,\}^T \\ \sigma_g &= \{\, \sigma_x \; \sigma_y \; \sigma_{yz} \; \sigma_{zx} \; \sigma_{xy} \,\}^T \\ \varepsilon_l &= \{\, \varepsilon_L \; \varepsilon_T \; \varepsilon_{TZ} \; \varepsilon_{ZL} \; \varepsilon_{LT} \,\}^T \\ \varepsilon_g &= \{\, \varepsilon_x \; \varepsilon_y \; \varepsilon_{yz} \; \varepsilon_{zx} \; \varepsilon_{xy} \,\}^T \end{aligned} \tag{2.19}$$

and

$$T_l = \begin{bmatrix} c^2 & s^2 & 0 & 0 & 2cs \\ s^2 & c^2 & 0 & 0 & -2cs \\ 0 & 0 & c & -s & 0 \\ 0 & 0 & s & c & 0 \\ -cs & cs & 0 & 0 & c^2-s^2 \end{bmatrix} \tag{2.20}$$

is a transformation matrix [2.91], in which

$$c = \cos\theta \; , \quad s = \sin\theta \; .$$

The inverse of the transformation matrix can be found by replacing θ by $-\theta$ in T_1.

In modern laminate of composite technology, the stress-strain relation for a lamina of fibre reinforced composite material in terms of the principal material direction (1, 2, 3) is given as

$$\begin{Bmatrix} \sigma_1 \\ \sigma_2 \\ \sigma_{23} \\ \sigma_{31} \\ \sigma_{12} \end{Bmatrix} = \begin{bmatrix} Q_{11} & Q_{12} & 0 & 0 & 0 \\ Q_{12} & Q_{22} & 0 & 0 & 0 \\ 0 & 0 & Q_{44} & 0 & 0 \\ 0 & 0 & 0 & Q_{55} & 0 \\ 0 & 0 & 0 & 0 & Q_{66} \end{bmatrix} \begin{Bmatrix} \varepsilon_1 \\ \varepsilon_2 \\ \varepsilon_{23} \\ \varepsilon_{31} \\ \varepsilon_{12} \end{Bmatrix} \tag{2.21}$$

or

$$\sigma_l = Q\ \varepsilon_l$$

where Q_{ij} is equivalent to C_{ij} and called reduced stiffness.

For most of engineering design problems, Q_{ij} can be calculated as following

$$\begin{aligned} Q_{11} &= \frac{E_1}{(1-\nu_{12}\nu_{21})}, \quad Q_{22} = \frac{E_2}{(1-\nu_{12}\nu_{21})}, \\ Q_{12} &= Q_{21} = \frac{\nu_{21}E_1}{(1-\nu_{12}\nu_{21})} = \frac{\nu_{12}E_2}{(1-\nu_{12}\nu_{21})}, \\ Q_{44} &= G_{23}, \quad Q_{55} = G_{13}, \quad Q_{66} = G_{12} \end{aligned} \tag{2.22}$$

where E_1 and E_2 are Young's moduli, ν_{12} and ν_{21} are Poisson's ratios and G_{12}, G_{13} and G_{23} are shear moduli.

To relate equation (2.21) to the x-y-z co-ordinate, it is substituted into equations (2.17) and (2.18). This leads to

$$\sigma_g = \bar{Q}\, \varepsilon_g \tag{2.23}$$

where

$$\bar{Q} = T_1^{-1}\, Q\, T_1 \tag{2.24}$$

and it is usually expressed as

$$\bar{Q} = \begin{bmatrix} \bar{Q}_{11} & \bar{Q}_{12} & 0 & 0 & \bar{Q}_{16} \\ \bar{Q}_{12} & \bar{Q}_{22} & 0 & 0 & \bar{Q}_{26} \\ 0 & 0 & \bar{Q}_{44} & \bar{Q}_{45} & 0 \\ 0 & 0 & \bar{Q}_{45} & \bar{Q}_{55} & 0 \\ \bar{Q}_{16} & \bar{Q}_{26} & 0 & 0 & \bar{Q}_{66} \end{bmatrix} \tag{2.25}$$

For a laminate, which is defined as a stack of plies (layers) or laminae bonded together, the overall constitutive relations are

$$N = A\varepsilon + B\chi\ , \quad M = B\varepsilon + D\chi\ , \quad Q_s = E\gamma \tag{2.26a,b,c}$$

If each ply or layer of the laminate has constant thickness, then

$$\begin{aligned} A_{ij} &= \sum_{k=1}^{n} (\bar{Q}_{ij})_k (h_k - h_{k-1}) && (i,j = 1, 2, 6) \\ B_{ij} &= \frac{1}{2} \sum_{k=1}^{n} (\bar{Q}_{ij})_k (h_k^2 - h_{k-1}^2) && (i,j = 1, 2, 6) \\ D_{ij} &= \frac{1}{3} \sum_{k=1}^{n} (\bar{Q}_{ij})_k (h_k^3 - h_{k-1}^3) && (i,j = 1, 2, 6) \\ E_{ij} &= \kappa_i \kappa_j \sum_{k=1}^{n} (\bar{Q}_{ij})_k (h_k - h_{k-1}) && (i,j = 4, 5) \end{aligned} \tag{2.27}$$

where h_k is the layer co-ordinate in the transverse direction at the bottom of the k'th layer (see Figure 2.4), and κ_i and κ_j are the shear correction factors.

The determination of shear correction factors has been discussed in references

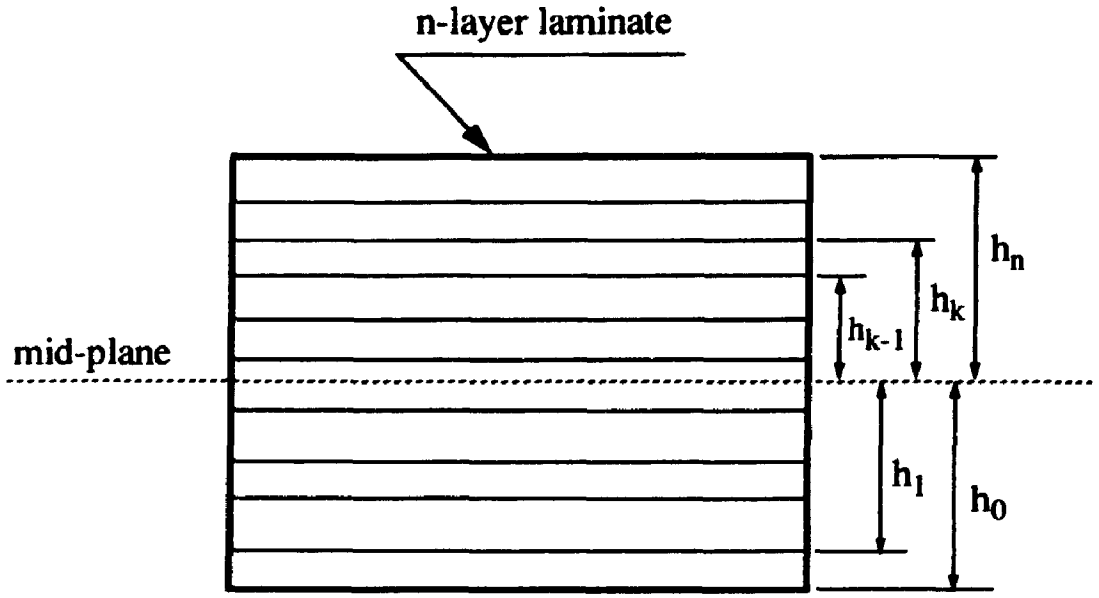

Figure 2.4 The layer co-ordinate system for
a laminated composite shell element

[2.92, 93] and [2.51]. When first-order shear deformation theory is adopted for analyzing laminated structures, the assumed transversal shear stress and strain distribution differ from the true distribution. To account for these differences, the shear correction factors must be used. For isotropic and homogeneous materials the shear correction factor κ = 5/6. However, for laminated structures, the shear correction factors κ_4 and κ_5 are closely related to detailed laminated constructions. More accurate procedures in determining the shear correction factors were introduced by Noor in reference [2.51].

2.5 Derivation of Element Matrices

In this section, details of the element matrices derivation are presented. The first sub-section gives the assumptions. The second and the third introduce the independently selected assumed displacement fields and strain fields, respectively. The fourth sub-section describes the procedures of deriving element stiffness matrices and load vectors. The fifth discusses the issue of explicit expressions.

2.5.1 Assumptions

In the current study, the global approximation of laminates is employed. It predicts gross responses of laminated structures rather than their local behaviours, such as delamination. This implies that we assume the plies of a laminate are perfectly bonded together.

The first-order shear deformable lamination theory is applied. In contrast to the classical lamination theory, the transversal shear effect is considered by assuming the linear distribution of the in-plane displacements in the thickness direction. It draws analogy to Reissner-Bolle-Mindlin plate theory and assumes that the normal of a plate or shell is straight and perpendicular to its middle surface before deformation and remains straight but not necessarily perpendicular to its surface after deformation. Meanwhile we assume that the original normal to the middle surface is inextensible and the elastic modulus in the normal direction is zero. Then, the three-dimensional elastic formulation is degenerated. However, the transversal shear deformation is still accounted for.

Though the formulation can handle the laminated composite structures with variable thickness, we assume that the laminates as well as individual ply have constant

thickness for the sake of simplifying the integrals for explicit element expressions. The materials of each ply are homogeneous.

2.5.2 Assumed displacement fields

The elements being developed are flat, three-node triangles. There are six DOF at each node. In formulating a low order hybrid flat shell triangle, To and Liu [2.33] developed a series of hybrid strain based elements by superposing membrane and bending elements. Considerable efforts were made in studying various formulations of the DDOF to further improve the flat shell elements. In their study, AT type of displacement field in the membrane part and linear in bending together with a nine parameter assumed strain field gave the best results.

Following in the same direction as To and Liu [2.33], the following sets of interpolation polynomials are adopted.

The first set for translational DOF is

$$\begin{aligned} u &= u_1\xi_1 + u_2\xi_2 + u_3\xi_3 + \bar{p}_1\theta_{t1} + \bar{p}_2\theta_{t2} + \bar{p}_3\theta_{t3} \\ v &= v_1\xi_1 + v_2\xi_2 + v_3\xi_3 + \bar{q}_1\theta_{t1} + \bar{q}_2\theta_{t2} + \bar{q}_3\theta_{t3} \\ w &= w_1\xi_1 + w_2\xi_2 + w_3\xi_3 \end{aligned} \tag{2.28}$$

and the second set is

$$\begin{aligned} u &= u_1\xi_1 + u_2\xi_2 + u_3\xi_3 + \bar{p}_1\theta_{t1} + \bar{p}_2\theta_{t2} + \bar{p}_3\theta_{t3} \\ v &= v_1\xi_1 + v_2\xi_2 + v_3\xi_3 + \bar{q}_1\theta_{t1} + \bar{q}_2\theta_{t2} + \bar{q}_3\theta_{t3} \\ w &= w_1\xi_1 + w_2\xi_2 + w_3\xi_3 - \bar{p}_1\theta_{r1} - \bar{p}_2\theta_{r2} - \bar{p}_3\theta_{r3} \\ &\quad - \bar{q}_1\theta_{s1} - \bar{q}_2\theta_{s2} - \bar{q}_3\theta_{s3} \,. \end{aligned} \tag{2.29}$$

The displacement field for the rotational DOF is linear. That is

$$\begin{aligned} \theta_r &= \theta_{r1}\xi_1 + \theta_{r2}\xi_2 + \theta_{r3}\xi_3 \\ \theta_s &= \theta_{s1}\xi_1 + \theta_{s2}\xi_2 + \theta_{s3}\xi_3 \\ \theta_t &= \theta_{t1}\xi_1 + \theta_{t2}\xi_2 + \theta_{t3}\xi_3 \end{aligned} \tag{2.30}$$

where

$$\begin{aligned} \bar{p}_1 &= (a_{31}\xi_3 - a_{12}\xi_2)\xi_1 \\ \bar{p}_2 &= (a_{12}\xi_1 - a_{23}\xi_3)\xi_2 \\ \bar{p}_3 &= (a_{23}\xi_2 - a_{31}\xi_1)\xi_3 \end{aligned} \tag{2.31a}$$

$$\begin{aligned} \bar{q}_1 &= (b_{31}\xi_3 - b_{12}\xi_2)\xi_1 \\ \bar{q}_2 &= (b_{12}\xi_1 - b_{23}\xi_3)\xi_2 \\ \bar{q}_3 &= (b_{23}\xi_2 - b_{31}\xi_1)\xi_3 \end{aligned} \tag{2.31b}$$

in which ξ_1, ξ_2 and ξ_3 are the area co-ordinates, a_{ij} and b_{ij} are element geometric constants. With reference to Figure 2.5, These geometric constants are defined as

$$a_{12} = \frac{1}{2} l_{12} \cos\gamma_{12} \quad , \quad b_{12} = \frac{1}{2} l_{12} \sin\gamma_{12} \quad ,$$

$$a_{23} = \frac{1}{2} l_{23} \cos\gamma_{23} \quad , \quad b_{23} = \frac{1}{2} l_{23} \sin\gamma_{23} \quad , \tag{2.31c}$$

$$a_{31} = \frac{1}{2} l_{31} \cos\gamma_{31} \quad , \quad b_{31} = \frac{1}{2} l_{31} \sin\gamma_{31} \quad .$$

From equations (2.29-31) one can see that the assumed translational displacement fields are quadratic when $\bar{p}$ and $\bar{q}$ terms are involved. The selection of these terms are

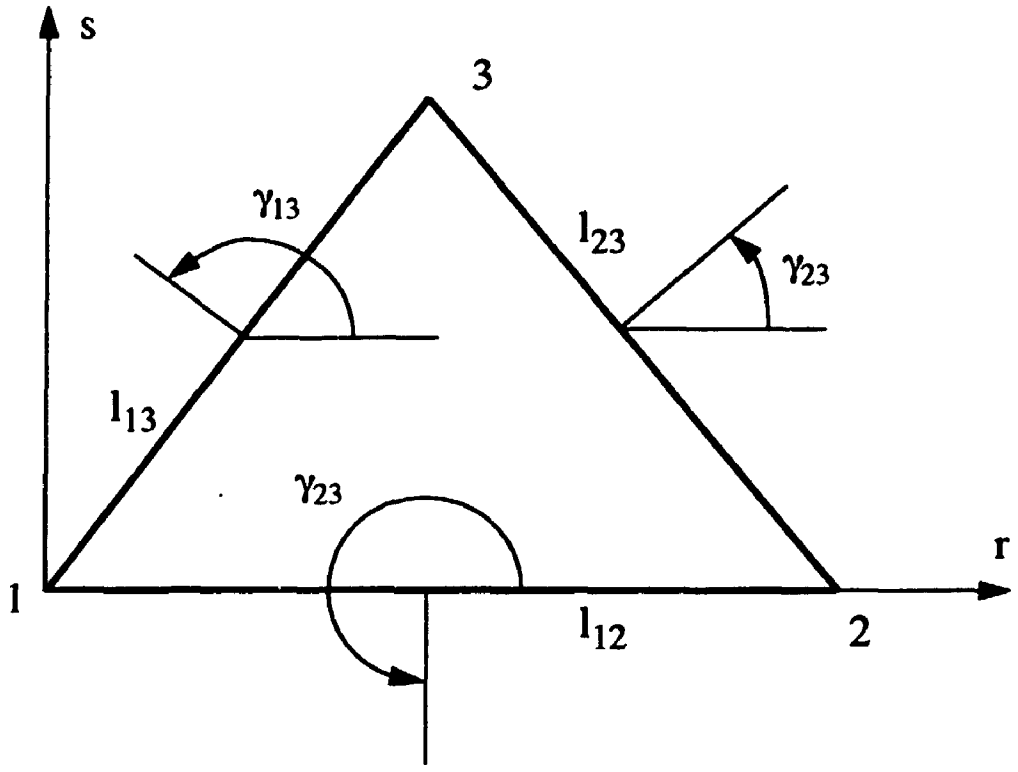

Figure 2.5 The geometry of the shell element

based on the strategy introduced by Allman [2.22]. The first set of the polynomials for translational DOF coincides with that used by To and Liu [2.33].

2.5.3 Assumed strain field

The selection of the independently assumed strain field is critical in developing hybrid finite elements. For low-order triangular elements, it is more difficult. Firstly, the selected field should be able to suppress all kinematic deformation modes. This requirement leads to a necessary condition on the minimum number of independent strain

parameters. In other words, this is the necessary condition to eliminate spurious mechanisms from the resulting elements and ensure the rank sufficiency for the stiffness matrices.

Saleeb, Chang and Graf [2.94] had discussed the assumed strain field selection guidelines. They pointed out that four considerations should be given to the selection of strain parameters. They should (1) enable stresses calculated from the assumed strain functions to satisfy the point-wise equilibrium condition; (2) suppress all kinematic deformation modes; (3) keep the element properties invariant; and (4) possess favourable constraint index counting.

From equation (2.26) one may notice that the assumed strain field should consist three parts: membrane strain ε^e_m, bending curvature χ^e and transverse shear strain γ^e. That is,

$$\varepsilon^e_m = P_m\ \alpha_m\ ,\quad \chi^e = P_b\ \alpha_b\ ,\quad \gamma^e = P_s\ \alpha_s\ . \tag{2.32}$$

As the DDOF is formulated independently, we consider a strain field with nine strain parameters and recast equation (2.32) as

$$\begin{Bmatrix} \varepsilon^e_r \\ \varepsilon^e_s \\ \varepsilon^e_{rs} \end{Bmatrix} = \begin{bmatrix} 1 & 0 & 0 \\ 0 & 1 & 0 \\ 0 & 0 & 1 \end{bmatrix} \begin{Bmatrix} \alpha_1 \\ \alpha_2 \\ \alpha_3 \end{Bmatrix}, \qquad \begin{Bmatrix} \chi^e_r \\ \chi^e_s \\ \chi^e_{rs} \end{Bmatrix} = \begin{bmatrix} 1 & 0 & 0 \\ 0 & 1 & 0 \\ 0 & 0 & 1 \end{bmatrix} \begin{Bmatrix} \alpha_4 \\ \alpha_5 \\ \alpha_6 \end{Bmatrix}, \tag{2.33a,b}$$

$$\begin{Bmatrix} \gamma^e_{st} \\ \gamma^e_{tr} \end{Bmatrix} = \begin{bmatrix} -s_3(1-2\xi_2) & s_3(1-2\xi_1) & 0 \\ -r_3(1-2\xi_2) & (r_3-r_2)(1-2\xi_1) & r_2(1-2\xi_3) \end{bmatrix} \begin{Bmatrix} \alpha_7 \\ \alpha_8 \\ \alpha_9 \end{Bmatrix}, \tag{2.33c}$$

where

$$\varepsilon_m^e=\{\varepsilon_r^e\ \varepsilon_s^e\ \varepsilon_{rs}^e\}^T\ ,\quad \chi^e=\{\chi_r^e\ \chi_s^e\ \chi_{rs}^e\}^T\ ,\quad \gamma^e=\{\gamma_{rt}^e\ \gamma_{st}^e\}^T\ ,$$

$$\alpha_m=\{\alpha_1\ \alpha_2\ \alpha_3\}^T\ ,\quad \alpha_b=\{\alpha_4\ \alpha_5\ \alpha_6\}^T\ ,\quad \alpha_s=\{\alpha_7\ \alpha_8\ \alpha_9\}^T\ ,$$

$$P_m=\begin{bmatrix}1&0&0\\0&1&0\\0&0&1\end{bmatrix},\qquad P_b=\begin{bmatrix}1&0&0\\0&1&0\\0&0&1\end{bmatrix},$$

$$P_s=\begin{bmatrix}-s_3(1-2\xi_2) & s_3(1-2\xi_1) & 0\\ -r_3(1-2\xi_2) & (r_3-r_2)(1-2\xi_1) & r_2(1-2\xi_3)\end{bmatrix}.$$

The nine strain parameters are evenly distributed over membrane, bending and shear strain fields. Equations (2.33a,b) indicates the constant membrane strain and bending curvature. In equation (2.33c) the non-constant shear transverse shear strain distribution was proposed in reference [2.21]. It has been used in both hybrid stress [2.21] and hybrid strain [2.33] formulations. This independently assumed transverse shear strain field is designed to eliminate shear locking when the structures being analyzed have large length-to-thickness ratio, μ. Reference [2.21] also pointed out that for elements with this non-constant shear stress or strain field assumption, accuracy may suffer for very thick structures. The example of length-to-thickness ratio given in Reference [2.21] is $\mu = l/h \leq 10$ to 15. In view of that the strain field assumption made in equations (2.33a-c) satisfies all four conditions mentioned above and in order to keep the new elements in their simplest form, this nine parameter strain field is used for the basic triangles, that is, the triangles without considering DDOF.

2.5.4 Derivation of element stiffness matrices and load vectors

Based on the degenerated three dimensional elastic solid theory and the co-ordinates system shown in Figure 2.1, the stress-strain relationship is then

$$\varepsilon^u=\begin{Bmatrix}\varepsilon_r^u\\ \varepsilon_s^u\\ \varepsilon_{rs}^u\end{Bmatrix}=\begin{Bmatrix}u_{,r}\\ v_{,s}\\ u_{,s}+v_{,r}\end{Bmatrix},\quad \chi^u=\begin{Bmatrix}\chi_r^u\\ \chi_s^u\\ \chi_{rs}^u\end{Bmatrix}=\begin{Bmatrix}\theta_{s,r}\\ -\theta_{r,s}\\ \theta_{s,s}-\theta_{r,r}\end{Bmatrix},\quad \gamma^u=\begin{Bmatrix}\gamma_{st}^u\\ \gamma_{rt}^u\end{Bmatrix}=\begin{Bmatrix}w_{,s}-\theta_r\\ w_{,r}+\theta_s\end{Bmatrix}. \tag{2.34}$$

This constitutive relationship is commonly used in formulating degenerated flat shell elements (for examples see references [2.21], [2.74] and [2.78]).

For the time being, we leave out θ_t from the assumed displacement fields and start to derive element stiffness matrices. However, the elements still have six nodal parameters, that is u_i, v_i, w_i, θ_{ri}, θ_{si} and θ_{ti}, at each node. From now on we refer these elements the basic triangles (BT).

Rewrite equations (2.28-30) in matrix form

$$u^u = \phi^l\, q\,, \qquad u^u = \phi^q\, q \tag{2.35a,b}$$

where the superscripts l and q are referred to linear and quadratic terms, respectivelv, and

$$u^u = \{\, u\ v\ w\ \theta_r\ \theta_s \,\}^T$$

$$q = \{\, u_1\ v_1\ w_1\ \theta_{r1}\ \theta_{s1}\ \theta_{t1}\ u_2 \ \ldots\ \ldots\ \theta_{t3}\ \}^T$$

and

$$\phi^l = [\ \phi_1^l \quad \phi_2^l \quad \phi_3^l\ ]\,,$$
$$\phi^q = [\ \phi_1^q \quad \phi_2^q \quad \phi_3^q\ ] \tag{2.36a,b}$$

in which

$$\phi_l^l = \begin{bmatrix} \xi_l & 0 & 0 & 0 & 0 & \bar{p}_l \\ 0 & \xi_l & 0 & 0 & 0 & \bar{q}_l \\ 0 & 0 & \xi_l & 0 & 0 & 0 \\ 0 & 0 & 0 & \xi_l & 0 & 0 \\ 0 & 0 & 0 & 0 & \xi_l & 0 \end{bmatrix} \tag{2.37a}$$

is corresponding to equations (2.28) and (2.30), and

$$\phi_l^q = \begin{bmatrix} \xi_l & 0 & 0 & 0 & 0 & \bar{p}_l \\ 0 & \xi_l & 0 & 0 & 0 & \bar{q}_l \\ 0 & 0 & \xi_l & -\bar{p}_l & -\bar{q}_l & 0 \\ 0 & 0 & 0 & \xi_l & 0 & 0 \\ 0 & 0 & 0 & 0 & \xi_l & 0 \end{bmatrix} \tag{2.37b}$$

is corresponding to equations (2.29) and (2.30).

Substituting equations (2.35-37) into equation (2.34) leads to

$$\begin{aligned} &\varepsilon_m^u = \bar{B}_1\, q\,, \quad \chi^u = \bar{B}_2\, q\,, \\ &\gamma^u = \bar{B}_3^l\, q \quad \text{or} \quad \gamma^u = \bar{B}_3^q\, q \end{aligned} \tag{2.38}$$

where

$$\bar{B}_1 = [\bar{B}_{11}\ \bar{B}_{12}\ \bar{B}_{13}]\,, \quad \bar{B}_2 = [\bar{B}_{21}\ \bar{B}_{22}\ \bar{B}_{23}]\,,$$

$$\bar{B}_3^l = [\bar{B}_{31}^l\ \bar{B}_{32}^l\ \bar{B}_{33}^l]\,, \quad \bar{B}_3^q = [\bar{B}_{31}^q\ \bar{B}_{32}^q\ \bar{B}_{33}^q]\,,$$

and

$$\bar{B}_{11} = \begin{bmatrix} \xi_{l,r} & 0 & 0 & 0 & 0 & \bar{p}_{l,r} \\ 0 & \xi_{l,s} & 0 & 0 & 0 & \bar{q}_{l,s} \\ \xi_{l,s} & \xi_{l,r} & 0 & 0 & 0 & \bar{p}_{l,s} + \bar{q}_{l,r} \end{bmatrix}, \tag{2.39}$$

$$\bar{B}_{2i} = \begin{bmatrix} 0 & 0 & 0 & 0 & \xi_{i,r} & 0 \\ 0 & 0 & 0 & -\xi_{i,s} & 0 & 0 \\ 0 & 0 & 0 & -\xi_{i,r} & \xi_{i,s} & 0 \end{bmatrix}, \tag{2.40}$$

$$\bar{B}_{3i}^{l} = \begin{bmatrix} 0 & 0 & \xi_{i,s} & -\xi_i & 0 & 0 \\ 0 & 0 & \xi_{i,r} & 0 & \xi_i & 0 \end{bmatrix}, \quad \bar{B}_{3i}^{q} = \begin{bmatrix} 0 & 0 & \xi_{i,s} & -\bar{p}_{i,s}-\xi_i & -\bar{q}_{i,s} & 0 \\ 0 & 0 & \xi_{i,r} & -\bar{p}_{i,r} & -\bar{q}_{i,r}+\xi_i & 0 \end{bmatrix}. \tag{2.41a,b}$$

The $\bar{B}$ matrices are the strain-displacement matrices, in which $\xi_{i,r}$ and $\xi_{i,s}$ (i=1, 2, 3) have been given in equation (2.10) and

$$\bar{p}_{1,r} = -\frac{a_{31}\,\xi_3}{r_2}, \quad \bar{p}_{2,r} = \frac{a_{23}\,\xi_3}{r_2}, \quad \bar{p}_{3,r} = \left(\frac{a_{31}}{r_2}+\frac{a_{23}}{r_2}\right)\xi_3, \tag{2.42a}$$

$$\bar{p}_{1,s} = \frac{(r_3-r_2)a_{31}\xi_3}{r_2 s_3}+\frac{a_{31}\xi_1}{s_3}, \quad \bar{p}_{2,s} = \frac{a_{23}\xi_2}{s_3}+\frac{r_3 a_{23}\xi_3}{r_2 s_3},$$
$$\bar{p}_{3,s} = \left(\frac{(r_3-r_2)a_{31}-a_{23}r_3}{r_2 s_3}\right)\xi_3+\frac{a_{23}\xi_2-a_{31}\xi_1}{s_3} \tag{2.42b}$$

$$\bar{q}_{1,r} = \frac{(b_{31}\xi_3-b_{12}\xi_2)-b_{12}\xi_1}{r_2},$$
$$\bar{q}_{2,r} = \frac{(b_{12}\xi_1-b_{23}\xi_3)-b_{12}\xi_2}{r_2}, \quad \bar{q}_{3,r} = \frac{(b_{31}+b_{23})\xi_3}{r_2}, \tag{2.42c}$$

$$\bar{q}_{1,s} = \left(\frac{(r_3-r_2)(b_{31}\xi_3-b_{12}\xi_2)}{r_2 s_3}\right)+\left(\frac{b_{12}r_3}{r_2 s_3}+\frac{b_{31}}{s_3}\right)\xi_1,$$

$$\bar{q}_{2,s} = \left(\frac{(r_3-r_2)b_{12}-r_2 b_{23}}{r_2 s_3}\right)\xi_2+\frac{r_3(b_{12}\xi_1-b_{23}\xi_3)}{r_2 s_3}, \tag{2.42d}$$

$$\bar{q}_{3,s} = \left(\frac{(r_3-r_2)b_{31}-r_3 b_{23}}{r_2 s_3}\right)\xi_3+\frac{b_{23}\xi_2-b_{31}\xi_1}{s_3}.$$

At the element level, applying equation (2.4) and let

$$I_1 = \int_a (N^T \varepsilon_m^u + M^T \chi^u + Q^T \gamma^u) \, da \tag{2.43}$$

Substituting equations (2.26), (2.33) and (2.38) into equation (2.43), noticing the fact that $A^T = A$, $B^T = B$, and $E^T = E$, gives

$$I_1 = \int_a \left[\left((\varepsilon_m^e)^T A^T + (\chi^e)^T B^T \right) \varepsilon_m^u + \left((\varepsilon_m^e)^T B^T + (\chi^e)^T D^T \right) \chi^u + (\gamma^e)^T E \gamma^u \right] da$$

$$= \int_a \{\alpha_m^T \ \alpha_b^T \ \alpha_s^T\} \begin{bmatrix} P_m^T & 0 & 0 \\ 0 & P_b^T & 0 \\ 0 & 0 & P_s^T \end{bmatrix} \begin{bmatrix} A & B & 0 \\ B & A & 0 \\ 0 & 0 & E \end{bmatrix} \begin{Bmatrix} \bar{B}_1 \\ \bar{B}_2 \\ \bar{B}_3 \end{Bmatrix} \{q\} \, da$$

$$= \{\alpha\}^T \int_a \begin{bmatrix} P_m^T A \bar{B}_1 + P_m^T B \bar{B}_2 \\ P_b^T B \bar{B}_1 + P_b^T D \bar{B}_2 \\ P_s^T E \bar{B}_3 \end{bmatrix} da \, \{q\}$$

or

$$I_1 = \alpha^T G_e \, q \tag{2.44}$$

where

$$G_e = \int_a \begin{bmatrix} P_m^T A \bar{B}_1 + P_m^T B \bar{B}_2 \\ P_b^T B \bar{B}_1 + P_b^T D \bar{B}_2 \\ P_s^T E \bar{B}_3 \end{bmatrix} da \ , \tag{2.45}$$

$$\alpha = \{ \alpha_m \ \alpha_b \ \alpha_s \}^T = \{ \alpha_1 \ \alpha_2 \ \dots \ \alpha_9 \}^T \ .$$

The second integral in equation (2.4) is

$$I_2 = -\frac{1}{2}\int_a \left(N^T \varepsilon_m^c + M^T \chi^c + Q^T \gamma^c \right) da \ . \qquad (2.46)$$

Following the same procedure in deriving equation (2.45) and substituting equations (2.26) and (2.33) into equation (2.46) leads to

$$I_2 = -\frac{1}{2}\,\alpha^T H\, \alpha \qquad (2.47)$$

where

$$H = \int_a \begin{bmatrix} P_m^T A P_m & P_m^T B P_b & 0 \\ P_b^T B P_m & P_b^T D P_b & 0 \\ 0 & 0 & P_s^T E P_s \end{bmatrix} da \ . \qquad (2.48)$$

In equations (2.45) and (2.48), the integrands are function of area co-ordinates. Thus, the integrations are evaluated by

$$\int_a \xi_1^k \xi_2^l \xi_3^m \, da = 2a \, \frac{k!\, l!\, m!}{(2+k+l+m)!} \qquad (2.49)$$

It is full integration and gives exact results. There is no reduced integration applied.

By making use of equations (2.44) and (2.47), the total potential energy within an element is

$$\pi_e(\alpha, q) = \alpha^T G_e q - \frac{1}{2}\alpha^T H \alpha - q^T \left(\int_v \phi^T \bar{f}\, dv + \int_a \phi^T \bar{t}\, da \right) \qquad (2.50)$$

Taking the variation with respect to α, one has

$$G_e q - H_e \alpha = 0 \ , \quad \alpha = H_e^{-1} G_e q \ . \qquad (2.51a,b)$$

Bringing equation (2.51) back into equation (2.50) and recasting the equation results in

$$\pi_e = \frac{1}{2} q^T G_e^T H_e^{-1} G_e q - q^T \left(\int_v \phi^T \bar{f} \, dv + \int_a \phi^T \bar{t} \, da \right) . \qquad (2.52)$$

Taking variation in equation (2.52) with respect to q gives

$$G_e^T H_e^{-1} G_e q - \left(\int_v \phi^T \bar{f} \, dv + \int_a \phi^T \bar{t} \, da \right) = 0 \ . \qquad (2.53)$$

Defining

$$k_e = G_e^T H_e^{-1} G_e \ , \quad f_e = \int_v \phi^T \bar{f} \, dv + \int_a \phi^T \bar{t} \, da \ , \qquad (2.54a,b)$$

equation (2.53) can be casted into the simpler form

$$k_e q = f_e \ , \qquad (2.55)$$

where

k_e is the element stiffness matrix,

f_e is the element consistent load vector due to body force and surface traction,

q is the nodal displacement vector in local co-ordinate.

Owing to the choices of using linear or quadratic approximation for w in the assumed displacement field, see equations (2.37a,b), two stiffness matrices for BT were obtained. They are indicated by k_e^l and k_e^q with l and q denoting linear and quadratic polynomials for w.

Up to now, k_e^l and k_e^q are still in terms of local co-ordinate. Introducing the co-ordinate transformation defined by equation (2.13) to equation (2.52) yields

$$\pi_e = \frac{1}{2} \{q'\}^T T^T k_e T \{q'\} - \{q'\}^T T^T f_e \ . \qquad (2.56)$$

Now define

$$K_e = T^T k_e T \,, \quad F_e = T^T f_e \,, \tag{2.57a,b}$$

where

K_e is the element stiffness in global co-ordinate,

F_e in the element consistent load vector in global co-ordinate.

Equation (2.56) represents the total potential energy for a typical element. When the finite element method is employed to analyze a laminated composite structure, the total potential energy of the structure is

$$\pi = \sum_{1}^{nel} \pi_e = \frac{1}{2} \sum_{1}^{nel} (q'^T K_e q') - \sum_{1}^{nel} (q'^T F_e) \tag{2.58}$$

where the summations are over the total number of elements (nel). Therefore, the assembled stiffness matrix, load vector and nodal displacement vector can be defined as

$$K = \sum_{i=1}^{nel} [K_e]_i \,, \quad F = \sum_{i=1}^{nel} \{F_e\}_i \,, \quad Q' = \sum_{i=1}^{nel} \{q'\}_i \tag{2.59a,b,c}$$

where $[K_e]_i$, $\{F_e\}_i$ and $\{q'\}_i$ are for the i'th element and they are recasted in the forms which have the same dimensions as K, F and Q', respectively. With these notations, the equilibrium equation is

$$K\,Q' = F \,. \tag{2.60}$$

The unknown nodal displacement vector Q' is then obtained by solving equation (2.60). To recover strain and stress vectors, apply equations (2.51b), (2.33) and (2.26). They are given bellow

$$\alpha = \{\alpha_m \ \alpha_b \ \alpha_s\}^T = H_e^{-1} G_e q \ ,$$

$$\varepsilon_m^e = P_m \alpha_m \ , \quad \chi^e = P_b \alpha_b \ , \quad \gamma^e = P_s \alpha_s \ , \tag{2.61}$$

$$N = A\varepsilon_m^e + B\chi^e \ , \quad M = B\varepsilon_m^e + D\chi^e \ , \quad Q_s = E\gamma^e \ .$$

2.5.5 Explicit expressions

During the course of derivation, algebraic manipulations were performed by using the computer algebra packages MACSYMA [2.95] and MAPLE [2.96]. There are no numerical integration and inversion involved. Thus, the resulting element matrices are explicit. Errors introduced by applying numerical integration and matrix inversion are therefore eliminated.

However, whether the obtained explicit solutions are acceptable for use in a computer program depends on the techniques applied in the process of simplifying the results. For example, in getting the inversion of the H matrix defined in equation (2.48), the resulting matrix, that is the inverted H matrix, is about ten thousand lines in Fortran code, if the original 9 × 9 H matrix is directly given to MACSYMA or MAPLE. Such a result is obviously not welcome.

To fully utilize the advantages of explicit expressions of element matrices the technique of inversion by partition is applied. Let

$$H = \begin{bmatrix} H_{11} & H_{12} \\ H_{21} & H_{22} \end{bmatrix} \tag{2.62}$$

where

H_{11} is the 4 × 4 submatrix at top-left of H,

H_{22} is the 5 × 5 submatrix at bottom-right of H,

H_{12} is the 4 × 5 submatrix at top-right of H,

H_{21} is the 5 × 4 submatrix at bottom-left of H.

Then,

$$H^{-1} = \begin{bmatrix} R_{11} & R_{12} \\ R_{21} & R_{22} \end{bmatrix} \tag{2.63}$$

where

$$\begin{aligned} R_{22} &= (H_{22} - H_{21} H_{11}^{-1} H_{12})^{-1} \quad , \\ R_{12} &= -H_{11}^{-1} H_{12} R_{22} \quad , \\ R_{21} &= -R_{22} H_{21} H_{11}^{-1} \quad , \\ R_{11} &= H_{11}^{-1} - H_{11}^{-1} H_{12} R_{21} \quad . \end{aligned} \tag{2.64}$$

The schemes of partitioning had been tried and compared for several times. The one shown in equation (2.62) gave the simplest solution if no further subpartition is conducted.

2.6 Improvements of DDOF

In previous sections, as the strain energy due to normal rotations was neglected, the total potential energy equation did not include the contribution of θ_t. In this section, the in-plane torsional shear strain energy due to normal rotations is considered. Thus, the DDOF are enhanced. The first subsection discusses briefly the history and importance of DDOF. The two subsequent subsections are concerned with formulations of DDOF by hybrid and displacement method, respectively.

2.6.1 The history and importance of DDOF

In the analysis of shell structures by using flat shell finite elements, a common problem may occur if the flat shell elements do not have DDOF in their nodal displacement vector. This is the singularity problem in the assembled structure stiffness matrix if several element are coplanar at a certain node. Physical shell structures have six rigid body motions. The corresponding finite element model should be able to predict these motions. However, if the normal rotations are neglected from a finite element, the latter can not correctly represent general rigid body motions. Thus it fails to meet the convergence criterion.

In the earlier days, efforts were mainly exerted on eliminating the singularities. One of the schemes is adding fictitious diagonal stiffness components to the element stiffness matrix. For example, if an three-node flat triangular element has five DOF at each node, after adding to it the artificial normal rotation stiffness, the element stiffness matrix becomes

$$[\,k\,]_{18\times18} = \begin{bmatrix} [k']_{15\times15} & [0]_{3\times15} \\ [0]_{15\times3} & [k_{\theta t}]_{3\times3} \end{bmatrix}_{18\times18} \tag{2.65}$$

where [k'] is the 15×15 stiffness matrix from the original element, $[0]_{15\times3}$ and $[0]_{3\times15}$ are null matrices, and the 3×3 matrix $[k_{\theta t}]$ is diagonal and contains three equally valued entries $k_{\theta t}$. In references [2.97] and [2.21] it was proposed to set $k_{\theta t} = 10^{-4}$, and $k_{\theta t} = 10^{-3}$ to 10^{-6} times of the smallest bending stiffness, respectively. Cook, Malkus and Plesha [2.98] and Zienkiewicz and Taylor [2.30] suggested the following matrix for $[k_{\theta t}]$,

$$[\,k_{\theta t}\,] = \alpha EV \begin{bmatrix} 1.0 & -0.5 & -0.5 \\ -0.5 & 1.0 & -0.5 \\ -0.5 & -0.5 & 1.0 \end{bmatrix}$$

in which E is the Young's modulus, V the element volume and α a value defined in the range $10^{-6} < \alpha < 10^{-2}$. This $[k_{\theta t}]$ provides each DDOF with a fictitious stiffness, but offers no resistance to the deformation mode $\theta_{t1} = \theta_{t2} = \theta_{t3} = 0.0$. Note that the values 10^{-4}, or 10^{-6} to 10^{-2}, and α are determined from numerical experiments and are thus truly artificial. This method provided nothing in improving elements' accuracy.

The AT and similar elements developed independently by Carpenter, Stolarski and Belytschko [2.24], at almost the same time, showed that the elements with DDOF may converge faster if the DDOF is properly formulated. Reference [2.24] also pointed out that introducing reduced integration to such formulation was essential if the element was to be successful in the analysis of shells. It referred this formulation as the degenerated LST. Later Cook [2.23] proved that AT could be regarded as the result of applying a co-ordinate transformation to an element that has mid-side nodes. By introducing a transformation matrix, one can transfer the linear strain triangle (LST) to AT. Similarly, it can transfer an eight-node quadrilateral element to a four-node Allman type quadrilateral element. References [2.22] and [2.23] showed that numerical results using the AT are better than those applying the constant strain triangle (CST), and they are not as good as those using the LST. However, in a large mesh the LST may produce more than twice as many DOF as the AT.

In contrast to those efforts solely on the choice of finite element interpolation fields, references [2.99] and [2.100] developed DDOF which relied on a variational

formulation employing an independent rotation field. This approach was based on Reissner's variational formulation [2.101] which utilized the skew-symmetric part of the stress tensor as a Lagrange multiplier to enforce the equality of independent rotations with the skew-symmetric part of the displacement gradient. Hughes and Brezzi [2.99] extended Reissner's formulation by recognizing the instability of discrete approximations and suggested a way to stabilize the instability of discrete approximation. Subsequently, reference [2.100] extended the application of Hughes and Brezzi [2.99] to combine an Allman-type interpolation for the displacement field with an independently interpolated rotation field. It demonstrated the high accuracy of the element developed by this approach.

In attempting to incorporate AT type of plane stress element into flat hybrid triangular shell elements, To and Liu [2.33] took the strategies introduced in references [2.22], [2.99-2.102] as starting point. They formulated the DDOF in the way of using constant or linear distribution of θ_t within the element. In reference [2.33], the formulation of DDOF in both hybrid and displacement sense were also proposed. In the hybrid formulation, the skew symmetric component of the in-plane torsional strain was considered. One strain parameter, which represents the constant in-plane torsional strain field within an element, was used. In the displacement type of DDOF formulation, it started with an energy equation and followed the traditional way of deriving element stiffness matrices. Numerical studies showed that the displacement type of DDOF formulation with linear θ_t and full integration gave the best results.

The revived interests, and increasing concern on formulating DDOF on a sound theoretical basis and a straightforward approach have reflected the importance of DDOF.

2.6.2 Hybrid formulation of DDOF

In Section 2.5, stiffness matrices for BT have been developed through the hybrid approach. In developing these stiffness matrices, the normal rotations at each element node had been included in the element nodal displacement vectors. But the strain energy due to normal rotations was neglected, the total potential energy equation did not include the contribution of θ_t. It seems that most of the Allman type elements available in the literature have neglected the torsional shear strain energy due to normal rotations. See for examples, references [2.22 - 2.24]. One may argue that this part of shear strain energy is very small compared with the others. Therefore, it can be disregarded. However, this may lead to problems, such as spurious modes. Reference [2.22] had reported an unusual type of zero energy mode in the AT. This phenomenon is most likely because the element lacks the internal "constrain". To eliminate this problem, the in-plane torsional shear strain energy due to normal rotations is considered.

By identifying [2.33]

$$\varepsilon^s_{rs} = \theta_t - \frac{1}{2}(v_{,r} - u_{,s}) \tag{2.66}$$

as the in-plane torsional shear strain related to the skew symmetric component of the in-plane shear stress tensor, one can write the total in-plane shear strains as

$$\varepsilon^t_{rs} = \varepsilon_{rs} + \varepsilon^s_{rs} \quad , \quad \varepsilon^t_{sr} = \varepsilon_{rs} - \varepsilon^s_{rs} \tag{2.67}$$

and the related shear stresses are

$$\sigma^t_{rs} = \sigma_{rs} + \sigma^s_{rs} \quad , \quad \sigma^t_{sr} = \sigma_{rs} - \sigma^s_{rs} \tag{2.68}$$

in which

$$\sigma_{rs} = G_{rs}\,\varepsilon_{rs} \quad , \qquad \sigma^{s}_{rs} = G_{rs}\,\varepsilon^{s}_{rs} \quad . \tag{2.69}$$

It should be noted that the symmetric part of the shear strain in equation (2.67) has been considered in the derivation of stiffness matrices of BT in Section 2.5. For the laminated composite shell elements, consistent with those BT, the stresses and strains are evaluated in an average sense. Therefore, the equivalent in-plane shear modulus for the laminate is

$$G_{rs} = \sum_{k=1}^{n} \frac{(G_{rs})_k (h_k - h_{k-1})}{h} \tag{2.70}$$

where $(G_{rs})_k$ is the in-plane shear modulus for k'th layer, h_k is the layer co-ordinate (see Figure 2.4), h the total thickness of the laminate and n the number of layers of the laminate.

In equation (2.29), the Allman type of interpolation functions has been assigned to u and v. As they are quadratic, their first order derivatives are linear. This makes sense to use a linear independent interpolation function of θ_t in equation (2.66). Thus, the linear field of θ_t from equation (2.30) is

$$\theta_t = \xi_1\,\theta_{t1} + \xi_2\,\theta_{t2} \qquad \xi_3 \quad . \tag{2.71}$$

Substituting equations (2.29) and (2.71) into equation (2.66) yields

$$\varepsilon^{s}_{rs} = \bar{B}_d\, q \quad , \tag{2.72}$$

$$\bar{B}_d = \left[\, \bar{B}_{d1}\ \bar{B}_{d2}\ \bar{B}_{d3} \,\right]_{1\times 18} \quad , \tag{2.73a}$$

where

$$\bar{B}_{di} = \left[\frac{1}{2}\xi_{i,s} \; -\frac{1}{2}\xi_{i,r} \; 0\;0\;0 \; \xi_i + \frac{1}{2}(\bar{p}_{i,s} - \bar{q}_{i,r})\right] . \tag{2.73b}$$

in which i = 1, 2, 3 and q is the nodal displacement vector defined in equation (2.35).

It is noted that in reference [2.33], the hybrid formulation of DDOF, identified there as k_d, was performed by using linear interpolation functions for u and v. Therefore, the displacement field is not Allman type.

For the assumed strain field of the skew symmetric in-plane shear strain, we use one strain parameter to represent a constant strain field while the symmetric components have already been considered in the assumed strain field for BT in Section 2.5

$$(\varepsilon^s_{rs})^\varepsilon = \alpha_{10} \tag{2.74}$$

Here, we do not invoke linear strain field because in that case we have to use three strain parameters which leads the formulation to its displacement-type counterpart.

With reference to equation (2.1), the strain energy due to the skew symmetric part of in-plane shear strains is

$$\pi^s = \int_v \left[(\varepsilon^s_{rs})^\varepsilon G_{rs} (\varepsilon^s_{rs})^u - \frac{1}{2} (\varepsilon^s_{rs})^\varepsilon G_{rs} (\varepsilon^s_{rs})^\varepsilon\right] dv \tag{2.75}$$

where the superscripts ε and u are again indicate the quantities from assumed strain and assumed displacement fields, respectively.

By following the same procedure in Section 2.5, the stiffness matrix k_{dh} due to the normal rotation is obtained as

$$k_{dh} = \frac{1}{a} \sum_{k=1}^{n} (G_{rs})_k (h_k - h_{k-1}) \int_a \bar{B}_d^T \, da \int_a \bar{B}_d \, da \, , \tag{2.76}$$

where the subscript dh indicates the stiffness of DDOF in hybrid sense.

The integrals are evaluated exactly. There is no numerical integration involved. Considering the element as a whole, equation (2.75) should be part of total potential energy. Adding this part to equation (2.4), the resulting element stiffness matrix in local co-ordinates becomes

$$k_e^h = k_e + k_{dh} \, . \tag{2.77a}$$

In global co-ordinate system, the element stiffness matrix is

$$K_e^h = K_e + K_{dh} \tag{2.77b}$$

in which

$$K_{dh} = T^T k_{dh} T \, . \tag{2.77c}$$

2.6.3 Displacement formulation of DDOF

Similar to previous hybrid formulation of DDOF, the in-plane torsional shear strain energy is considered. This consideration enhances the DDOF in the BT.

The in-plane torsional strain has been defined in equation (2.66). The potential energy due to in-plane torsional strain can be written as

$$\pi_t = \frac{1}{2} \int_v G_{rs} \left[\theta_t - \frac{1}{2} (v_{,r} - u_{,s}) \right]^2 dv \tag{2.78}$$

where G_{rs} is the in-plane shear modulus and defined in equation (2.70). Thus, we can recast equation (2.78) into a more convenient form

$$\pi_t = \frac{1}{2}\sum_{k=1}^{n}(G_{rs})_k (h_k - h_{k-1}) \int_a \left[\theta_t - \frac{1}{2}(v_{,r} - u_{,s})\right]^2 da \tag{2.79}$$

To adopt a linear field for θ_t and quadratic field for u and v, we substitute equations (2.29) and (2.71) into equation (2.79) and write

$$\left[\theta_t - \frac{1}{2}(v_{,r} - u_{,s})\right] = \bar{B}_d\, q \tag{2.80}$$

in which

$$\begin{aligned}\bar{B}_d = \frac{1}{2}\Bigg[& \frac{r_3 - r_2}{r_2 s_3}\cdot\frac{1}{r_2},\ 0,\ 0,\ 0,\ 2\xi_1 + \bar{p}_{1,s} - \bar{q}_{1,r}, \\ & -\frac{r_3}{r_2 s_3},\ -\frac{1}{r_2},\ 0,\ 0,\ 0,\ 2\xi_2 + \bar{p}_{2,s} - \bar{q}_{2,r}, \\ & \frac{1}{s_3},\ 0,\ 0,\ 0,\ 0,\ 2\xi_3 + \bar{p}_{3,s} - \bar{q}_{3,r}\Bigg]_{1\times 18} .\end{aligned} \tag{2.81}$$

Equation (2.81) is identical to that defined in equation (2.73a). By defining

$$k_{dd} = \sum_{k=1}^{n}(G_{rs})_k (h_k - h_{k-1}) \int_a \bar{B}_d^T\, \bar{B}_d\, da\ , \tag{2.82}$$

equation (2.79) can be rewritten as

$$\pi_t = \frac{1}{2}\, q^T\, k_{dd}\, q\ . \tag{2.83}$$

The stiffness matrix k_{dd} defined in equation (2.82) is that due to the in-plane shear strain energy of DDOF developed through displacement formulation. As equation (2.83) is the strain energy due to normal rotations, it should be added to equation (2.4). Therefore, the overall stiffness matrix for the flat laminated composite shell element in local co-ordinate system is

$$k_e^d = k_e + k_{dd} \tag{2.84a}$$

and the one in global co-ordinate system is

$$K_e^d = K_e + K_{dd} \tag{2.84b}$$

where the subscript dd denotes the stiffness of DDOF developed through displacement approach and

$$K_{dd} = T^T k_{dd} T \, . \tag{2.84c}$$

By evaluating the integral in equation (2.82) with exact or full integration, k_{dd} is obtained explicitly. If the integral is evaluated by one point quadrature or the reduced integration scheme, one has the equivalent

$$\int_a \bar{B}_d^T \tilde{B}_d \, da = \frac{1}{a} \int_a \bar{B}_d^T \, da \int_a \bar{B}_d \, da$$

Therefore, equation (2.76) and (2.82) are identical. It means that one point quadrature for evaluating equation (2.82), that is, reduced integration of equation (2.82) is equivalent to the hybrid formulation of DDOF.

2.7 Remarks

The hybrid strain based BT developed in Section 2.5 has six fundamental DOF at their nodes which include DDOF. Because of the absence of the in-plane shear strain energy due to the skew symmetric part of in-plane shear strain from the total potential energy equation, the DDOF formulation in the BT is not complete. To enhance DDOF in the BT, the skew symmetric part of the in-plane torsional shear strain was considered, which accounted for the contribution from θ_t. The resulting stiffness matrices k_{dh} and k_{dd} in Section 2.6 hinge on more sound theoretical basis. Therefore, the proposed laminated composite shell elements with enhanced DDOF are expected to give the best performance among those same type and available. In the following chapters, numerical studies will illustrate superior performance.

To summarize the hybrid laminated composite triangular shell (HLCTS) elements developed in this chapter, each element is identified as follows

(1) HLCTS^{lh} $k_e^{lh} = k_e^{l} + k_{dh}$, linear w in BT + hybrid DDOF;

(2) HLCTS^{qh} $k_e^{qh} = k_e^{q} + k_{dh}$, quadratic w in BT + hybrid DDOF;

(3) HLCTS^{ld} $k_e^{ld} = k_e^{l} + k_{dd}$, linear w in BT + displacement DDOF;

(4) HLCTS^{qd} $k_e^{qd} = k_e^{q} + k_{dd}$, quadratic w in BT + displacement DDOF.

That is, each of the above element stiffness matrix contains two parts. One is from the BT, and the another from the independently formulated DDOF. All these elements are three-node flat laminated composite triangular shell elements. They all have six DOF at each node. Thus, they are the simplest elements for general laminated composite shell analysis. Note also that for the special cases of single layer shell elements, k_e^{lh} becomes $AT+(k_t^{1})'$ and k_e^{ld} reduces to $AT+(k_t^{3})'$ in reference [2.23].

Comparing these four elements, HLCTS^{qd} is most favourable with respect to accuracy and rank sufficiency. HLCTS^{ld} and HLCTS^{qd} are rank sufficient since the displacement formulation of DDOF is equivalent to employing three strain parameters in the strain field if the hybrid formulation is performed. In this sense, HLCTS^{ld} and HLCTS^{qd} provide no inconsistency to the hybrid formulation though the displacement type of DDOF is adopted. As HLCTS^{qd} is formulated by assuming a quadratic field for w, it improves the accuracy over the HLCTS^{ld}.

CHAPTER 3

STATIC ANALYSIS OF LAMINATED COMPOSITE PLATE AND SHELL STRUCTURES

The hybrid strain based triangular laminated composite shell elements proposed in the last chapter are used to solve static problems in this chapter. Several typical cases are selected to illustrate the performance of the new elements. Both plate and shell problems are included. The first section is concentrated on single layer plates. The second is on multilayer plates. The third section is concerned with the analysis of single layer shells and the fourth multilayer shells. Closing remarks are included in the final section.

3.1 Analysis of Single Layer Plates

Results of numerical analysis of a variety of plate problems by using the elements are presented. These numerical studies are used to examine the performance of the flat shell elements on predicting responses of plates. The samples studied are a plane stress cantilever beam, square plates and rhombic plates. In the analysis, different loading and boundary conditions are imposed.

3.1.1 Plane stress cantilever subjected to a tip load

A cantilever beam of rectangular cross-section is selected to test the membrane part of the new elements. This application has been used for testing plane stress elements, see for examples, references [3.1-5]. The cantilever beam is subjected to a tip load shown

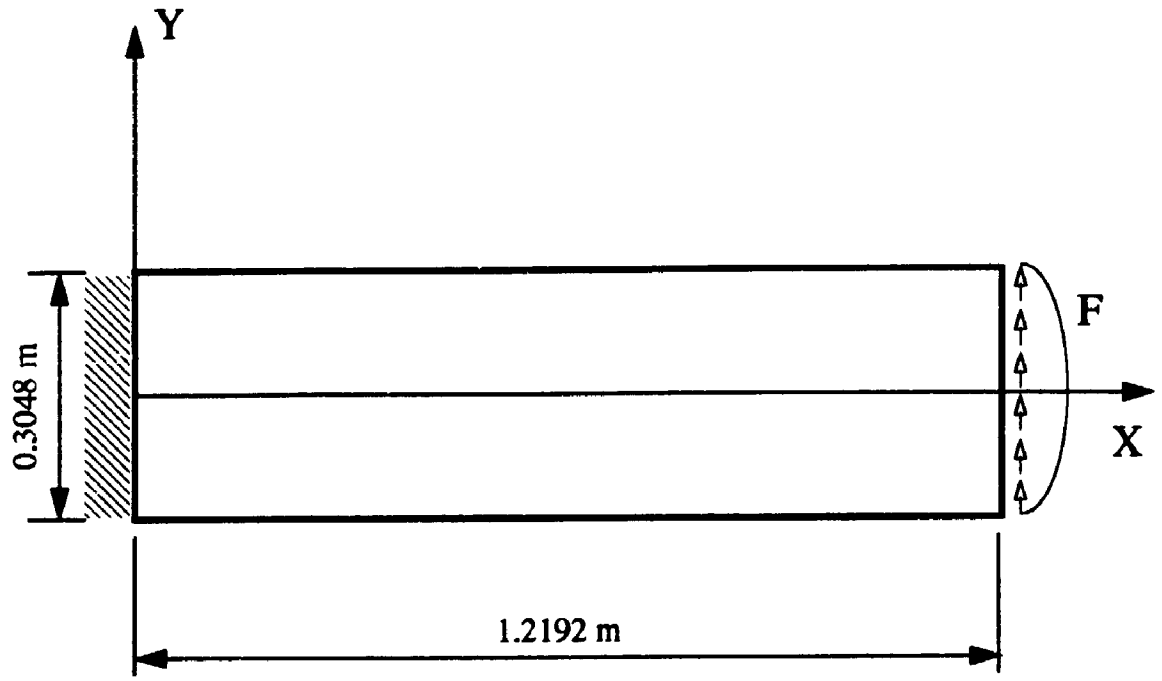

Figure 3.1 Plane stress cantilever beam
(E=2.0685×10^{11} N/m^2; ν=0.25; F=177920 N; thickness = 0.0254 m)

in Figure 3.1. The load is a parabolically distributed shear stress applied at the free end of the beam. The total load F is 177920 N (40,000 lb). The geometrical dimensions of the beam are: length = 1.2192 m (48 in); height = 0.348 m (12 in) and thickness = 0.0254 m (1 in). The material properties are: Young's modulus E = 2.0685×10^{11} N/m^2 (3.0×10^7 psi) and Poisson's ratio ν = 0.25. The exact in-plane tip deflection and rotation were quoted as 9.0373×10^{-3} m (0.3558 in) and 0.0106 radians in references [3.2] and [3.5].

In the numerical studies, the cantilever beam was discretized and modeled by seven different meshes: 4 × 1 B, 4 × 1 D, 8 × 2 C, 8 × 2 D, 16 × 4 A, 16 × 4 E and 16 × 4 D. The detail layout of these meshes are shown in Figures 3.2, 3.3 and 3.4. The parabolically distributed tip load is approximated by the concentrated loads applied at the corresponding nodal points. For different meshes, the load distributions on the nodes at the end of the beam are illustrated in Figure 3.5. In order to test the membrane part of the elements, all W, Θ_x and Θ_y DOF at element nodes were constrained. The boundary conditions at the fixed end are U = V = Θ_z = 0.0. As the transversal displacement W has been constrained in the analysis, the linear or quadratic field for w does not affects the results.

Table 3.1 includes computed tip displacements by using the finite elements. The results are normalized with respected to the exact solution. In the table, BT+k_{dd} denotes the results obtained by using $HLCTS^{ld}$ or $HLCTS^{qd}$; BT+k_{dh} denotes those obtained by using $HLCTS^{lh}$ or $HLCTS^{qh}$; CST refers to the results given by a hybrid strain based CST element [2.33] and neq. is the number of unknowns or equations being solved in which the equations correspond to the constrained DOF have been eliminated. Compared with CST results, the new elements appeared to be more accurate and converged faster. The results also show that the cross diagonal meshes, 4 × 1 D, 8 × 2 D and 16 × 4 D give better results. The 4 × 1 D mesh has 16 elements and 24 unknowns predicted the displacements with errors 5.73% and 5.34% by using BT+k_{dd} and BT+k_{dh}, respectively, while the corresponding errors given by the 8 × 2 C mesh are 9.39% and 8.93%. The 8 × 2 C mesh has 32 elements and 72 unknowns. Similarly, mesh 8 × 2 D has just half of the elements that the meshes 16 × 4 A and 16 × 4 E have, but it gives more accurate

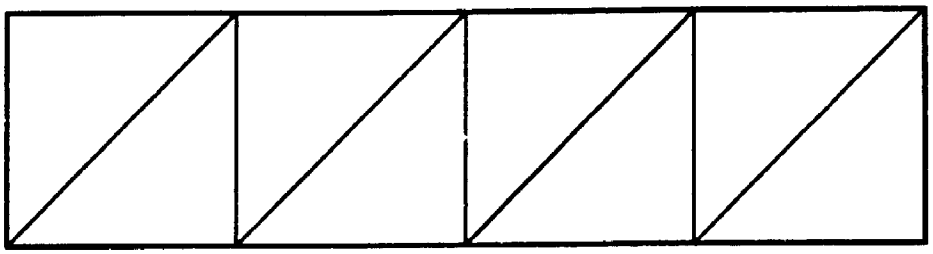

4×1 B

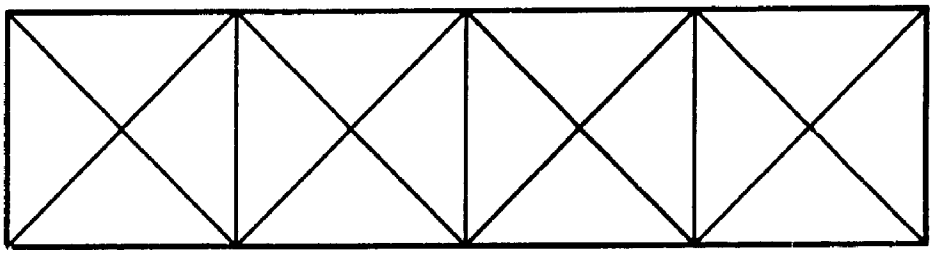

4×1 D

Figure 3.2 4 × 1 meshes for the plane stress cantilever beam

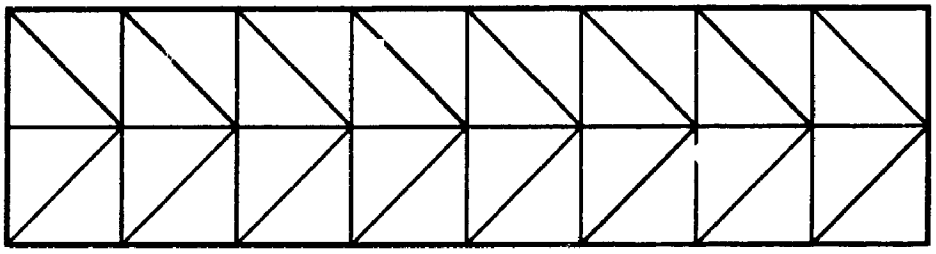

8×2 C

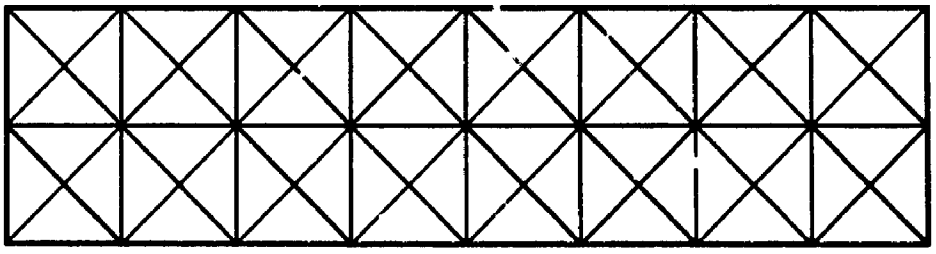

8×2 D

Figure 3.3 8 × 2 meshes for the plane stress cantilever beam

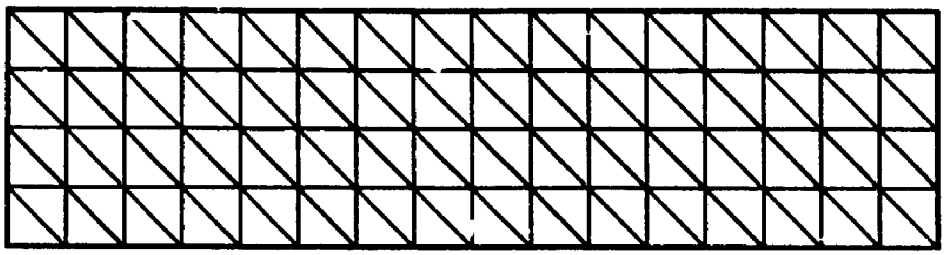

16×4 A

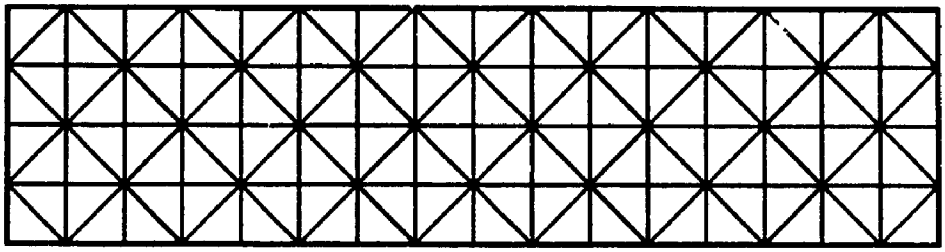

16×4 E

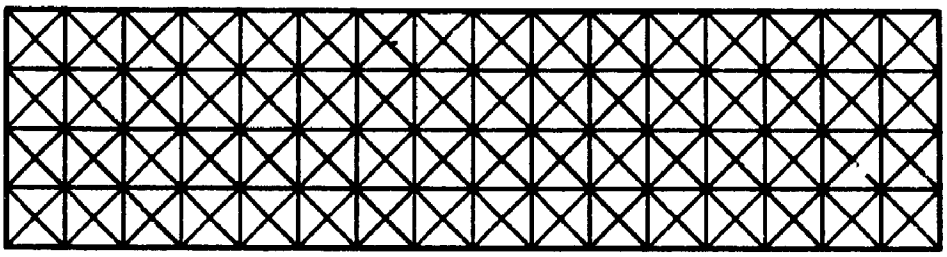

16×4 D

Figure 3.4 16×4 meshes for the plane stress cantilever beam

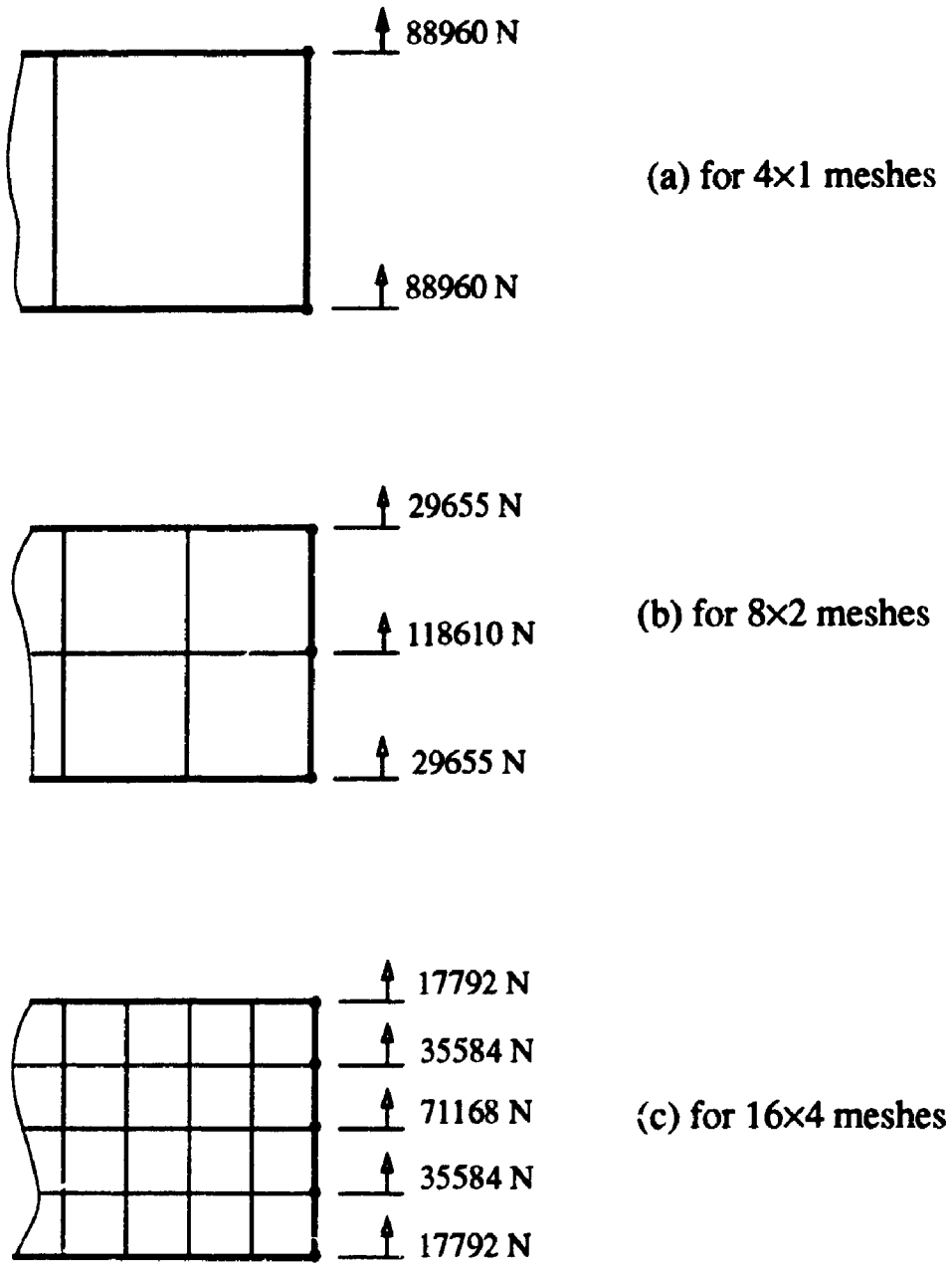

Figure 3.5 Load distributions on the nodes at the end of the beam

Table 3.1 Normalized tip displacement of the cantilever beam

mesh	neq.	Normalized tip displacement		
		CST	BT + k_{dd}	BT + k_{dh}
4 × 1 B	24	0.2551	0.7487	0.7584
4 × 1 D	36	0.5784	0.9427	0.9466
8 × 2 C	72	0.5583	0.9061	0.9107
8 × 2 D	120	0.8385	0.9806	0.9817
16 × 4 A	240	0.8265	0.9685	0.9694
16 × 4 E	240	-	0.9733	0.9744
16 × 4 D	432	0.9530	0.9944	0.9947

results than the other two. When comparing the results given by BT+k_{dd} and BT+k_{dh}, BT+k_{dh} predicted 0.49% more accurate response than BT+k_{dd} with 4 × 1 B mesh. As k_{dd} is from displacement formulation, BT+k_{dd} is stiffer than BT+k_{dh}, in which k_{dh} is obtained by hybrid formulation. When meshes are refined the difference vanished and the results from both elements converged to the analytical solution.

The normalized tip rotations obtained by using BT+k_{dd} and BT+k_{dh} are given in Table 3.2. It shows that even the coarse meshes predicted accurate tip rotations. The same trend shown in Table 3.1 can also be found in Table 3.2. The cross diagonal meshes (D meshes) provide more accurate results though less elements are used when compared with other type of meshes.

A comparison made with other finite elements is presented in Table 3.3. These

elements are those from Olson and Bearden (OB) [3.1], Allman [3.4] and the linear strain triangle (LST) [3.6], respectively. In the table, the numbers inside brackets are the total number of DOF before the application of boundary conditions. The values of the tip displacement obtained by using the present elements are better than OB and very close to those by AT. The differences given by BT+k_{dd}, with respect to AT, are 1.18%, 1.13% and 0.23% for the meshes 4 × 1 B, 8 × 2 C and 16 × 4 E, respectively. The differences by BT+k_{dh} are 0.09%, 0.63% and 0.11%. It can be seen that LST gives the best result. But for the same mesh, LST has more than twice as many DOF as that applying the new elements.

Table 3.2 Normalized tip rotation of the cantilever beam

mesh	neq.	Normalized tip rotation	
		BT + k_{dd}	BT + k_{dh}
4 × 1 B	24	0.8980	0.9478
4 × 1 D	36	0.9896	0.9943
8 × 2 C	72	0.8754	0.8617
8 × 2 D	120	0.9830	0.9840
16 × 4 A	240	0.9774	0.9792
16 × 4 E	240	0.9811	0.9849
16 × 4 D	432	0.9972	0.9972

Table 3.3 Comparison of the results obtained by using different elements

element	Normalized tip displacement		
	4 × 1 B	8 × 2 C	16 × 4 E
OB	0.6470 (30)	0.8384 (81)	0.9250 (255)
AT	0.7577 (30)	0.9165 (81)	0.9755 (255)
LST	-	0.9977 (170)	0.9994 (594)
BT + k_{dd}	0.7487 (30)	0.9061 (81)	0.9733 (255)
BT + k_{dh}	0.7584 (30)	0.9107 (81)	0.9744 (255)

3.1.2 Simply supported plate under uniformly distributed load

In this sample, we select a square plate which is simply supported at all four sides (S4). The side length, b, of the plate is 1 m (39.37 in). The material properties are Young's modulus E = 2.0685×10^{11} N/m^2 (3.0×10^7 psi); ν = 0.3. The analytical solution for simply supported square plates subjected to uniformly distributed loading can be found in reference [3.7]. If the load with intensity f_0 transversally applied to the plate, the maximum deflection occurs at the centre of the plate. The value of the deflection is

$$W_{max} = 0.00406 \frac{f_0 b^4}{D} \tag{3.1}$$

where

$$D = \frac{E h^3}{12(1-\nu^2)}$$

2

PM-1 3½"x4" PHOTOGRAPHIC MICROCOPY TARGET
NBS 1010a ANSI/ISO #2 EQUIVALENT

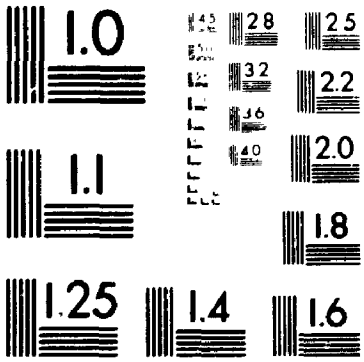

PRECISION[SM] RESOLUTION TARGETS

is the bending rigidity, in which h is the thickness of the plate.

Three sets of thicknesses and loadings are used: (1) h = 0.01 m (0.3937 in), f_0 = 1000 N/m^2 (0.14504 psi); (2) h = 0.001 m (0.03937 in), f_0 = 1 N/m^2 (0.14504×10^{-3} psi); (3) h = 0.0001 m (0.003937 in), f_0 = 0.001 N/m^2 (0.14504×10^{-6} psi). The reason for selecting different loading while changing the thickness is to present some realistic responses that confine to the linear theory at this stage of the investigation.

The analytical solution calculated from equation (3.1) for this problem is 2.14335 $\times$ 10^{-4} m for all three sets of data. In the finite element analysis, one quarter of the plate is considered due to symmetry of geometry and loading (see Figure 3.6). Though different types of finite element meshes were used during the tests, only a D type is adopted here. The D type mesh is the cross diagonal mesh shown in Figures 3.6 and 3.7. Mesh D gives more reliable results when compared with other types of meshes, such as cross hatch. Figure 3.7 shows six D meshes: 1 $\times$ 1 D, 2 $\times$ 2 D, 3 $\times$ 3 D, 4 $\times$ 4 D, 5 $\times$ 5 D and 6 $\times$ 6 D. The integers indicates the number of elements along the sides of the models. The 1 $\times$ 1 D mesh can also be looked at as a macro element which has five nodes. It consists of four triangular elements. The other meshes are composed by a number of the macro elements. To test the bending components of the new elements, the membrane part is constrained: U = V = Θ_z = 0.0. The boundary conditions for the S4 plate are interpreted and applied to the finite element model as follows: on the symmetrical lines, Θ_x = 0.0 for the side parallel to x axis and Θ_y = 0.0 for the one parallel to y axis; at the central point Θ_x = Θ_y = 0.0; on the simply supported edges, transversal displacement is constrained, that is W = 0.0, while setting Θ_x = 0.0 for the nodes on y axis and Θ_y = 0.0 for those on x axis (see Figure 3.6). The shear correction

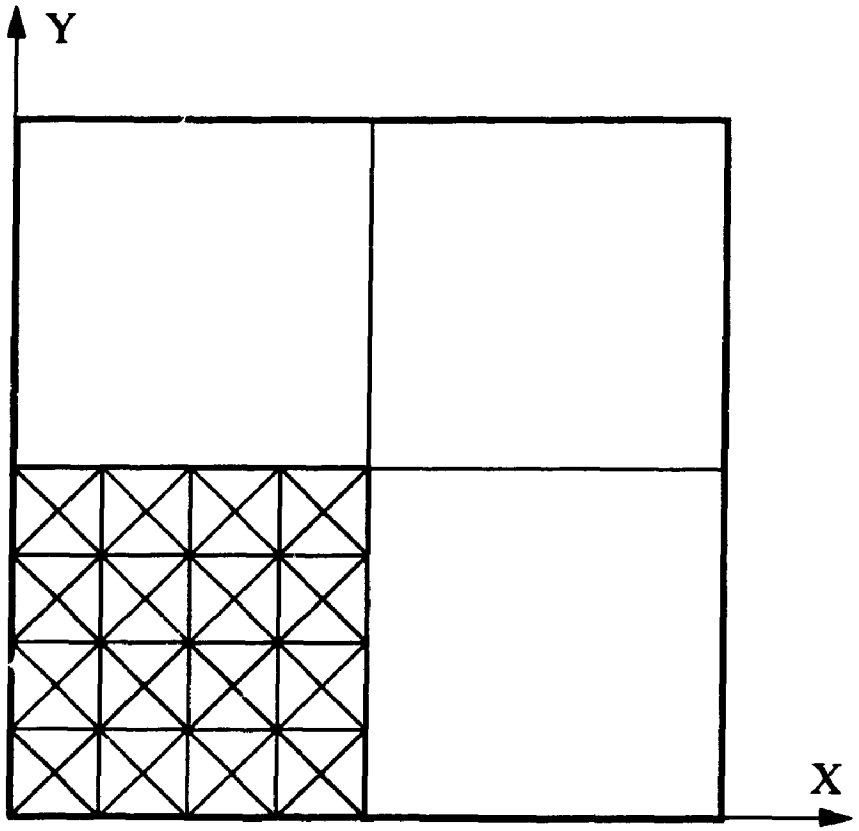

Figure 3.6 A 4 × 4 D mesh for modeling quarter of a square plate

factor is set to $\kappa = 5/6$. Table 3.4 presents the finite element results. The latter are normalized by the analytical solution given in equation (3.1). As all normal rotations were constrained, only the results by HLCTS^{ld} and HLCTS^{qd} are shown in Table 3.4.

The results in Table 3.4 show good convergence rate. HLCTS^{qd} predicted the maximum deflections with an error of 28% by using the 1 × 1 D mesh (2 elements) When 2 × 2 D mesh (16 elements) used, the error is about 6.5%. For the refined meshes, 4 × 4 D (64 elements), 5 × 5 D (100 elements) and 6 × 6 D (144 elements) the errors rapidly reduced to 1.6%, 1.0% and 0.7%, respectively. Compared with

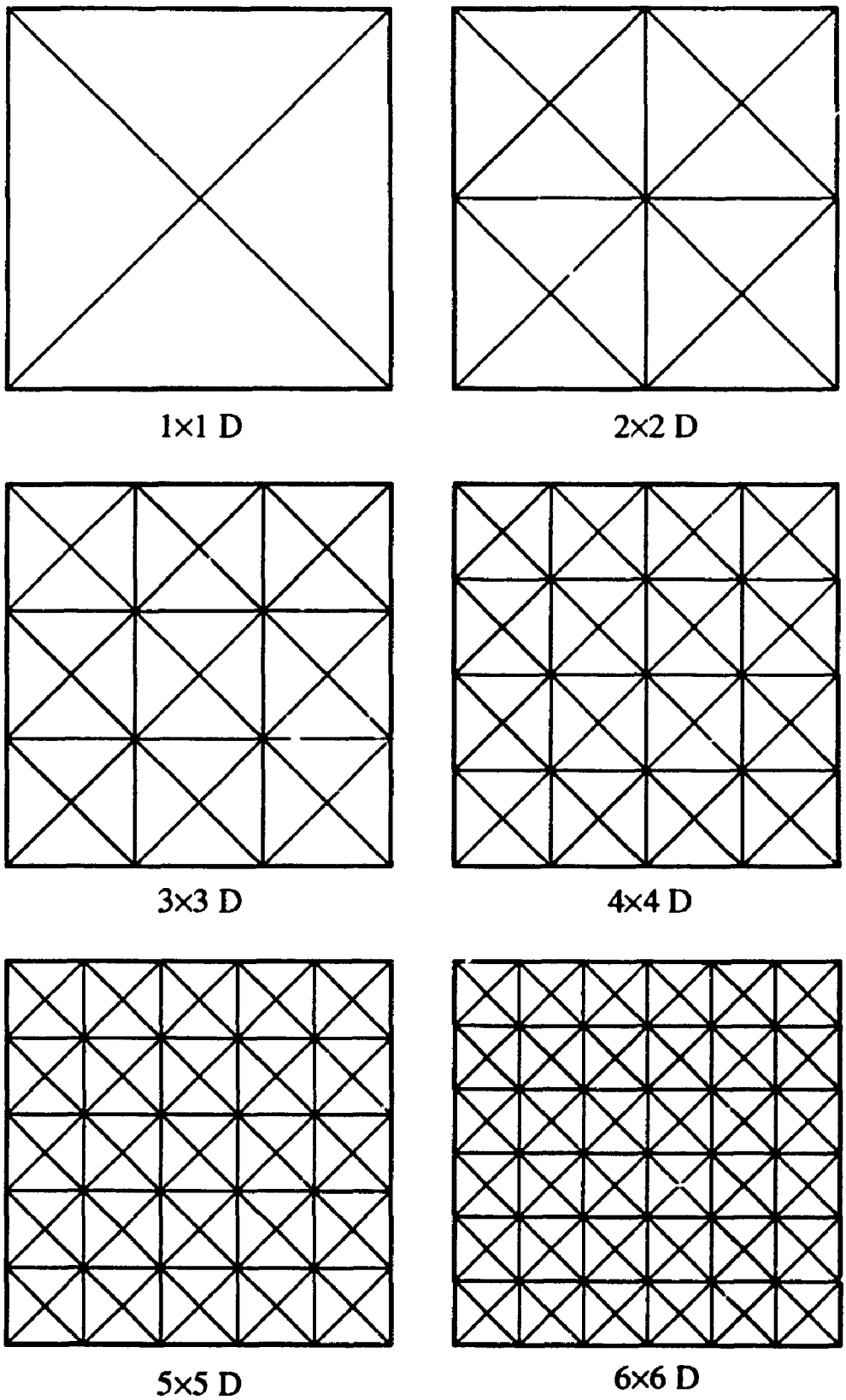

Figure 3.7 Meshes for square plates

Table 3.4 Normalized maximum displacement of the S4 plate under uniformly distributed load

mesh	μ	$f_0(N/m^2)$	neq.	Normalized maximum displacement	
				HLCTS^{ld}	HLCTS^{qd}
1 × 1 D	10^2	1000.0	6	-	0.7227
	10^3	1.0	6	-	0.7218
	10^4	0.001	6	-	0.7218
2 × 2 D	10^2	1000.0	24	0.9131	0.9359
	10^3	1.0	24	0.9121	0.9345
	10^4	0.001	24	0.9121	0.9345
3 × 3 D	10^2	1000.0	54	-	0.9723
	10^3	1.0	54	-	0.9709
	10^4	0.001	54	-	0.9695
4 × 4 D	10^2	1000.0	96	0.9793	0.9854
	10^3	1.0	96	0.9779	0.9840
	10^4	0.001	96	0.9779	0.9840
5 × 5 D	10^2	1000.0	150	-	0.9910
	10^3	1.0	150	-	0.9900
	10^4	0.001	150	-	0.9900
6 × 6 D	10^2	1000.0	216	0.9919	0.9942
	10^3	1.0	216	0.9905	0.9933
	10^4	0.001	216	0.9900	0.9928

HLCTS^{qd}, HLCTS^{ld} predicted slightly small deflection. In 2 × 2 D mesh case, this difference is about 2.3% of the analytical solution. For 4 × 4 D and 6 × 6 D mesh, the respective differences are about 0.6% and 0.25%. It can be seen that HLCTS^{qd} results converged faster than HLCTS^{ld}. In coarse meshes, HLCTS^{qd} provides better solutions. The analytical solution from equation (3.1) is based on the classical plate theory, and therefore, is for thin plates. The side length to thickness ratios μ = b/h tested in this sample are 100, 1000 and 10000. As μ becomes higher, the elements seem to predict less accurate deflections. However, by using 4 × 4 D and finer meshes, the differences are never more than 0.14%. In passing it is noted that no shear locking has been detected during the computational experiments.

3.1.3 Simply supported plate subjected to a point load

The S4 plate considered above is adopted here, except that the uniformly distributed load is now replaced by a central point load. The geometrical and material properties remain the same. The analytical solution for simply supported square plates subjected to a transversal concentrated load was given in reference [3.7]. From reference [3.7], the maximum displacement at the centre of the plate is

$$W_{max} = 0.01160 \frac{F\, b^2}{D} \quad . \tag{3.2}$$

Three cases are considered in this example. The thicknesses and loads for these three cases are : (1) h = 0.01 m (0.3937 in), F = 1000 N (224.8 lbf); (2) h = 0.001 m (0.03937 in), F = 1 N (0.2248 lbf); (3) h = 0.0001 m (0.003937 in), F = 0.001 N (0.0002248 lbf). The analytical solution calculated from equation (3.2) for this problem

is 6.1239×10^{-4} m for all three cases. As one quarter of the plate is considered, the load applied to the quarter plate is one fourth of the total load. The boundary conditions applied have been explained previously. The results obtained by using the HLCTS^{qd} element are normalized with respect to the analytical solutions and presented in Table 3.5. The discrepancies in this case corresponding to the six meshes from coarse to fine are, respectively, 32.49%, 12.65%, 6.40%, 3.77%, 2.43% and 1.63% for the length to thickness ratio $\mu = 100$. The results for the other two length to thickness ratios, 1000 and 10000, have slightly more discrepancies compared with the ratio of 100. The discrepancies, with respect to analytical solution, are 4.2%, 2.4% and 2.1%, respectively for the 4 × 4 D, 5 × 5 D and 6 × 6 D meshes. But, one may have noticed that the results for the ratios of $\mu = 1000$ and $\mu = 10000$ are closely similar when the same meshes are used. Another property of the elements shown in Tables 3.4 and 3.5 is that the results approach the analytical solutions from below, or, the elements predict lower bound responses.

3.1.4 Fully clamped plate under uniformly distributed load or point load

The plate used for the simply supported cases is now fully clamped. It is designated by C4. When the clamped boundary condition is applied to the finite element models, all DOF of the nodes at the clamped boundary are constrained. The boundary condition at the symmetry lines are the same as in the S4 plates. In this test example, the membrane component of the shell element is still constrained. That is, $U = V = \Theta_z = 0.0$. The analytical solution for uniformly distributed load is

$$W_{max} = 0.00126 \frac{f_0 b^4}{D} , \tag{3.3}$$

and for central point load is

$$W_{max} = 0.00560 \frac{F b^2}{D} . \tag{3.4}$$

These solutions are for thin plates [3.7]. For the given loads and corresponding thicknesses, the analytical solutions calculated from equations (3.3) and (3.4) are $W_{max} = 0.66517 \times 10^{-4}$ m and $W_{max} = 0.2956 \times 10^{-3}$ m, respectively.

In Table 3.6, the central displacements, W_c, predicted by using HLCTS^{qd} is normalized with the analytical solution, W_{max}. The results for the C4 plate under uniformly distributed loads are again better than point loads. In the case of $\mu = 100$ and 6×6 D mesh, the discrepancies are 1.8% for distributed load and 3.6% for point load. Convergence trend similar to Tables 3.4 and 3.5 can be found in Table 3.6. Excellent convergence rate is observed. The results are less satisfactory than those of the S4 plate. To improve the accuracy finer meshes are required for the fully clamped plates. Another method of improving the results is by refining the mesh along the clamped edges where severe changes of bending moment are expected.

3.1.5 Fully clamped rhombic plate under uniform load

Skew plate problem has been the subject of considerable interest in the finite element literature. It was chosen as a finite element test case by many researchers. See, for examples, references [3.8 - 3.15].

Table 3.5 Normalized maximum displacement of the S4 plate subjected to central point load

mesh	μ	F (N)	neq.	normalized displacement
1 × 1 D	10^2	1000.0	6	0.6751
	10^3	1.0	6	0.6734
	10^4	0.001	6	0.6734
2 × 2 D	10^2	1000.0	24	0.8735
	10^3	1.0	24	0.8700
	10^4	0.001	24	0.8699
3 × 3 D	10^2	1000.0	54	0.9360
	10^3	1.0	54	0.9318
	10^4	0.001	54	0.9300
4 × 4 D	10^2	1000.0	96	0.9623
	10^3	1.0	96	0.9577
	10^4	0.001	96	0.9576
5 × 5 D	10^2	1000.0	150	0.9757
	10^3	1.0	150	0.9710
	10^4	0.001	150	0.9710
6 × 6 D	10^2	1000.0	216	0.9837
	10^3	1.0	216	0.9788
	10^4	0.001	216	0.9788

Table 3.6 Normalized maximum displacement of the C4 plate under uniformly distributed load or central point load

mesh	μ	neq.	distributed load		point load	
			$f_0(N/m^2)$	W_c/W_{max}	F (N)	W_c/W_{max}
2 × 2 D	10^2	20	1000.0	0.7807	1000.0	0.7053
	10^3	20	1.0	0.7751	1.0	0.6976
	10^4	20	0.001	0.7750	0.001	0.6976
3 × 3 D	10^2	48	1000.0	0.8986	1000.0	0.8488
	10^3	48	1.0	0.8917	1.0	0.8390
	10^4	48	0.001	0.8870	0.001	0.8349
4 × 4 D	10^2	88	1000.0	0.9461	1000.0	0.9120
	10^3	88	1.0	0.9389	1.0	0.9012
	10^4	88	0.001	0.9387	0.001	0.9012
5 × 5 D	10^2	140	1000.0	0.9689	1000.0	0.9445
	10^3	140	1.0	0.9619	1.0	0.9334
	10^4	140	0.001	0.9617	0.001	0.9334
6 × 6 D	10^2	204	1000.0	0.9816	1000.0	0.9635
	10^3	204	1.0	0.9746	1.0	0.9520
	10^4	204	0.001	0.9737	0.001	0.9509

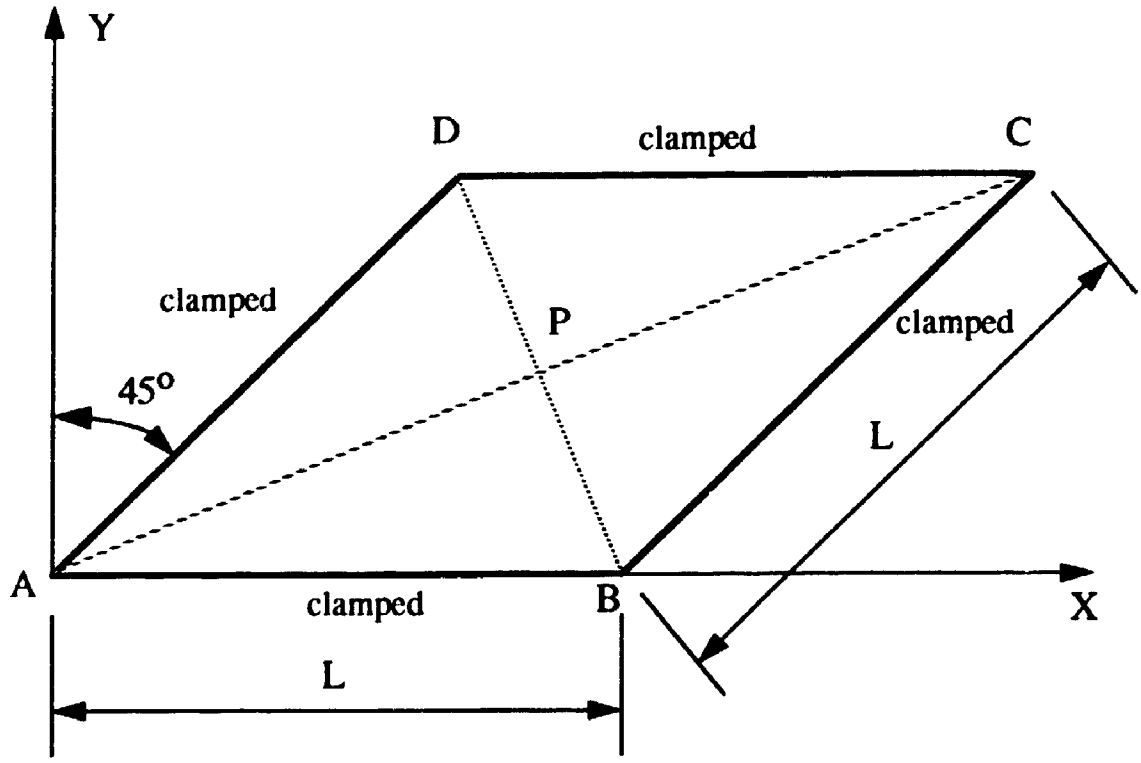

Figure 3.8 Fully clamped skew rhombic plate

Figure 3.8 shows a fully clamped (C4) rhombic plate under transversally applied uniform pressure. The load intensity is f_0 = 766.11 N/m^2 (16 lb/ft^2). The geometrical and material properties of the rhombic plate are: side length L = 2.4384 m (8 ft); thickness h = 0.024384 m (0.08 ft); Young's modulus E = 0.4183 × 10^{10} N/m^2 (8.736 × 10^7 lb/ft^2) and Poisson's ratio ν = 0.3. The length to thickness ratio μ = 100. The skew angle is 45°. The analytical solution for the central displacement (at point P) was reported in reference [3.16] to be W_{an} = 1.8385 × 10^{-3} m (6.032 × 10^{-3} ft).

In the finite element analysis, type D meshes are used. A 4 × 4 D mesh for the

rhombic plate is shown in Figure 3.9 (a). The shear correction factor is chosen to be $\kappa = 5/6$. The boundary conditions applied at the four clamped edges are $W = \Theta_x = \Theta_y = 0.0$. All DOF of U, V and Θ_z are constrained. The finite element results obtained by using HLCTS^{qd} are normalized with respect to W_{an} and presented in Table 3.7. A 10 × 10 A mesh, see Figure 3.9 (b), is also used to solve this problem. The results in the table show that this problem need relatively refined mesh. The mesh 10 × 10 D gives better results than 10 × 10 A does. Taking into the consideration of the number of unknown solved, mesh type D gives more accurate results in the foregoing analysis of rectangular plates, while mesh type A and D in this case provide similar accuracy. This is because elements in D mesh are distorted when modelling the rhombic plate (see Figure 3.9). That is, the element side length ratio is large, and the elements in mesh type A have a side length ratio closed to one which is preferred. Nevertheless, both mesh A and D give satisfactory results in analyzing the C4 rhombic plate.

Table 3.7 Normalized central displacement of the C4 rhombic plate

mesh	neq.	W_p/W_{an}
4 × 4 D	75	0.6464
6 × 6 D	183	0.8554
8 × 8 D	339	0.9312
10 × 10 A	243	0.8927
10 × 10 D	543	0.9644
12 × 12 D	795	0.9811

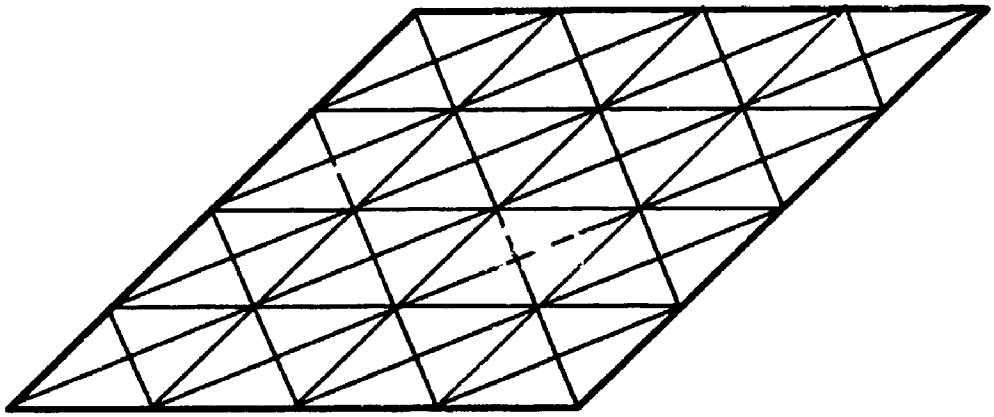

(a) 4 × 4 D mesh

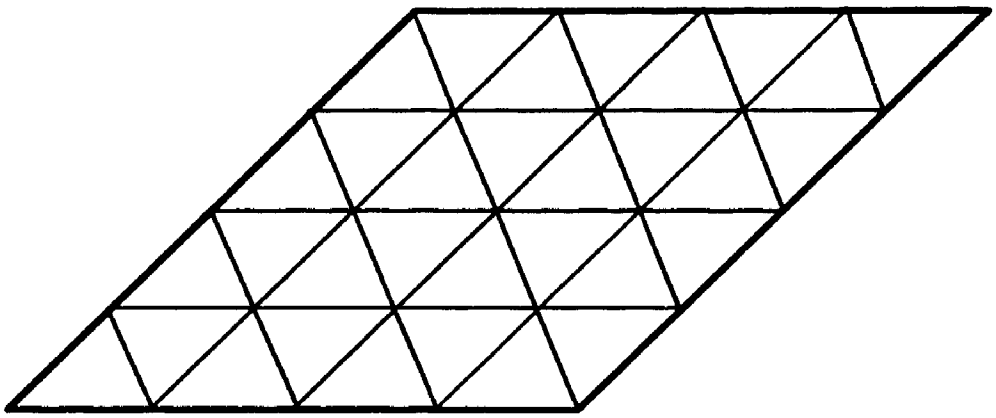

(b) 4 × 4 A mesh

Figure 3.9 Meshes for rhombic plate

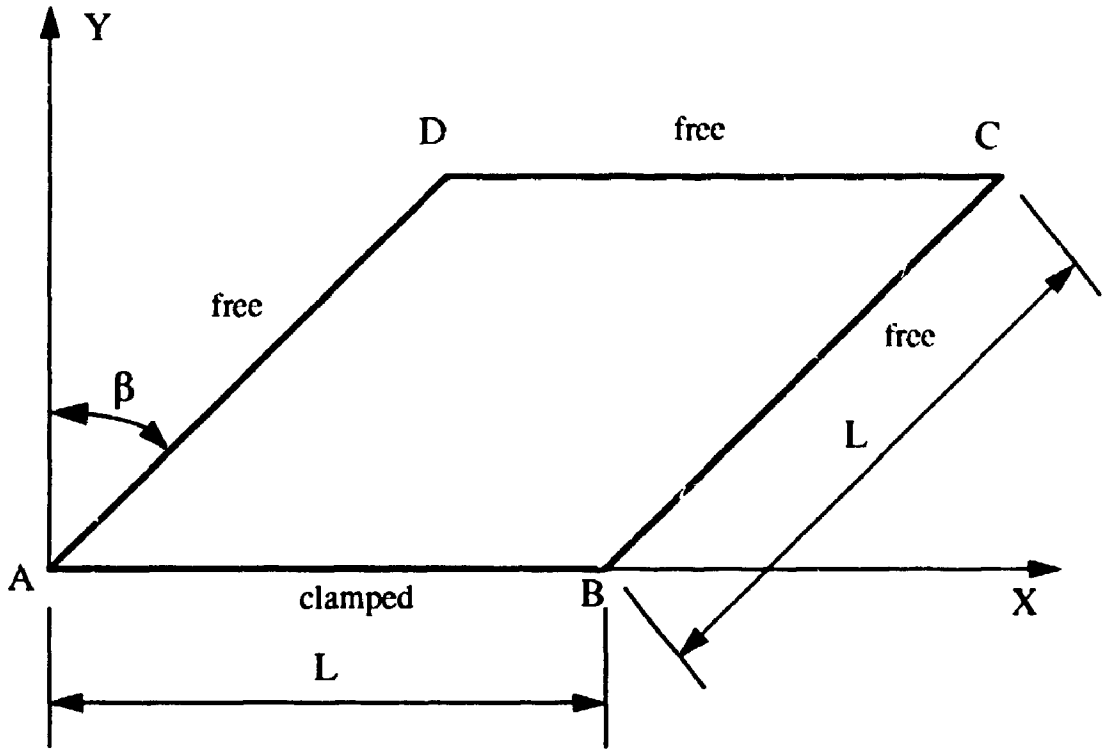

Figure 3.10 Cantilever rhombic plate

3.1.6 Cantilever rhombic plate under uniform load

A cantilever rhombic plate is shown in Figure 3.10. This problem is solved for the skew angle β = 20°, 40° and 60°, respectively. The plate is subjected to a transversally applied uniform distributed load with the load intensity f_0 = 1000 N/m^2 (0.1450 psi). The side length L = 1.0 m (39.37 in) and the thickness h = 0.04 m (1.5748 in). Thus, the length to thickness ratio is μ = 25. The material properties are: Young's modulus E = 2.0685×10^{11} N/m^2 (3.0×10^7 psi); Poisson's ratio ν = 0.3.

The finite element analysis is carried out by using type A meshes. A 4 × 4 A

mesh layout is illustrated in Figure 3.9 (b). The shear correction factor is $\kappa = 5/6$. The boundary conditions applied at the clamped edge is the same as those for C4 rhombic plate. The membrane part of the elements is neglected for this bending problem. The displacements at the point C and D are solved. The dimensionless displacements $W' = WEh^3/f_0L^4$ at point C and D are given in Table 3.8 and 3.9, respectively. The tables show the convergence rate with the five selected meshes, 2 × 2 A, 4 × 4 A, 6 × 6 A, 8 × 8 A and 10 × 10 A. Comparison to results obtained by researchers using other finite elements or approach are shown in Table 3.10. These results are obtained from a flat triangular element derived based on the concepts of natural mode and matrix displacement methods together with decomposition and lumping ideas (called LACOT) [3.12], a cubic isoparametric element [3.13], parallelogrammic elements [3.14, 15] and the variational method [3.17]. The $HLCTS^{ld}$ and $HLCTS^{qd}$ results are given by using the 10 × 10 A mesh. It can be seen that $HLCTS^{ld}$ and $HLCTS^{qd}$ results agree very well with those from other sources. In the $\beta = 20^\circ$ case, the average dimensionless deflection at point C predicted by finite elements and variational approach in references [3.12 - 3.15] and [3.17] is 1.4213. A value of 1.4205 is predicted by using $HLCTS^{ld}$ and $HLCTS^{qd}$. The discrepancy is 0.056%. The maximum discrepancy found is in the case $\beta = 20^\circ$ and the deflection at point D. Reference [3.13] reported a value of 1.0442 which is the largest one reported in the five references. The current analysis using $HLCTS^{qd}$ gives a value of 1.0474 which is 0.31% higher than that reported in reference [3.13]. The defection W' at point C reported in reference [3.17] for $\beta = 40^\circ$ and 60° are not considered in this comparison.

Table 3.8 Dimensionless displacement at point C of the cantilever rhombic plate under uniformly distributed load

mesh	neq.	W'	
		HLCTS^{ld}	HLCTS^{qd}
$\beta = 20°$			
2 × 2 A	18	1.1457	1.1928
4 × 4 A	60	1.3230	1.3358
6 × 6 A	126	1.3874	1.3927
8 × 8 A	216	1.4086	1.4125
10 × 10 A	330	1.4205	1.4205
$\beta = 40°$			
2 × 2 A	18	0.7980	0.7694
4 × 4 A	60	1.0261	1.0179
6 × 6 A	126	1.1110	1.1069
8 × 8 A	216	1.1433	1.1409
10 × 10 A	330	1.1590	1.1574
$\beta = 60°$			
2 × 2 A	18	0.6119	0.5216
4 × 4 A	60	0.7122	0.6875
6 × 6 A	126	0.7718	0.7601
8 × 8 A	216	0.8009	0.7943
10 × 10 A	330	0.8179	0.8135

Table 3.9 Dimensionless displacement at point D of the cantilever rhombic plate under uniformly distributed load

mesh	neq.	W'	
		$HLCTS^{ld}$	$HLCTS^{qd}$
$\beta = 20^{\circ}$			
2 × 2 A	18	1.0415	1.1443
4 × 4 A	60	1.0264	1.0521
6 × 6 A	126	1.0363	1.0478
8 × 8 A	216	1.0409	1.0476
10 × 10 A	330	1.0432	1.0474
$\beta = 40^{\circ}$			
2 × 2 A	18	0.4451	0.4937
4 × 4 A	60	0.5029	0.5158
6 × 6 A	126	0.5282	0.5340
8 × 8 A	216	0.5371	0.5404
10 × 10 A	330	0.5412	0.5433
$\beta = 60^{\circ}$			
2 × 2 A	18	0.0859	0.0975
4 × 4 A	60	0.1251	0.1282
6 × 6 A	126	0.1397	0.1410
8 × 8 A	216	0.1463	0.1469
10 × 10 A	330	0.1499	0.1504

Table 3.10 Comparison of the results from different sources for the cantilever rhombic plate under uniformly distributed load

source	W'		
	$\beta = 20^{\circ}$	$\beta = 40^{\circ}$	$\beta = 60^{\circ}$
at point C			
ref. [3.12]	1.4137	1.1400	0.7942
ref. [3.13]	1.4297	1.1818	0.8520
ref. [3.14]	1.4109	1.1302	0.7360
ref. [3.15]	1.4196	1.1695	0.8146
ref. [3.17]	1.4327	0.9894	0.3276
HLCTS^{ld}	1.4205	1.1590	0.8179
HLCTS^{qd}	1.4205	1.1574	0.8135
at point D			
ref. [3.12]	1.0414	0.5363	0.1439
ref. [3.13]	1.0442	0.5468	0.1562
ref. [3.14]	1.0396	0.5416	0.1562
ref. [3.15]	1.0374	0.5384	0.1529
ref. [3.17]	1.0101	0.5424	0.1365
HLCTS^{ld}	1.0432	0.5412	0.1499
HLCTS^{qd}	1.0474	0.5433	0.1504

3.2 Analysis of Multilayer Plates

Multilayer plate problems are solved in this section. The test cases chosen for analysis are cross-ply and angle-ply laminated composite plates and a hybrid cantilever rhombic plate. Different boundary conditions are imposed. Finite element results are presented and compared with those obtained by analytical approaches or finite element method available in the literature.

3.2.1 Cross-ply laminated plate with simply supported edges

In the analysis of laminated composite plates, cross-ply laminates have been given considerable attention. The cross-ply lay-up is a special case of the general angle-ply layer arrangement. When the fibre orientations of layers for a laminate are alternately set to zero and ninety degrees, this set-up is called cross-ply. If each layer of a laminate is orthotropic, the laminate exhibits orthotropic property as an whole.

A nine layers cross-ply symmetrically laminated square plate is considered here. The detail lay-up is (0/90/0/90/0/90/0/90/0), where the numbers indicates the fibre orientation for each layer and they are in degrees. The total thickness of the 0° and 90° layers is the same. The side length, b, of the plate is 1.0 m (39.37 in). The material used here is a high modulus graphite/epoxy composite. Its material properties are

$$E_1 = 2.0685\times10^{11}\ \text{N/m}^2\ (3.0\times10^7\ \text{psi});$$

$$E_2 = 5.1713\times10^{9}\ \text{N/m}^2\ (0.75\times10^6\ \text{psi});$$

$$G_{12} = 3.1028\times10^{9}\ \text{N/m}^2\ (0.45\times10^6\ \text{psi});$$

$$G_{13} = G_{23} = 2.5856\times10^{9}\ \text{N/m}^2\ (0.375\times10^6\ \text{psi});$$

and Poisson's ratio $\nu_{12} = 0.25$. As the following relation exists

$$\frac{\nu_{12}}{\nu_{21}} = \frac{E_1}{E_2} \quad , \tag{3.5}$$

therefore, ν_{21} can be obtained.

The laminated plate is simply supported at four edges and the transversally applied uniform distributed load has a intensity f_0. Owing to symmetrical conditions that the problem has, one quarter of the laminated plate is modeled (see Figure 3.6). The boundary conditions for the finite element model are the same as the S4 plate in subsection 3.1.2. The total thickness of the laminate and the load intensity used in the finite element analysis are: (1) h = 0.1 m (3.9370 in), $f_0 = 10^6$ N/m^2 (145.04 psi); (2) h = 0.01 m (0.3937 in), $f_0 = 1000$ N/m^2 (0.14504 psi); and (3) h = 0.001 m (0.03937 in), $f_0 = 1$ N/m^2 (0.14504×10^{-3} psi).

This problem has been solved in reference [3.8] by using a high-order triangular plate bending element (called TRIPLT). This element has three nodes and fifteen DOF at each node. For the purpose of comparison, in the current analysis the shear correction factors are set to unity. The finite element results obtained by using HLCTS^{ld} and HLCTS^{qd} are expressed in dimensionless quantities and are presented in Table 3.11. Results in Table 3.11 converge as meshes are refined. A comparison is made in Table 3.12 to the results using TRIPLT [3.8] and the analytical solution reported in reference [3.9]. It can be seen that for the length to thickness ratios μ = 100 and 1000, HLCTS^{ld} and HLCTS^{qd} give very good results. The discrepancies are 0.09% and 0.37% given by HLCTS^{ld} and HLCTS^{qd}, respectively, when compared with the analytical solution for μ = 100. In this case, HLCTS^{ld} and HLCTS^{qd} results are from 6 × 6 D mesh with 255

DOF. The corresponding TRIPLT result is from a 4 × 4 mesh, which has 375 DOF. For $\mu = 1000$, the respective discrepancies made by HLCTS^{ld} and HLCTS^{qd} are 1.16% and 0.03% compared with analytical solution. Meanwhile, TRIPLT gives a discrepancy of 0.47%. However, to provide this accuracy, a 6 × 6 mesh with 735 DOF has to be used for the TRIPLT element. The total DOF stated above are those before the application of boundary conditions. For the very thin cross-ply laminated composite plate under uniformly distributed load, HLCTS^{qd} is more efficient and accurate compared with TRIPLT.

It should be pointed out that for $\mu = 10$, HLCTS^{ld} and HLCTS^{qd} over predict the deflection by about 27%. This is because the non-constant shear strain field assumption can not generally admit a non-zero constant state of transverse shear strain. Such shear deformation states are not important for thin plates, but when the plates is very thick ($\mu > 15$) or extensive bending and membrane deformations are involved the deterioration effect can be significant [3.10].

3.2.2 Cross-ply laminated plate with clamped edges

The same cross-ply laminated high modulus graphite/epoxy composite square plate analyzed above is considered here. Now, its four sides are clamped. The boundary conditions applied have been specified in subsection 3.1.4. The results due to HLCTS^{qd} are given in Table 3.13. For this cross-ply C4 laminated plate, there is no analytical solution available. But the converged solutions obtained by using TRIPLT [3.8] and another shear deformable element SQH [3.9] are included for comparison. The element SQH is a four node quadrilateral element. When used for plate problems, it has 48 DOF.

Table 3.11 Central displacement of the nine layer cross-ply S4 plate under uniformly distributed load

mesh	μ	$f_0(N/m^2)$	neq.	$W_c E_2 h^3 \times 10^3/f_0 b^4$	
				HLCTS[ld]	HLCTS[qd]
1 × 1 D	10	10^6	6	5.9573	6.3400
	100	10^3	6	2.8773	3.2341
	1000	1.0	6	2.8437	3.1190
2 × 2 D	10	10^6	24	7.0381	7.1416
	100	10^3	24	4.1127	4.2167
	1000	1.0	24	4.0776	4.1815
3 × 3 D	10	10^6	54	7.3691	7.4156
	100	10^3	54	4.3770	4.4251
	1000	1.0	54	4.2968	4.3444
4 × 4 D	10	10^6	96	7.3484	7.3743
	100	10^3	96	4.4349	4.4618
	1000	1.0	96	4.4039	4.4313
6 × 6 D	10	10^6	216	7.4053	7.4156
	100	10^3	216	4.4897	4.5021
	1000	1.0	216	4.4602	4.4721

Table 3.12 Comparison of the solutions from different sources for the nine layer cross-ply S4 plate under uniformly distributed load

μ	$W_c E_2 h^3 \times 10^3 / f_0 b^4$			
	HLCTS^{ld}	HLCTS^{qd}	TRIPLT [3.8]	analytical [3.9]
10	7.4053	7.4156	5.8481	5.8480
100	4.4897	4.5021	4.4846	4.4855
1000	4.4602	4.4721	4.4508	4.4718

These results along with those given by HLCTS^{qd} with 6 × 6 D mesh are compared in Table 3.14. From the table, good agreement can be seen for μ = 100 and 1000 cases. For μ = 10, HLCTS^{qd} over predicts about 67% compared with the other two. This is due to the severe changes of bending moment near the clamped edges. It has been discussed in the nine layer cross-ply S4 case, that the performance of HLCTS elements will deteriorate when the plate is thick and undergoing a strong bending action because of the non-constant strain field.

3.2.3 Angle-ply laminated plate with simply supported edges

To examine the performance of HLCTS elements in the analysis of angle-ply laminated composite plates, a nine layer, symmetrical, angle-ply laminate of (θ/-θ/θ/-θ/θ/-θ/θ/-θ/θ) lay-up with $0 \le \theta \le 45°$ is chosen for the investigation. The total thickness of the θ and -θ layers is equal. The side length, b, of the plate is still 1.0 m (39.37 in). The material is the same high modulus graphite/epoxy composite as used previously. The

Table 3.13 Central displacement of the nine layer cross-ply C4 plate under uniformly distributed load

mesh	μ	$f_0(N/m^2)$	neq.	$W_c E_2 h^3 \times 10^3 / f_0 b^4$
2 × 2 D	10	10^6	20	3.7725
	100	10^3	20	0.7654
	1000	1.0	20	0.7188
3 × 3 D	10	10^6	48	3.8955
	100	10^3	48	0.9308
	1000	1.0	48	0.8765
4 × 4 D	10	10^6	88	3.8650
	100	10^3	88	0.9220
	1000	1.0	88	0.8781
6 × 6 D	10	10^6	204	3.8857
	100	10^3	204	0.9536
	1000	1.0	204	0.9148

Table 3.14 Comparison of the solutions from different sources for the nine layer cross-ply C4 plate under uniformly distributed load

μ	$W_c E_2 h^3 \times 10^3 / f_0 b^4$		
	HLCTS^{qd}	TRIPLT [3.8]	SQH [3.9]
10	3.8857	2.3199	2.3191
100	0.9536	0.9628	0.9634
1000	0.9148	0.9341	0.9494

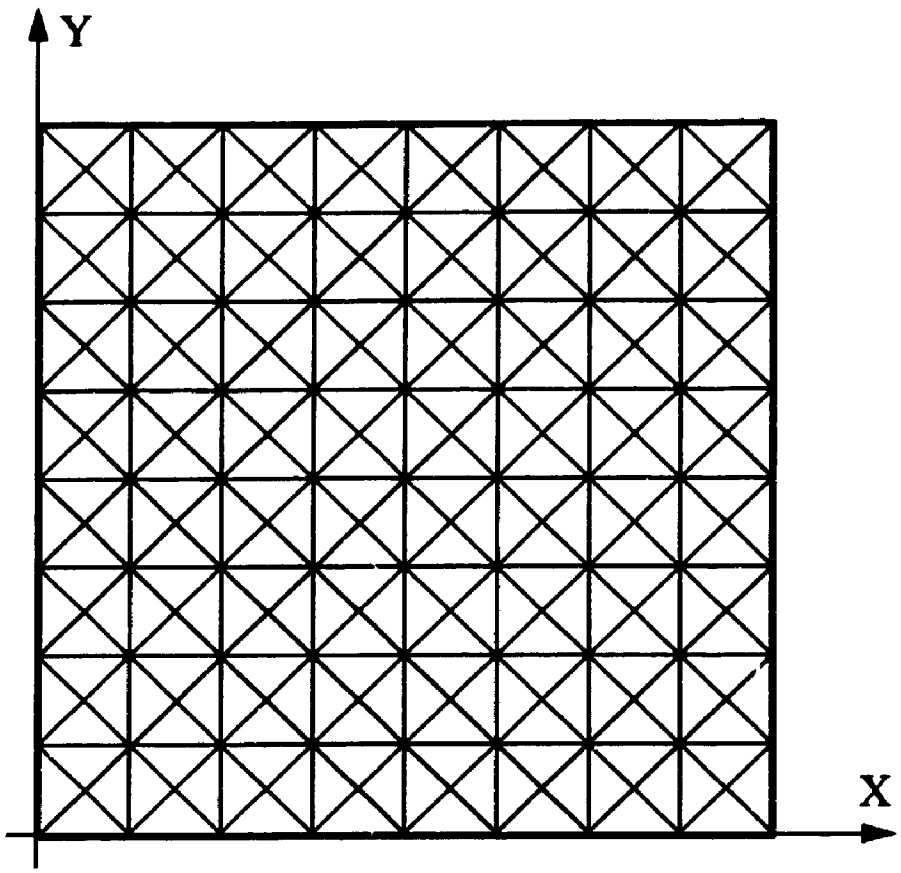

Figure 3.11 8×8 D mesh for a square plate

boundary conditions are similar to those in subsection 3.1.2. The shear correction factor is unity. The plate is under uniformly distributed load with intensity f_0. The HLCTS^{qd} results of the central deflection for $\theta = 30°$ and $\theta = 45°$ are presented in Table 3.15. It should be noted that, generally, as the symmetry conditions do not exist for angle-ply laminates, the maximum displacement may not occur at the centre of plate. For the same reason, the whole structure is represented by the finite elements. In Table 3.15, the results shown are obtained by using 6×6 D, 8×8 D, 10×10 D, and 12×12 D meshes for the entire plate. Figure 3.11 shows a 8×8 D mesh for a square plate.

Table 3.15 Central displacement of nine layer angle-ply S4 plates under uniformly distributed load

mesh	μ	$f_0(N/m^2)$	neq.	$W_c E_2 h^3 \times 10^3 / f_0 b^4$	
				$\theta = 30^o$	$\theta = 45^o$
6 × 6 D	10	10^6	203	-	5.2696
	100	10^3	203	2.6761	2.3333
	1000	1.0	203	2.6420	2.2961
8 × 8 D	10	10^6	367	-	5.2902
	100	10^3	367	2.7149	2.3648
	1000	1.0	367	2.6808	2.3276
10 × 10 D	10	10^6	579	-	5.3006
	100	10^3	579	2.7335	2.3798
	1000	1.0	579	2.6994	2.3431
12 × 12 D	10	10^6	839	-	5.3109
	100	10^3	839	2.7439	2.3886
	1000	1.0	839	2.7097	2.3519

For this problem, there are no analytical solutions available. In the (45/-45/4^c - 45/45/-45/45/-45/45) case, comparison is made with the results from TRIPLT [3.8] and SQH [3.9]. They are given in Table 3.16. For the length to thickness ratio μ = 100, the results agree very well. The difference is less than 0.8%. For μ = 1000, the HLCTS^{qd} result differs from SQH by 1.7%, while it differs from TRIPLT by 7.2%, with respect to the SQH result. As shown in previous examples, TRIPLT predicts less accurate response for very thin laminated plates. It is believed that HLCTS^{qd} and SQH results are

more reliable in this case.

When the lay-up is (30/-30/30/-30/30/-30/30/-30/30), the converged results of the dimensionless central deflection given by HLCTS^{qd} are 2.7439 and 2.7097 for μ = 100 and 1000, respectively (see Table 3.15). The SQH and TRIPLT results are approximately 2.722 for μ = 100 which can be found in Figure 9 of reference [3.8]. For μ = 1000, there is no result available for comparison.

Table 3.16 Comparison of the solutions from different sources for the nine layer 45° angle-ply S4 plate under uniformly distributed load

μ	$W_c E_2 h^3 \times 10^3 / f_0 b^4$		
	HLCTS^{qd}	TRIPLT [3.8]	SQH [3.9]
10	5.3109	3.7323	2.7323
100	2.3886	2.3999	2.4079
1000	2.3519	2.2231	2.3943

3.2.4 Hybrid rhombic cantilever plate

A class of recently emerged hybrid plates [3.12, 3.19] is studied in this subsection. The hybrid plates combine metals with unidirectional or bidirectional composite layers. As an example, a cantilever rhombic plate comprising three aluminum (AL) layers and two unidirectional layers of glass c · carbon fibers impregnated within a matrix material such as epoxy or thermoplastic is analyzed. The geometry of the rhombic

plate is shown in Figure 3.10. The side length L = 1.0 m (39.37 in). The length to thickness ratio μ = L/h = 100, where h is the total thickness of the hybrid plate. The skew angle β = 45°. The layer properties are as follows:

Aluminum layer:

Young's modulus $E = 9.0 \times 10^{10}$ N/m^2 (1.3053×10^7 psi);

Poisson's ratio ν = 0.3;

thickness h_{AL} = 0.0025 m (0.0984 in).

Fiber reinforced composite layer:

$E_1 = 14.05 \times 10^{10}$ N/m^2 (2.0377×10^7 psi);

$E_2 = 1.0 \times 10^{10}$ N/m^2 (1.4503×10^6 psi);

$G_{12} = 5.0 \times 10^9$ N/m^2 (7.2516×10^5 psi);

$G_{13} = G_{23} = 3.5 \times 10^9$ (5.0761×10^5 psi);

ν_{12} = 0.3 and h_c = 0.00125 m (0.0492 in).

The layer arrangement is (AL/0°/AL/0°/AL). The hybrid rhombic plate is under uniformly distributed pressure with intensity f_0 = 100.0 N/m^2 (0.0145 psi). The boundary conditions applied in the analysis is the same as those introduced in subsection 3.1.6. In addition, the shear correction factors are $\kappa_4 = \kappa_5 = (5/6)^{1/2}$, which were not specified in reference [3.12]. The finite element solutions of the transversal displacements at point C and D with different mesh size are given in Table 3.17. At point C, HLCTS^{ld} predicts larger deflection than HLCTS^{qd} does when coarse meshes are employed. At point D, the HLCTS^{qd} results are larger than those given by using HLCTS^{ld} for coarse meshes. However, the discrepancies vanished when meshes are refined. As point D is closer to the clamped boundary, severe bending moment and stress changes are more likely to

Table 3.17 Displacements at point C and D of the 5-layer cantilever hybrid rhombic plate under uniformly distributed load

mesh	neq.	W ($\times 10^{-3}$ m)	
		HLCTS^{ld}	HLCTS^{qd}
at point C			
2 × 2 A	18	0.7588	0.7083
4 × 4 A	60	0.8829	0.8707
6 × 6 A	126	1.067	1.061
8 × 8 A	216	1.172	1.168
10 × 10 A	330	1.225	1.223
12 × 12 A	468	1.254	1.253
14 × 14 A	630	1.272	1.270
16 × 16 A	815	1.282	1.282
at point D			
2 × 2 A	18	0.3882	0.4316
4 × 4 A	60	0.4180	0.4291
6 × 6 A	126	0.4648	0.4699
8 × 8 A	216	0.4940	0.4969
10 × 10 A	330	0.5085	0.5103
12 × 12 A	468	0.5159	0.5172
14 × 14 A	630	0.5200	0.5210
16 × 16 A	815	0.5225	0.5232

affect the accuracy. In this case, HLCTS^{qd} converges better than HLCTS^{ld} does. A comparison made to the result given in reference [3.12] by using the element called LACOT is presented in Table 3.18. It is observed that the displacements at point C predicted by HLCTS and LACOT differ by only about 0.4% with respect to LACOT result. At point D, the discrepancy is about 3.4%.

In closing, it should be pointed out that the presently developed low-order hybrid elements, have demonstrated excellent performance in plate problems. Their convergence rate can even be compared with some high-order displacement type elements, such as TRIPLT [3.8] and SHQ [3.9]. However, HLCTS are less satisfactory for thick plates.

Table 3.18 Comparison of different finite element results for the displacements at point C and D of the hybrid rhombic plate

source	neq.	W ($\times 10^{-3}$ m)	
		at point C	at point D
LACOT (10×10 A)	660	1.277	0.506
HLCTS^{ld} (14×14 A)	630	1.272	0.520
HLCTS^{qd} (14×14 A)	630	1.270	0.521
HLCTS^{ld} (16×16 A)	815	1.282	0.523
HLCTS^{qd} (16×16 A)	815	1.282	0.523

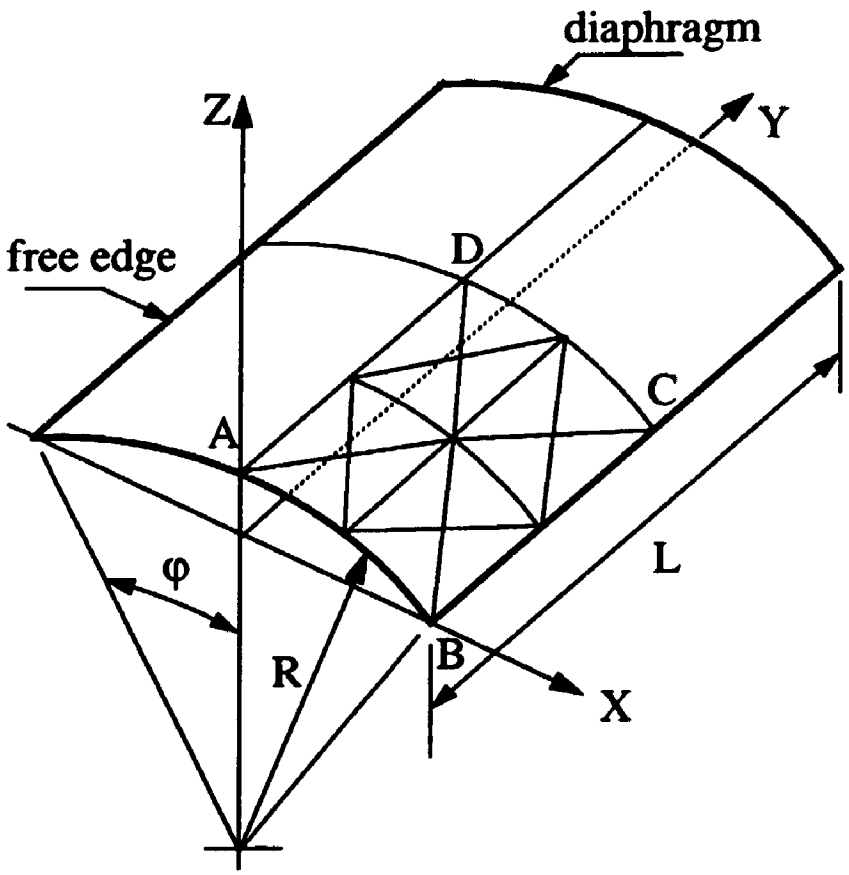

Figure 3.12 Scordelis-Lo roof and a 2 x 2 D mesh for one quarter of the shell

3.3 Analysis of Single Layer Shell

In order to examine the performance of the present elements, HLCTS, in the analysis of single layer isotropic shell problems, a single layer cylindrical shell and a single layer spherical shell are chosen for the study. In applying HLCTS for single layer cases, $E = E_1 = E_2$, $G = G_{12} = G_{13} = G_{23}$ and the "fiber orientation" is zero. The results obtained in the analysis are compared with those available in the literature.

3.3.1 Cylindrical shell under its own dead weight

A cylindrical shell shown in Figure 3.12 is frequently referred to as Scordelis-Lo

roof. It has been commonly used to assess the performance of shell elements. See for examples, references [3.1], [3.3], [3.10], [3.18] and [3.20 - 3.22]. It is supported at the two curved edges by diaphragms. The two straight edges are free. The shell is loaded by its own dead weight. Thus, the load can be characterized as the uniformly distributed load which is in -Z direction and parallel to Z axis. This load creates significant coupling of membrane and bending actions in the shell. The pertinent data of the shell are: radius R = 7.62 m (25.0 ft), length L = 15.24 m (50.0 ft), thickness h = 0.0762 m (0.25 ft), angle φ = 40°, Young's modulus E = 2.0685 × 10^{10} N/m^2 (3.0 × 10^6 psi), Poisson's ratio ν = 0.0 and the dead weight intensity f_0 = 4309.2 N/m^2 (90 lb/ft^2).

Considering the symmetry of the shell's geometry and load, a quarter of the shell is modeled by HLCTS elements. Figure 3.12 shows a 2 × 2 D mesh for the quarter shell. The boundary conditions imposed in the finite element analysis are: U = W = Θ_y = 0.0 at the arc AB; V = Θ_x = Θ_z = 0.0 at the arc DC; U = Θ_y = Θ_z = 0.0 at the line AD and all DOF are free at the free edge BC. At point D, W is free and all other DOF are constrained. The shear correction factor is κ = 5/6. Four meshes, 2 × 2 D, 4 × 4 D, 6 × 6 D and 8 × 8 D, are used in the analysis. The analytical solutions from shallow shell theory [3.1, 3.23] are used for comparison. The values of the solutions are $W_{C(an)}$ = - 0.09406 m (- 0.3086 ft), $U_{C(an)}$ = - 0.04988 m (- 0.16364 ft) and $V_{B(an)}$ = - 0.003894 m (- 0.012775 ft), where the subscripts C and B refer to the respective displacements at the points and (an) indicates that the result is the analytical solution. The finite element solutions obtained in the present analysis are reported in Table 3.19. In the latter, the symbols BT^l and BT^q denote the basic triangles which have linear or quadratic field for w, respectively. The finite element results are normalized with the corresponding

analytical solutions. It is seen that all four HLCTS elements and the two BT give excellent results. It is also noticed that for coarse meshes the six elements predict the deflections very closed to the converged solution. For examples, with 4 × 4 D mesh the respective discrepancies of W_c by using HLCTS^{ld}, HLCTS^{qd}, HLCTS^{lh}, HLCTS^{qh}, BT^{l} and BT^{q} are 3.95%, 4.73%, 3.76%, 4.54%, 3.27% and 4.05% with respect to analytical solution. This indicates a very rapid converging rate. For W_c obtained by using 8 × 8 D mesh, the discrepancies are 2.69%, 2.88%, 2.62%, 2.85, 2.56% and 2.75%, respectively.

The finite element results converged at a value about 3% lower than that of analytical solution reported in references [3.1] and [3.23]. As mentioned earlier, this analytical solution was obtained based on shallow shell theory. The Scordelis-Lo roof is a marginal problem. There has been analytical solution based on deep shell theory, see for example, reference [3.24]. The deep shell solution reported in reference [3.24] is W_c = - 0.09169 m (- 0.3008 ft). It appears that no deep shell solutions for the displacements at other points are available. Table 3.20 shows the finite element results normalized with respect to the deep shell solution. It is seen that the finite element results converged to values in between the shallow and deep shell solutions. The finite element results are closer to the deep shell solution. Those obtained by using 8 × 8 D mesh differ from the deep shell solution by 0.17%, 0.37%, 0.10%, 0.33%, 0.03% and 0.23% for HLCTS^{ld}, HLCTS^{qd}, HLCTS^{lh}, HLCTS^{qh}, BT^{l} and BT^{q}, respectively.

To compare HLCTS elements with other flat shell elements, results from different sources are given in Table 3.21. The results are normalized with respect to the shallow shell solution.

Table 3.19 Normalized displacements of the Scordelis-Lo roof

(normalized with respect to the shallow shell solution)

mesh	neq.	HLCTS^{ld}	HLCTS^{qd}	HLCTS^{lh}	HLCTS^{qh}	BT^{l}	BT^{q}
$W_C/W_{C(an)}$							
2×2 D	54	0.8373	0.8143	0.8477	0.8240	0.8688	0.8445
4×4 D	204	0.9605	0.9527	0.9624	0.9546	0.9673	0.9595
6×6 D	450	0.9614	0.9576	0.9624	0.9585	0.9644	0.9605
8×8 D	792	0.9731	0.9712	0.9738	0.9715	0.9744	0.9725
$U_C/U_{C(an)}$							
2×2 D	54	0.8297	0.8018	0.8404	0.8120	0.8625	0.8328
4×4 D	204	0.9823	0.9729	0.9842	0.9748	0.9886	0.9792
6×6 D	450	0.9849	0.9798	0.9855	0.9804	0.9874	0.9823
8×8 D	792	0.9981	0.9956	0.9987	0.9962	0.9994	0.9968
$V_B/V_{B(an)}$							
2×2 D	54	0.7478	0.7522	0.7556	0.7601	0.7729	0.7781
4×4 D	204	0.9387	0.9387	0.9411	0.9411	0.9518	0.9518
6×6 D	450	0.9779	0.9771	0.9787	0.9787	0.9845	0.9845
8×8 D	792	0.9959	0.9959	0.9967	0.9967	1.0000	1.0000

Table 3.20 Normalized displacements of the Scordelis-Lo roof

(normalized with respect to the deep shell solution)

mesh	neq.	$W_C/W_{C(an)}$					
		HLCTS^{ld}	HLCTS^{qd}	HLCTS^{lh}	HLCTS^{qh}	BT^{l}	BT^{q}
2×2 D	54	0.8590	0.8354	0.8697	0.8454	0.8913	0.8664
4×4 D	204	0.9854	0.9774	0.9874	0.9794	0.9924	0.9844
6×6 D	450	0.9864	0.9824	0.9874	0.9834	0.9894	0.9854
8×8 D	792	0.9983	0.9963	0.9990	0.9967	0.9997	0.9977

Table 3.21 Comparison of the displacement at point C of the Scordelis-Lo roof

predicted by using different flat shell finite elements

mesh	$W_C/W_{C(an)}$					
	HLCTS^{ld}	HLCTS^{qd}	DKT-CST	DKT-LR	HMSH3	BDS
2 × 2	0.837	0.814	0.643	1.023	-	1.220
4 × 4	0.961	0.953	0.778	0.986	0.842	0.937
6 × 6	0.961	0.958	0.876	0.980	0.896	0.947
8 × 8	0.973	0.971	0.916	0.977	0.940	0.956
10 × 10	-	-	0.934	0.976	0.965	-
12 × 12	-	-	0.948	0.975	-	-
14 × 14	-	-	-	-	0.975	-

In the table, DKT-CST and DKT-LR results are from reference [3.3]. The DKT-CST element is the combination of the DKT bending element and the CST membrane element while DKT-LR is composed of the DKT for bending and an Allman type of membrane element with reduced integration scheme. Both DKT-CST and DKT-LR are triangular elements. The HMSH3 results are from reference [3.18]. The element is a C^0-triangular hybrid stress element. The BDS element was proposed in reference [3.20]. The element is a four-node quadrilateral with bilinear displacement field and degenerated type of shell element. For triangular elements in Table 3.21, the meshes are of D type. All these elements have six DOF per node. It should be noted that the results from reference [3.3] were originally normalized with respect to a value of - 0.09211 m (- 0.3022 ft) which was reported in reference [3.25]. In Table 3.21, all results are normalized with respect to the shallow shell solution for the purpose of comparison. As can be seen in the table, HLCTS elements converge faster and are more accurate than DKT-CST, HMSH3 and BDS, especially for coarse meshes. The convergence rate and accuracy for HLCTS and DKT-LR are about the same. However, the DKT-LR results converge from upper bound and tend to converge to a value smaller than the deep shell solution.

3.3.2 Spherical shell segment subjected to concentrated load

A spherical shell segment is shown in Figure 3.13. It is subjected to a concentrated load at the central point A of the shell. The load is $F = 2.0 \times 10^4$ N (4.496×10^3 lbf) and applied in the negative Z direction. The geometrical and material properties are: radius R = 2.5400 m (100 in); thickness h = 0.09945 m (3.915 in); projected side length a = 1.5698 m (61.803 in); the ratio μ = a/h = 15.78; Young's

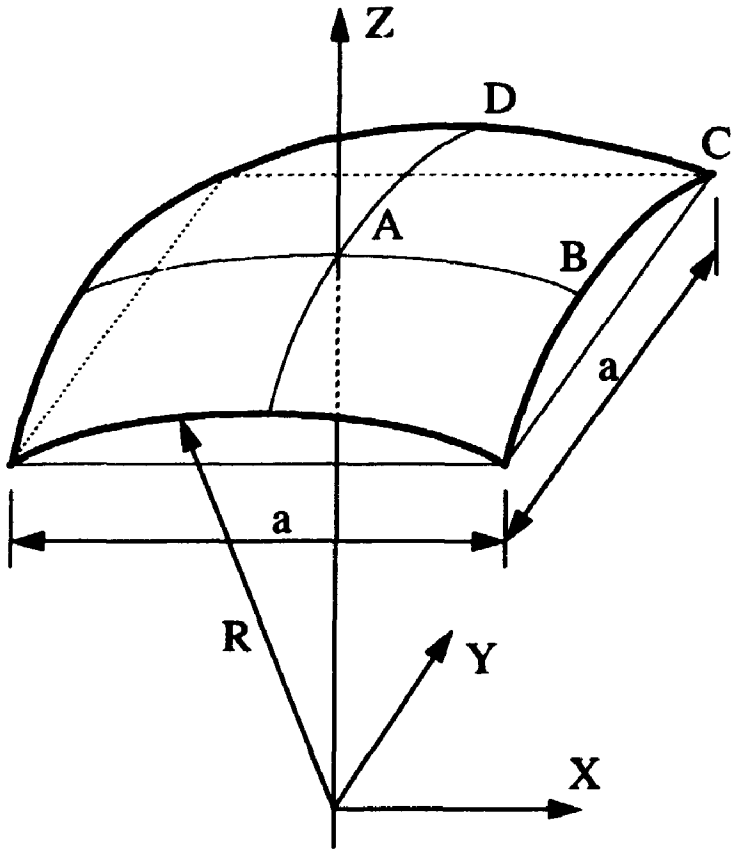

Figure 3.13 Spherical shell segment

modulus E = 6.895 × 10^7 N/m^2 (1.0 × 10^4 psi); ν = 0.3. The shell segment is hinged at four sides.

Taking the advantage of symmetry, one quarter of the shell segment is modeled and solved. The boundary conditions applied on the model are: V = Θ_x = Θ_z = 0.0 at AB; U = Θ_y = Θ_z = 0.0 at AD; U = V = W = Θ_x = Θ_z = 0.0 at BC and U = V = W = Θ_y = Θ_z = 0.0 at DC. All DOF at point C are constrained. At point A, only W is free. The finite element results are presented in Table 3.22 for the cases of shear correction factors κ = 5/6 and 1.0.

This problem has not been found in the literature for linear analysis. However, it can be compared to those solutions from non-linear analysis if the load and deflection levels are sufficiently low. Reference [3.26] reported the central deflection W_A = -0.028 m for a load of 2.0×10^4 N by using a flat triangular element, and reference [3.27] predicted a value of W_A = -0.029 m with the same load using a four-node element. A series solution in reference [3.28] based on shallow shell theory was W_A = -0.030 m. The data are obtained from figures in the references. It is seen that HLCTS elements over

Table 3.22 Displacement at point A of the spherical shell segment subjected to a concentrated load

mesh	neq.	W_A (m)		
		HLCTS^{qd}	HLCTS^{qh}	BT^{q}
κ = 5/6				
2 × 2 D	41	- 0.02123	- 0.02123	- 0.02125
4 × 4 D	177	- 0.02729	- 0.02729	- 0.02731
6 × 6 D	409	- 0.02947	- 0.02947	- 0.02948
8 × 8 D	737	- 0.03069	- 0.03069	- 0.03070
κ = 1.0				
2 × 2 D	41	- 0.02048	- 0.02049	- 0.02050
4 × 4 D	177	- 0.02631	- 0.02631	- 0.02632
6 × 6 D	409	- 0.02830	- 0.02830	- 0.02831
8 × 8 D	737	- 0.02939	- 0.02939	- 0.02940

predict the central deflection by 2.3% when $\kappa = 5/6$ and under estimate by 2.0% when $\kappa = 1.0$. This comparison is made with respect to the series solution in reference [3.28]. As the ratio $\mu = a/h = 15.78$, the shell is relatively thick. Thus, the slight over estimate by HLCTS elements, when the shear correction factor is $\kappa = 5/6$, is consistent with the findings reported in previous sections.

3.4 Analysis of Multilayer Shells

In this section multilayer laminated composite shells are studied by using HLCTS elements. The test cases include cylindrical shells and spherical panels. Both cross-ply and angle-ply cases are considered. For cross-ply laminated composite shells, the laminates are orthotropic and for angle-ply, the laminates are generally anisotropic. In the case of angle-ply laminates, bending and membrane coupling exists. The prediction of their responses is more complicated and difficult. In the current investigation, comparisons made to the results using other finite elements or analytical solutions show excellent agreement.

3.4.1 Cross-ply cylindrical shell clamped at both ends

A 4-layer cross ply, (0/90/90/0), cylindrical shell is considered in this subsection. The shell is subjected to a internal pressure with intensity $f_0 = 1.4068 \times 10^4$ N/m^2 (2.0404 psi). As shown in Figure 3.14, the cylindrical shell is clamped at both ends. The length L and the shell radius R are equal. It is L = R = 0.508 m (20.0 in). The layer material properties are:

$$E_1 = 5.1713 \times 10^{10} \text{ N/m}^2 \ (7.5 \times 10^6 \text{ psi});$$

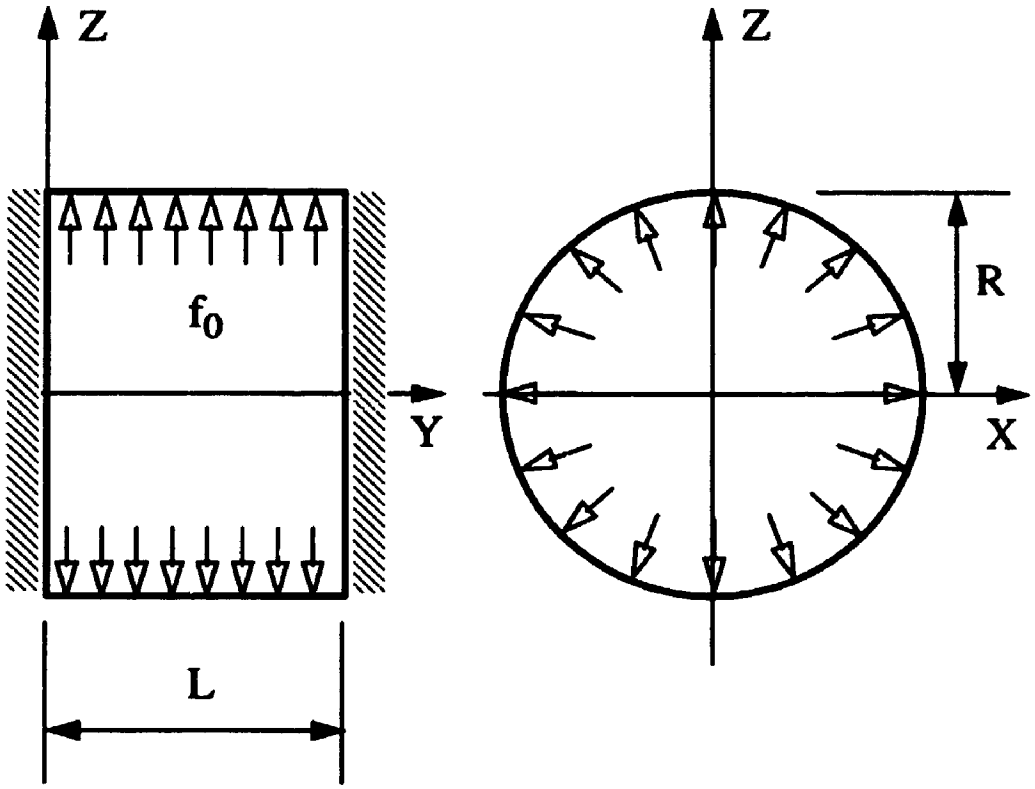

Figure 3.14 Clamped cylindrical shell under internal pressure

$E_2 = 1.3790 \times 10^{10}$ N/m^2 (2.0×10^6 psi);

$G_{12} = 8.6188 \times 10^9$ N/m^2 (1.25×10^6 psi);

$G_{13} = G_{23} = 4.3094 \times 10^9$ (0.625×10^6 psi);

and Poisson's ratio $\nu_{12} = 0.25$.

Making use of the symmetry in layup design, geometry and load, we take one eighth of this cylindrical shell for the analysis. This part of the shell are modeled using four D type meshes, 2 × 2 D, 4 × 4 D, 6 × 6 D and 8 × 8 D. The 2 × 2 D mesh is

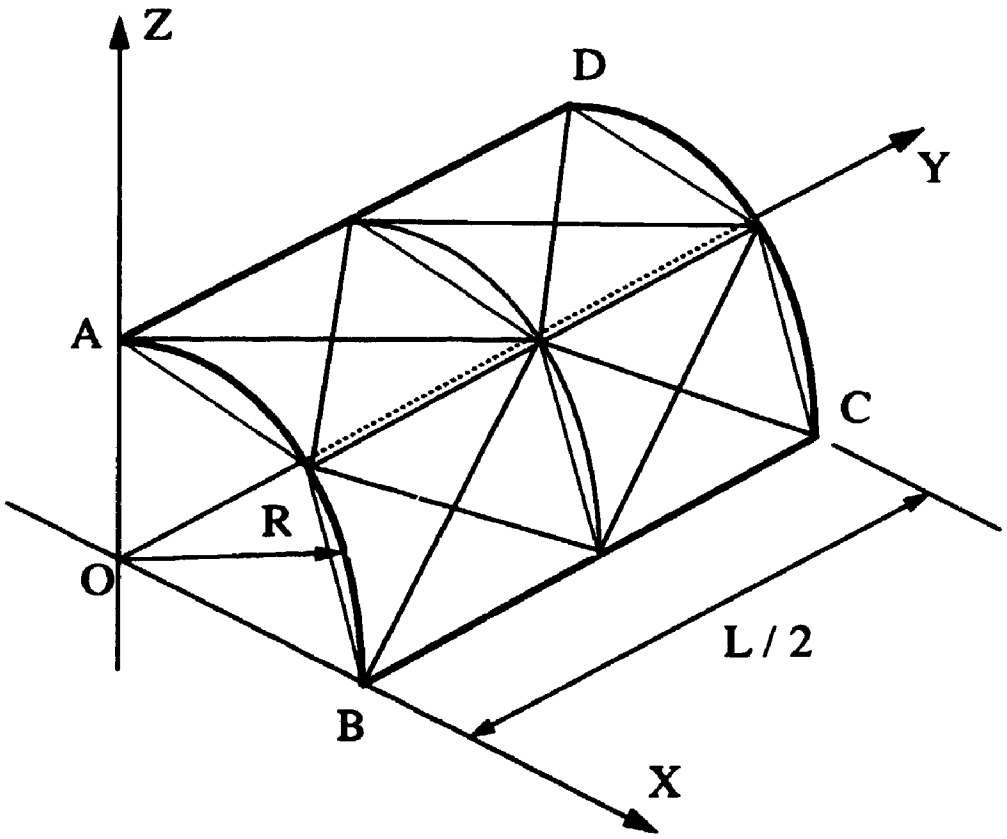

Figure 3.15 A 2 × 2 D mesh for one eighth of the cylindrical shell

shown in Figure 3.15. As the elements are flat with straight edges, any line between two nodes should be actually a straight line. The curve lines in the figure are used to illustrate the original shape of the shell only. The boundary conditions applied to the finite element models are: all DOF are constrained at arc AB; $W = \Theta_x = \Theta_y = 0.0$ at line AB; $V = \Theta_x = \Theta_z = 0.0$ at arc DC and $U = \Theta_y = \Theta_z = 0.0$ at line AD. For the node at point C, $V = W = \Theta_x = \Theta_y = \Theta_z = 0.0$ (and $U \neq 0.0$) and at point D, $U = V = \Theta_x = \Theta_y = \Theta_z = 0.0$ (and $W \neq 0.0$). The shear correction factors are $\kappa_4 = \kappa_5 = (5/6)^{1/2}$. Two radius to thickness ratios, $\mu = R/h = 20$ and $\mu = 100$, are selected, in which h is the total

thickness of the shell. Therefore, the thickness of each layer of the shell is h/4.

Membrane action is substantial near the centre of the shell. In the area near the clamped ends, bending action becomes dominant. The maximum radial displacements predicted by using HLCTS^{qd} and HLCTS^{qh} are given in Table 3.23. It is found that the results from HLCTS^{qd} and HLCTS^{qh} converged to the same value. There is no analytical solution available for comparison. The comparison is made to the results reported in reference [3.29] and presented in Table 3.24. The results from reference [3.29] were

Table 3.23 Maximum radial displacement of the 4-layer cross-ply clamped cylindrical shell under internal pressure

mesh	neq.	W_{max} ($\times 10^{-3}$ m)	
		HLCTS^{qd}	HLCTS^{qh}
μ = 20			
2 × 2 D	41	0.004166	0.004173
4 × 4 D	179	0.004460	0.004460
6 × 6 D	413	0.004498	0.004501
8 × 8 D	743	0.004506	0.004506
μ = 100			
2 × 2 D	41	0.020975	0.021008
4 × 4 D	179	0.020960	0.020963
6 × 6 D	413	0.021422	0.021425
8 × 8 D	743	0.021532	0.021532

obtained by employing a nine-node assumed strain isoparametric finite element (CSHEL9). It has five DOF per node, 45 DOF per element. The CSHEL9 results in Table 3.24 were from a 8 × 8 mesh and the total DOF were 1445. The HLCTS results are obtained by using the 8 × 8 D mesh and the total DOF are 870. The discrepancies are, respectively, 0.51% for $\mu = 20$ and 0.65% for $\mu = 100$, with respect to HLCTS results. The HLCTS elements predict less deflection than CSHEL9 does in $\mu = 20$ case and larger in $\mu = 100$ case. There is no sufficient evidence to say which result is more accurate. However, the small discrepancies showed that HLCTS elements are comparable to the nine-node isoparametric element in terms of efficiency and accuracy.

Table 3.24 Comparison of the maximum radial displacement of the 4-layer cross-ply clamped cylindrical shell

μ	W_{max} (× 10^{-3} m)		
	HLCTS^{ld}	HLCTS^{qd}	CSHEL9
20	0.004506	0.004506	0.004529
100	0.021532	0.021532	0.021392

3.4.2 Angle-ply cylindrical shell clamped at both ends

A 4-layer cylindrical shell with the same geometric and layer material properties in subsection 3.4.1 is now considered with a symmetrical 45° angle-ply layups (45/-45/-45/45). The shell is under internal pressure with the same intensity as that for the cross-ply cylindrical shell. Again, one octant of the shell is modeled by the finite elements with

four different meshes. The shell is also clamped at both ends. Thus, the boundary conditions applied to the finite element models remain the same. The shear correction factors are also the same. The HLCTS^{qd} and HLCTS^{qh} results are reported in Table 3.25 and the comparison to CSHEL9 results are made in Table 3.26. The same trend found in the cross-ply cylindrical shell case is repeated here. Slightly larger discrepancies between the HLCTS and CSHEL9 results for the maximum radial displacement are found. The discrepancies are 3.27% and 2.11%, respectively, for μ = 20 and μ = 100.

Table 3.25 Maximum radial displacement of the 4-layer 45° angle-ply clamped cylindrical shell under internal pressure

mesh	neq.	W_{max} ($\times 10^{-3}$ m)	
		HLCTS^{qd}	HLCTS^{qh}
μ = 20			
2 × 2 D	41	0.005392	0.005408
4 × 4 D	179	0.005794	0.005794
6 × 6 D	413	0.005910	0.005910
8 × 8 D	743	0.005908	0.005908
μ = 100			
2 × 2 D	41	0.028677	0.028804
4 × 4 D	179	0.027635	0.027635
6 × 6 D	413	0.027737	0.027737
8 × 8 D	743	0.027712	0.027712

Table 3.26 Comparison of the maximum radial displacement of the 4-layer 45° angle-ply clamped cylindrical shell

μ	W_{max} ($\times 10^{-3}$ m)		
	HLCTS^{ld}	HLCTS^{qd}	CSHEL9
20	0.005908	0.005908	0.006101
100	0.027712	0.027712	0.027127

3.4.3 Simply supported cross-ply spherical panel under uniform load

In the analysis of doubly curved laminated composite shells, a nine layers cross-ply symmetrically laminated spherical panel is considered here. The shell geometry is shown in Figure 3.13. Each layer of the laminate is orthotropic and the fibre orientations of layers for the laminate are alternately set to zero and ninety degrees, (0/90/0/90/0/90/0/90/0). The total thickness of the 0° and 90° layers is the same. The projected side length of the shell is a = 1.0 m (39.37 in). The radius, R, is 10 m (393.7 in). Two cross-ply spherical shell panels are solved. One is with the total thickness h = 0.01 m (0.3937 in) and the another is with h = 0.001 m (0.03937 in). The material of the spherical shell panels is the high modulus graphite/epoxy composite. The material properties are:

$E_1 = 2.0685\times10^{11}$ N/m^2 (3.0×10^7 psi);

$E_2 = 5.1713\times10^9$ N/m^2 (0.75×10^6 psi);

$G_{12} = 3.1028\times10^9$ N/m^2 (0.45×10^6 psi);

$G_{13} = G_{23} = 2.5856\times10^9$ N/m^2 (0.375×10^6 psi);

and Poisson's ratio $\nu_{12} = 0.25$. Equation (3.5) can be employed to calculate ν_{21}.

The laminated spherical shell panel is simply supported at four curved edges and a uniformly distributed load, which is always normal and pointing to the shell's inner surface, is applied. The load intensity f_0 is 1.0×10^3 N/m^2 (0.14504 psi) for the thicker shell panel and is 1.0 N/m^2 (0.14504×10^{-3} psi) for the thinner shell panel. One quarter of the laminated shell panel is modeled by using finite elements. The boundary conditions applied at the symmetry lines and simply supported boundaries are: $V = \Theta_x = \Theta_z = 0.0$ at AB; $U = \Theta_y = \Theta_z = 0.0$ at AD; $V = W = \Theta_x = 0.0$ at BC and $U = W = \Theta_y = 0.0$ at DC. The constraints applied to the four corners of the quarter shell panel are: $U = V = \Theta_x = \Theta_y = \Theta_z = 0.0$ at point A; $V = W = \Theta_x = \Theta_z = 0.0$ at point B; all DOF = 0.0 at point C and $U = W = \Theta_y = \Theta_z = 0.0$ at point D. The shear correction factors are $\kappa_4 = \kappa_5 = (5/6)^{1/2}$.

The results obtained in the current analysis are given in Table 3.27. The central deflections are presented in dimensionless form: $W' = WE_2h^3/f_0a^4$. In the table, the symbol μ is the ratio of the projected length to thickness, a/h. The results in the table show a rapid convergence rate. This problem was solved analytically and reported in reference [3.9]. The comparison of HLCTS results to the analytical solution is made in Table 3.28. The results obtained by using HLCTS^{qd} and HLCTS^{ld} differ from the analytical solution by +0.13% and +0.03%, respectively, for $\mu = 100$ case. The corresponding discrepancies are -0.51% and -0.68% for $\mu = 1000$.

3.4.4 Simply supported 45° angle-ply spherical panel under uniform load

In this subsection, we consider a laminated composite spherical shell panel

constructed by using the high modulus graphite/epoxy composite given in subsection 3.4.3. The shell has nine layers. The detail layup is (45/-45/45/-45/45/-45/45/-45/45).

Table 3.27 Dimensionless displacement at point A of the cross-ply spherical shell panel under uniform pressure load

mesh	neq.	W' ($\times 10^{-3}$)	
		HLCTS^{qd}	HLCTS^{ld}
$\mu = 100$, $f_0 = 1.0 \times 10^3$ N/m^2			
2 × 2 D	47	2.5241	2.4631
4 × 4 D	191	2.6694	2.6539
6 × 6 D	431	2.7005	2.6932
8 × 8 D	767	2.7108	2.7072
10 × 10 D	1199	2.7170	2.7144
$\mu = 1000$, $f_0 = 1.0$ N/m^2			
2 × 2 D	47	0.0578	0.0573
4 × 4 D	191	0.0583	0.0581
6 × 6 D	431	0.0584	0.0586
8 × 8 D	767	0.0589	0.0588
10 × 10 D	1199	0.0589	0.0588

Table 3.28 Comparison of the dimensionless displacement at point A of the cross-ply spherical shell panel under uniform pressure load

μ	W' (× 10^{-3})		
	HLCTS^{qd}	HLCTS^{ld}	analytical [3.8]
100	2.7170	2.7144	2.7135
1000	0.0589	0.0588	0.0592

The total thickness of the 45° and -45° layers are the same. The shell panel is simply supported at four curved sides. One quarter of the shell is analyzed due to symmetry. Boundary conditions and load applied are the same as those specified for the cross-ply spherical shell panel in subsection 3.4.3.

The HLCTS^{qd} and HLCTS^{ld} results obtained by using five different mesh sizes, 2 × 2 D, 4 × 4 D, 6 × 6 D, 8 × 8 D and 10 × 10 D, are shown in Table 3.29. The results are the predicted central deflections in the dimensionless form: $W' = WE_2h^3/f_0a^4$. The HLCTS^{qd} and HLCTS^{ld} results for 10 × 10 D are W' = 0.5259 × 10^{-3} and 0.5254 × 10^{-3}, respectively for μ = 100. The analytical solution reported in Figure 21 of reference [3.9] is about 0.52 × 10^{-3}. For μ = 1000, the 10 × 10 D HLCTS^{qd} and HLCTS^{ld} results are W' = 0.01011 × 10^{-3} and 0.01005 × 10^{-3}, respectively. In this case there is no solution available in the literature for comparison.

Table 3.29 Dimensionless displacement at point A of the 45° angle-ply spherical shell panel under uniform pressure load

mesh	neq.	W' ($\times 10^{-3}$)	
		HLCTS^{qd}	HLCTS^{ld}
$\mu = 100$, $f_0 = 1.0 \times 10^3$ N/m^2			
2 × 2 D	47	0.5285	0.5218
4 × 4 D	191	0.5249	0.5228
6 × 6 D	431	0.5254	0.5244
8 × 8 D	767	0.5259	0.5254
10 × 10 D	1199	0.5259	0.5254
$\mu = 1000$, $f_0 = 1.0$ N/m^2			
4 × 4 D	191	0.00812	0.00781
6 × 6 D	431	0.00942	0.00927
8 × 8 D	767	0.00978	0.00970
10 × 10 D	1199	0.01011	0.01005

3.5 Remarks

The HLCTS elements developed in Chapter 2 have been used to study an extensive collection of single layer, multilayer plate and shell structures. The test cases selected and presented in this chapter have demonstrated the excellent performance of HLCTS elements. Comparisons have been made to reliable analytical or numerical

solutions whenever they are available in the literature to ensure the validity of HLCTS results. Detail information on geometrical and material properties of the structures, and load as well as boundary conditions are included in every example.

The numerical study shows that HLCTS elements are more accurate and converge faster when compared with other low-order finite elements. In some cases they can even be compared with high-order elements (see, for example, SQH [3.9] in subsection 3.2.3). No shear-locking phenomenon was detected in using HLCTS elements during the investigation. However, inferior mesh design, topology or severely distorted meshes may induce shear-locking [3.18, 3.22]. The numerical study also shows that mesh topology affects the accuracy of triangular finite element results. The consistent use of D type mesh in this investigation has proved that such mesh can provide good results.

Among the four HLCTS elements, $HLCTS^{qd}$, $HLCTS^{ld}$, $HLCTS^{qh}$ and $HLCTS^{lh}$, and the two basic triangles, BT^{q} and BT^{l}, $HLCTS^{qd}$ and $HLCTS^{ld}$ are the most favourite ones in terms of both accuracy and rank sufficiency. However, this does not exclude the use of $HLCTS^{qh}$, $HLCTS^{lh}$, BT^{q} and BT^{l}. With proper mesh layout and introducing certain constraints, singularity in the entire finite element model of a plate or shell structure caused by rank-deficient may be avoided. The numerical studies in this chapter have shown some good results obtained by using $HLCTS^{qh}$, $HLCTS^{ih}$, BT^{q} and BT^{l}.

In formulating HLCTS elements, see Chapter 2, the elements have been designed to handle thin and moderately thick laminated composite plate and shell structures. In some references, researchers had given the limit of length to thickness ratios for degenerated or shear deformable type of finite elements. See, for example, reference [3.18]. However, in the current numerical investigation, one can hardly find a clear cut

on the thickness limit for laminated structures. In other words, in analyzing laminated plate and shell structures, it is hard to set up a limit to distinguish thick and moderately thick. It is seen that marginal problems depend very much on boundary conditions, force applied and the design of layups. This is because all these factors have effects on the actual distribution of the transversal shear. Multilayer structures make this distribution more complicated. Thus, relatively thick laminated structures under severe load conditions should be handled with care.

CHAPTER 4

VIBRATION ANALYSIS OF LAMINATED COMPOSITE PLATE AND SHELL STRUCTURES

The hybrid strain laminated composite triangular shell finite elements for linear analysis have been proposed in Chapter 2. In this chapter, these elements are adopted for vibration analysis of laminated composite plate and shell structures. The focus is on free vibration. The stiffness matrices of HLCTS elements have been derived and obtained explicitly in Chapter 3. In vibration analysis element mass matrices are also required and they are derived in this chapter.

This chapter consists of seven sections. The first section is a brief introduction and the second section presents the derivation of consistent element mass matrices. The sections following are the numerical studies of free vibration problems for single layer plates, multilayer plates, single layer shells and multilayer shells, respectively. The last section includes closing remarks.

It may be appropriate to note that in the finite element discretizations whole structures are considered unless stated otherwise. When the whole structure is considered a complete set of eigenvalues and eigenvectors are obtained.

4.1 Introduction

Dynamic analysis is essential in the design of modern engineering structures. Natural frequencies, mode shapes and dynamic responses to different kinds of time-

varying loads are essential and fundamental in dealing with practical problems. The theoretical basis of dynamic analysis of single layer isotropic structures is extended and developed for laminated composite structures.

A series of review papers by Leissa [4.1-4.4] covered the general plate vibration problems during the period of 1970's and earlier 80's. His two monographs [4.5, 6] had collected enormous information on plate and shell vibration analysis, respectively. A survey paper on shallow shell vibrations was presented by Qatu [4.7]. The general surveys on dynamic analysis of composite structures include those of Bert [4.8-11], Kapania and Raciti [4.12, 13] and Ren [4.14]. Several survey papers have specialized sections on this subject. For example, Reddy has reviewed finite element modelling of laminated composite plates [4.15] and refined theories of laminated composite plates [4.16]. Kapania has considered the analysis of laminated shells [4.17]. Yang, Saigal and Liaw discuss on thin shell finite elements and applications [4.18] while Noor and Burton discuss computational models for multilayered composite shells [4.19].

Shear deformation theories have received considerable attention in linear vibration analysis of laminated composite structures. A variety of solution schemes based on first order shear deformable theory have been employed to solve vibration problems of laminated composite plates [4.20-24]. References [4.25-27] are the application of finite elements on such structures. Examples of first order shear deformation theory used for finite element analysis of laminated composite shell structures can be found in references [4.28, 4.29]. An earlier report by Noor and Mathers [4.30] included shear deformation effect for a number of displacement and mixed shear-flexible finite laminated composite plate and shell elements when applied to linear vibration problems. For references on

applications of high order shear deformation and other theories, readers are referred to references [4.19] and [4.31].

Generally speaking, shell elements are more complicated than plate elements. If layer-by-layer theories, three dimensional elastic theories and high order displacement fields are simultaneously utilized in shell element formulations, the elements developed are likely to be computationally inflexible for large scale finite element analysis. One of the objectives of the current study in this chapter is to develop the mass matrices for HLCTS elements, which have been derived in Chapter 2 and used in linear static analysis in Chapter 3, and apply these elements to vibration analysis of laminated composite plate and shell structures. Another objective is to assess the performance of these elements in vibration analysis.

4.2 Element Mass Matrices

The formulations of element mass matrix are categorized mainly into lumped mass matrix and consistent mass matrix.

The so-called lumped mass matrix is a diagonal matrix. For simple elements, it is obtained by placing particle masses m_i at the node i of the element, such that the sum of m_i is the total element mass. This method can hardly be used for higher order elements with both rotational and curvature DOF in addition to the translational DOF. A recommended lumping scheme for arbitrary elements is the Hinton-Rock-Zienkiewicz (HRZ) lumping method [4.32] which combines the 'consistent' and 'lumping' schemes.

Consistent mass formulation involves using the same displacement shape functions in forming the stiffness matrix. Consistent mass matrix produces more accurate results

for flexural problems and therefore it is adopted in the present investigation.

4.2.1 Shape functions

To formulate consistent mass matrix, the same shape functions or displacement interpolation functions adopted in the derivation of element stiffness matrix are used. In the following we use the same co-ordinate systems defined in Chapter 2.

There are two sets of displacement interpolation functions used in Chapter 2 to formulate element stiffness matrices. They are adopted in this subsection to derive the element mass matrix. The two sets differ only in the interpolating polynomial for w. Equations (2.28) through (2.31) are applied here.

4.2.2 Derivation of consistent mass matrices

The general expression of consistent mass matrix is given as

$$m = \int_V \rho[\phi]^T[\phi]\, dV \tag{4.1}$$

where ρ is the mass density and $[\phi]$ is the shape function matrix. When an element has only translational DOF, equation (4.1) can be adopted directly. For elements which have translational DOF, rotational DOF and DDOF, Liu and To [4.33] recommended that the consistent mass matrix should be formulated according to the following equation

$$m = \int_V [\phi]^T[\rho][\phi]\, dV \tag{4.2}$$

where

$$[\rho] = \begin{bmatrix} \rho & 0 & 0 & 0 & 0 & 0 \\ 0 & \rho & 0 & 0 & 0 & 0 \\ 0 & 0 & \rho & 0 & 0 & 0 \\ 0 & 0 & 0 & \rho h^2/12 & 0 & 0 \\ 0 & 0 & 0 & 0 & \rho h^2/12 & 0 \\ 0 & 0 & 0 & 0 & 0 & J \end{bmatrix}_{6\times6} \tag{4.3}$$

in which

$$J = \rho \frac{[\, r_2^2+s_3^2+r_3(r_3-r_2)\,]}{18} \quad . \tag{4.4}$$

Equation (4.3) defines the generalized mass density matrix. But, it should be noted that the density of polar moment of inertia, J, defined in equation (4.4) is particularly for a three-node flat triangular element with the chosen local co-ordinate.

For the laminated composite HLCTS elements, analogy to equation (4.2) is drawn and the element consistent mass matrix is defined as

$$m_e = \sum_{k=1}^{n} \int_a [\phi]^T [\rho]_k [\phi] \, da \tag{4.5}$$

where n is the total number of layers and the mass density matrix for the k'th layer is

$$[\rho]_k = \begin{bmatrix} \rho_k(h_k-h_{k-1}) & 0 & 0 & 0 & 0 & 0 \\ 0 & \rho_k(h_k-h_{k-1}) & 0 & 0 & 0 & 0 \\ 0 & 0 & \rho_k(h_k-h_{k-1}) & 0 & 0 & 0 \\ 0 & 0 & 0 & I_r & 0 & 0 \\ 0 & 0 & 0 & 0 & I_s & 0 \\ 0 & 0 & 0 & 0 & 0 & J_d \end{bmatrix}_{6\times6} \tag{4.6}$$

and

$$I_r = I_s = \rho_k \frac{(h_k^3 - h_{k-1}^3)}{3} \quad ,$$

$$J_d = \rho_k (h_k - h_{k-1}) \frac{[\, r_2^2 + s_3^2 + r_3(r_3 - r_2)\,]}{18} \quad . \qquad (4.7a,b)$$

In equations (4.6) and (4.7a,b), h_k is the layer co-ordinate in the transverse direction at the top of the k'th layer (see Figure 2.4).

The mass matrix defined in equation (4.5) is in the local co-ordinate system shown in Figure 2.1. Before assembling mass matrices, they should be transferred to the global co-ordinate system by applying equation (2.13). The consistent element mass matrix in the global co-ordinate is then

$$M_e = T^T m_e T \quad . \qquad (4.8)$$

The above consistent element mass matrices are derived and obtained explicitly by using the computer algebra packages MACSYMA [4.34]. There are no numerical integrations involved. The explicit expressions are consistent with the element stiffness matrices developed in Chapter 2. Thus, the HLCTS elements obtained for vibration analysis are entirely in explicit expressions.

Using the mass matrices derived in this subsection and the stiffness matrices derived in Chapter 2, one can compose six elements for vibration analysis of laminated composite plate and shell structures. These elements are denoted by $HLCTS_r^{qd}$, $HLCTS_r^{ld}$, $HLCTS_r^{qh}$, $HLCTS_r^{lh}$, $HLCTS_t^{qd}$ and $HLCTS_t^{qh}$ where the meaning of the superscripts q, l, d and h has been defined in Chapter 2. For the subscript r, it denotes that the moment of inertia and polar moment of inertia have been considered. For the subscript t, it means

that only the mass corresponding to translational DOF has been considered in the mass matrix formulation.

When HLCTS elements are employed for vibration analysis of single layer plate and shell structures of isotropic materials, the $HLCTS_r^{qd}$ element reduces to that using formulation 16 proposed by Liu and To in reference [4.33].

4.3 Vibration Analysis of Single Layer Plates

In this section, the results of free vibration analysis of single layer isotropic plate problems by using the HLCTS elements are presented. The chosen examples are a square plate and a rhombic plate. The plates are investigated under the boundary conditions of simply supported at four sides, fully clamped at four sides and cantilevered.

For plate flexural vibration, the two in-plane DOF, U and V, and the DDOF of the HLCTS elements are constrained. The DOF left for HLCTS elements are associated with the bending part, that is, the transversal displacement W and two rotational DOF, Θ_x and Θ_y. Therefore, only the $HLCTS_r^{qd}$, $HLCTS_r^{ld}$ and $HLCTS_t^{qd}$ elements are used in the investigation.

For the analysis of single layer isotropic plates in this section, the shear correction factor is set to $\kappa = 5/6$ for all of the cases.

Before describing the details of the free vibration analysis of different sample cases, it should be mentioned that a single element test has been conducted to detect rigid-body modes and zero energy modes. In the test, all the eighteen element DOF are left free. The results are: the $HLCTS_r^{qd}$, $HLCTS_r^{ld}$ and $HLCTS_t^{qd}$ elements have six rigid-body modes and have no zero energy modes; the $HLCTS_r^{qh}$, $HLCTS_r^{lh}$ and $HLCTS_t^{qh}$

elements have six rigid-body modes and two zero energy modes; the BT^q and BT^l elements have six rigid-body modes and three zero energy modes. The zero energy modes are all associated with the in-plane torsional rotations. In other words, the BT elements developed in Chapter 2 have three zero energy modes; the $HLCTS^{qh}$ and $HLCTS^{lh}$ elements have two zero energy modes and the $HLCTS^{qd}$ and $HLCTS^{ld}$ elements do not have any zero energy modes. Thus, the improved formulation of DDOF by displacement approach introduced in subsection 2.6 has eliminated the spurious modes from the elements.

4.3.1 Free vibration of square plates

The plate considered here is an isotropic square plate with side length b = 1.0 m and thickness h = 0.005 m. Its material properties are: Young's modulus $E = 2.0 \times 10^{11}$ N/m^2; Poisson's ratio $\nu = 0.3$ and mass density $\rho = 7800.0$ kg/m^3.

Four different meshes, 2 × 2 D, 4 × 4 D, 6 × 6 D and 8 × 8 D shown in Figure 4.1, are used to discretize the entire plate. The global co-ordinate system for the finite element model is also shown in the figure.

Firstly, consider the case of a plate simply supported on four sides. The boundary conditions are: W = 0.0 at all simply supported edges, $\Theta_x = 0.0$ at the edges parallel to Y axis and $\Theta_y = 0.0$ at the edges parallel to X axis. All DOF at four corners of the plate are constrained. The first three natural frequencies obtained by using HLCTS elements are given in Table 4.1. The frequencies are presented in a dimensionless parameter form. The frequency parameter is defined as

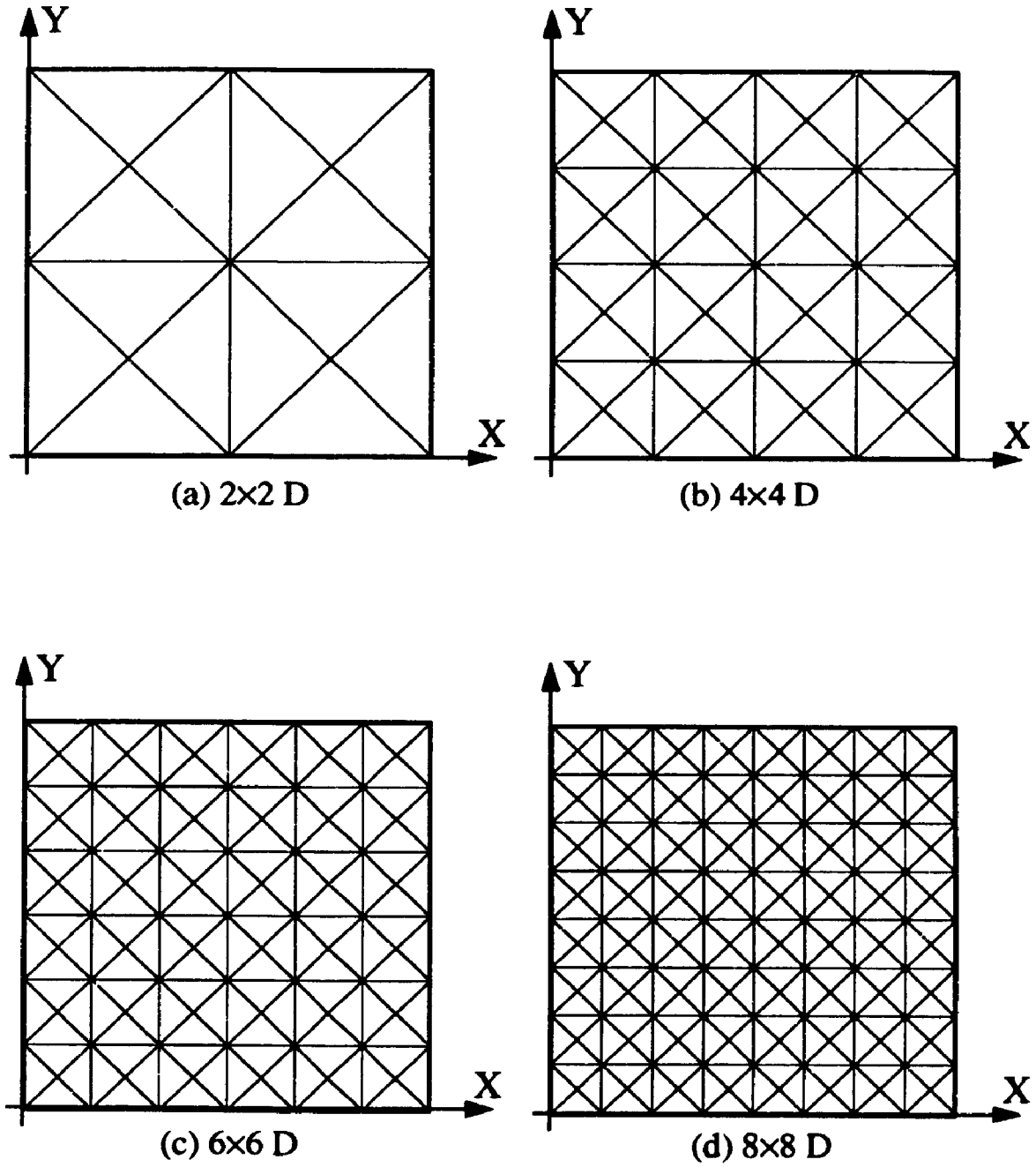

Figure 4.1 Four meshes and the co-ordinates for square plates

Table 4.1 First three dimensionless natural frequencies

of the simply supported isotropic square plate

mesh	neq.	mode sequence		
		1	2	3
$HLCTS_r^{qd}$				
2 × 2 D	19	21.95	62.06	62.06
4 × 4 D	87	20.29	54.29	54.29
6 × 6 D	203	20.00	51.43	51.43
8 × 8 D	367	19.90	50.52	50.52
$HLCTS_r^{ld}$				
2 × 2 D	19	27.76	135.68	135.68
4 × 4 D	87	21.40	62.45	62.45
6 × 6 D	203	20.47	54.56	54.56
8 × 8 D	367	20.16	52.20	52.20
$HLCTS_t^{qd}$				
2 × 2 D	19	21.95	62.06	62.06
4 × 4 D	87	20.29	54.30	54.30
6 × 6 D	203	20.00	51.43	51.43
8 × 8 D	367	19.90	50.52	50.52
analytical				
ref. [4.35]		19.74	49.35	49.35

$$\Omega = 2\pi f \frac{b^2}{h}\left(\frac{12\rho(1-\nu^2)}{E}\right)^{1/2} , \tag{4.9}$$

where f is the natural frequency in Hz, b is the side length of the square plate, h is the thickness of the plate. In the table, neq. is the total number of equations of the constrained system. Analytical solutions [4.35] are included in the table for comparison.

The results obtained show clearly that the $HLCTS_r^{qd}$ element converges faster than $HLCTS_r^{ld}$. This is due to the use of quadratic polynomials in the displacement field of the translational DOF w. The quadratic approximation of the transversal displacement field is more accurate than linear approximation. When using the four meshes, 2 × 2 D, 4 × 4 D, 6 × 6 D and 8 × 8 D, the dimensionless frequency parameters for the first natural frequency obtained by using the $HLCTS_r^{qd}$ element differ from the analytical solution by 11.2%, 2.8%, 1.3% and 0.8%, respectively, while $HLCTS_r^{ld}$ results differ by 40.6%, 8.4%, 3.7% and 2.1%. For the second and third modes, the $HLCTS_r^{qd}$ element with the 8 × 8 D mesh overestimates the analytical solution by 2.4%. In this case, the $HLCTS_t^{qd}$ results are almost identical to those using $HLCTS_r^{qd}$. The small differences appear only after the third or fourth decimal places. This implies that whether the moment of inertia and the in-plane rotary inertia are included in the consistent element mass matrix formulation or not, there is virtually no significant difference in this particular case.

The second case is a fully clamped square plate. The same plate analyzed above is now clamped at four sides. The clamped boundary conditions are imposed by constraining all the DOF at the four sides of the plate. The HLCTS results are given in Table 4.2 together with the analytical solution from reference [4.35].

As expected, slightly larger discrepancies are found with the same mesh for the

Table 4.2 First three dimensionless natural frequencies

of the fully clamped isotropic square plate

mesh	neq.	mode sequence		
		1	2	3
$HLCTS_r^{qd}$				
2 × 2 D	15	979.38	1593.99	1593.99
4 × 4 D	75	41.92	101.87	101.87
6 × 6 D	183	38.52	83.64	83.64
8 × 8 D	339	37.39	78.81	78.81
$HLCTS_r^{ld}$				
2 × 2 D	15	1047.95	1936.13	1936.13
4 × 4 D	75	45.04	125.45	125.45
6 × 6 D	183	39.67	90.05	90.05
8 × 8 D	339	38.01	81.98	81.98
$HLCTS_t^{qd}$				
2 × 2 D	15	979.40	1594.04	1594.04
4 × 4 D	75	41.93	101.88	101.88
6 × 6 D	183	38.51	83.65	83.65
8 × 8 D	339	37.40	78.82	78.82
analytical				
ref. [4.35]		35.99	73.41	73.41

simply supported case. For the $HLCTS_r^{qd}$ results, they overpredict the fundamental frequency reported in reference [4.35] by 16.5%, 7.0% and 3.9% with 4 × 4 D, 6 × 6 D and 8 × 8 D meshes, respectively. The corresponding discrepancies given by $HLCTS_r^{ld}$ are 25.1%, 10.2 and 5.6%. Since there are few equations left in the 2 × 2 D mesh model, the result is not considered. To obtain more accurate result, either finer mesh for the plate or finer mesh near the clamped boundaries should be implemented.

Having analyzed the simply supported and clamped square plates, the natural frequencies for a cantilever plate are computed. The geometrical and material properties of the plate remain the same. Now only one side of the square plate is clamped. On this edge, all DOF are constrained and on the other three edges W, Θ_x and Θ_y are left free.

Calculated dimensionless natural frequencies for the cantilever plate are given in Table 4.3. In predicting the fundamental natural frequency and using the four meshes listed in the first column of the table, the respective discrepancies with respect to the analytical solution given in reference [4.35] are 4.7%, 1.2%, 0.4% and 0.1% for $HLCTS_r^{qd}$ results and 3.7%, 1.0%, 0.3% and 0.1% for $HLCTS_r^{ld}$ results. The comparison shows excellent agreement between HLCTS results and analytical solution. High convergence rate is also seen in this case.

4.3.2 Free vibration of rhombic plates

To further examine the performance of the HLCTS elements in the analysis of single layer isotropic plates, rhombic plates are studied. An example is shown in Figure 4.2. The side length of the rhombic plate is L = 1.0 m. The thickness h is 0.005 m. The

Table 4.3 First three dimensionless natural frequencies

of the cantilevered isotropic square plate

mesh	neq.	mode sequence		
		1	2	3
$HLCTS_r^{qd}$				
2 × 2 D	31	3.655	10.020	33.254
4 × 4 D	108	3.533	8.968	23.503
6 × 6 D	234	3.506	8.732	22.279
8 × 8 D	408	3.495	8.643	21.859
$HLCTS_r^{ld}$				
2 × 2 D	31	3.620	10.073	35.722
4 × 4 D	108	3.527	8.999	24.164
6 × 6 D	234	3.504	8.746	22.551
8 × 8 D	408	3.494	8.650	22.007
$HLCTS_t^{qd}$				
2 × 2 D	31	3.655	10.020	33.256
4 × 4 D	108	3.533	8.968	23.503
6 × 6 D	234	3.506	8.732	22.280
8 × 8 D	408	3.495	8.643	21.860
analytical				
ref. [4.35]		3.492	8.525	21.43

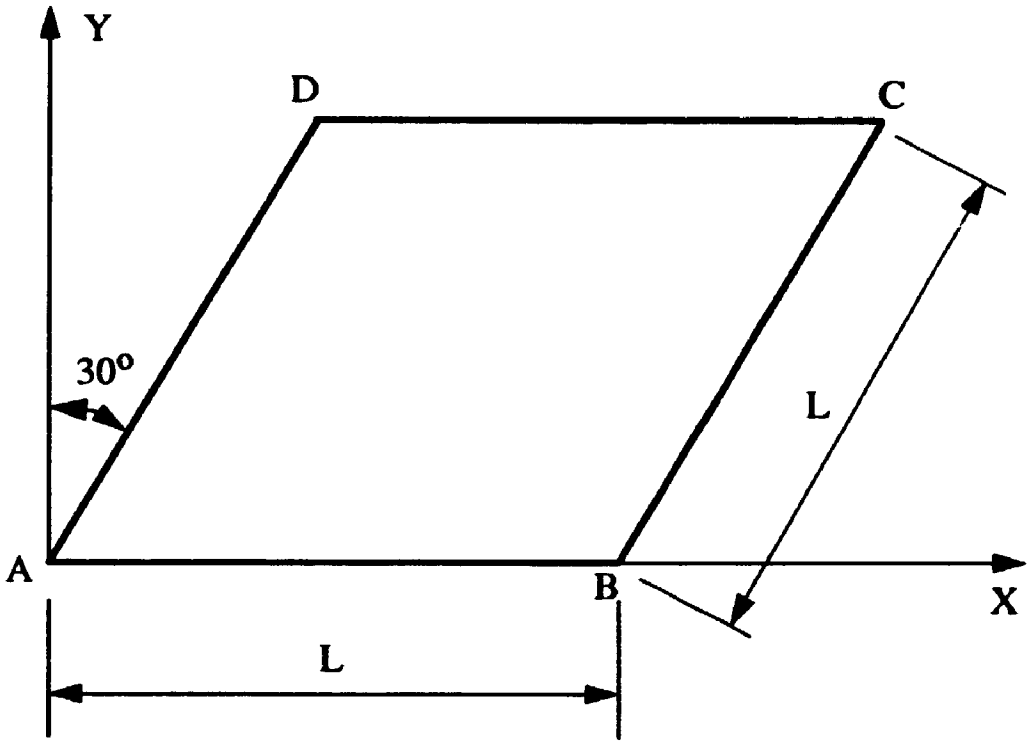

Figure 4.2 An isotropic single layer rhombic plate

skew angle is 30 degree. Its material properties are the same as the square plate considered above.

In the finite element analysis, a global co-ordinate system is attached to the rhombic plate as shown in Figure 4.2. Four meshes, 2 × 2 D, 4 × 4 D, 6 × 6 D and 8 × 8 D are used to model the plate. Two typical mesh layouts are given in Figure 4.3. The rhombic plate is analyzed under three different boundary conditions, simply supported at four sides, fully clamped and cantilevered.

When the rhombic plate is simply supported at four sides, the boundary conditions

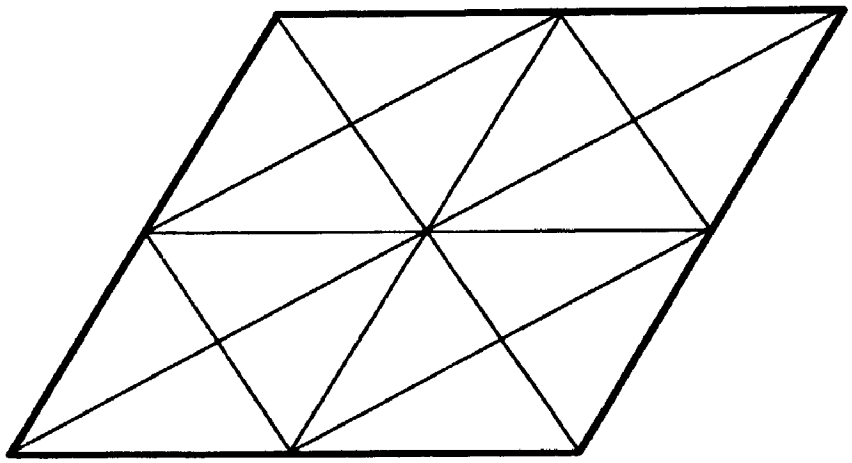

(a) 2×2 D mesh

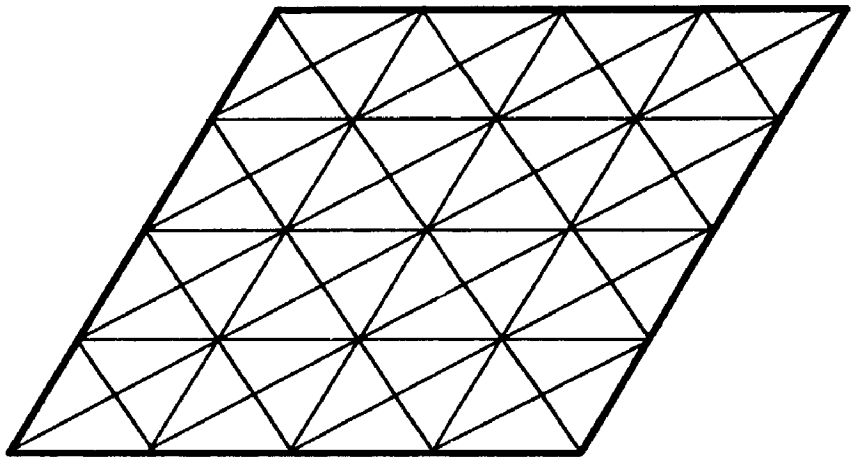

(b) 4×4 D mesh

Figure 4.3 Two typical meshes for rhombic plates

are not straight forward. Here, W is zero at all four simply supported edges. For rotational DOF, Θ_y equals zero at the edges parallel to X axis. However, the two rotational DOF Θ_x and Θ_y are unconstrained at the two inclined edges. All DOF at four corners of the plate are constrained.

Table 4.4 shows the first three natural frequencies obtained by using HLCTS elements. The frequencies are presented in the form of dimensionless frequency parameter which is defined by equation (4.9) with b replaced with L in this case. The HLCTS results are compared with the analytical results from reference [4.36]. By using the 8 × 8 D mesh with $HLCTS_r^{qd}$ and $HLCTS_r^{ld}$ elements, the fundamental frequency results differ from the analytical solution by 4.1% and 5.5%, respectively.

For the fully clamped rhombic plate, all the DOF at the clamped edges are constrained. Numerical results are given in Table 4.5. With the 8 × 8 D mesh and the first mode, the $HLCTS_r^{qd}$ result differs the analytical solution [4.36] by 4.7% and the $HLCTS_r^{ld}$ result differs by 6.6%. The trend is the same as for the fully clamped square plate.

Finally, the dimensionless frequency parameters calculated by using HLCTS elements for the cantilevered case are reported in Table 4.6. For 8 × 8 D mesh and the first mode, the $HLCTS_r^{qd}$ result overestimates the analytical solution by 0.6% and the $HLCTS_r^{ld}$ result overestimates by 0.5%. For the second mode, the discrepancies are -5.4% and -5.2%, respectively. Both results underestimate the analytical ones.

4.4 Vibration Analysis of Multilayer Plates

This section presents numerical results for laminated plates with different

Table 4.4 First three dimensionless natural frequencies

of the simply supported isotropic rhombic plate

mesh	neq.	mode sequence		
		1	2	3
$HLCTS_r^{qd}$				
2 × 2 D	21	32.65	58.41	111.70
4 × 4 D	93	27.35	58.09	86.19
6 × 6 D	213	26.36	54.99	78.33
8 × 8 D	381	25.93	53.93	75.76
$HLCTS_r^{ld}$				
2 × 2 D	21	41.29	127.77	243.31
4 × 4 D	93	28.90	67.19	99.30
6 × 6 D	213	27.00	58.53	83.26
8 × 8 D	381	26.28	55.83	78.38
$HLCTS_t^{qd}$				
2 × 2 D	21	32.65	58.41	111.71
4 × 4 D	93	27.35	58.09	99.50
6 × 6 D	213	26.36	55.00	78.33
8 × 8 D	381	25.93	53.93	75.77
analytical				
ref. [4.36]		24.91	52.67	71.79

Table 4.5 First three dimensionless natural frequencies

of the fully clamped isotropic rhombic plate

mesh	neq.	mode sequence		
		1	2	3
$HLCTS_r^{qd}$				
2 × 2 D	15	978.60	1502.14	1898.46
4 × 4 D	75	56.03	127.76	153.25
6 × 6 D	183	50.21	97.00	122.76
8 × 8 D	339	48.32	89.39	114.33
$HLCTS_r^{ld}$				
2 × 2 D	15	104.97	1934.19	2366.53
4 × 4 D	75	60.29	157.17	188.35
6 × 6 D	183	51.81	105.01	132.19
8 × 8 D	339	49.18	93.37	119.02
$HLCTS_t^{qd}$				
2 × 2 D	15	978.61	1502.26	1898.53
4 × 4 D	75	56.03	127.77	153.27
6 × 6 D	183	50.21	97.01	122.77
8 × 8 D	339	48.32	89.39	114.34
analytical				
ref. [4.36]		46.14	81.20	105.50

Table 4.6 First three dimensionless natural frequencies

of the cantilevered isotropic rhombic plate

mesh	neq.	mode sequence		
		1	2	3
$HLCTS_r^{qd}$				
2 × 2 D	30	4.409	11.233	36.116
4 × 4 D	108	4.108	10.110	28.147
6 × 6 D	234	4.022	9.779	26.815
8 × 8 D	408	3.985	9.637	26.279
$HLCTS_r^{id}$				
2 × 2 D	30	4.319	11.259	38.523
4 × 4 D	108	4.090	10.178	29.231
6 × 6 D	234	4.014	9.813	27.257
8 × 8 D	408	3.981	9.657	26.498
$HLCTS_t^{qd}$				
2 × 2 D	30	4.410	11.233	36.118
4 × 4 D	108	4.108	10.110	28.149
6 × 6 D	234	4.022	9.779	26.816
8 × 8 D	408	3.985	9.638	26.281
analytical				
ref. [4.36]		3.961	10.19	-

lamination schemes, boundary conditions and aspect ratios. A nine layers cross-ply symmetrically laminated square plate, an eight layers antisymmetric laminated angle-ply square plate, and a four layers antisymmetric laminated angle-ply rectangular plate with different side-length ratios and length to thickness ratios are studied. The HLCTS results are compared with analytical or other finite element solutions that are available in the literature.

4.4.1 Vibration of nine layers cross-ply plate

A nine layers cross-ply symmetrically laminated square plate with fibre orientation (0/90/0/90/0/90/0/90/0) is chosen for free vibration analysis. The side length, b, of the plate is 1.0 m (39.37 in). The total thickness of the 0° and 90° layers is the same. The thickness of the laminate is h = 0.01 m (0.3937 in). The material is the high modulus graphite/epoxy composite with $E_1/E_2 = 40$, $G_{12}/E_2 = 0.6$ and $G_{13}/E_2 = G_{23}/E_2 = 0.5$, in which $E_1 = 2.0685\times10^{11}$ N/m^2 (3.0×10^7 psi), $\rho = 1605$ kg/m^3 (0.058 lb/in^3) and Poisson's ratio $\nu_{12} = 0.25$.

In this first case, the plate is simply supported at four sides. The whole plate is modeled by the four finite element meshes shown in Figure 4.1. The shear correction factors are $\kappa_4 = \kappa_5 = (5/6)^{1/2}$. The boundary conditions are the same as for the single layer S4 plates (see subsection 4.3.1). The HLCTS element results are given in Table 4.7. Here, the dimensionless frequency parameters are defined by

$$\Omega = 2\pi f\, b \left(\frac{\rho}{E_2}\right)^{1/2} \times 10 \quad . \tag{4.10}$$

Table 4.7 First three dimensionless natural frequencies

of the 9-layers cross-ply S4 plate

mesh	neq.	mode sequence		
		1	2	3
$HLCTS_r^{qd}$				
2 × 2 D	19	2.08427	6.48111	6.83126
4 × 4 D	87	1.92484	5.55288	6.00242
6 × 6 D	203	1.89712	5.25759	5.70811
8 × 8 D	367	1.88774	5.17046	5.62086
$HLCTS_r^{ld}$				
2 × 2 D	19	2.62976	13.29262	13.92842
4 × 4 D	87	2.02886	6.35132	6.00242
6 × 6 D	203	1.94123	5.56773	5.70811
8 × 8 D	367	1.91216	5.33761	5.62086
$HLCTS_t^{qd}$				
2 × 2 D	19	20.8444	6.48249	6.83270
4 × 4 D	87	1.92500	5.55397	6.00359
6 × 6 D	203	1.89728	5.25862	5.70922
8 × 8 D	367	1.88790	5.17147	5.62195
analytical				
ref. [4.30]		1.88576	-	-

The analytical solution for the first mode in the table is taken from reference [4.30] in which shear deformation was considered. There is no analytical solution available for the second and third modes. The $HLCTS_r^{qd}$ results for the first mode differ from the analytical one by 10.5%, 2.1%, 0.6% and 0.1%, respectively, for the 2 × 2 D, 4 × 4 D, 6 × 6 D and 8 × 8 D meshes. The corresponding discrepancies given by $HLCTS_r^{ld}$ results are 39.5%, 7.6%, 2.9% and 1.4%. It shows consistently that the $HLCTS_r^{qd}$ element has a better performance than the $HLCTS_r^{ld}$ element.

To compare the $HLCTS_r^{qd}$ element with other finite elements, the numerical results for the same problem obtained by different finite element models are included in Table 4.8. Those other finite element results are taken from reference [4.30]. The elements are all shear-deformable type and vary in formulation, element shape, and approximation of the displacement field. The relatively detailed descriptions of these elements are tabulated in Table 4.9. Table 4.8 shows the convergence trend of each element. The $HLCTS_r^{qd}$ element is the simplest element listed in the table. Although it is difficult to make direct comparison when the element shape and number of nodes are different, the accuracy and efficiency can be compared when the total number of DOF of a finite element model is taken into consideration. It seems that the $HLCTS_r^{qd}$ element results converge faster than the ST6 (displacement type, triangular, 6 nodes, 18 DOF per element), MT3 (mixed type, triangular, 3 nodes, 24 DOF per element), SQ4 (displacement type, quadrilateral, 4 nodes, 12 DOF per node), SQ8 (displacement type, quadrilateral, 8 nodes, 24 DOF per element), SQ9 (displacement type, quadrilateral, 9 nodes, 27 DOF per element) and comparable to all the remaining elements including high-order elements, such as ST10 (displacement type, triangular, 10 nodes, 30 DOF per

Table 4.8 Comparison of the convergence on the dimensionless fundamental natural frequency of the 9-layers cross-ply S4 plate by using different finite elements

source	mesh (quarter plate)			
	2 × 2	3 × 3	4 × 4	5 × 5
SQ4	-	-	4.232	3.558
ST6	2.010	1.939	1.910	-
SQ8	1.932	1.899	1.891	1.888
SQ9	1.921	1.898	1.891	-
SQ11	1.905	1.891	-	-
ST10	1.892	1.887	-	-
SQ12	1.896	1.887	-	-
SQH	1.886	-	-	-
MT3	1.836	1.879	1.884	-
MQ4	1.877	1.884	1.885	-
MT6	1.887	-	-	-
$HLCTS_r^{qd}$	1.925	1.897	1.888	-
analytical [4.30]	1.88576			

Table 4.9 Description of characteristics of the shear-flexible finite elements listed in Table 4.8

element	formulation	element shape	approximation	number of nodes	total DOF (for plate)
SQ4	displacement	quadrilateral	bilinear	4	12
ST6	displacement	triangular	quadratic	6	18
SQ8	displacement	quadrilateral	quadratic	8	24
SQ9	displacement	quadrilateral	quadratic	9	27
SQ11	displacement	quadrilateral	quadratic	11	33
ST10	displacement	triangular	cubic	10	30
SQ12	displacement	quadrilateral	cubic	12	36
SQH	displacement	quadrilateral	product of first-order Hermitian polynomials	4	48
MT3	mixed	triangular	linear	3	24
MQ4	mixed	quadrilateral	bilinear	4	32
MT6	mixed	triangular	quadratic	6	48
$HLCTS_r^{qd}$	hybrid	triangular	quadratic for transversal displacement, linear for rotations	3	9

element). For example, the MT6 element case has 200 DOF with a 2 × 2 mesh and prior to the application of boundary conditions while the $HLCTS_r^{9d}$ element model has only 123 DOF with a 4 × 4 D mesh, and yet their results are in excellent agreement.

The nine layers cross-ply laminated square plate is then analyzed with the fully clamped and cantilevered boundary conditions. The boundary conditions imposed to finite element models are the same as for the single layer counterparts in subsection 4.3.1. The results are presented in Table 4.10 and Table 4.11, respectively. There is no analytical or finite element solution for comparison in the C4 and CFFF cases. In Table 4.10, the frequency parameter results are defined in equation (4.10). However, in Table 4.11, they are given as

$$\Omega = 2\pi f\, b \left(\frac{\rho}{E_2}\right)^{1/2} \times 100 \quad . \tag{4.11}$$

4.4.2 Vibration of eight layers angle-ply plate

An eight layers angle-ply square plate is considered in this subsection. The plate is antisymmetrically laminated with a 45 degree angle (45/-45/45/-45/45/-45/45/-45). The side length of the plate is b = 1.0 m and the thickness is h = 0.01 m. The thickness of each layer is 0.01/8 m. The material properties are $E_1/E_2 = 40$, $G_{12}/E_2 = G_{13}/E_2 = 0.6$ and $G_{23}/E_2 = 0.5$, in which $E_1 = 2.0685\times10^{11}$ N/m^2 (3.0×10^7 psi), $\rho = 1605$ kg/m^3 (0.058 lb/in^3) and Poisson's ratio $\nu_{12} = 0.25$. The plate is simply supported at four sides. The entire plate is modeled in the finite element analysis. The boundary conditions imposed to finite element models are the same as for previous S4 plates. The shear

Table 4.10 First three dimensionless natural frequencies

of tne 9-layers cross-ply C4 plate

mesh	neq.	mode sequence		
		1	2	3
$HLCTS_r^{qd}$				
2 × 2 D	15	17.0777	27.8824	27.9487
4 × 4 D	75	4.5920	10.2280	10.8644
6 × 6 D	183	4.2712	8.7165	9.3168
8 × 8 D	339	4.1768	8.3357	8.9238
$HLCTS_r^{ld}$				
2 × 2 D	15	18.2221	33.4794	33.5038
4 × 4 D	75	4.9001	11.9939	12.6767
6 × 6 D	183	4.3907	9.2996	9.9290
8 × 8 D	339	4.2414	8.6385	9.2435
$HLCTS_t^{qd}$				
2 × 2 D	15	17.0783	27.8860	27.9522
4 × 4 D	75	4.5925	10.2304	10.8670
6 × 6 D	183	4.2716	8.7184	9.3189
8 × 8 D	339	4.1772	8.3375	8.9257

Table 4.11 First three dimensionless natural frequencies

of the 9-layers cross-ply cantilever plate

mesh	neq.	mode sequence		
		1	2	3
$HLCTS_r^{qd}$				
2 × 2 D	30	4.5147	6.6778	37.7556
4 × 4 D	108	4.3719	5.7041	28.6511
6 × 6 D	234	4.3497	5.5261	27.4863
8 × 8 D	408	4.3432	5.4701	27.1613
$HLCTS_r^{ld}$				
2 × 2 D	30	4.4628	6.5573	39.3530
4 × 4 D	108	4.3615	5.6933	29.6046
6 × 6 D	234	4.3453	5.5224	27.8890
8 × 8 D	408	4.3409	5.4680	27.3852
$HLCTS_t^{qd}$				
2 × 2 D	30	4.5148	6.6782	37.7644
4 × 4 D	108	4.3720	5.7045	28.6551
6 × 6 D	234	4.3497	5.5265	27.4900
8 × 8 D	408	4.3434	5.4704	27.1649

correction factors are $\kappa_4 = \kappa_5 = (\pi^2/12)^{1/2}$.

Results by using HLCTS elements are reported in Table 4.12. The first three natural frequencies are given in dimensionless frequency parameters defined by

$$\Omega = 2\pi f \frac{b^2}{h}\left(\frac{\rho}{E_2}\right)^{1/2} . \tag{4.12}$$

This problem has been solved in reference [4.37] by applying the first-order shear deformation plate theory (FSDPT) and the high-order shear deformation plate theory (HSDPT). The corresponding results are included in the table for comparison. The $HLCTS_r^{qd}$ results differ from the FSDPT solution by 12.7%, 4.2%, 2.8% and 2.3%, respectively, for the 2 × 2 D, 4 × 4 D, 6 × 6 D and 8 × 8 D meshes. The corresponding discrepancies given by the $HLCTS_r^{ld}$ element are 42.0%, 9.8%, 5.2% and 3.6%.

4.4.3 Vibration of four layers angle-ply plate

A four layers antisymmetric, angle-ply laminated rectangular plate is considered here for the effects of plate aspect ratio (a/b) and length to thickness ratio (a/h) on the fundamental frequency of the plate. The lamination scheme of the simply supported plate is (45/-45/45/-45). Every ply of the laminate has an equal thickness. The layer material properties and shear correction factors are the same as the nine layers cross-ply square plate in subsection 4.4.1.

Firstly, the plate with geometrical properties, a = 2.0 m, b = 1.0 m and h = 0.04 m is analyzed by using the HLCTS elements. The entire plate is discretized by five finite element meshes, 4 × 2 D, 6 × 3 D, 8 × 4 D, 10 × 5 D and 12 × 6 D. The first

Table 4.12 First three dimensionless natural frequencies of the simply supported eight layers angle-ply square plate

mesh	neq.	mode sequence		
		1	2	3
$HLCTS_r^{qd}$				
2 × 2 D	19	28.382	73.097	73.097
4 × 4 D	87	26.235	62.500	62.500
6 × 6 D	203	25.875	59.690	59.690
8 × 8 D	367	25.758	58.848	58.848
$HLCTS_r^{ld}$				
2 × 2 D	19	35.750	148.149	148.149
4 × 4 D	87	27.646	71.505	71.505
6 × 6 D	203	26.474	63.211	63.211
8 × 8 D	367	26.090	60.748	60.748
$HLCTS_t^{qd}$				
2 × 2 D	19	28.385	73.113	73.113
4 × 4 D	87	26.237	62.512	62.512
6 × 6 D	203	25.877	59.702	59.702
8 × 8 D	367	25.760	58.859	58.859
analytical [4.37]				
FSDPT		25.176	-	-
HSDPT		25.174	-	-

integer is the number of elements on side a and the second is on side b. The dimensionless frequency parameter results are given in Table 4.13. They are defined by

$$\Omega = 2\pi f \frac{a^2}{h}\left(\frac{\rho}{E_2}\right)^{1/2} . \tag{4.13}$$

The analytical solution from reference [4.38] is also presented.

By changing the width and thickness of the rectangular plate, different aspect ratios and length to thickness ratios are studied. In this analysis, one quarter of the plate is modeled by the $HLCTS_r^{qd}$ element. A 7 × 5 D mesh is used for the quarter plate which has an aspect ratio a/b = 1.4. When a/b = 1.0 and 2.0, the 5 × 5 D and 10 × 5 D meshes are employed, respectively. The computed fundamental frequency parameters are given in Table 4.14. The frequency parameter is given by equation (4.13). For comparison, finite element results from reference [4.39] and analytical solutions from reference [4.38] are also included in the table. Clearly the agreement between the present results and those from references [4.38, 39] is excellent.

Table 4.13 First three dimensionless natural frequencies of the simply supported four layers angle-ply rectangular plate

mesh	neq.	mode sequence		
		1	2	3
$HLCTS_r^{qd}$				
4 × 2 D	41	58.589	100.001	158.545
6 × 3 D	98	56.456	95.182	144.967
8 × 4 D	179	55.804	93.729	141.141
10 × 5 D	284	55.516	93.084	139.457
12 × 6 D	413	55.364	92.736	138.553
$HLCTS_r^{ld}$				
4 × 2 D	41	66.095	119.742	204.410
6 × 3 D	98	59.462	102.769	162.452
8 × 4 D	179	57.435	97.767	150.262
10 × 5 D	284	56.543	95.600	145.081
12 × 6 D	413	56.070	94.459	142.379
$HLCTS_t^{qd}$				
4 × 2 D	41	58.627	100.084	158.724
6 × 3 D	98	56.492	95.262	145.244
8 × 4 D	179	55.740	93.808	141.299
10 × 5 D	284	55.552	93.1606	139.613
12 × 6 D	413	55.399	92.814	138.709
analytical				
ref. [4.38]		52.29	-	-

Table 4.14 Effects of plate aspect ratio (a/b) and length-to-thickness ratio (a/h) on the dimensionless fundamental frequency parameter of a simply supported four layers angle-ply (45/-45/45/-45) rectangular plate

a/h	source		
	$HLCTS_r^{qd}$	ref. [4.39]	ref. [4.38]
a/b = 1.0			
20	21.827	22.584	21.87
30	23.824	23.676	22.74
40	24.665	24.118	23.08
50	25.087	24.434	23.24
a/b = 1.4			
20	29.659	31.401	30.68
30	33.263	33.457	32.38
40	34.877	34.397	33.05
50	35.790	34.742	33.37
a/b = 2.0			
20	42.798	46.789	46.26
30	49.828	51.132	49.98
40	53.278	53.012	51.52
50	55.145	53.989	52.29

4.5 Vibration Analysis of Single Layer Shells

This section deals with single layer isotropic shell problems. Free vibration analysis of a cylindrical shell panel and a spherical shell segment is performed. The shells are analyzed under simply supported and fully clamped boundary conditions. For the analysis of single layer isotropic shells employing the developed HLCTS elements, the shear correction factor is $\kappa = 5/6$.

4.5.1 Free vibration of cylindrical shells

An isotropic single layer cylindrical shell panel shown in Figure 3.12 is considered. This panel has a square projection plane with side length b = 1.0 m, where b is L in Figure 3.12. The radius of the shell is R = 10.0 m and the thickness of the shell is h = 0.005 m. Thus, one has the ratios R/b = 10 and b/h = 200. The open angle of the panel is $2\varphi = 5.73197$ degree. The material properties of the panel are: Young's modulus $E = 2.0 \times 10^{11}$ N/m^2, Poisson's ratio $\nu = 0.3$ and the density $\rho = 7800.0$ kg/m^3.

Figure 3.12 shows a 2 × 2 D mesh for one quarter of the cylindrical shell panel. Similar to the 2 × 2 D mesh, meshes of 3 × 3 D, 4 × 4 D and 5 × 5 D are also considered for the quarter shell panel. The global co-ordinate systems for the finite element model is shown in the figure.

For the case that the panel is simply supported on both curved and straight sides, the boundary conditions applied to the finite element model are: $U = W = \Theta_y = 0.0$ at curve AB, $V = W = \Theta_x = 0.0$ at straight edge BC, $V = \Theta_x = \Theta_z = 0.0$ at symmetry curved line CD and $U = \Theta_y = \Theta_z = 0.0$ at symmetry straight line AD. For the four

corners, V and Θ_x are free at point A. All DOF are constrained at point B. U and Θ_y are free at point C. W is free at D. With this set of boundary conditions imposed, one can solve for doubly symmetrical modes of the simply supported cylindrical shell panel.

The first three natural frequencies of the double symmetric modes of the panel are obtained by using HLCTS elements and the numerical results are given in Table 4.15. The frequencies are non-dimensionalized by

$$\Omega = 2\pi f R (\rho/E)^{1/2} \quad , \tag{4.15}$$

where Ω is the frequency parameter and f is the natural frequency in Hz. An approximated analytical solution from reference [4.36] for the first double symmetric mode is included in the table for comparison.

The HLCTS element family consists of eight elements for use in vibration analysis of single layer and laminated composite shell structures. They are $HLCTS_r^{qd}$, $HLCTS_r^{ld}$, $HLCTS_t^{qd}$, $HLCTS_r^{qh}$, $HLCTS_r^{lh}$, $HLCTS_t^{qh}$, BT_r^{q} and BT_t^{q}. Though, in the analysis these elements give different predictions, the major difference is due to the quadratic or linear displacement field adopted for the transversal deflection DOF w. This can be seen clearly from Table 4.15. The results presented in the table indicate that the elements with quadratic w are more accurate. This trend is more profound in coarse mesh cases. The results in Table 4.15 also show a rapid convergence rate. For example, the first doubly symmetric mode $HLCTS_r^{qd}$ results of 0.59662, 0.58532 and 0.58465 are obtained, respectively, by using 2 × 2 D, 4 × 4 D and 5 × 5 D meshes. The corresponding differences compared with the value of 0.58242 from reference [4.36] are 2.44%, 0.50% and 0.38%. In the case of using 2 × 2 D mesh, there are only 47 active DOF. The $HLCTS_r^{ld}$ element overestimates the approximated analytical solution by 8.01%, 1.81%

and 1.20%, respectively, with the meshes 2 × 2 D, 4 × 4 D and 5 × 5 D.

Table 4.16 contains the HLCTS results for a fully clamped single layer isotropic cylindrical panel. The panel has the same material and geometrical properties as the simply supported one. One quarter of the panel is solved. All DOF at the curved and straight edges are constrained.

4.5.2 Free vibration of spherical shells

An isotropic single layer spherical shell segment shown in Figure 3.13 is considered. This spherical shell segment is doubly curved and has a square projection plane with side length a = 1.0 m. The radius, R is 10.0 m and the thickness, h is 0.005 m. Thus, the ratios R/a = 10 and a/h = 200. The material properties of the shell are: Young's modulus $E = 2.0 \times 10^{11}$ N/m^2, Poisson's ratio $\nu = 0.3$ and the density ρ = 7800.0 kg/m^3.

In the following the spherical shell segment simply supported on its four curved edges is considered first. Taking one quarter of the shell for analysis, one may model the shell with the 2 × 2 D, 3 × 3 D, 4 × 4 D and 5 × 5 D meshes. The simply supported boundary conditions are: $V = \Theta_x = \Theta_z = 0.0$ at symmetry line AB, $V = W = \Theta_x = 0.0$ at curve edge BC, $U = W = \Theta_y = 0.0$ at curve edge CD and $U = \Theta_y = \Theta_z = 0.0$ at symmetry line AD. For the four corners of the finite element model ABCD, all DOF are constrained except W at point A, the centre of the shell segment. U and Θ_y are free at point B. All DOF are constrained at C while V and Θ_x are free at point D. Note that these boundary conditions are for doubly symmetrical modes.

Table 4.15 First three dimensionless natural frequencies for the doubly symmetric modes of the simply supported isotropic cylindrical shell panel

source	neq.	mode sequence		
		1	2	3
2 × 2 D				
$HLCTS_r^{qd}$	47	0.59662	1.8782	2.1077
$HLCTS_r^{ld}$	47	0.62910	2.5976	2.9148
$HLCTS_t^{qd}$	47	0.59668	1.8784	2.1080
$HLCTS_r^{qh}$	47	0.59646	1.8779	2.1067
$HLCTS_r^{lh}$	47	0.62893	2.5973	2.9134
$HLCTS_t^{qh}$	47	0.59648	1.8782	2.1070
BT_r^{q}	47	0.59282	1.8775	2.0996
BT_t^{q}	47	0.59284	1.8777	2.0998
4 × 4 D				
$HLCTS_r^{qd}$	191	0.58532	1.5767	1.8160
$HLCTS_r^{ld}$	191	0.59295	1.6857	1.9416
$HLCTS_t^{qd}$	191	0.58533	1.5768	1.8161
$HLCTS_r^{qh}$	191	0.58528	1.5767	1.8158
$HLCTS_r^{lh}$	191	0.59291	1.6857	1.9414
$HLCTS_t^{qh}$	191	0.58529	1.5768	1.8160
BT_r^{q}	191	0.58394	1.5765	1.8146
BT_t^{q}	191	0.58395	1.5767	1.8148
5 × 5 D				
$HLCTS_r^{qd}$	299	0.58465	1.5454	1.7881
$HLCTS_r^{ld}$	299	0.58943	1.6118	1.8651
$HLCTS_t^{qd}$	299	0.58466	1.5455	1.7883
$HLCTS_r^{qh}$	299	0.58462	1.5453	1.7880
$HLCTS_r^{lh}$	299	0.58947	1.6118	1.8650
$HLCTS_t^{qh}$	299	0.58463	1.5455	1.7882
BT_r^{q}	299	0.58372	1.5452	1.7872
BT_t^{q}	299	0.58373	1.5454	1.7874
ref. [4.36]		0.58242	-	-

Table 4.16 First three dimensionless natural frequencies for the doubly symmetric modes of the fully clamped isotropic cylindrical shell panel

source	neq.	mode sequence		
		1	2	3
3 × 3 D				
$HLCTS_r^{qd}$	91	1.0479	2.5583	2.7069
$HLCTS_r^{ld}$	91	1.0804	2.9951	3.1724
$HLCTS_t^{qd}$	91	1.0479	2.5586	2.7073
$HLCTS_r^{qh}$	91	1.0479	2.5582	2.7066
$HLCTS_r^{lh}$	91	1.0803	2.9950	3.1720
$HLCTS_t^{qh}$	91	1.0479	2.5585	2.7069
BT_r^{q}	91	1.0473	2.5580	2.7051
BT_t^{q}	91	1.0474	2.5584	2.7055
4 × 4 D				
$HLCTS_r^{qd}$	169	1.0338	2.2947	2.4457
$HLCTS_r^{ld}$	169	1.0516	2.4815	2.6472
$HLCTS_t^{qd}$	169	1.0338	2.2950	2.4460
$HLCTS_r^{qh}$	169	1.0338	2.2947	2.4456
$HLCTS_r^{lh}$	169	1.0516	2.4814	2.6470
$HLCTS_t^{qh}$	169	1.0338	2.2950	2.4459
BT_r^{q}	169	1.0338	2.2946	2.4448
BT_t^{q}	169	1.0334	2.2949	2.4451
5 × 5 D				
$HLCTS_r^{qd}$	271	1.0310	2.1912	2.3479
$HLCTS_r^{ld}$	271	1.0424	2.2986	2.4648
$HLCTS_t^{qd}$	271	1.0311	2.1915	2.3482
$HLCTS_r^{qh}$	271	1.0310	2.1912	2.3479
$HLCTS_r^{lh}$	271	1.0424	2.2987	2.4647
$HLCTS_t^{qh}$	271	1.0311	2.1914	2.3481
BT_r^{q}	271	1.0307	2.1911	2.3473
BT_t^{q}	271	1.0308	2.1914	2.3476

Table 4.17 shows the numerical values of the first three non-dimensional frequency parameters corresponding to the first three doubly symmetric modes. The frequency parameters have been defined in equation (4.15). In the table, the result from reference [4.36] for comparison is an approximated analytical solution for the first mode.

Similar to the cylindrical panel, very good agreement between the HLCTS results and the approximated analytical solution can be found in the table. In the case of using the 5 × 5 D mesh and comparing with the solution from reference [4.36], the discrepancies in predicting the fundamental frequency are 0.15% by using $HLCTS_r^{qd}$, $HLCTS_t^{qd}$, $HLCTS_r^{qh}$ and $HLCTS_t^{qh}$, 0.98% by $HLCTS_r^{ld}$ and $HLCTS_r^{lh}$, 0.13% by BT_r^q and BT_t^q. For the coarse 2 × 2 D mesh with 47 active DOF, the $HLCTS_r^{qd}$ element result differs the approximated analytical solution by 1.03%. For the 4 × 4 D mesh, this difference is 0.34%.

It is also observed that the fundamental frequency of the single layer spherical segment is about 79% higher than that of the single layer cylindrical shell panel investigated in previous subsection. This is because the double curvatures has stiffened the simple structure.

The single layer spherical shell segment is then considered for fully clamped boundary conditions. One quarter of the shell is solved for the first three doubly symmetric frequencies. The resulting dimensionless frequency parameters defined by equation (4.15) are given in Table 4.18. It is noticed that the fundamental frequencies predicted by the $HLCTS_r^{qd}$ element differ each other by 0.52% or less. For the $HLCTS_r^{ld}$ element, they are not more than 2.53%. The number of active DOF in the three finite

Table 4.17 First three dimensionless natural frequencies for the doubly symmetric modes of the simply supported isotropic spherical shell segment

source	neq.	mode sequence		
		1	2	3
2 × 2 D				
$HLCTS_r^{qd}$	47	1.0545	2.1307	2.1362
$HLCTS_r^{ld}$	47	1.1119	2.9470	2.9545
$HLCTS_t^{qd}$	47	1.0545	2.1310	2.1364
$HLCTS_r^{qh}$	47	1.0543	2.1297	2.1352
$HLCTS_r^{lh}$	47	1.1116	2.9456	2.9532
$HLCTS_t^{qh}$	47	1.0543	2.1300	2.1355
BT_r^q	47	1.0529	2.1233	2.1294
BT_t^q	47	1.0529	2.1235	2.1296
4 × 4 D				
$HLCTS_r^{qd}$	191	1.0472	1.8645	1.8701
$HLCTS_r^{ld}$	191	1.0608	1.9935	1.9991
$HLCTS_t^{qd}$	191	1.0472	1.8647	1.8703
$HLCTS_r^{qh}$	191	1.0471	1.8643	1.8699
$HLCTS_r^{lh}$	191	1.0608	1.9933	1.9993
$HLCTS_t^{qh}$	191	1.0472	1.8645	1.8701
BT_r^q	191	1.0468	1.8630	1.8687
BT_t^q	191	1.0469	1.8632	1.8689
5 × 5 D				
$HLCTS_r^{qd}$	299	1.0453	1.8379	1.8413
$HLCTS_r^{ld}$	299	1.0539	1.9170	1.9205
$HLCTS_t^{qd}$	299	1.0453	1.8381	1.8415
$HLCTS_r^{qh}$	299	1.0453	1.8378	1.8412
$HLCTS_r^{lh}$	299	1.0539	1.9169	1.9204
$HLCTS_t^{qh}$	299	1.0453	1.8380	1.8414
BT_r^q	299	1.0451	1.8371	1.8403
BT_t^q	299	1.0451	1.8372	1.8405
ref. [4.36]		1.0437	-	-

Table 4.18 First three dimensionless natural frequencies for the doubly symmetric modes of the fully clamped isotropic spherical shell segment

source	neq.	mode sequence		
		1	2	3
3 × 3 D				
$HLCTS_r^{qd}$	91	1.4814	2.7309	2.7807
$HLCTS_r^{ld}$	91	1.5298	3.2016	3.2477
$HLCTS_t^{qd}$	91	1.4814	2.7312	2.7811
$HLCTS_r^{qh}$	91	1.4813	2.7305	2.7804
$HLCTS_r^{lh}$	91	1.5297	3.2013	3.2473
$HLCTS_t^{qh}$	91	1.4813	2.7309	2.7808
BT_r^{q}	91	1.4801	2.7285	2.7790
BT_t^{q}	91	1.4802	2.7289	2.7794
4 × 4 D				
$HLCTS_r^{qd}$	169	1.4738	2.4843	2.5463
$HLCTS_r^{ld}$	169	1.5015	2.6898	2 7481
$HLCTS_t^{qd}$	169	1.4736	2.4847	2.5466
$HLCTS_r^{qh}$	169	1.4735	2.4842	2.5462
$HLCTS_r^{lh}$	169	1.5014	2.6896	2.7479
$HLCTS_t^{qh}$	169	1.4735	2.4845	2.5465
BT_r^{q}	169	1.4726	2.4829	2.5455
BT_t^{q}	169	1.4727	2.4832	2.5458
5 × 5 D				
$HLCTS_r^{qd}$	271	1.4740	2.3836	2.4579
$HLCTS_r^{ld}$	271	1.4921	2.5027	2.5751
$HLCTS_t^{qd}$	271	1.4741	2.3839	2.4582
$HLCTS_r^{qh}$	271	1.4740	2.3835	2.4579
$HLCTS_r^{lh}$	271	1.4921	2.5026	2.5750
$HLCTS_t^{qh}$	271	1.4740	2.3848	2.4581
BT_r^{q}	271	1.4733	2.3825	2.4574
BT_t^{q}	271	1.4733	2.3828	2.4577

element models are 91, 169 and 271, respectively. This once again shows the rapid convergence rate.

4.6 Vibration Analysis of Multilayer Shells

In this section, free vibration behaviours of laminated composite shell structures are studied. A two layers antisymmetric angle-ply laminated cylindrical panel, a four layers symmetric cross-ply laminated cylindrical panel and a nine layers symmetric cross-ply laminated spherical shell segment are included. The results by using HLCTS elements are compared with the existing solutions in the literature.

4.6.1 Free vibration of multilayer cylindrical shells

The first case considered in this subsection is a two layers antisymmetric, angle-ply cylindrical shell panel. The shell panel is constructed by two equal thickness layers with fibre orientation of (60/-60). The quantities in the bracket are in degree and measured from the positive direction of the X axis (see Figure 3.12 where L is b here). The cylindrical shell panel has a square projection plan with side length b = 1.0 m. The total thickness of the shell is h = 0.05 m. The radius is R = 2.8794 m and the open angle is 2ϕ = 20 degree. The radius to side length ratio R/b = 2.8794 and the side length to thickness ratio b/h = 20. The material used is graphite/epoxy composite with the moduli ratios: E_1/E_2 = 40, $G_{12}/E_2 = G_{13}/E_2$ = 0.6, G_{23}/E_2 = 0.5. The material properties are

$$E_1 = 2.0685\times10^{11}\ \text{N/m}^2\ (3.0\times10^7\ \text{psi}),$$

$$\rho = 1605\ \text{kg/m}^3\ (0.058\ \text{lb/in}^3)\text{; and } \nu_{12} = 0.25.$$

The cylindrical shell panel is simply supported. However, it is different from those studied above. For this shell panel, U or V perpendicular to the boundary edges are also constrained. One quarter of the panel is analyzed. Symmetry conditions are applied. The details of the constraints are: $V = W = \theta_y = 0.0$ at curve AB, $U = W = \theta_x = 0.0$ at straight edge BC, $V = \theta_x = \theta_z = 0.0$ at curved symmetry line CD and $U = \theta_y = \theta_z = 0.0$ at straight symmetry line AD. The constraints for the four corners are the same as those for the single layer isotropic cylindrical panel in subsection 4.5.1. The shear correction factors are $\kappa_4 = \kappa_5 = (\pi^2/12)^{1/2}$.

Table 4.19 contains results by using 2 × 2 D and 4 × 4 D mesh of HLCTS elements. It also contains analytical result from reference [4.40]. The latter gave the dimensionless frequency parameter of the first mode as 18.80. The parameter is defined by equation (4.12). In the analysis, the 4 × 4 D mesh results differ from the analytical solution by no more than 2.20%.

The second laminated cylindrical shell panel considered is a four layer symmetric cross-ply cylindrical shell panel (see Figure 3.12 where L is b here). The shell is constructed by four layers with the fibre orientation in zero and ninety degree directions (0/90/90/0). The geometrical properties of the panel are: R = 1.270 m (50 in), b = 0.254 m (10 in), h = 0.00254 m (0.1 in). Thus, one has R/b = 5 and b/h = 100. The layer material properties are

$$E_1 = 5.1713\times10^{10}\ \text{N/m}^2\ (7.5\times10^6\ \text{psi}),$$

$$\rho = 27680\ \text{kg/m}^3\ (1.0\ \text{lb/in}^3) \text{ and } \nu_{12} = 0.25.$$

The moduli ratios are $E_1/E_2 = 25$, $G_{12}/E_2 = G_{13}/E_2 = 0.5$, $G_{23}/E_2 = 0.2$.

The cylindrical shell panel is simply supported on four sides. One quarter of the

shell is solved in the current study. The boundary conditions imposed are the same as those specified in subsection 4.5.1 for the single layer simply supported cylindrical shell panel. The shear correction factors are unity. The HLCTS element results with 2 × 2 D and 4 × 4 D meshes are presented in Table 4.20. The results are given in dimensionless frequency parameter defined in equation (4.12). The analytical solution for this problem reported in reference [4.41] is 20.360 for the first mode. This Navier-type solution was obtained based on the higher-order shear deformation theory. The HLCTS element results in the table differ from the analytical one by no more than 1.3%.

4.6.2 Free vibration of multilayer spherical shells

As shown in Figure 3.13, the laminated spherical shell segment considered here has a square projection. The spherical shell is a nine layers cross-ply laminate with fibre orientation (0/90/0/90/0/90/0/90/0). The spherical shell segment is symmetrically laminated. The side length, a, of the shell segment is 1.0 m (39.37 in). The total thickness of the 0° and 90° layers is the same. The thickness of the laminate is h = 0.01 m (0.3937 in). The material of the laminate is high modulus graphite/epoxy composite with $E_1/E_2 = 40$, $G_{12}/E_2 = 0.6$ and $G_{13}/E_2 = G_{23}/E_2 = 0.5$, in which

$$E_1 = 2.0685 \times 10^{11} \text{ N/m}^2 \ (3.0 \times 10^7 \text{ psi}),$$

$$\rho = 1605 \text{ kg/m}^3 \ (0.058 \text{ lb/in}^3)$$

and Poisson's ratio $\nu_{12} = 0.25$.

The shell segment is simply supported at four sides. One quarter of shell segment is modeled. Three finite element meshes: 2 × 2 D, 3 × 3 D and 4 × 4 D are considered. The shear correction factors are $\kappa_4 = \kappa_5 = (5/6)^{1/2}$. The boundary conditions

Table 4.19 First three dimensionless natural frequencies for the doubly symmetric modes of the simply supported 2-layers angle-ply cylindrical shell panel

source	neq.	mode sequence		
		1	2	3
2 × 2 D				
$HLCTS_r^{qd}$	45	21.167	66.668	79.451
$HLCTS_r^{ld}$	45	22.135	77.095	87.935
$HLCTS_t^{qd}$	45	21.199	66.975	79.651
$HLCTS_r^{qh}$	45	21.144	66.510	79.414
$HLCTS_r^{lh}$	45	22.110	76.972	87.905
$HLCTS_t^{qh}$	45	21.176	66.820	79.619
BT_r^q	45	20.407	64.329	77.137
BT_t^q	45	20.443	64.696	77.480
4 × 4 D				
$HLCTS_r^{qd}$	189	19.214	51.173	68.417
$HLCTS_r^{ld}$	189	19.413	53.499	70.789
$HLCTS_t^{qd}$	189	19.244	51.464	68.621
$HLCTS_r^{qh}$	189	19.200	51.150	68.361
$HLCTS_r^{lh}$	189	19.399	53.476	70.734
$HLCTS_t^{qh}$	189	19.230	51.441	68.566
BT_r^q	189	18.552	49.477	65.710
BT_t^q	189	18.582	49.789	65.9463
ref. [4.40]		18.800	-	-

Table 4.20 First three dimensionless natural frequencies for the doubly symmetric modes of the simply supported 4-layers cross-ply cylindrical shell panel

source	neq.	mode sequence		
		1	2	3
2 × 2 D				
$HLCTS_r^{qd}$	47	21.184	92.300	116.498
$HLCTS_r^{ld}$	47	22.327	124.107	153.930
$HLCTS_t^{qd}$	47	21.186	92.350	116.546
$HLCTS_r^{qh}$	47	21.182	92.283	116.498
$HLCTS_r^{lh}$	47	22.324	124.086	153.928
$HLCTS_t^{qh}$	47	21.184	92.334	116.544
BT_r^q	47	21.094	91.796	116.478
BT_t^q	47	21 096	91.852	116.525
4 × 4 D				
$HLCTS_r^{qd}$	191	20.357	82.341	111.341
$HLCTS_r^{ld}$	191	20.620	87.781	118.262
$HLCTS_t^{qd}$	191	20.358	82.374	111.381
$HLCTS_r^{qh}$	191	20.356	82.338	111.341
$HLCTS_r^{lh}$	191	20.620	87.778	118.262
$HLCTS_t^{qh}$	191	20.358	82.372	111.381
BT_r^q	191	20.313	82.249	111.338
BT_t^q	191	20.314	82.283	111.378
ref. [4.41]		20.360	-	-

are the same as for the single layer spherical shell segment studied in subsection 4.5.2. The HLCTS element results are given in Table 4.21. The numerical values in the table are dimensionless frequency parameters which are defined in equation (4.11) with b replaced by h. The analytical solutions for the first three doubly symmetrical modes in the table are from reference [4.30] in which shear deformation was considered. For the first mode and by using 4 × 4 D mesh, results applying the HLCTS elements with quadratic polynomial for w converged at the same value 0.2420 which differs from the analytical solution by 0.37%. The results applying two elements with linear displacement field for w converged to 0.2451 which is 1.66% higher than the analytical one. When using the coarse mesh, 2 × 2 D, the respective discrepancies given by these two groups of elements are about 2.57% and 8.09%. That is, the HLCTS elements with quadratic field for w converge faster than those with linear field. The 2.57% discrepancy also indicates that the elements are very efficient as there are only 47 active DOF for this 2 × 2 D mesh model. For the higher modes, it can be seen in the table that refined meshes are required for more accurate result.

A comparison with other finite elements is shown in Table 4.22. The elements include ST6, SQ8, SQ9, SQ11, ST10, SQ12 and SQH. Their properties and characteristics have been described in Table 4.9. The respective number of DOF for the elements are 30, 40, 45, 55, 50, 60 and 80. The elements are of shear deformable type. For brevity, the first and second doubly symmetric natural frequencies expressed in the frequency parameter by equation (4.11) with b replaced by h. are given in the table. As the other HLCTS element results for this problem are presented in Table 4.21 only the results of $HLCTS_r^{qd}$ are included in the table. The other finite element results and

analytical solutions in the table are from reference [4.30]. Since the SQ4 results are much different from the analytical solutions they are not reported here. The overall performance and efficiency of the $HLCTS_t^{qd}$ element is the best in Table 4.22.

The non-dimensionalized frequency parameters for the fully clamped spherical shell segment are include in Table 4.23. All the geometrical and material properties remain the same as the simply supported one investigated above. It may be noted that there is no analytical or numerical solution available in the literature.

4.7 Remarks

In this chapter, the consistent mass matrices for HLCTS elements have been developed. The following points should be mentioned.

(1) Together with the element stiffness matrices developed in Chapter 2, the HLCTS elements are all in explicit expressions. There is no numerical inversion or integration involved.

(2) The HLCTS elements have been applied to solve free vibration problems of single layer and multilayer plates and shells in this chapter. These elements show excellent performance. The comparisons made to the analytical solutions and numerical results obtained by using other finite elements proved that the HLCTS elements are more accurate and efficient than other lower-order elements and even comparable to some high-order elements (see sections 4.4 and 4.6). Note that in the vibration analysis higher mode natural frequencies and mode shapes were obtained but not included here for brevity.

(3) In the investigation, there is no shear locking phenomenon detected. The hybrid strain formulation seems to be effective in eliminating shear locking which is

Table 4.21 First three dimensionless natural frequencies for the doubly symmetric modes of the simply supported 9-layers cross-ply spherical shell segment

source	neq.	mode sequence		
		1	2	3
2 × 2 D				
$HLCTS_r^{qd}$	47	0.2473	1.3010	1.4165
$HLCTS_r^{ld}$	47	0.2606	1.7145	1.8548
$HLCTS_t^{qd}$	47	0.2473	1.3016	1.4170
$HLCTS_r^{qh}$	47	0.2473	1.3010	1.4164
$HLCTS_r^{lh}$	47	0.2606	1.7144	1.8548
$HLCTS_t^{qh}$	47	0.2473	1.3015	1.4170
BT_r^{q}	47	0.2471	1.3000	1.4155
BT_t^{q}	47	0.2471	1.3006	1.4161
3 × 3 D				
$HLCTS_r^{qd}$	107	0.2428	1.2247	1.2866
$HLCTS_r^{ld}$	107	0.2485	1.3691	1.4390
$HLCTS_t^{qd}$	107	0.2429	1.2251	1.2871
$HLCTS_r^{qh}$	107	0.2428	1.2246	1.2866
$HLCTS_r^{lh}$	107	0.2485	1.3691	1.4390
$HLCTS_t^{qh}$	107	0.2429	1.2251	1.2871
BT_r^{q}	107	0.2428	1.2243	1.2863
BT_t^{q}	107	0.2428	1.2247	1.2867
4 × 4 D				
$HLCTS_r^{qd}$	191	0.2420	1.1281	1.2750
$HLCTS_r^{ld}$	191	0.2451	1.2003	1.3546
$HLCTS_t^{qd}$	191	0.2420	1.1285	1.2755
$HLCTS_r^{qh}$	191	0.2420	1.1281	1.2750
$HLCTS_r^{lh}$	191	0.2451	1.2003	1.3546
$HLCTS_t^{qh}$	191	0.2420	1.1285	1.2755
BT_r^{q}	191	0.2420	1.1278	1.2748
BT_t^{q}	191	0.2420	1.1283	1.2752
ref. [4.30]		0.2411	1.063	1.292

Table 4.22 Comparison of convergence on the dimensionless natural frequency of the 9-layers cross-ply S4 spherical shell segment by using different finite elements

source	mesh (quarter plate)		
	2 × 2	3 × 3	4 × 4
first doubly symmetric mode			
ST6	0.2538	0.2459	-
SQ8	0.2452	0.2422	0.2416
SQ9	0.2433	0.2422	-
SQ11	0.2428	-	-
ST10	0.2417	-	-
SQ12	0.2419	-	-
SQH	0.2412	-	-
$HLCTS_r^{qd}$	0.2473	0.2428	0.2420
analytical [4.30]	0.2411		
second doubly symmetric mode			
ST6	1.350	1.173	-
SQ8	1.303	1.136	1.094
SQ9	1.265	1.134	-
SQ11	1.182	-	-
ST10	1.094	-	-
SQ12	1.099	-	-
SQH	1.084	-	-
$HLCTS_r^{qd}$	1.301	1.225	1.128
analytical [4.30]	1.063		

problematic in lower-order finite elements employing displacement formulation.

(4) The numerical study confirms that the HLCTS elements with quadratic displacement field for w are more accurate and converge faster than those with linear field. Whether the moment of inertia is included or not it seems to have no significant

Table 4.23 First three dimensionless natural frequencies for the doubly symmetric modes of the fully clamped 9-layers cross-ply spherical shell segment

source	neq.	mode sequence		
		1	2	3
4 × 4 D				
$HLCTS_r^{qd}$	169	0.6741	1.5775	1.7393
$HLCTS_r^{ld}$	169	0.6850	1.6837	1.8510
$HLCTS_t^{qd}$	169	0.6742	1.5781	1.7399
$HLCTS_r^{qh}$	169	0.6741	1.5775	1.7393
$HLCTS_r^{lh}$	169	0.6850	1.6837	1.8510
$HLCTS_t^{qh}$	169	0.6741	1.5781	1.7399

effect on results of thin plate and shell structures.

(5) The improved formulation of DDOF has eliminated the zero energy modes or spurious modes from the HLCTS elements. With the displacement formulation of DDOF, all three zero energy modes are eliminated from the HLCTS elements while the hybrid formulation eliminates one.

(6) Finally, in Chapter 3, the $HLCTS^{qd}$ and $HLCTS^{ld}$ elements have been found to be the most favourite ones in terms of both accuracy and rank sufficiency. In this chapter, the results from vibration analysis show that $HLCTS_r^{qd}$ converges faster than $HLCTS_r^{ld}$. Therefore, in the next chapter, the hybrid strain triangular shell element $HLCTS_r^{qd}$ is further developed for geometrically non-linear analysis of laminated composite shell structures.

CHAPTER 5

THEORIES AND FINITE ELEMENT FORMULATIONS FOR GEOMETRICALLY NONLINEAR LAMINATED COMPOSITE SHELL STRUCTURES

Having formulated the HLCTS finite elements for the linear analysis of laminated composite shell structures in Chapter 2, studied linear static and dynamic problems of such structures in Chapter 3 and Chapter 4, the studies of geometrical nonlinearity of laminated composite shell structures are pursued in this chapter. The objectives are finding a solid theoretical basis for formulating a simple and efficient laminated composite shell element for geometrically nonlinear analysis, and derivation of the element stiffness and consistent mass matrices for large scale analysis. Thus, the theories and finite element formulations for the analysis of geometrically nonlinear laminated composite shell structures are discussed and the derivation of a simple three-node, six degree-of-freedom (DOF) per node, hybrid strain based laminated composite triangular shell finite element for large scale geometrically nonlinear analysis is performed. Numerical studies of geometrically nonlinear laminated composite plate and shell structures are presented in the next chapter.

This chapter consists of seven sections. Section 5.1 outlines various features of the present formulation. Section 5.2 reviews the development on the finite element analysis of geometrically nonlinear laminated composite shell structures. In particular, the focus is on triangular shell elements that are efficient for large scale computational analysis.

Section 5.3 presents the incremental formulation of the hybrid laminated composite triangular shell elements for geometrically nonlinear shell problems. Constitutive relations are discussed in section 5.4, while the element mass matrices are derived in section 5.5. Section 5.6 deals with configuration and stress updating. This chapter concludes with the remarks in section 5.7.

5.1 Features of Present Formulation

General nonlinear shell analysis is challenged by many conceptual, theoretical, as well as computational difficulties. Even when the scope is confined to static and quasi-static analysis, these difficulties may include: (1) consistent linearization of the underlying variational form of the governing equations; (2) use of objective measures of stress and strain, and their rate, that are suitable for the particular form of the constitutive relation used; (3) treatment of large rotations, in both stiffness derivation and configuration updating; and (4) the proper representation of nonlinear material behaviours. In the context of isotropic nonlinear shell structures, the foregoing issues were discussed by Liu and To [5.1]. In their studies hybrid strain based three node flat triangular shell elements were developed for large scale analysis of general shell structures. They have six degrees-of-freedom (DOF) per node. The updated Lagrangian formulation and incremental Hellinger-Reissner variational principle were adopted. The independently assumed fields were the incremental displacements and strains. The incremental stress and strain measures selected were the incremental second Piola-Kirchhoff stress and the incremental Washizu strain. Variable thickness of the shell was also considered so as to account for the "thinning effect" due to large strain. The companion numerical studies of To and Liu

[5.2] have shown that the hybrid strain based flat triangular shell elements are excellent for nonlinear static and dynamic analysis of general shell structures that are undergoing large deformation of finite strain and finite rotation. In addition, it is relatively simple to formulate and easy to input data describing the shell geometry. It is capable of representing rigid body motions. The element matrices were obtained by making use of a combination of manual and computer assisted derivations, and therefore it eliminates the need for numerical integration. They are degenerated in nature and thus are applicable to moderately thick and thick shells.

Consequently, in the investigation reported here the theory and formulation presented by Liu and To [5.1] are applied to the derivation of composite laminated shell finite elements for geometrically nonlinear analysis.

5.2 Review of the Finite Element Analysis of Geometrically Nonlinear Laminated Composite Shell Structures

A significant amount of work on the study of geometrical nonlinearity of structures has been directed to laminated composite shells. When the geometry and loading conditions are complicated analytical approaches often fail to provide adequate solution. Therefore, the finite element method is the logical alternative. In parallel to the development of nonlinear shell theories and laminated composite shell theories, the development of efficient finite elements has been given notable consideration.

Experience in linear and nonlinear analysis of laminated composite structures indicates that the application of shear deformable theory in nonlinear analysis may be very important due to the fact that the shear moduli are usually much smaller than those of

principal ones. Earlier work of geometrically nonlinear analysis using finite elements shown that, in the course of seeking for simple and efficient finite element procedures, shear deformable theories were commonly employed.

In 1974, Noor and Mathers [5.3] developed an eight node and a twelve node quadrilateral shell elements to study geometrically nonlinear behaviours of laminated shells. These elements are displacement type. Later, in 1977, Noor and Hartley [5.4] proposed a mixed formulation for an eight node and a nine node quadrilateral elements which are shear deformable. The elements were developed based on a form of the shallow shell theory. The fundamental unknowns consisted of thirteen stress resultants and generalized displacements of the shell. The total number of DOF of the eight and nine node elements were 104 and 117, respectively. In the computational procedure, total Lagrangian description was adopted. Noor and Anderson [5.5], studied a class of mixed elements in 1982. These included four, eight, nine, twelve and sixteen node quadrilateral elements. Similar to those proposed in reference [5.4], the elements were based on shallow shell theory with the effects of transverse shear deformation considered. The fundamental unknowns were eight stress resultants and five generalized displacements. Total Lagrangian formulation was used. The focuses were on identifying classes of equivalent mixed models and reduced or selective integration displacement models for curved shell structures and discussing the merits of using mixed models. These elements differ from those of reference [5.4] by the fact that the stress resultants are discontinuous at interelement boundaries and are eliminated on the element level. An eight node and a nine node degenerated isoparametric elements for large deformation analysis of laminated anisotropic shells were presented by Chang and Sawamiphakdi [5.6] in 1981. These two

quadrilateral elements have five DOF at each node. The derivations of the nonlinear geometric element stiffness matrices were made on the basis of update Lagrangian description. In the same year, Reddy [5.7] performed the large deformation analysis of multilayered anisotropic shells using several shell theories. In 1984, Chao and Reddy [5.8] proposed a degenerated three dimensional element based on the total Lagrangian description of motion of the layered anisotropic composite medium. The element is quadrilateral, eight node and displacement type. Both static and dynamic analysis of geometrically nonlinear laminated anisotropic shells were performed. Later in 1985, Reddy and Chandrashekhara [5.9] presented a doubly curved shear deformable shell element. The element has nine nodes and was developed on the basis of extended Sander's shell theory that accounts for the shear deformation and the von Karman strains. This displacement type element was used for bending analysis of laminated composite shells. At the same time, in their other paper [5.10], Reddy and Chandrashekhara developed a four node and a nine node quadrilateral shear deformable elements for transient analysis of geometrically nonlinear (in von Karman sense) laminated composite shells. These two elements have five DOF at each node. Thus, for the four node element the total DOF are 20 and for the nine node element are 45. A general curved laminated composite shell element was given by Saigal, Kapania and Yang [5.11] in 1986. The formulation and computational procedures were developed for the finite element analysis of laminated anisotropic composite thin shells including imperfections. The element is quadrilateral in shape and has four nodes. Each node possesses 12 DOF. There are 48 DOF for this element. It was based on Kirchhoff-Love shell theory with total Lagrangian description. In this reference, both perfect and imperfect laminated shell were studied and

numerical results presented. In 1987, Rothert and Dehmel [5.12] derived a class of degenerated laminated plate and shell elements for nonlinear analysis. The elements could be four, eight or nine node elements. Hybrid stress approach was utilized in formulating the elements. To avoid shear locking, the terms for stress and strain were split into two parts during the derivation. One part satisfied completely the kinematic field equations. In the part, the strain-displacement compatibility was satisfied in a weak form. In the same year, Wu, Yang and Saigal [5.13] performed free and forced vibration analysis of geometrically nonlinear laminated composite shells of general form. The element used was a higher-order curved shell element. Similar to the element proposed in reference [5.11], the element is quadrilateral has four nodes. Each node has 12 DOF. This 48 DOF displacement type laminated shell element was based on the Kirchhoff-Love theory. Yeom and Lee [5.14] developed a nine node quadrilateral element for the analysis of geometrically nonlinear laminated composite shells. It was also based on the degenerated solid shell concept and a set of assumed strain field was utilized as well as assumed displacement field. Liao and Reddy [5.15] combined a degenerated three-dimensional shell element and an associated curved beam element for the analysis of stiffened composite shells with geometrical nonlinearity. The shell element has nine nodes and the beam element has three nodes. The incremental equations of motion was developed by using the total Lagrangian description. The nonlinear formulation admits arbitrarily large displacements of small strain. Large rotations of small strain were claimed to be included in the formulation. However, no detailed treatment of large rotation was given in this reference [5.15]. It seems that the elements in the foregoing references have some common features. They include the ability to deal with large deflections but small strain.

On the other hand, the problem of accurately representing large rotations has received relatively less attention over the years. Recently, an element formulated for laminated anisotropic shells by applying a moderate rotation theory was reported by Palmerio, Reddy and Schmidt [5.16, 17]. Reference [5.16] discussed the theory and [5.17] presented the finite element analysis. In this proposed formulation, the magnitude of strains was limited to a small value. The element proposed was nine node quadrilateral element with five DOF at each node. More recently, Rothert and Di [5.18] presented a simple general shell element with four corner nodes and arbitrary curvatures for geometrically nonlinear analysis of layered shell structures. It is based on a modified incremental Hellinger-Reissner variational principle and a total Lagrangian description with large rotation of small strain. Each corner node has 5 DOF. When the higher order terms of the displacement were included the each corner node has 9 DOF.

Triangular shell elements were also developed for geometrically nonlinear analysis of laminated composite shell structures. One of the earlier work is due to Noor and Mathers [5.3]. In the latter a mixed type triangular element was proposed. The element has six nodes, and 78 DOF. This element is similar to those quadrilateral elements given in the reference except that it is triangular. It was derived based on shallow shell theory and was shear deformable. Recently, in 1991, Lin, Fafard, Beaulieu and Massicotte [5.19] developed a finite element procedure to analyze composite bridges. The finite element procedure was based on small elasto-plastic strains and updated Lagrangian formulation. The element used was flat and constructed by the superposition of a discrete Kirchhoff bending element and a linear strain triangular membrane element. It has six nodes. There are three translational and three rotational DOF at its corner nodes and three

translational DOF at mid-side nodes. In 1994, Madenci and Barut [5.20] proposed a flat triangular shell element based on the free formulation concept for analyzing geometrically nonlinear thin composite shells. A corotation form of the updated Lagrangian formulation is utilized. The theoretical basis was on the geometrically nonlinear Kirchhoff plate theory without considering the effects of transverse shear deformation. The element is of displacement type. It has three nodes and six DOF for each node. A more recent contribution on triangular elements is made in 1995 by Zhu [5.20]. The natural approach is used to construct a curved triangular shell element for analysis of geometrically nonlinear sandwich and composite shell structures. The element has six nodes. There are six DOF at each corner node and three DOF at each mid-side node. Updated Lagrangian description was adopted in the procedure. In the element formulation the transverse shear deformation was considered by assuming constant transverse shear stress distribution.

5.3 Formulation of Element Stiffness Matrices

In this section, finite element formulation for the derivation of a family of simple three-node, six DOF per node, hybrid strain based laminated composite triangular shell finite elements for large scale geometrically nonlinear analysis is given. Large deflection of finite strains and finite rotations are emphasized. The first order shear deformation theory and the degenerated three dimensional solid concept are adopted. In particular, element matrices for one member of the family are derived explicitly with the help of the symbolic computer algebra package MACSYMA [5.22]. To minimize the algebraic manipulation involved in the derivation, updated Lagrangian description is employed in the incremental formulation of the finite element procedure. In essence, the present

formulation is an extension of the work by Liu and To [5.1] for isotropic materials to multi-layer laminated composite materials. Therefore, in the development the present approach follows closely that of reference [5.1]. However, it must be noted that the amount of algebraic manipulation is substantially increased while the first order lamination theory is incorporated.

5.3.1 Incremental variation principle

The Hellinger-Reissner Functional π_{HR} can be written as

$$\pi_{HR} = \int [(e^{\varepsilon})^T C e^{u} - \frac{1}{2}(e^{\varepsilon})^T C (e^{\varepsilon}) \, dV - W \tag{5.1}$$

where,

e^{ε} is the independently assumed strain field;

e^{u} is the strain due to displacement;

C is the material stiffness matrix or elasticity matrix;

W is the work done by external forces,

and the superscripts ε and u indicate that the quantities are from independently assumed strain field and displacement field, respectively.

For geometrically nonlinear analysis with incremental formulation and updated Lagrangian description, the static and kinematic variables in current equilibrium configuration at time t are assumed to be known quantities and the objective is to determine their values in the unknown subsequent equilibrium configuration at time $t+\Delta t$. For a time increment Δt, that is from time t to $(t+\Delta t)$, one has

$$\Delta \pi_{HR} = \Delta \pi_{HR}(\Delta u, \Delta e^{\varepsilon}) = \pi_{HR}(t+\Delta t) - \pi_{HR}(t) \, , \tag{5.2}$$

or, with reference to equation (5.1),

$$\Delta\pi_{HR} = \int [(e^t)^T C(\Delta e^u) + (\Delta e^t)^T C(\Delta e^u) - \frac{1}{2}(\Delta e^t)^T C(\Delta e^t) - (\Delta e^t)^T C(e^t - e^u)]\, dV - \Delta W' . \tag{5.3}$$

where,

Δu is the vector of incremental displacement;

Δe^t is the vector of independently assumed incremental updated Green strains;

Δe^u is the vector of incremental updated Green 'geometric' strains or incremental Washizu strains;

e^t is the Almansi strain vector at time t which is accumulated from assumed incremental strains,

e^u is the vector of Almansi strains at time t (due to displacement);

ΔW is the work-equivalent term corresponding to prescribed body forces and surface tractions in configuration $C^{t+\Delta t}$.

Equation (5.3) represents the incremental form of Hellinger-Reissner variational principle. For updated Lagrangian description, the integral is evaluated at the current configuration. In the equation, the term

$$\int (\Delta e^t)^T C(e^t - e^u)\, dV$$

is the so-called compatibility-mismatch. In reference [5.38], numerical results showed that though totally discarding the term resulted in convergence difficulties, while including the term in only the first iteration of every load step yielded essentially the same results as those having the term under all circumstances. However, references [5.1, 5.22] reported

no difficulties for convergence when the term was ignored. In these two references, hybrid strain formulation was employed for the elements. In the current study, this term is also ignored. Then equation (5.3) can be recasted as

$$\Delta\pi_{HR} = \int [\ \sigma^T \Delta e^u + (\Delta e^\varepsilon)^T C(\Delta e^u) - \frac{1}{2}(\Delta e^\varepsilon)^T C(\Delta e^\varepsilon)\ ]\, dV - \Delta W\ , \tag{5.4}$$

where $\sigma^T = (e^\varepsilon)^T C$ is the Cauchy (true) stress vector at the current configuration. In this equation, the incremental Washizu strain Δe^u can be expressed in two parts

$$\Delta e_{ij}^u = \Delta\varepsilon_{ij}^u + \Delta\eta_{ij}^u \tag{5.5a}$$

and they are related to the incremental displacement by

$$\Delta\varepsilon_{ij}^u = \frac{1}{2}(\Delta u_{i,j} + \Delta u_{j,i})\ ,\quad \Delta\eta_{ij}^u = \frac{1}{2}\Delta u_{k,i}\Delta u_{k,j} \tag{5.5b,c}$$

where the Einstein summation convention for indices has been adopted and the differentiation is with respect to reference co-ordinates at the current configuration C^t.

Substituting equation (5.5a) into (5.4) yields

$$\Delta\pi_{HR} = \int [-\frac{1}{2}(\Delta e^\varepsilon)^T C(\Delta e^\varepsilon) + (\Delta e^\varepsilon)^T C(\Delta\varepsilon^u) + \sigma^T\Delta\varepsilon^u + \sigma^T\Delta\eta^u + (\Delta e^\varepsilon)^T C\Delta\eta^u\ ]\, dV - \Delta W\ . \tag{5.6}$$

Discarding the higher order term, $(\Delta e^t)^T C\Delta\eta^u$, results in

$$\Delta\pi_{HR} = \int [-\frac{1}{2}(\Delta e^\varepsilon)^T C(\Delta e^\varepsilon) + (\Delta e^\varepsilon)^T C(\Delta\varepsilon^u) + \sigma^T\Delta\varepsilon^u + \sigma^T\Delta\eta^u]\, dV - \Delta W\ . \tag{5.7}$$

5.3.2 Hybrid strain formulation

Element stiffness matrices for an hybrid strain based finite element can be derived directly from equation (5.7). Generally the independently assumed strain field and displacement field can be written as

$$\Delta e^{\varepsilon} = P\,\Delta\alpha\ ,\quad \Delta u = \phi\,\Delta q \tag{5.8a,b}$$

where P is the strain distribution matrix, ϕ is the displacement shape function matrix, $\Delta\alpha$ is the vector of incremental strain parameters and Δq is the incremental nodal displacement. Substituting equations (5.8a, b) into (5.7) gives

$$\begin{aligned}\Delta\pi_{HR}(\Delta q,\Delta\alpha) = \sum\{\int_{V_e}[&-\frac{1}{2}\Delta\alpha^{T}P^{T}CP\Delta\alpha\\ &+\Delta\alpha^{T}P^{T}CB_{L}\Delta q+\sigma^{T}B_{L}\Delta q\\ &+\frac{1}{2}\Delta q^{T}B_{NL}^{T}\sigma_{C}^{T}B_{NL}\Delta q\,]\,dV_{e}-\Delta W\}\ ,\end{aligned} \tag{5.9}$$

where the summation is over the entire system and V_e is the volume of an element at the current configuration. Note that the following definitions have been employed in obtaining equation (5.9)

$$\begin{aligned}\Delta\varepsilon^{u} &= B_{L}\,\Delta q\ ,\\ \sigma^{T}\Delta\eta &= \frac{1}{2}\Delta q^{T}B_{NL}^{T}\sigma_{C}^{T}B_{NL}\Delta q\ .\end{aligned} \tag{5.10a,b}$$

where B_L and B_{NL} are the linear and nonlinear strain-displacement matrices and σ_C is a matrix that contains the Cauchy stress components at the current configuration. By defining

$$H = \int_{V_\bullet} P^T C P \, dV_\bullet , \quad G = \int_{V_\bullet} P^T C B_L \, dV_\bullet ,$$
$$k_{NL} = \int_{V_\bullet} B_{NL}^T \sigma_C^T B_{NL} \, dV_\bullet , \quad F_1 = \int_{V_\bullet} B_L^T \sigma \, dV_\bullet , \tag{5.11}$$

equation (5.9) becomes,

$$\Delta\pi_{HR}(\Delta q, \Delta\alpha) = \sum \{ -\frac{1}{2}\Delta\alpha^T H \Delta\alpha \; \Delta\alpha^T G \Delta q$$
$$+ F_1^T \Delta q + \frac{1}{2}\Delta q^T k_{NL} \Delta q - F^T \Delta q \} \tag{5.12}$$

with F being the external nodal force vector in the neighbour configuration associated with the ΔW term in equation (5.9).

Taking variation of equation (5.12) with respect to $\Delta\alpha$ and Δq, respectively, leads to

$$\Delta\alpha = H^{-1} G \Delta q \tag{5.13}$$

and

$$(k_L + k_{NL}) \Delta q = F - F_1 \tag{5.14a}$$

where

$$k_L = G^T H^{-1} G \tag{5.14b}$$

is the element "linear" stiffness matrix. The term k_{NL} defined in equation (5.11) is the "nonlinear" or initial stress stiffness matrix and F_1 is the pseudo-force vector. The right hand side of equation (5.14a) is the equilibrium imbalance.

5.3.3 Description of incremental displacement field

In Chapter 2, the derivation of linear HLCTS elements has been presented. Here, for geometrically nonlinear analysis, the derivation of the element stiffness matrices is extended from the element HLCTS^{qd}. Figure 2.1 shows a flat laminated composite shell element and its co-ordinate systems. The same co-ordinate systems are selected in the incremental element formulation. An arbitrary point within an element is defined by the local co-ordinates as

$$\begin{Bmatrix} r^t \\ s^t \\ t^t \end{Bmatrix} = \sum_{i=1}^{3} \xi_i \begin{Bmatrix} r_i^t \\ s_i^t \\ 0 \end{Bmatrix} + \zeta^t \sum_{i=1}^{3} \xi_i V_i^t \tag{5.15}$$

where the superscript t denotes at the time "t". In the equation, the element nodal co-ordinates r_i, s_i and t_i are defined on the mid-surface of the element. Thus, t_i is always zero. The rotations, directors and their increments are also defined on the mid-surface. The symbol V_i^t (i=1,2,3) denotes the director of node i at the time "t", and ξ_i (i=1,2,3), is the natural or area co-ordinates while ζ^t is the co-ordinate along the director direction and satisfies

$$-\frac{h^t}{2} \le \zeta^t \le \frac{h^t}{2} \tag{5.16}$$

with h^t being the total thickness of the laminated composite shell at time "t". In the current study, h is assumed to be a constant at each incremental time step.

In equation (5.15), the first summation represents the position of the mid-surface while the second summation indicates that the director orthogonal frame is interpolated in exactly the same way as the mid-surface r and s co-ordinates. References [5.23-28]

named such an interpolation scheme "continuum consistent interpolation". Compared with the other two interpolation schemes proposed in references [5.23-28], continuum consistent interpolation is simple and easy to implement.

The incremental displacements of an arbitrary point within the element can be expressed as

$$\begin{Bmatrix} \Delta u^t \\ \Delta v^t \\ \Delta w^t \end{Bmatrix} = \sum_{i=1}^{3} \xi_i \begin{Bmatrix} \Delta u_i^t \\ \Delta v_i^t \\ \Delta w_i^t \end{Bmatrix} + \zeta^t \sum_{i=1}^{3} \xi_i \, (\Delta V_i^t) \, , \tag{5.17}$$

in which, the element's nodal incremental displacements in the first summation are at the mid-surface of the element.

In equation (5.17) the first summation represents the incremental displacements of an arbitrary point located on the mid-surface. The second summation reflects the change in orientation of director of the arbitrary point on the mid-surface which is interpolated from ΔV_i^t (i=1,2,3), the increment of director at node i. References [5.1, 2, 23] applied the exponential mapping scheme to obtain the increment of director ΔV_i^t. It is defined by

$$\begin{aligned} \Delta V_i^t &= (\Delta \theta_i')^t \times V_i^t = -V_i^t \times (\Delta \theta_i')^t \\ &= -\Omega_i^t (\Delta \theta_i')^t \end{aligned} \tag{5.18}$$

where $(\Delta \theta_i')^t$ is the incremental rotational vector of node i, relative to the director orthogonal frame attached to the same node. If the components of V_i^t are $[V_{ri}^t, V_{si}^t, V_{ti}^t]^T$, Ω_i^t is then a skew-symmetric matrix associated with V_i^t of node i:

$$\Omega_i^t = \begin{bmatrix} 0 & -V_{ti}^t & V_{si}^t \\ V_{ti}^t & 0 & -V_{ri}^t \\ -V_{si}^t & V_{ri}^t & 0 \end{bmatrix}. \tag{5.19}$$

It should be noted that $(\Delta\theta_i')^t$ is defined with respect to V_i^t which generally does not coincide with the t-axis. The transformation

$$(\Delta\theta_i')^t = \Gamma_i^t (\Delta\theta_i)^t \tag{5.20}$$

is the so-called exponential mapping, in which $(\Delta\theta_i)^t$ is the incremental rotational vector relative to the r-s-t axes and Γ_i^t is an orthogonal matrix associated with node i. The latter, matrix Γ_i^t satisfies

$$V_i^t = \Gamma_i^t e_3 \tag{5.21}$$

where $e_3 = [0,0,1]^T$ is the unit vector of the t-axis and V_i^t is the position vector of director at node i of the reference configuration and can be calculated from configuration updating. Another way of determining Γ_i^t is, according to references [5.30-35],

$$\Gamma_i^t = a I_3 + \hat{B} + \frac{1}{1+a} B B^T \tag{5.22}$$

where I_3 is a 3×3 identity matrix, $a = V_i^t \cdot e_3$, $B = e_3 \times V_i^t$ and $\hat{B}$ is a skew-symmetric matrix constructed from vector $B = [B_1, B_2, B_3]^T$ according to the following equation

$$\hat{B} = \begin{bmatrix} 0 & -B_3 & B_2 \\ B_3 & 0 & -B_1 \\ -B_2 & B_1 & 0 \end{bmatrix}. \tag{5.23}$$

Equation (5.18) indicates that V_i^t, ΔV_i^t and $(\Delta\theta_i')^t$ are mutually normal. Considering the normality condition between $(\Delta\theta_i')^t$ and V_i^t, one writes

$$\begin{aligned}(\Delta\theta_i')^t \cdot V_i^t &= \left[(\Delta\theta_i')^t\right]^T V_i^t = \left[(\Delta\theta_i)^t\right]^T (\Gamma_i^t)^T \Gamma_i^t \, e_3 \\ &= \left[(\Delta\theta_i)^t\right]^T e_3 = (\Delta\theta_i)^t \cdot e_3 = 0 \, .\end{aligned} \tag{5.24}$$

This condition is satisfied only if $\Delta\theta_{ti}^t = 0$.

Substituting equations (5.18) and (5.20) into (5.17) leads to

$$\begin{Bmatrix} \Delta u^t \\ \Delta v^t \\ \Delta w^t \end{Bmatrix} = \sum_{i=1}^{3} \xi_i \begin{Bmatrix} \Delta u_i^t \\ \Delta v_i^t \\ \Delta w_i^t \end{Bmatrix} + \zeta^t \sum_{i=1}^{3} \xi_i \begin{bmatrix} \Lambda_{i(11)}^t & \Lambda_{i(12)}^t \\ \Lambda_{i(21)}^t & \Lambda_{i(22)}^t \\ \Lambda_{i(31)}^t & \Lambda_{i(32)}^t \end{bmatrix} \begin{Bmatrix} \Delta\theta_{ri}^t \\ \Delta\theta_{si}^t \end{Bmatrix}, \tag{5.25}$$

where the 3×2 matrix Λ_i^t is defined by

$$\Lambda_i^t = -\Omega_i^t \bar{\Gamma}_i^t \tag{5.26}$$

in which $\bar{\Gamma}_i^t$ consists of the first two columns of Γ_i^t.

Reference [5.1] pointed out that both Ω_i^t and Γ_i^t are dependent of the director V_i^t while Λ_i^t also depends on the current position of the director. The interpolation of incremental displacements requires Λ_i^t for every node at every time step. Therefore, it is necessary to update the director. To employ quadratic polynomials for the translational DOF and include the DDOF as recommended in reference [5.1], equation (5.25) is extended to

$$\begin{Bmatrix} \Delta u^t \\ \Delta v^t \\ \Delta w^t \end{Bmatrix} = \sum_{i=1}^{3} \xi_i \begin{Bmatrix} \Delta u_i^t \\ \Delta v_i^t \\ \Delta w_i^t \end{Bmatrix} + \zeta^t \sum_{i=1}^{3} \xi_i \begin{bmatrix} \Lambda_{i(11)}^t & \Lambda_{i(12)}^t \\ \Lambda_{i(21)}^t & \Lambda_{i(22)}^t \\ \Lambda_{i(31)}^t & \Lambda_{i(32)}^t \end{bmatrix} \begin{Bmatrix} \Delta\theta_{ri}^t \\ \Delta\theta_{si}^t \end{Bmatrix}$$

$$+ \sum_{i=1}^{3} \begin{bmatrix} 0 & 0 & \bar{p}_i \\ 0 & 0 & \bar{q}_i \\ -\bar{p}_i & -\bar{q}_i & 0 \end{bmatrix} \begin{Bmatrix} \Delta\theta_{ri}^t \\ \Delta\theta_{si}^t \\ \Delta\theta_{ti}^t \end{Bmatrix} \tag{5.27}$$

where $\bar{p}_i$ and $\bar{q}_i$ have been defined in equations (2.31a,b).

Comparing equations (5.15) and (5.27) it is seen that the present element formulation is sub-parametric as different interpolation schemes has been employed for geometry and displacements.

5.3.4 Assumed incremental strain field

The independently assumed incremental strain field is in close analogy to the assumed strain field in linear analysis (see subsection 2.5.3). It is defined as

$$\Delta e^e = \begin{Bmatrix} \Delta\varepsilon_m^e \\ \Delta\gamma^e \end{Bmatrix} + \zeta \begin{Bmatrix} \Delta\chi^e \\ 0 \end{Bmatrix} \tag{5.28}$$

where

$$\Delta e^e = \{ \Delta e_r^e \ \Delta e_s^e \ \Delta e_{rs}^e \ \Delta e_{st}^e \ \Delta e_{tr}^e \}^T \tag{5.29a}$$

and

$$\Delta\varepsilon_m^e = \{\Delta\varepsilon_r^e \ \Delta\varepsilon_s^e \ \Delta\varepsilon_{rs}^e\}^T ,$$

$$\Delta\chi^e = \{\Delta\chi_r^e \ \Delta\chi_s^e \ \Delta\chi_{rs}^e\}^T , \quad \Delta\gamma^e = \{\Delta\gamma_{st}^e \ \Delta\gamma_{tr}^e\}^T \tag{5.29b}$$

in which $\Delta\varepsilon_m^e$, $\Delta\chi^e$ and $\Delta\gamma^e$ are the assumed incremental membrane strain, bending curvature and transverse strain, respectively. Consequently the assumed incremental strain fields are interpolated by nine incremental strain parameters

$$\Delta\varepsilon_m^e = P_m\Delta\alpha_m\ ,\quad \Delta\chi^e = P_b\Delta\alpha_b\ ,\quad \Delta\gamma^e = P_s\Delta\alpha_s \tag{5.30a}$$

with

$$\Delta\alpha_m=\{\Delta\alpha_1\ \Delta\alpha_2\ \Delta\alpha_3\}^T\ ,$$

$$\Delta\alpha_b=\{\Delta\alpha_4\ \Delta\alpha_5\ \Delta\alpha_6\}^T\ ,\quad \Delta\alpha_s=\{\Delta\alpha_7\ \Delta\alpha_8\ \Delta\alpha_9\}^T\ , \tag{5.30b}$$

and

$$P_m = \begin{bmatrix}1 & 0 & 0\\ 0 & 1 & 0\\ 0 & 0 & 1\end{bmatrix},\qquad P_b = \begin{bmatrix}1 & 0 & 0\\ 0 & 1 & 0\\ 0 & 0 & 1\end{bmatrix},$$

$$P_s = \begin{bmatrix}-s_3(1-2\xi_2) & s_3(1-2\xi_1) & 0\\ -r_3(1-2\xi_2) & (r_3-r_2)(1-2\xi_1) & r_2(1-2\xi_3)\end{bmatrix}. \tag{5.30c}$$

5.3.5 Element stiffness matrices

To derive the incremental form of element linear stiffness matrix, equation (5.27) is rewritten as

$$\{\Delta u\} = \sum_{i=1}^{3}[\phi_p]_i\{\Delta q\}_i + \zeta\sum_{i=1}^{3}[\phi_R]_i\{\Delta q\}_i \tag{5.31}$$

where

$$\{\Delta u\} = \{\ \Delta u\ \Delta v\ \Delta w\ \}^T\ , \tag{5.32a}$$

$$\{\Delta q\}_i = \{\ \Delta u_i\ \Delta v_i\ \Delta w_i\ \Delta\theta_{ri}\ \Delta\theta_{si}\ \Delta\theta_{ti}\ \}^T\ , \tag{5.32b}$$

$$[\phi_p]_i = \begin{bmatrix} \xi_i & 0 & 0 & 0 & 0 & \bar{p}_i \\ 0 & \xi_i & 0 & 0 & 0 & \bar{q}_i \\ 0 & 0 & \xi_i & -\bar{p}_i & -\bar{q}_i & 0 \end{bmatrix}, \tag{5.32c}$$

$$[\phi_R]_i = \left[[0]_{3\times3} \; \xi_i[\Lambda]_i \; \{0\}_{3\times1} \right]_{3\times6}, \tag{5.32d}$$

and

$$[\Lambda]_i = \begin{bmatrix} \Lambda_{i(11)} & \Lambda_{i(12)} \\ \Lambda_{i(21)} & \Lambda_{i(22)} \\ \Lambda_{i(31)} & \Lambda_{i(32)} \end{bmatrix}. \tag{5.32e}$$

With the definition of following

$$\phi_p = \left[[\phi_p]_1 \; [\phi_p]_2 \; [\phi_p]_3 \right]_{3\times18}, \tag{5.33a}$$

$$\phi_R = \left[[\phi_R]_1 \; [\phi_R]_2 \; [\phi_R]_3 \right]_{3\times18}, \tag{5.33b}$$

$$\Delta q = \left\{ \{\Delta q\}_1^T \; \{\Delta q\}_2^T \; \{\Delta q\}_3^T \right\}^T \tag{5.33c}$$

equation (5.31) becomes

$$\{\Delta u\} = \phi \; \Delta q \tag{5.34}$$

where

$$\phi = \phi_p + \zeta\phi_R \tag{5.35}$$

is the displacement shape function matrix. Taking the derivatives of the incremental displacements with respect to the local co-ordinates (j = r,s,t) gives

$$\{\Delta u\}_{,j} = (\phi_p + \zeta\phi_R)_{,j} \; \Delta q \quad . \tag{5.36}$$

It should be noted that

$$[\Phi_p]_{i,j} = \begin{bmatrix} \xi_{i,j} & 0 & 0 & 0 & 0 & \bar{p}_{i,j} \\ 0 & \xi_{i,j} & 0 & 0 & 0 & \bar{q}_{i,j} \\ 0 & 0 & \xi_{i,j} & -\bar{p}_{i,j} & -\bar{q}_{i,j} & 0 \end{bmatrix}, \tag{5.37a}$$

$$[\Phi_R]_{i,j} = \left[\; [0]_{3\times3} \;\; \xi_{i,j}[\Lambda]_i \;\; \{0\}_{3\times1} \; \right]_{3\times6} \tag{5.37b}$$

when j = r, s; while the derivative with respect to the co-ordinate t is

$$\{\Delta u\}_{,t} = \Phi_R \, \Delta q \, . \tag{5.37c}$$

The linear component of incremental Washizu strain has been defined in equation (5.5b). Writing equation (5.5b) in vector form with engineering strains leads to

$$\Delta e^u = \begin{Bmatrix} \Delta u_{,r} \\ \Delta v_{,s} \\ \Delta u_{,s} + \Delta v_{,r} \\ \Delta v_{,t} + \Delta w_{,s} \\ \Delta w_{,r} + \Delta u_{,t} \end{Bmatrix} = [L_1] \begin{Bmatrix} \{\Delta u\}_{,r} \\ \{\Delta u\}_{,s} \\ \{\Delta u\}_{,t} \end{Bmatrix} \tag{5.38}$$

where

$$[L_1] = \begin{bmatrix} 1 & 0 & 0 & 0 & 0 & 0 & 0 & 0 & 0 \\ 0 & 0 & 0 & 0 & 1 & 0 & 0 & 0 & 0 \\ 0 & 1 & 0 & 1 & 0 & 0 & 0 & 0 & 0 \\ 0 & 0 & 0 & 0 & 0 & 1 & 0 & 1 & 0 \\ 0 & 0 & 1 & 0 & 0 & 0 & 1 & 0 & 0 \end{bmatrix}_{5\times9}, \tag{5.39}$$

and

$$\{ \{\Delta u\}_{,r} \{\Delta u\}_{,s} \{\Delta u\}_{,t} \}^T = (\Phi_0 + \zeta \Phi_\zeta) \, \Delta q \tag{5.40}$$

in which

$$\Phi_0 = [\ [\phi_p]_{,r}\ [\phi_p]_{,s}\ [\phi_R]\ ]^T\ ,$$
$$\Phi_\zeta = [\ [\phi_R]_{,r}\ [\phi_R]_{,s}\ [0]\ ]^T\ . \qquad (5.41a,b)$$

Therefore, equation (5.38) can also be written as

$$\Delta\varepsilon^u = B_L \Delta q \qquad (5.42)$$

where

$$B_L = (\ B_0 + \zeta B_\zeta\ )$$
$$B_0 = [L_1]\ \Phi_0\ ,\quad B_\zeta = [L_1]\ \Phi_\zeta\ . \qquad (5.43)$$

It should be pointed out that to comply with the first order shear deformation theory, the transverse shear strain in equation (5.42) should be constant over the thickness. Thus, the transverse shear components are to be evaluated at the mid-surface of the element where $\zeta = 0$.

In accordance with the degenerated 3-D elastic concept, the material stiffness matrix is a 5×5 matrix. The detail construction of this matrix will be discussed in the next section, see equation (5.71). Here, it is defined as

$$C = \begin{bmatrix} [C_a]_{3\times3} & [C_{ab}]_{3\times2} \\ [C_{ba}]_{2\times3} & [C_b]_{2\times2} \end{bmatrix}. \qquad (5.44)$$

As the material stiffness matrix is symmetric, thus

$$[C_a] = [C_a]^T\ ,\ [C_b] = [C_b]^T\ ,\ [C_{ba}] = [C_{ab}]^T\ .$$

The general procedures of formulating hybrid strain elements has been briefly reviewed in subsection 5.3.2. However, for laminated composite structures, the

constitutive equations are more complex. Thus, the derivation of the element linear stiffness matrix should start with equation (5.7).

Substituting equation (5.28) into the integral

$$I_1 = \int (\Delta e^e)^T C (\Delta e^e)\, dV \tag{5.45}$$

which is part of equation (5.7), it leads to

$$\begin{aligned} I_1 = & \int_V \left((\Delta \varepsilon_m^e)^T C_a \Delta \varepsilon_m^e + (\Delta \gamma^e)^T C_{ab}^T \Delta \varepsilon_m^e + (\Delta \varepsilon_m^e)^T C_{ab} \Delta \gamma^e + (\Delta \gamma^e)^T C_b \Delta \gamma^e \right) dV \\ & + \int_V \left((\Delta \chi^e)^T \zeta C_a \Delta \varepsilon_m^e + (\Delta \chi^e)^T \zeta C_{ab} \Delta \gamma^e \right) dV \\ & + \int_V \left((\Delta \varepsilon_m^e)^T \zeta C_a \Delta \chi^e + (\Delta \gamma^e)^T \zeta C_{ab}^T \Delta \chi^e + (\Delta \chi^e)^T \zeta^2 C_a \Delta \chi^e \right) dV . \end{aligned} \tag{5.46}$$

Applying equation (5.30a) and integrating in the transversal direction results in

$$\begin{aligned} I_1 = & \int_a \left(\Delta \alpha_m^T P_m^T A' P_m \Delta \alpha_m + \Delta \alpha_s^T P_s^T C_A^T P_m \Delta \alpha_m \right) da \\ & + \int_a \left(\Delta \alpha_m^T P_m^T C_A P_s \Delta \alpha_s + \Delta \alpha_s^T P_s^T E' P_s \Delta \alpha_s \right) da \\ & + \int_a \left(\Delta \alpha_b^T P_b^T P' P_m \Delta \alpha_m + \Delta \alpha_b^T P_b^T C_B^T P_s \Delta \alpha_s \right) da \\ & + \int_a \left(\Delta \alpha_m^T P_m^T B' P_b \Delta \alpha_b + \Delta \alpha_s^T P_s^T C_B^T P_b \Delta \alpha_b + \Delta \alpha_b^T P_b^T D' P_b \Delta \alpha_b \right) da \end{aligned} \tag{5.47}$$

where

$$\begin{aligned} & A' = \sum_{k=1}^{n} (C_a)_k (h_k - h_{k-1}) , \quad B' = \frac{1}{2} \sum_{k=1}^{n} (C_a)_k (h_k^2 - h_{k-1}^2) , \\ & D' = \frac{1}{3} \sum_{k=1}^{n} (C_a)_k (h_k^3 - h_{k-1}^3) , \quad E' = \kappa_1 \kappa_j \sum_{k-1}^{n} (C_b)_k (h_k - h_{k-1}) , \end{aligned} \tag{5.48a}$$

$$C_A = \sum_{k=1}^{n} (C_{ab})_k (h_k - h_{k-1}) \ , \quad C_B = \frac{1}{2} \sum_{k=1}^{n} (C_{ab})_k (h_k^2 - h_{k-1}^2) \tag{5.48b}$$

in which κ_i and κ_j are the shear correction factors that have been defined in equation (2.27). By defining

$$\begin{gathered}
H_{mm} = \int_a P_m^T A' P_m \, da \ , \quad H_{sm} = \int_a P_s^T C_A^T P_m \, da \ , \\
H_{ms} = \int_a P_m^T C_A P_s \, da \ , \quad H_{ss} = \int_a P_s^T E' P_s \, da \ , \\
H_{bm} = \int_a P_b^T B' P_m \, da \ , \quad H_{bs} = \int_a P_b^T C_B^T P_s \, da \ , \\
H_{mb} = \int_a P_m^T B' P_b \, da \ , \quad H_{sb} = \int_a P_s^T C_B^T P_b \, da \ , \quad H_{bb} = \int_a P_b^T D' P_b \, da
\end{gathered} \tag{5.49}$$

and

$$H = \begin{bmatrix} H_{mm} & H_{mb} & H_{ms} \\ H_{bm} & H_{bb} & H_{bs} \\ H_{sm} & H_{sb} & H_{ss} \end{bmatrix}_{9\times 9} \tag{5.50}$$

equation (5.47) becomes

$$I_1 = \Delta\alpha^T H \, \Delta\alpha \tag{5.51}$$

where

$$\Delta\alpha = \{ \, \Delta\alpha_m \ \Delta\alpha_b \ \Delta\alpha_s \, \}^T \ . \tag{5.52}$$

For the second term in equation (5.7)

$$I_2 = \int (\Delta e^c)^T C (\Delta \varepsilon^u) \, dV \tag{5.53}$$

the operation is similar to the foregoing. Writing the linear part of incremental Washizu strain in the same format as the assumed incremental strains shown in equation (5.28)

gives

$$\Delta\varepsilon^u = \begin{Bmatrix} \Delta\varepsilon_m^u \\ \Delta\gamma^u \end{Bmatrix} + \zeta \begin{Bmatrix} \Delta\chi^u \\ 0 \end{Bmatrix} \tag{5.54}$$

where

$$\begin{aligned} \Delta\varepsilon_m^u &= \{\Delta\varepsilon_r^u \ \Delta\varepsilon_s^u \ \Delta\varepsilon_{rs}^u\}^T , \\ \Delta\chi^u = \{\Delta\chi_r^u \ \Delta\chi_s^u \ \Delta\chi_{rs}^u\}^T &, \quad \Delta\gamma^u = \{\Delta\gamma_{st}^u \ \Delta\gamma_{tr}^u\}^T \end{aligned} \tag{5.55}$$

in which $\Delta\varepsilon_m{}^u$, $\Delta\chi^u$ and $\Delta\gamma^u$ are, respectively, the incremental membrane strain, bending curvature and transverse strain due to displacements. By substituting from equations (5.28) and (5.54) for equation (5.53) yields

$$\begin{aligned} I_2 = \int_V \left((\Delta\varepsilon_m^s)^T C_a \Delta\varepsilon_m^u + (\Delta\gamma^s)^T C_{ab}^T \Delta\varepsilon_m^u + (\Delta\varepsilon_m^s)^T C_{ab} \Delta\gamma^u + (\Delta\gamma^s)^T C_b \Delta\gamma^u\right) dV \\ + \int_V \left((\Delta\chi^s)^T \zeta C_a \Delta\varepsilon_m^u + (\Delta\chi^s)^T \zeta C_{ab} \Delta\gamma^u\right) dV \\ + \int_V \left((\Delta\varepsilon_m^s)^T \zeta C_a \Delta\chi^u + (\Delta\gamma^s)^T \zeta C_{ab}^T \Delta\chi^u + (\Delta\chi^s)^T \zeta^2 C_a \Delta\chi^u\right) dV \ . \end{aligned} \tag{5.56}$$

With the consideration of equations (5.30a), (5.42) and (5.48), equation (5.56) can be rewritten as

$$\begin{aligned} I_2 = \int_a \left(\Delta\alpha_m^T P_m^T A' B_m \Delta q + \Delta\alpha_s^T P_s^T C_A^T B_m \Delta q\right) da \\ + \int_a \left(\Delta\alpha_m^T P_m^T C_A B_s \Delta q + \Delta\alpha_s^T P_s^T E' B_s \Delta q\right) da \\ + \int_a \left(\Delta\alpha_b^T P_b^T B' B_m \Delta q + \Delta\alpha_b^T P_b^T C_B^T B_s \Delta q\right) da \\ + \int_a \left(\Delta\alpha_m^T P_m^T B' B_b \Delta q + \Delta\alpha_s^T P_s^T C_B^T B_b \Delta q + \Delta\alpha_b^T P_b^T D' B_b \Delta q\right) da \end{aligned} \tag{5.57}$$

in which B_m, B_b and B_s are, respectively, the linear strain-displacement relations matrices for the membrane, bending and shear components. They have been defined implicitly in equations (5.43) and (5.37a,b). The B_m matrix is the first three rows of B_0. The B_b is the first three rows of B_ζ and B_s is the last two rows of B_L. As mentioned above, to have constant transverse shear over the thickness, B_s is actually the last two rows of matrix B_0. The simpler form of equation (5.57) is

$$I_2 = \Delta\alpha^T \, G \, \Delta q \tag{5.58}$$

with

$$G = \begin{bmatrix} G_{mm} + G_{mb} + G_{ms} \\ G_{bm} + G_{bb} + G_{bs} \\ G_{sm} + G_{sb} + G_{ss} \end{bmatrix}_{9\times 18} \tag{5.59}$$

and

$$\begin{aligned} G_{mm} &= \int_a P_m^T A' B_m \, da \,, \quad G_{sm} = \int_a P_s^T C_A^T B_m \, da \,, \\ G_{ms} &= \int_a P_m^T C_A B_s \, da \,, \quad G_{ss} = \int_a P_s^T E' B_s \, da \,, \\ G_{bm} &= \int_a P_b^T B' B_m \, da \,, \quad G_{bs} = \int_a P_b^T C_B^T B_s \, da \,, \\ G_{mb} &= \int_a P_m^T B' B_b \, da \,, \quad G_{sb} = \int_a P_s^T C_B^T B_b \, da \,, \quad G_{bb} = \int_a P_b^T D' B_b \, da \,. \end{aligned} \tag{5.60}$$

Having obtained H and G matrices, the element linear stiffness can be constructed according to equation (5.14b). However, to derive the linear stiffness matrix explicitly, obtaining the inverse of matrix H is the most difficult part as now H is a full matrix. The same technique discussed in subsection 2.5.5 is employed here with the help of the computer algebra package MACSYMA [5.22]. All integrals involved in evaluating H and

G matrix are also obtained explicitly. The improved displacement formulation of DDOF introduced in section 2.6 is adopted for this linear stiffness matrix. Therefore, the complete k_L is

$$k_L = k'_L + k_{dd} \tag{5.61}$$

where k'_L is the element linear stiffness matrix defined in equation (5.14b) and k_{dd} is the stiffness matrix due to the consideration of DDOF and is obtained through the displacement formulation. The matrix k_{dd} has been given in equation (2.82).

The "nonlinear" or initial stress stiffness matrix k_{NL} defined in equation (5.11) can be obtained if the nonlinear strain-displacement matrix B_{NL} and the matrix σ_C which contains the Cauchy stress components at the current configuration are available. The former B_{NL} is defined by

$$\{ \{\Delta u\}_{,r} \{\Delta u\}_{,s} \{\Delta u\}_{,t} \}^T = (\Phi_0 + \zeta\Phi_\zeta) \Delta q \tag{5.62}$$

in which Φ_0 and Φ_ζ have been given in equations (5.41a,b).

The σ_C matrix is constructed from the Cauchy stress vector σ and defined as

$$\sigma_C = \begin{bmatrix} \sigma_{11} I_3 & \sigma_{12} I_3 & \sigma_{31} I_3 \\ \sigma_{12} I_3 & \sigma_{22} I_3 & \sigma_{23} I_3 \\ \sigma_{31} I_3 & \sigma_{23} I_3 & O_3 \end{bmatrix} \tag{5.63}$$

with I_3 being the 3×3 identity matrix and O_3 a 3×3 null matrix. The transverse stress components of σ are considered constant over the thickness, and all components of σ are calculated and updated for each time step at the centroid of each element.

Having obtained the element stiffness matrices, a simplified version of the stiffness matrices are also formulated. The derivation procedure is the same as the one introduced

in reference [5.1]. In the simplified version, it is assumed that V_i^t coincides with the t-axis all the time. The simplified version can be used in cases where the directors are not uniquely defined or difficult to determine.

5.4 Constitutive Equations

In subsection 2.4.3, constitutive equations for linear analysis of laminated composite structures have been discussed. These equations can also be used in geometrically nonlinear analysis if the structure studied undergoes large deformation but small strain. However, for finite strain problems in the elastic range, the reduced stiffness matrix is a function of stresses. In this case the constitutive relations appears to be nonlinear elastic [5.29]. To incorporate finite strains in the analysis, several approaches can be applied. References [5.30, 31] recommended to perform numerical integration on rate constitutive equations and reference [5.29] suggested using Jaumann rate. These approaches are relatively complicated and numerical integration has to be employed. A simpler and more direct approach proposed and utilized in reference [5.1, 32-34] is to add the linear elastic matrix a correction matrix which is a function of Cauchy stress. The following equation gives the correction terms in tensor form

$$C'_{ijkl} = -\frac{1}{2}(\sigma_{ik}\delta_{jl}+\sigma_{jk}\delta_{il}+\sigma_{il}\delta_{jk}+\sigma_{jl}\delta_{ik}) \tag{5.64}$$

where δ_{mn} is the Kronecker delta. Note that this equation comes as a result of transforming the Jaumann stress rate to the incremental second Piola-Kirchhoff stress. If the stress and strain vectors are

$$\begin{aligned} \sigma &= \{\sigma_{11}\ \sigma_{22}\ \sigma_{33}\ \sigma_{12}\ \sigma_{23}\ \sigma_{31}\}^T, \\ e &= \{e_{11}\ e_{22}\ e_{33}\ e_{12}\ e_{23}\ e_{31}\}^T \end{aligned} \tag{5.65}$$

the matrix form of equation (5.64) is

$$C' = -\frac{1}{2}\begin{bmatrix} 4\sigma_{11} & 0 & 0 & 2\sigma_{12} & 0 & 2\sigma_{13} \\ 0 & 4\sigma_{22} & 0 & 2\sigma_{12} & 2\sigma_{23} & 0 \\ 0 & 0 & 4\sigma_{33} & 0 & 2\sigma_{23} & 2\sigma_{13} \\ 2\sigma_{12} & 2\sigma_{12} & 0 & \sigma_{11}+\sigma_{22} & \sigma_{13} & \sigma_{23} \\ 0 & 2\sigma_{23} & 2\sigma_{23} & \sigma_{13} & \sigma_{22}+\sigma_{33} & \sigma_{12} \\ 2\sigma_{13} & 0 & 2\sigma_{13} & \sigma_{23} & \sigma_{12} & \sigma_{11}+\sigma_{33} \end{bmatrix} . \tag{5.66}$$

As in the current investigation the degenerated concept is adopted, the elastic modulus in the normal direction to the plane of the shell structures is considered zero and consequently the stress and strain in the transversal direction are ignored. In the linear analysis the constitutive relations for a lamina have been defined in equations (2.23-25). Rearranging the terms in these equations one has

$$\sigma = \bar{Q}\, e \tag{5.67}$$

where

$$\begin{aligned} \sigma &= \{\sigma_x\ \sigma_y\ \sigma_{xy}\ \sigma_{yz}\ \sigma_{zx}\}^T , \\ e &= \{\, e_x\ e_y\ e_{xy}\ e_{yz}\ e_{zx}\}^T \end{aligned} \tag{5.68}$$

and

$$\bar{Q} = \begin{bmatrix} \bar{Q}_{11} & \bar{Q}_{12} & \bar{Q}_{16} & 0 & 0 \\ \bar{Q}_{12} & \bar{Q}_{22} & \bar{Q}_{26} & 0 & 0 \\ \bar{Q}_{16} & \bar{Q}_{26} & \bar{Q}_{66} & 0 & 0 \\ 0 & 0 & 0 & \bar{Q}_{44} & \bar{Q}_{45} \\ 0 & 0 & 0 & \bar{Q}_{45} & \bar{Q}_{55} \end{bmatrix} . \tag{5.69}$$

The corresponding matrix from equation (5.66) is

$$C' = -\frac{1}{2}\begin{bmatrix} 4\sigma_x & 0 & 2\sigma_{xy} & 0 & 2\sigma_{zx} \\ 0 & 4\sigma_y & 2\sigma_{xy} & 2\sigma_{yz} & 0 \\ 2\sigma_{xy} & 2\sigma_{xy} & \sigma_x+\sigma_y & \sigma_{zx} & \sigma_{yz} \\ 0 & 2\sigma_{yz} & \sigma_{zx} & \sigma_y & \sigma_{xy} \\ 2\sigma_{zx} & 0 & \sigma_{yz} & \sigma_{xy} & \sigma_x \end{bmatrix} . \tag{5.70}$$

Then, the material stiffness matrix for a lamina becomes

$$C = \bar{Q} + C' \tag{5.71}$$

This equation is the detailed construction of equation (5.44) which has been used in subsection 5.3.5 to develop element stiffness matrices.

With the consideration of large deformation and finite strain, the constitutive equations for a multilayered structure or laminate can be written as

$$\begin{Bmatrix} N \\ M \\ Q_s \end{Bmatrix} = \begin{bmatrix} A' & B' & C_A \\ B' & D' & C_B \\ C_A^T & C_B^T & E' \end{bmatrix}_{8\times 8} \begin{Bmatrix} \epsilon_m \\ \chi \\ \gamma \end{Bmatrix} \tag{5.72}$$

or

$$\sigma_N = \bar{C}\, e_N \tag{5.73}$$

where N, M and Q_s are the vectors of stress resultants corresponding to membrane, bending and transverse shear, respectively. The matrices A', B', D', E', C_A and C_B have been defined in equations (5.48a,b).

5.5 Element Mass Matrix

In the current study, with the updated Lagrangian description, the consistent mass matrix is formulated in the reference configuration. The mass matrix is then updated in each step as the configuration changing. The assumptions made before the derivation are that the angular velocities and accelerations are small enough to be discarded. By following the procedures suggested in reference [5.1] the consistent mass matrix can be obtained.

Equation (5.15) has defined an arbitrary point within an element. For simplicity, one may rewrite it as

$$\Phi = \varphi + \zeta V \tag{5.74}$$

where φ and V represent the first and the second summation terms in equation (5.15), respectively. It should be noted that the quantities are all defined in the reference configuration C^1. For a point on the mid-surface, the linear and angular momentum fields are defined as

$$p = \int_{-h/2}^{+h/2} \rho \dot{\Phi}\, d\zeta = \rho h \dot{\varphi} \tag{5.75}$$

and

$$\psi = \int_{-h/2}^{+h/2} \rho(\Phi - \varphi) \times \dot{\Phi}\, d\zeta = \rho \frac{h^3}{12} V \times \dot{V} \tag{5.76}$$

where h is the total thickness of the laminate and

$$\rho = \frac{\sum_{k=1}^{n} \rho_k (h_k - h_{k-1})}{h} \tag{5.77}$$

is the density of the laminate obtained in "average" sense, in which, ρ_k is the density of k'th layer, h_k and h_{k-1} are the layer co-ordinates of the top and bottom of the k'th layer (see Figure 2.4). The integer n is the total number of layers of the laminate. Then, the weak form of momentum balance is

$$\int_a (\Delta\varphi^T\dot{p} + \Delta\beta^T\psi)\, da + G_{sta}(\Phi, \Delta\varphi, \Delta\beta) = 0 \tag{5.78}$$

where $\Delta\varphi$ is the virtual displacement at the mid-surface and $\Delta\beta$ is the virtual rotation of the director field. The static part of the weak form equation, G_{sta} is in fact the energy functional related to the static forces discussed in section 5.3. These forces include internal force, pseudo force and external force. The dynamic part, that is the integral in equation (5.78), can be decomposed into two parts

$$G_M = G_{tra} + G_{rot} = \int_a \Delta\varphi^T\dot{p}\, da + \int_a \Delta\beta^T\psi\, da \tag{5.79}$$

where

$$\begin{aligned} \dot{p} &= \rho h\ddot{\phi}\ , \\ \psi &= I_\rho(\dot{V}\times\dot{V} + V\times\ddot{V}) = I_\rho(V\times\ddot{V}) \end{aligned} \tag{5.80a,b}$$

with

$$I_\rho = \rho\frac{h^3}{12}\ . \tag{5.81}$$

Taking variation of G_M with respect to $\dot{p}$ gives

$$\Delta G_{tra} = \int_a \Delta\varphi^T\Delta\dot{p}\, da = \int_a \rho h\Delta\varphi^T\Delta\ddot{\varphi}\, da = \Delta q^T m_{tra}\Delta\ddot{q} \tag{5.82}$$

where Δq is the vector of incremental nodal displacement defined in equation (5.33c), $\Delta \ddot{q}$ is the vector of incremental acceleration of nodal DOF and

$$m_{tra} = \int_a \rho h \phi_p^T \phi_p \, da \tag{5.83}$$

is the consistent mass matrix associated with translational DOF. In arriving at equations (5.82, 83), the relations

$$\Delta \varphi = \phi_p \Delta q \quad , \quad \Delta \ddot{\varphi} = \phi_p \Delta \ddot{q} \tag{5.84a,b}$$

have been applied and ϕ_p has been defined in equation (5.33a). It is seen that m_{tra} is identical to its counterpart in the consistent mass matrix of the $HLCTS_r^{qd}$ element derived in section 4.2 except that m_{tra} is defined in the current configuration and has to be updated for each incremental time step.

The variation with respect to V and $\tilde{V}$ leads to

$$\begin{aligned} \Delta G_M &= \int_a I_\rho \Delta \beta^T (\Delta V \times \tilde{V} + V \times \Delta \tilde{V}) \, da \\ &\approx \int_a I_\rho \Delta \beta^T (V \times \Delta \tilde{V}) \, da \end{aligned} \tag{5.85}$$

where $\tilde{V}$ represents the angular accelerations as the directors are assumed to be unit length. In this equation, the term $\Delta V \times \tilde{V}$ is ignored because negligible small angular velocities and accelerations have been assumed. With this assumption in mind and applying equation (5.18) one has

$$\Delta \tilde{V} = (\Delta \tilde{\beta} \times V + \Delta \beta \times \tilde{V}) \approx \Delta \tilde{\beta} \times V \quad . \tag{5.86}$$

Assuming

$$\Delta\beta = \Gamma\phi_r\Delta q \quad , \quad \Delta\ddot{\beta} = \Gamma\phi_r\Delta\ddot{q} \tag{5.87a,b}$$

in which Γ is the orthogonal matrix defined in equations (5.20, 21) and $\Gamma^T\Gamma$ is an identity matrix, and substituting equation (5.86) into (5.85) results in

$$\begin{aligned}\Delta G_M &= \int_a I_\rho \Delta\beta^T V\times(-V\times\Delta\ddot{\beta})\, da \\ &= \int_a I_\rho \Delta\beta^T\Delta\ddot{\beta}\, da = \Delta q^T m_{rot}\Delta\ddot{q}\end{aligned} \tag{5.88}$$

where

$$m_{rot} = \int_a I_\rho \phi_t^T\phi_r\, da \tag{5.89}$$

is the consistent mass matrix associated with rotations $\Delta\theta_r$ and $\Delta\theta_s$.

As the DDOF is independent of directors, the mass associated with DDOF has not been considered so far. Thus, discarding the third row which is in accordance with the DDOF, the shape functions in equation (5.89) become

$$\phi_r = [\ [\phi_r]_1\ [\phi_r]_2\ [\phi_r]_3\ ] \tag{5.90}$$

where

$$[\phi_r]_i = \begin{bmatrix} 0 & 0 & 0 & -\xi_i\Lambda_{i(21)} & -\xi_i\Lambda_{i(22)} & 0 \\ 0 & 0 & 0 & \xi_i\Lambda_{i(11)} & \xi_i\Lambda_{i(12)} & 0 \end{bmatrix} . \tag{5.91}$$

Note that here ϕ_r is different from the ϕ_R defined in equation (5.33b) because the former is the shape functions of rotations at an arbitrary point on the mid-surface within an element, that is

$$\{\Delta\theta_r \ \Delta\theta_s\}^T = \phi_r \Delta q \quad . \tag{5.92}$$

Now, one can write the consistent mass matrix as the sum of three parts

$$m = m_{tra} + m_{rot} + m_d \tag{5.93}$$

in which m_{tra} and m_{rot} have been given in equations (5.83) and (5.89) respectively. The matrix m_d is the part associated with DDOF and is exactly the same in expression as the components derived for the $HLCTS_r^{qd}$ element in section 4.2

It should be pointed out that if the directors are coincide with t-axis, the consistent mass matrix developed in this section reduced to the one for the $HLCTS_r^{qd}$ element in section 4.2. When it is used for the incremental formulation with updated Lagrangian description, updating relevant quantities at each incremental step are required before evaluating the mass matrix. To be consistent with element stiffness matrices, the consistent element mass matrix derived in this section has also a director version and a simplified version. All these mass matrices are obtained explicitly with the help of the symbolic computer algebra package MACSYMA [5.22].

5.6 Configuration and Stress Updating

For each incremental step, configurations and stresses should be updated in the finite element procedure. Concerning configuration updating, position vectors and directors are the quantities to be updated. The updated position vectors and directors describe an arbitrary point within an element at configuration $C^{t+\Delta t}$. The position vector defines an arbitrary point on the mid-surface of an element. At configuration $C^{t+\Delta t}$, it is given by

$$\begin{Bmatrix} r^{t+\Delta t} \\ s^{t+\Delta t} \\ t^{t+\Delta t} \end{Bmatrix} = \begin{Bmatrix} r^{t} \\ s^{t} \\ t^{t} \end{Bmatrix} + \begin{Bmatrix} \Delta u \\ \Delta v \\ \Delta w \end{Bmatrix} \tag{5.94}$$

in which the co-ordinates and displacements are all defined on the mid-surface. To update directors, one may follow the procedure employed in references [5.1, 23-28, 35]. Once the incremental rotation $\Delta\theta = \{ \Delta\theta_r, \Delta\theta_s, \Delta\theta_t \}^T$ are solved, the director at configuration $C^{t+\Delta t}$ can be calculated by using

$$V_i^{t+\Delta t} = T_v V_i^t \tag{5.95}$$

where

$$T_v = \cos(|\Delta\theta|) I_3 + \frac{\sin(|\Delta\theta|)}{|\Delta\theta|} \Delta\hat{\theta} \tag{5.96}$$

in which

$$\Delta\hat{\theta} = \begin{bmatrix} 0 & -\Delta\theta_t & \Delta\theta_s \\ \Delta\theta_t & 0 & -\Delta\theta_r \\ -\Delta\theta_s & \Delta\theta_r & 0 \end{bmatrix}. \tag{5.97}$$

Consequently, the angular velocity and acceleration of the directors are updated by

$$\omega^{t+\Delta t} = \frac{\gamma}{\beta\delta}\Delta\theta - T_v\left\{\omega^t + \left(\frac{\gamma}{\beta} - 2\right)\left(\omega^t + \frac{\delta}{2}\dot{\omega}^t\right)\right\}$$
$$\dot{\omega}^{t+\Delta t} = \frac{1}{\gamma\delta}\omega^{t+\Delta t} - T_v\left\{\frac{1}{\gamma\delta}\omega^t + \left(\frac{1}{\gamma} - 1\right)\dot{\omega}^t\right\} \tag{5.98a,b}$$

in which the parameters β (it should not be confused with β in section 5.5) and γ are those from the Newmark family of direct integration algorithms, and δ is the size of time step.

As the continuous changes in the geometry and volume, the updating procedure for mass density and thickness requires the calculation of "relative" deformation gradient [5.27], which is

$$F^{t+\Delta t} = \begin{bmatrix} \frac{\partial(\Delta u)}{\partial r} & \frac{\partial(\Delta u)}{\partial s} & \frac{\partial(\Delta u)}{\partial t} \\ \frac{\partial(\Delta v)}{\partial r} & \frac{\partial(\Delta v)}{\partial s} & \frac{\partial(\Delta v)}{\partial t} \\ \frac{\partial(\Delta w)}{\partial r} & \frac{\partial(\Delta w)}{\partial s} & \frac{\partial(\Delta w)}{\partial t} \end{bmatrix} \tag{5.99}$$

where the incremental displacements have been defined in equation (5.17). Then the mass density and thickness at configuration $C^{t+\Delta t}$ are given by

$$\rho^{t+\Delta t} = \frac{\rho^t}{\det(F^{t+\Delta t})} ,$$

$$h^{t+\Delta t} = h^t \det(F^{t+\Delta t}) \frac{a^t}{a^{t+\Delta t}} \tag{5.100a,b}$$

where det( ) denotes the "determinant of" and a is the area of the triangular element.

The calculation of updated stress is considered. From equations (5.8a) and (5.13) the incremental Green strain can be obtained. Then, the incremental second Piola-Kirchhoff stress is

$$\Delta S = C \, \Delta e \quad . \tag{5.101}$$

As ΔS and the Cauchy stress σ^t are both defined with respect to the current configuration C^t, one has

$$S^{t+\Delta t} = \sigma^t + \Delta S \tag{5.102}$$

which is the second Piola-Kirchhoff stress at the deformation state "$t+\Delta t$" measured with

respect to the reference configuration $\mathbf{C}^t$. The following equation [5.1, 32, 35] defines the relation or transformation between the second Piola-Kirchhoff stress and the Cauchy stress

$$\sigma^{t+\Delta t} = \frac{1}{\det(F^{t+\Delta t})} F^{t+\Delta t}\, S^{t+\Delta t}\, (F^{t+\Delta t})^T \tag{5.103}$$

where $F^{t+\Delta t}$ is the deformation gradient given in equation (5.99).

5.7 Remarks

In this chapter, the theories for the analysis of geometrically nonlinear laminated composite shell structures have been presented. The emphasis has been on establishing a sound theoretical basis for the formulation of simple and efficient finite elements for large scale geometrically nonlinear analysis of laminated composite shell structures. Clearly, geometrically nonlinear problems for laminated composite shell structures are more complicated than isotropic shells.

In the course of developing the finite elements, the updated Lagrangian description has been employed. The consideration of reducing the algebra manipulations in obtaining element matrices to a minimum is one of the major reasons for using updated Lagrangian description. Consequently, the element linear and nonlinear stiffness matrices, the element consistent mass matrix and the pseudo-load vector have all been obtained explicitly.

In particular, the element developed in this chapter is based on the $HLCTS_r^{qd}$ element proposed in Chapter 2 and Chapter 4 for linear analysis. It is an extension of the work in reference [5.1] which is for the analysis of isotropic shell structures. The element has independently assumed incremental strain and displacement fields. The formulation

has taken in consideration many important aspects of geometrically nonlinear analysis of laminated composite structures, such as, transverse shear deformation, large deflection of finite strain and large rotation. The finite element procedure developed here is also capable of dealing with the "thinning" effect and handling cases in which the directors are not unique or difficult to evaluate.

To verify the effectiveness and simplicity of using the element developed in this chapter, applications of the element for various geometrically nonlinear problems are made and presented in the next chapter.

CHAPTER 6

NUMERICAL STUDIES OF GEOMETRICALLY NONLINEAR LAMINATED COMPOSITE PLATE AND SHELL STRUCTURES

The incremental finite element procedure developed in the last chapter is expected to be simple and efficient for the analysis of large scale geometrically nonlinear laminated composite plate and shell structures. This is because the formulation has incorporated considerations of large deformation with finite rotations and finite strains. In this chapter, to verify the validity of the derived element matrices in geometrically nonlinear analysis, a number of nonlinear problems are studied. These problems cover geometrically nonlinear analysis of both static and dynamic cases. The latter includes plates and shells of isotropic and laminated composite structures subjected to different types of static and dynamic loads. The HLCTS element results are compared with analytical or numerical solutions available in the literature.

This chapter consists of five sections. The first two sections are concerned with static analysis of plate and shell structures of isotropic and laminated composite materials, respectively, while the third and fourth deal with dynamic analysis. The final section presents closing remarks.

6.1 Static Analysis of Structures of Isotropic Materials

The current finite element formulations are developed for the analysis of

geometrically nonlinear laminated composite structures. However, for the structures of isotropic materials, they are special cases. In this section three problems are studied to show the excellent performance of HLCTS elements in geometrically nonlinear analysis of structures made of isotropic materials, which include a cantilever beam subjected to an end moment, cylindrical bending of a plate under a line load and a spherical cap subjected to a concentrated load.

6.1.1 Cantilever beam subjected to an end moment

The problem considered is a cantilever beam subjected to a concentrated bending moment at the free end. This example has been used widely as a testing case for large deformation analysis [6.1-4]. The cantilever beam is depicted in Figure 6.1(a). The geometrical and material properties of the beam are: length L = 12.0 m, width b = 1.0 m, thickness h = 1.0 m, Young's modulus $E = 3.0 \times 10^7$ N/m^2 and Poisson's ratio $\nu = 0.0$.

In the analysis, the beam is discretized by a 12 × 1 A mesh as shown in Figure 6.1(b). At the fixed end, all DOF are constrained. For the remaining nodes, $V = \Theta_x = \Theta_z = 0.0$. After applying the boundary conditions, the total number of equations (neq.) are 72. The shear correction factor is $\kappa = 5/6$.

Analytical solution for this pure bending problem indicates that the beam is forced into a circular arc when the end moment is applied. The deformed beam of radius ρ is related to the bending moment by

$$\frac{1}{\rho} = \frac{M}{EI} \quad . \tag{6.1}$$

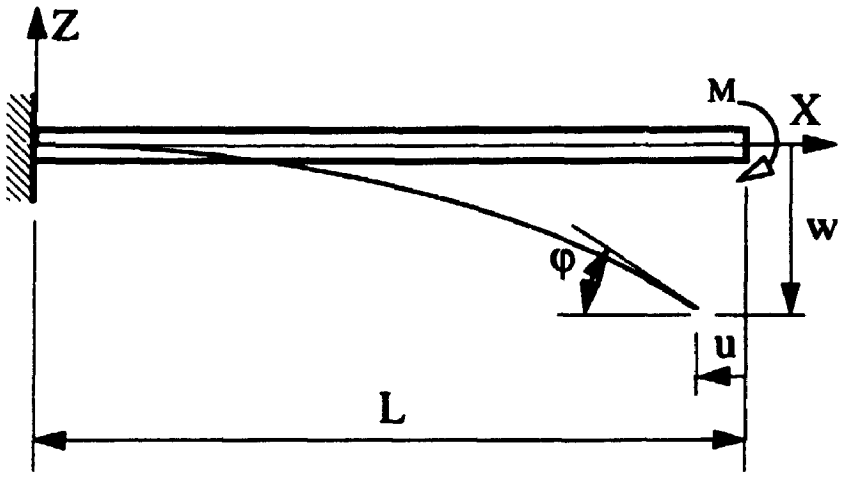

(a) Geometry

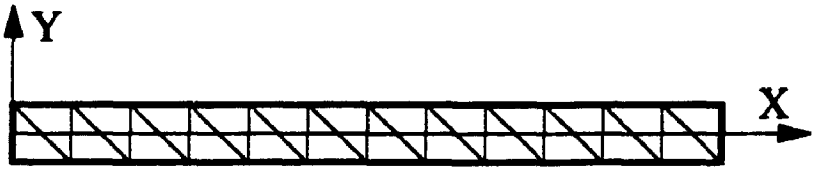

(b) 12 ×1 A mesh

Figure 6.1 A cantilever beam subjected to an end moment

It is seen that when M reaches

$$M_0 = \frac{2\pi EI}{L} \tag{6.2}$$

the beam rolls into a circle with a radius of

$$\rho = \frac{L}{2\pi} \quad . \tag{6.3}$$

Figure 6.2 shows the computed results obtained by using the HLCTS element with $M = M_0$ applied. The beam indeed rolls into a complete circle. Figure 6.3 gives

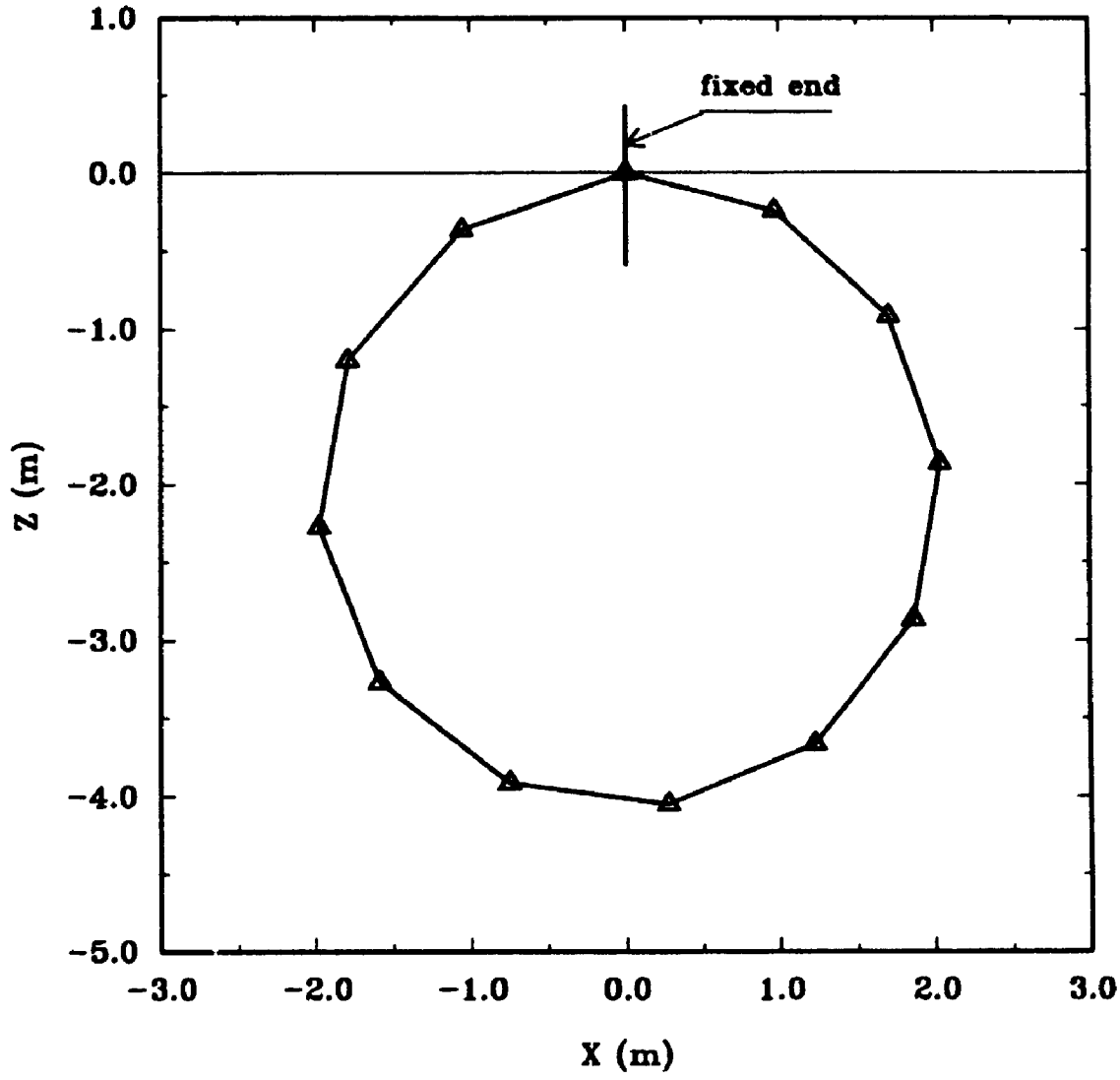

Figure 6.2 Deformed configuration of the cantilever beam at $M = M_0$

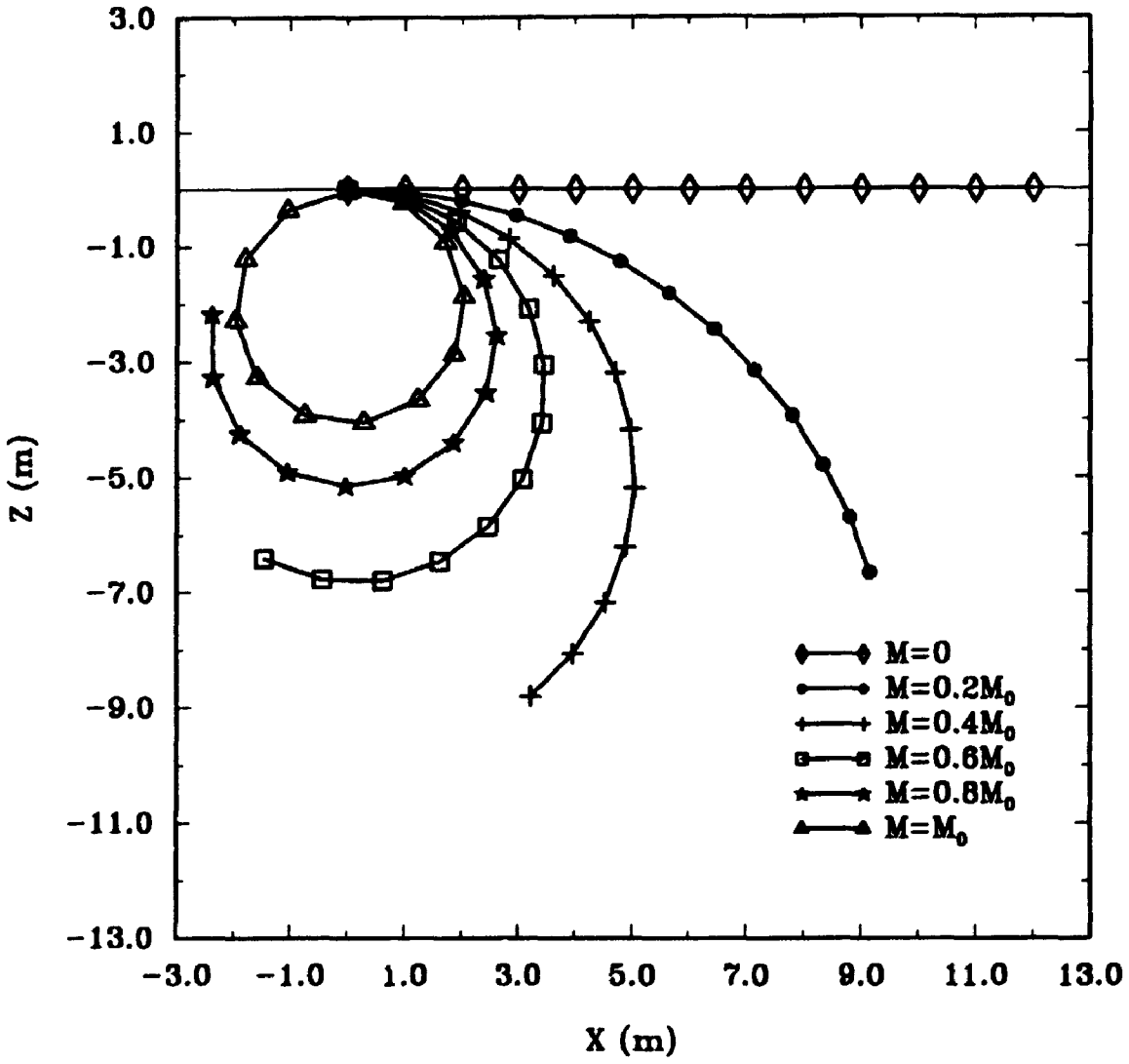

Figure 6.3 Deformed configurations of the cantilever beam at different load level

deformed configurations of the beam under different levels of loads. In Figure 6.4, the applied end moments are plotted against the normalized axial displacement U/L, lateral displacement W/L and the rotation of the normal $\varphi/2\pi$ at the end of the beam. In the solution process, 130 steps were used for the load to reach to M_0. The total number of iterations was six.

It should be point out that, the results shown in Figures 6.2-6.3 were obtained with the options of constant thickness, large strain and inclusion of directors in the HLCTS element formulation. The options of large strain and small strain in the computation make no difference in the results as the beam is still within small strain range though the deflection and rotation are considerably large. The inclusion of directors gives better results in the investigation. This is mainly due to the large rotations involved. In reference [6.2], the problem has been discussed in relatively details. For brevity, they are not repeated here.

6.1.2 Cylindrical bending of a plate under a line load

A very thin plate shown in Figure 6.5 is selected for the study of the so-called plate cylindrical bending problem. The plate is square with side length 2L = 1280 mm, thickness h = 0.8 mm, Young's modulus E = 2.07×10^5 N/mm^2 and Poisson's ratio ν = 0.3. The length to thickness ratio μ = 1600. The plate is simply supported at two opposite sides. The other two sides of the plate are free. It is subjected to a line force 2P = 0.474 N/mm^2 applied cross the centre line parallel to the simply supported edges.

One quarter of the plate is considered due to the symmetry of geometry, boundary conditions and loading. A 4 × 4 C mesh which has 32 elements is adopted to model the

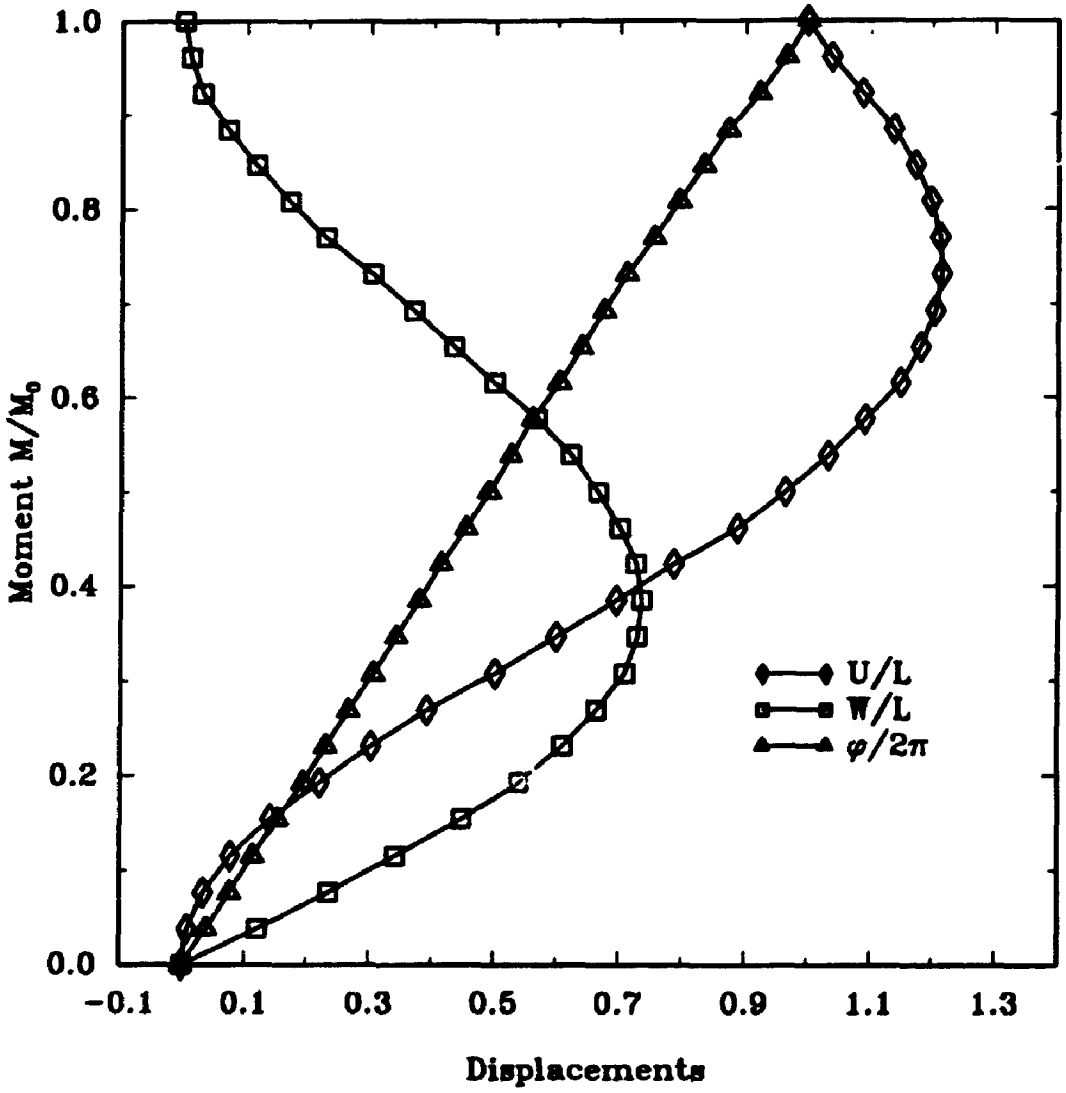

Figure 6.4 Load-displacement curve for the cantilever beam

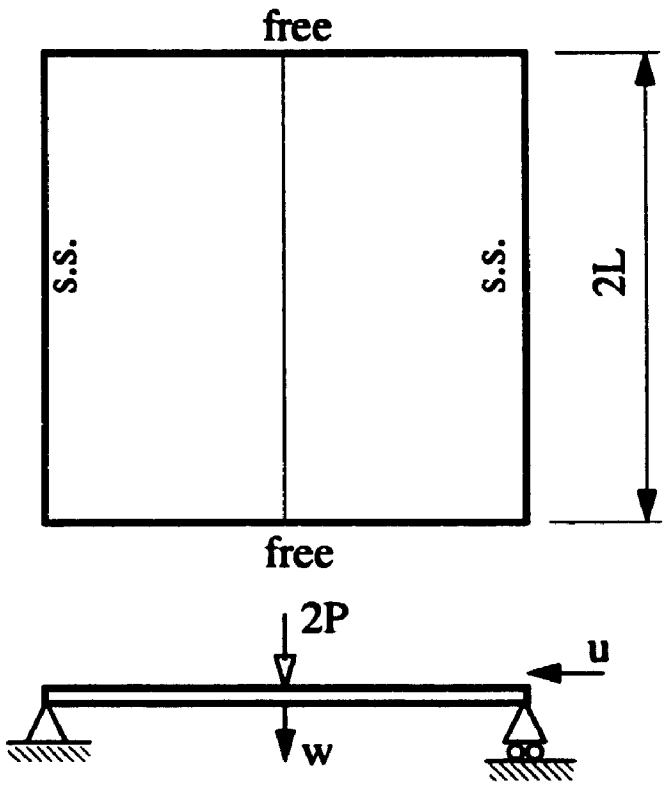

Figure 6.5 A square plate subjected to a line load

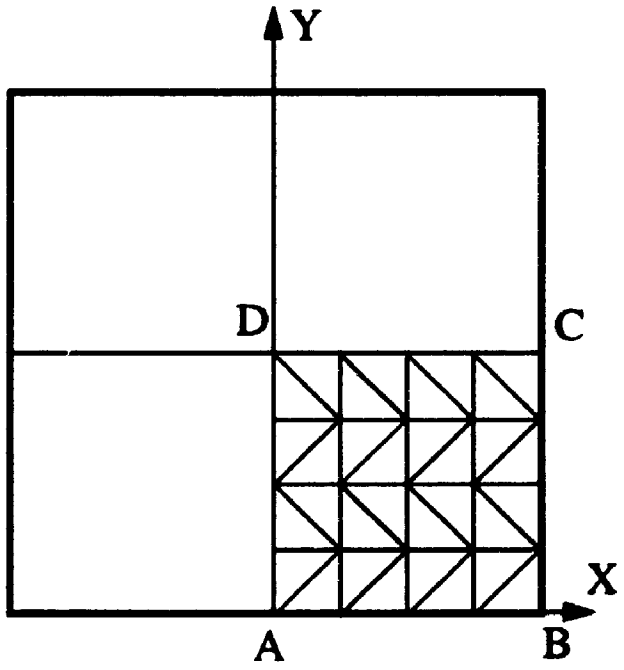

Figure 6.6 A 4×4 C mesh for a quarter of the square plate

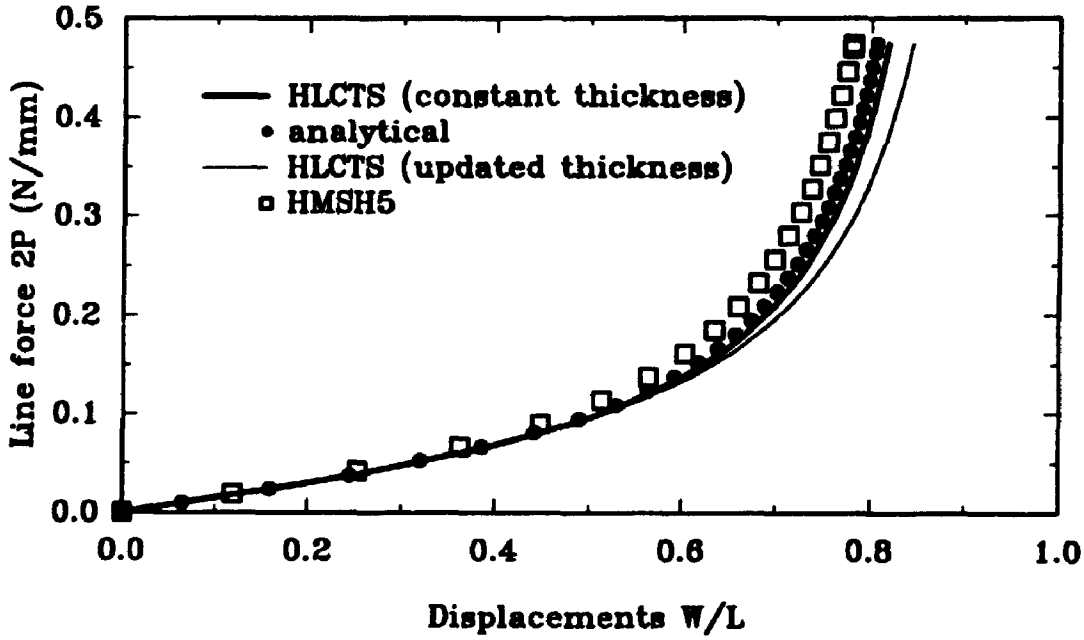

Figure 6.7 Load-displacement curve for the square plate subjected to a line load

quarter plate. The mesh layout is illustrated in Figure 6.6. To ensure cylindrical bending, Θ_x and Θ_z at all the nodes are constrained. In addition, W = 0.0 is applied to the nodes at the simply supported edge BC, V = 0.0 to the symmetry line CD and U = Θ_y = 0.0 along AD. The total unknowns of the constrained quarter plate are 80. As the plate is extremely thin, the shear correction factor has no significant effects on the final results. Thus, it is set to unity in this case.

The HLCTS element results with constant and updated thickness options are presented in Figure 6.7. The results were obtained by employing 100 load steps without

iterations. The comparisons are made to the analytical solution from reference [6.5] and finite element results from reference [6.3]. The finite element results are denoted by HMSH5. The HMSH5 results were obtained by using 5 × 5 and 7 × 7 mesh for a quarter of plate. The HMSH5 finite element is a quadrilateral C^0 element of hybrid type.

Figure 6.7 shows that the HLCTS element result with constant thickness option is in excellent agreement with the analytical solution. It overpredicts the deflection by approximately 4.0%, with respect to the analytical solotion, at the full load level when considering thinning effects. As the updated thickness procedure reduces the effective thickness as the plate deforming, larger deflection is anticipated. It should be pointed that the maximum deflection in this case is over 600 times larger than the plate thickness. Thus, the plate is undergoing large deformation. However, the problem is of small strain type as the options of large or small strain lead to almost the same results. The HLCTS element results presented here are identical to those reported in reference [6.2] in which this problem was solved by utilizing the same mesh shown in Figure 6.6.

6.1.3 Spherical cap subjected to a concentrated load

The shell problem considered in this section is a spherical cap. The shell is clamped circumferentially and subjected to a concentrated load P at its apex as shown in Figure 6.8. The geometrical and material properties of the shell are: radius R = 0.1209 mm (4.76 in), thickness h = 0.0004 mm (0.01576 in), crown height H = 0.00218 mm (0.0859 in), open angle $2\varphi = 21.8°$, Young's modulus $E = 6.895 \times 10^{10}$ N/m^2 (10^7 psi) and Poisson's ratio $\nu = 0.3$.

One quarter of the spherical shell is discretized by 80 nodes, 128 element mesh

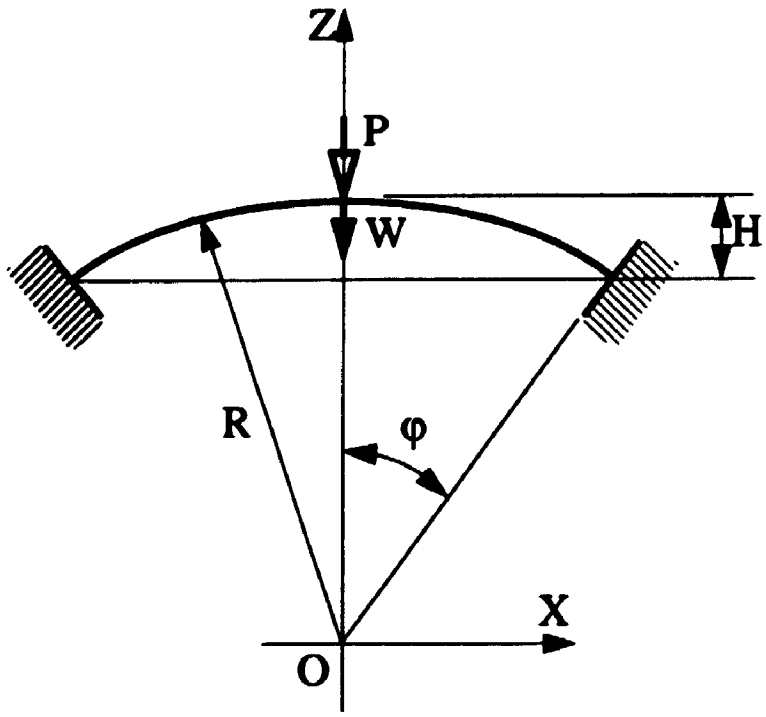

Figure 6.8 A spherical cap subjected to a concentrated apex load

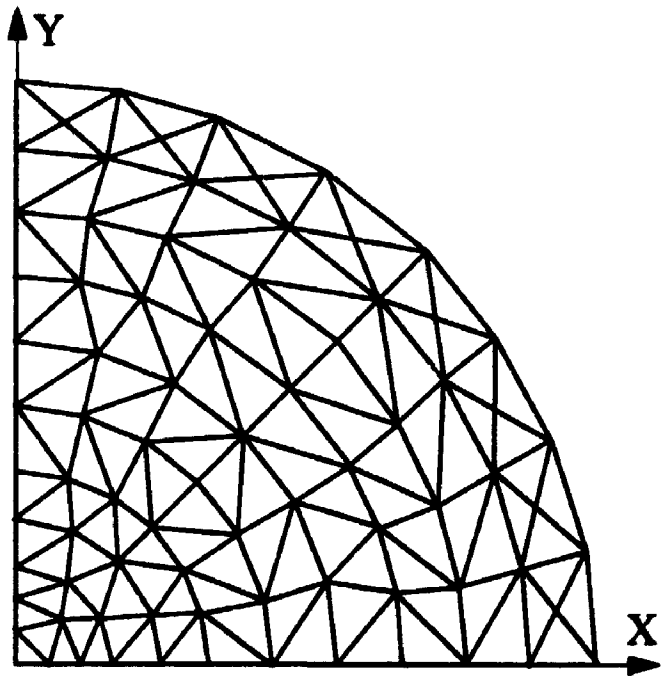

Figure 6.9 A 80 node, 178 element mesh for a quarter of the spherical cap

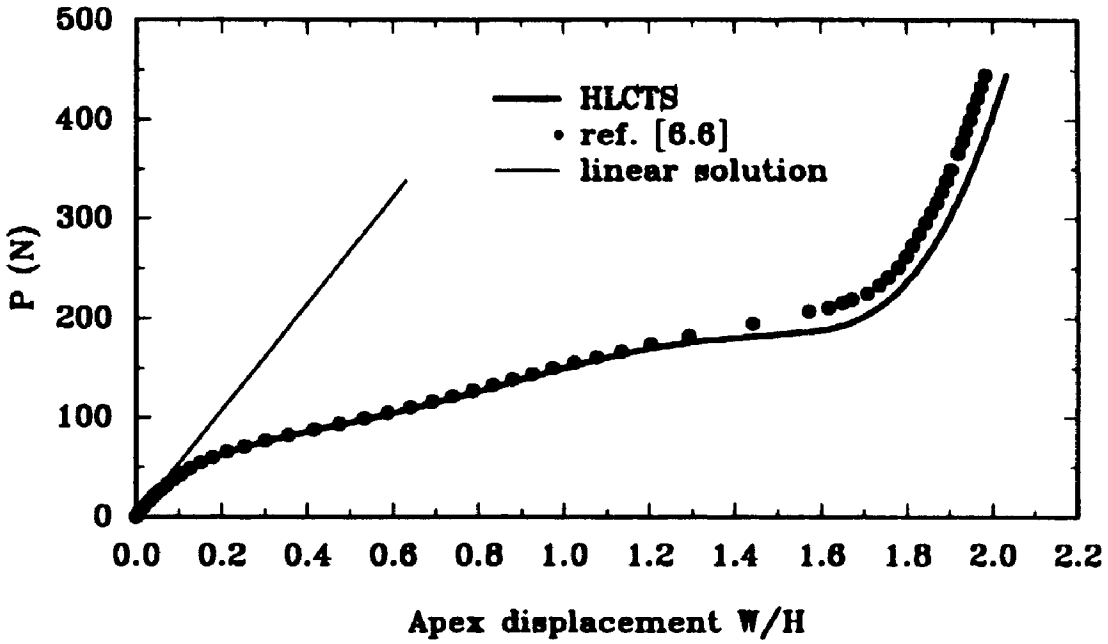

Figure 6.10 Load-displacement curve for the clamped spherical cap

as shown in Figure 6.9. The mesh has finer grid at the apex area and region close to the clamped circumference. The boundary conditions imposed are: all DOF at the clamped edge are constrained, $V = \Theta_x = \Theta_z = 0.0$ at the symmetry line cutting by the XOZ plane and $U = \Theta_y = \Theta_z = 0.0$ at the symmetry line cutting by the YOZ plane. The shear correction factor is $\kappa = 5/6$. The total unknowns to be solved in this case are 364.

The results obtained by using HLCTS element are plotted in Figure 6.10. It is compared with those given in reference [6.6] which are from an analysis by using 10 eight node axisymmetric shell elements. From the results shown in the figure one can

observe that a very small increase of the load around P = 200 N causes a relative large deflection and then the trend suddenly reversed. The softening behaviour turns to hardening. This indicates that the solution process is relatively difficult near this region. Coarse meshes or large load increments may induce computational singularity. Solution procedures which are lack of control near the singularity point may also have difficulties in this case. Reference [6.2] has reported such difficulties in solving this problem. Later, they obtained good results [6.13] by refining meshes (one of the meshes is the same as the one shown in Figure 6.9) and load increments. In the current study, 400 equal load increments are used without iteration. The efficiency can be improved by applying varying load increments. That is to say, using smaller load increments in the sensitive region.

It is found that results with options of including the directors and finite strain have no significant difference from those without directors and using constant thickness.

6.2 Static Analysis of Structures of Laminated Composite Materials

The HLCTS elements have given very good results in the analysis of geometrically nonlinear plate and shell structures of isotropic materials as seen from last section. Now, the present concern is on laminated composite plate and shell structures. The problems studied and presented in this section are an angle-ply sandwich plate subjected to tension, plates under uniformly distributed load, antisymmetrically laminated cylindrical panels subjected to central point load and a symmetrically laminated spherical shell segment subjected to different loadings.

6.2.1 Angle-ply sandwich plate subjected to a tension load

The sandwich plate considered here is shown in Figure 6.11(a). It is rectangular and clamped at X = 0.0. The geometrical properties of the plate are: length a = 2.0 m, width b = 0.8 m, and the total thickness h = 0.04 m. The sandwich plate has three layers. The top and bottom layers are carbon reinforced epoxy and they have an equal thickness of 0.004 m. The fibre orientations of the top and bottom layers are +30° and -30°, respectively. For the top and bottom layers, the material properties are: $E_1 = 2.11 \times 10^{11}$ N/m^2, $E_2 = 5.27 \times 10^9$ N/m^2, $G_{12} = G_{13} = G_{23} = 2.64 \times 10^9$ N/m^2 and $\nu_{12} = 0.25$. For the kernel, $E = 5.00 \times 10^8$ N/m^2 and $\nu = 0.0$. The core layer is isotropic and has a thickness of 0.032 m. The plate is loaded with a concentrated force $P = 1.4818 \times 10^6$ N at the middle point of the free end.

Figure 6.11(b) shows a 5 × 2 D mesh used for the finite element analysis. All DOF are constrained at the clamped end. Other boundary conditions are: $V = W = \Theta_y = \Theta_z = 0.0$ for nodes on the centre line, and $\Theta_z = 0.0$ for the remaining nodes. There are 110 unknowns to be solved in this finite element model. Shear correction factors are unity. During the solution process, 15 load increments are utilized without invoking iteration. The HLCTS element results with those from reference [6.7] are plotted in Figure 6.12. The results from reference [6.7] are obtained by using a four node rectangular element with a 4 × 2 mesh. It has been tested that the options of large strain, updating thickness and including directors lead to insignificant difference between the results. From Figure 6.12 one can see that the concentrated tension load causes warping. That is, at point B, there is a large transversal deflection W_B due to the in-plane tension force P. It may need to point out that if an uniformly distributed tension load, whose

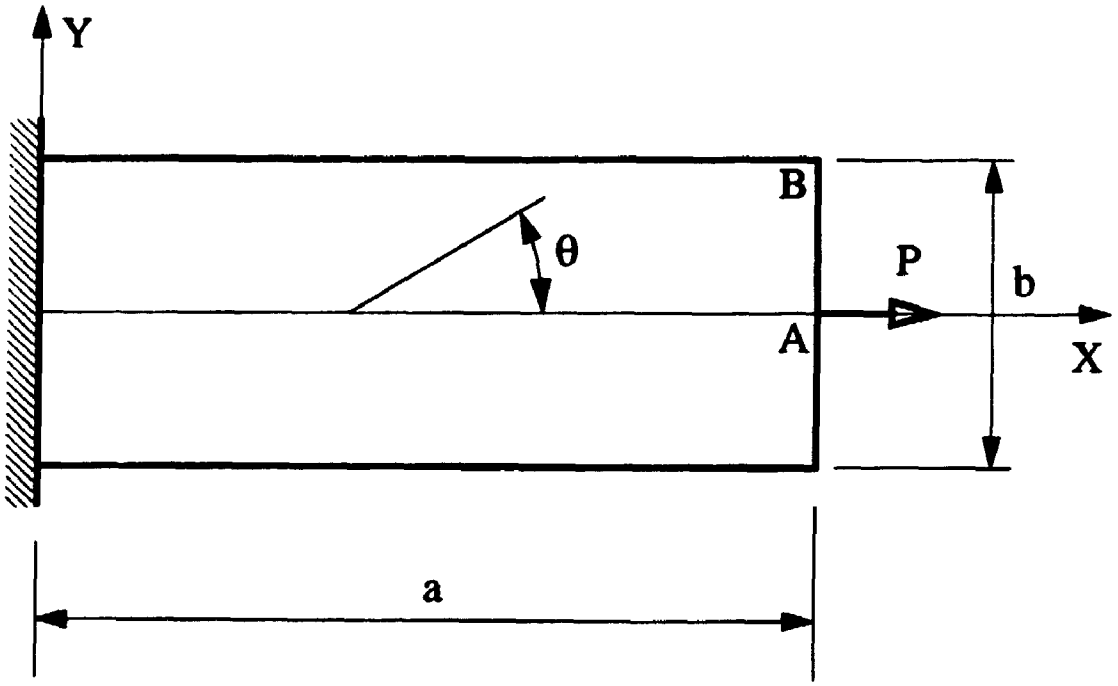

(a) Geometry

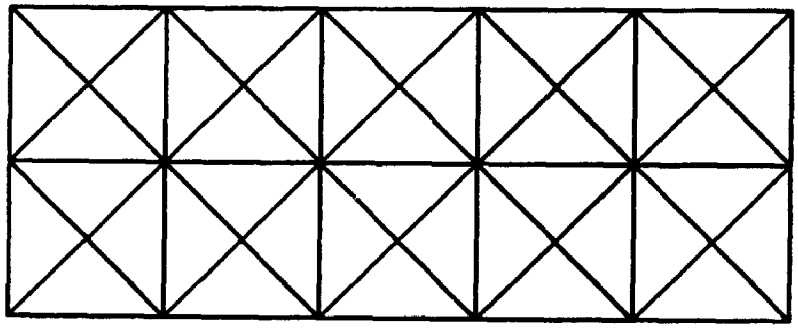

(b) 5 × 2 D mesh

Figure 6.11 A laminated plate subjected to a concentrated tensional load

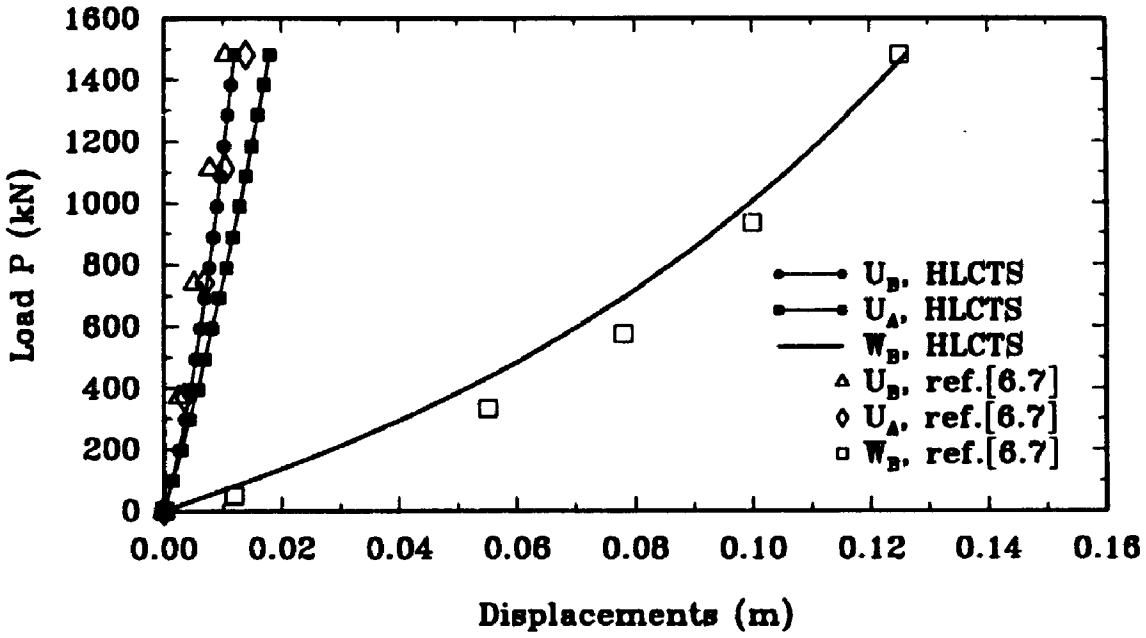

Figure 6.12 Load-displacement curve for the cantilever plate subjected to tension

resultant has an equal value as P, is applied to the free end, W_B is much smaller than the case of concentrated load. Therefore, in reference [6.7] the statement that "the stresses σ_x are represented by the resultant P" seems to be incorrect since their results matches the case with a concentrated load.

6.2.2 Plates under uniformly distributed load

In the analysis of laminated composite plates, cross-ply laminates have been given considerable attention. The cross-ply layup is a special case of the general angle-ply layer

arrangement. Thus, a two layer cross-ply (90/0) square plate under uniformly distributed load is studied first. This is followed by a four layer symmetrically laminated angle-ply plate.

The square plate has a side length, b = 0.2286 m (9 in), and a total thickness h = 1.016×10^{-3} m (0.04 in). Each layer has an equal thickness. The material is a graphite/epoxy composite. Its material properties are:

$$E_1 = 1.379\times10^{11} \text{ N/m}^2 \ (2.0\times10^7 \text{ psi});$$

$$E_2 = 9.653\times10^{9} \text{ N/m}^2 \ (1.4\times10^6 \text{ psi});$$

$$G_{12} = G_{13} = 4.827\times10^{9} \text{ N/m}^2 \ (0.7\times10^6 \text{ psi});$$

$$G_{23} = 3.448\times10^{9} \text{ N/m}^2 \ (0.5\times10^6 \text{ psi});$$

and Poisson's ratio $\nu_{12} = 0.3$.

The laminated plate is simply supported at four edges and under transversally applied uniformly distributed load. Owing to symmetry, one quarter of the laminated plate is modeled by a 3 × 3 D mesh (see Figure 6.13). For the finite element model, the boundary conditions imposed are: $V = \Theta_x = 0.0$ at AB, $W = \Theta_x = 0.0$ at BC, $W = \Theta_y = 0.0$ at CD and $U = \Theta_y = 0.0$ at AD. At point A, centroid of the plate, W is free and all other DOF are constrained. With these boundary conditions, there are 120 unknowns to be solved. The shear correction factors are $\kappa_4 = \kappa_5 = (5/6)^{1/2}$.

This problem has been solved by Yeom and Lee [6.8], and Sun [6.9]. In reference [6.8], a degenerated three-dimensional hybrid strain based element was employed. The element has 9 nodes and 5 DOF for each node. It is capable of dealing with large deformation of small strain and finite rotation. It also considered transversal shear effect. Reference [6.9] uses the von Karman plate theory which can not handle finite rotation.

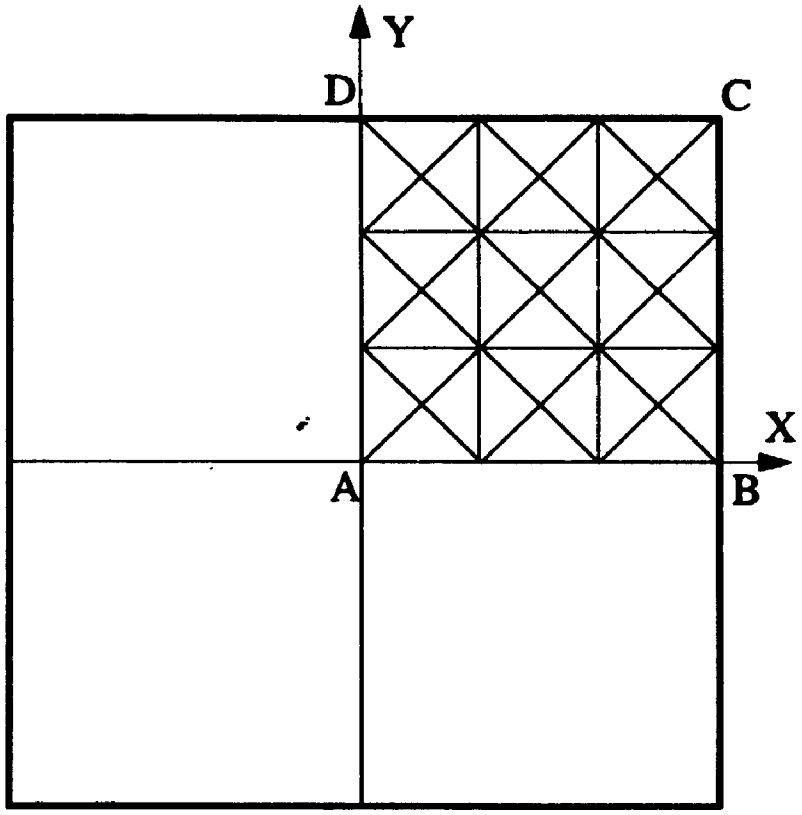

Figure 6.13 A 3×3 D mesh for a quarter of the laminated square plate

The results obtained by using the HLCTS element and those from references [6.8] as well as [6.9] are given in Figure 6.14. In the present investigation, 50 load increments are applied with a total of 10 iterations. The results of reference [6.8] were obtained from a 3 × 3 mesh.

Under the current level of applied load, this problem remains in the small strain range as the results differ insignificantly from those applying the large strain and updating thickness options.

Now a four layer symmetrically laminated angle-ply plate is analyzed. The

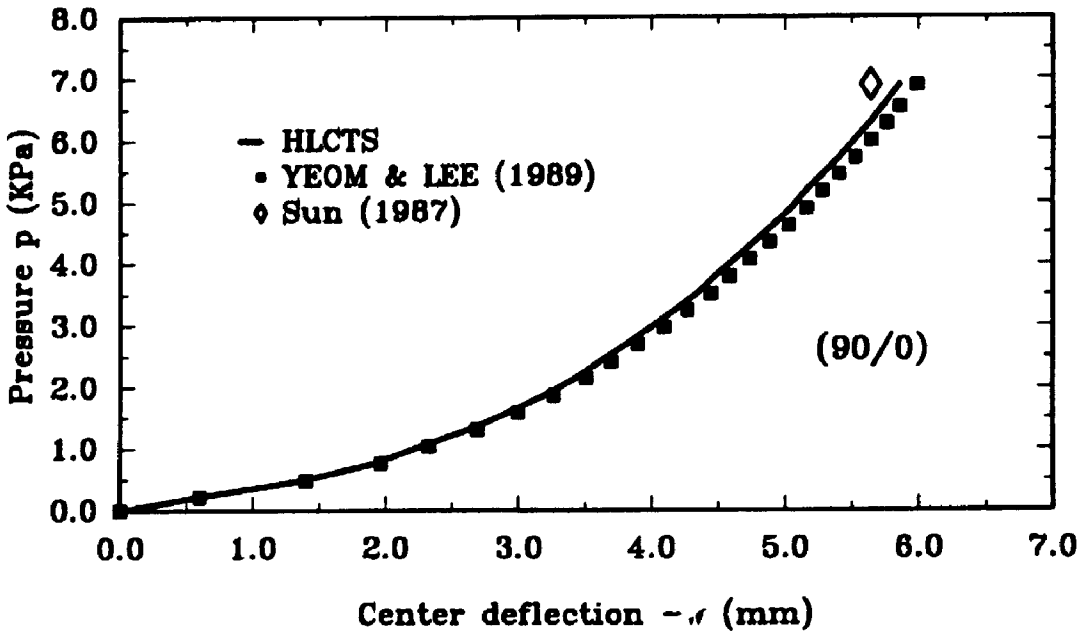

Figure 6.14 Load-displacement curve for the cross-ply plate

geometrical and material properties of this plate have been given above. The detailed lamination scheme is (-45/45/45/-45). All the layers of the laminate have equal thickness and the total thickness of the plate is 1.016×10^{-3} m (0.04 in). The boundary conditions and load applied are also the same as the two layer cross-ply plate.

Figure 6.15 shows the transversal deflections obtained by using a 3 × 3 D mesh for one quarter of the plate. The comparison is made between those using 30 and 60 load increments. In both cases, there is one iteration for every five load increments. The two set of results appear to be very close to one another except that, the one with 60 load

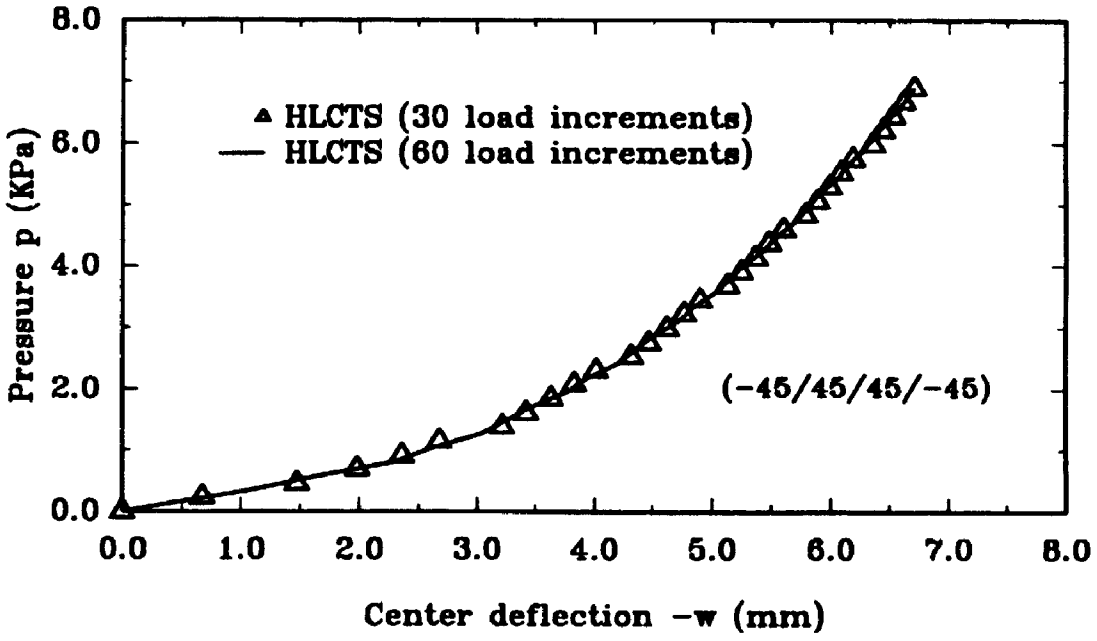

Figure 6.15 Load-displacement curve for the angle-ply plate

increments gives a more smooth plot.

6.2.3 Antisymmetrically laminated cylindrical panels subjected to a central point load

A two layers angle-ply cylindrical shell panel is considered here. The panel and a 2 × 2 D mesh for one quarter of the panel are shown in Figure 6.16. It is subjected to a central point load P. The length of the panel b = 0.508 m (20.0 in), shell radius R = 2.54 m (100 in), open angle 2φ = 0.2 rad and total thickness h = 0.0124 m (0.496 in). The layer material properties are:

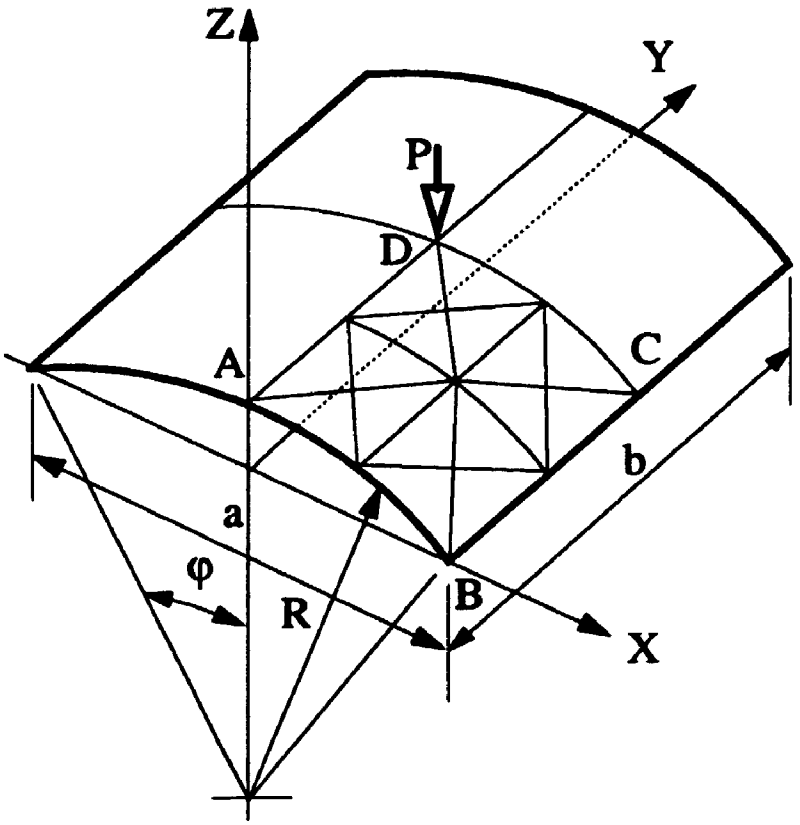

Figure 6.16 A laminated cylindrical panel subjected to a point load

$E_1 = 3.2993 \times 10^9$ N/m^2 (4.785×10^5 psi);

$E_2 = 1.0998 \times 10^9$ N/m^2 (1.595×10^5 psi);

$G_{12} = G_{13} = 6.5985 \times 10^8$ N/m^2 (0.957×10^5 psi);

$G_{23} = 4.4128 \times 10^8$ N/m^2 (0.64×10^5 psi);

and Poisson's ratio $\nu_{12} = 0.25$.

The cylindrical shell panel is constructed as (45/-45) and the angle is measured from Y-axis in this case. It is hinged along the straight edges and free on the curved sides. Making use of the symmetry, one quarter of the panel is applied for the analysis.

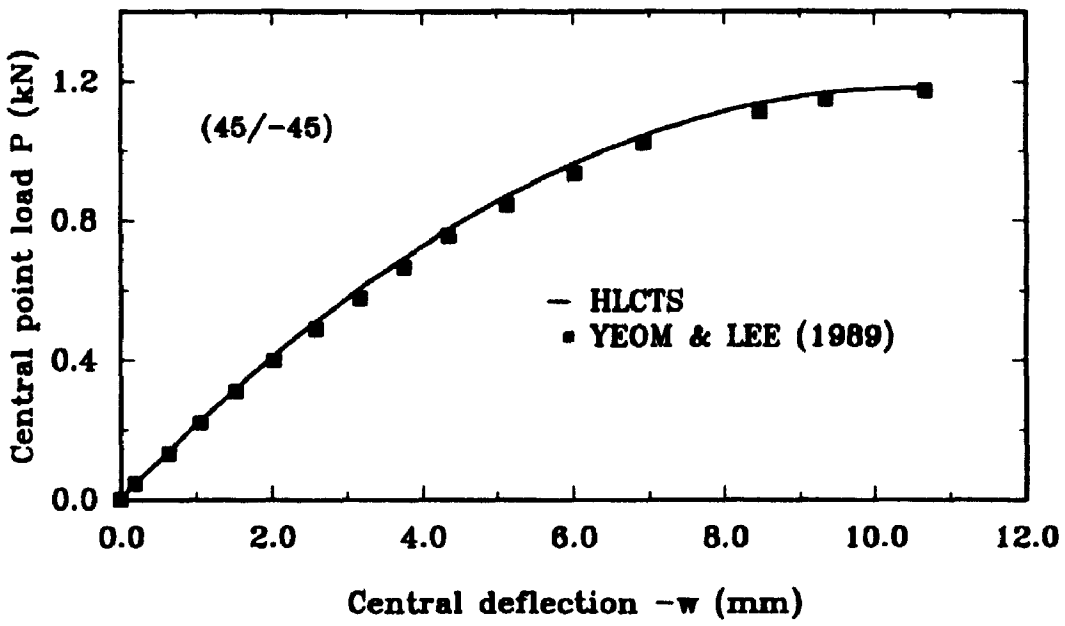

Figure 6.17 Load-displacement curve for the angle-ply cylindrical panel

This quarter of panel is modeled by a 4 × 4 D mesh. The boundary conditions imposed on the finite element model are: $U = V = W = \Theta_x = \Theta_z = 0.0$ at BC, $V = \Theta_x = \Theta_z = 0.0$ at CD and $U = \Theta_y = \Theta_z = 0.0$ at AD. It has 195 unknowns. The shear correction factors are $\kappa_4 = \kappa_5 = (5/6)^{1/2}$.

In this analysis, the load increment adopted is 2.224 N (0.5 lb) and there is no iteration applied. The computed results denoted by HLCTS are compared with those presented by Yeom and Lee [6.8] applying the same degenerated three-dimensional hybrid strain based element mentioned in last subsection. They are given in Figure 6.17. The

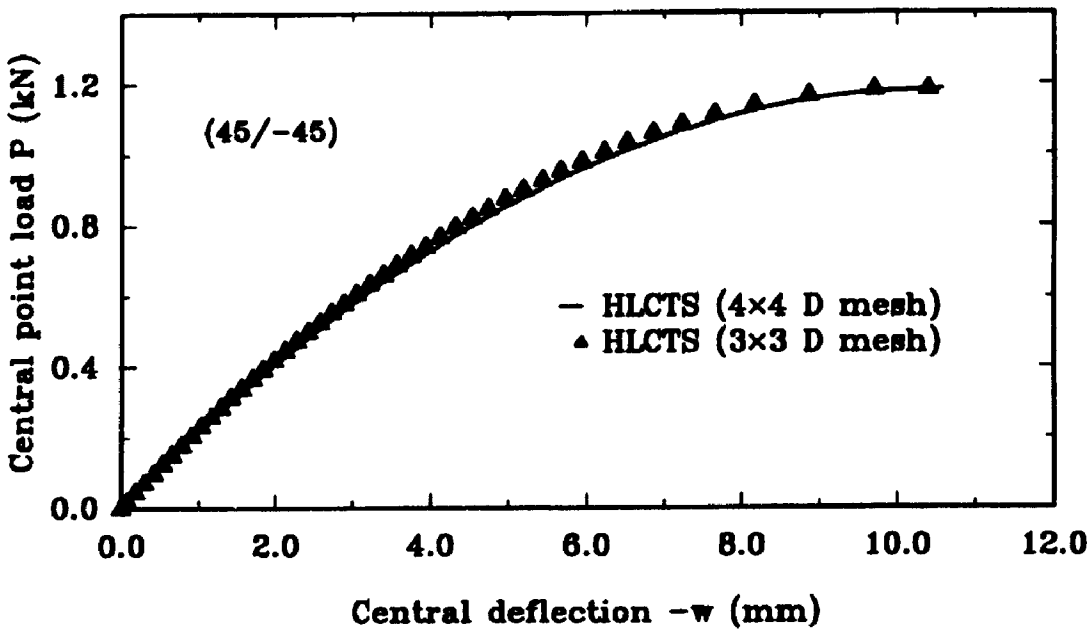

Figure 6.18 Comparison of results from different meshes

results by Yeom and Lee were obtained by using a 4 × 4 mesh for a quarter of the shell panel. Figure 6.18 gives the comparison of HLCTS element results by using 4 × 4 D and 3 × 3 D meshes. The two sets of results differ from each other slightly. However, they have the limit point at the same load level. This singular point is where the snap-through starts.

The (45/-45) shell panel and a (90/0) cylindrical shell panel which has the same geometrical and layer material properties as those given above are also investigated under a uniformly distributed pressure load p. The boundary conditions are still the same.

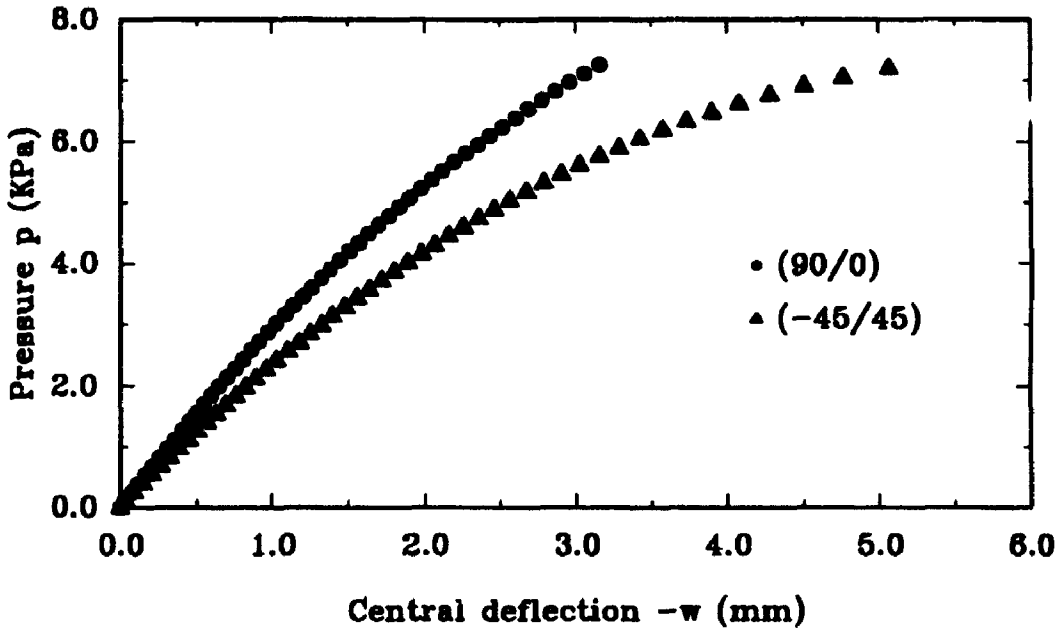

Figure 6.19 Load-displacement curve for cylindrical panels under pressure load

Figure 6.19 shows the results obtained by using the HLCTS element. It can be seen that the (90/0) lamination scheme provides larger stiffness or stiffer panel. In the solution process, 150 load increments were applied without introducing iterations. There is no solution available in the literature for comparison in these cases.

6.2.4 Symmetrically laminated spherical shell segment subjected to different loadings

A nine layers cross-ply symmetrically laminated doubly curved spherical shell segment is analyzed first. The shell is shown in Figure 6.20. Its layup is

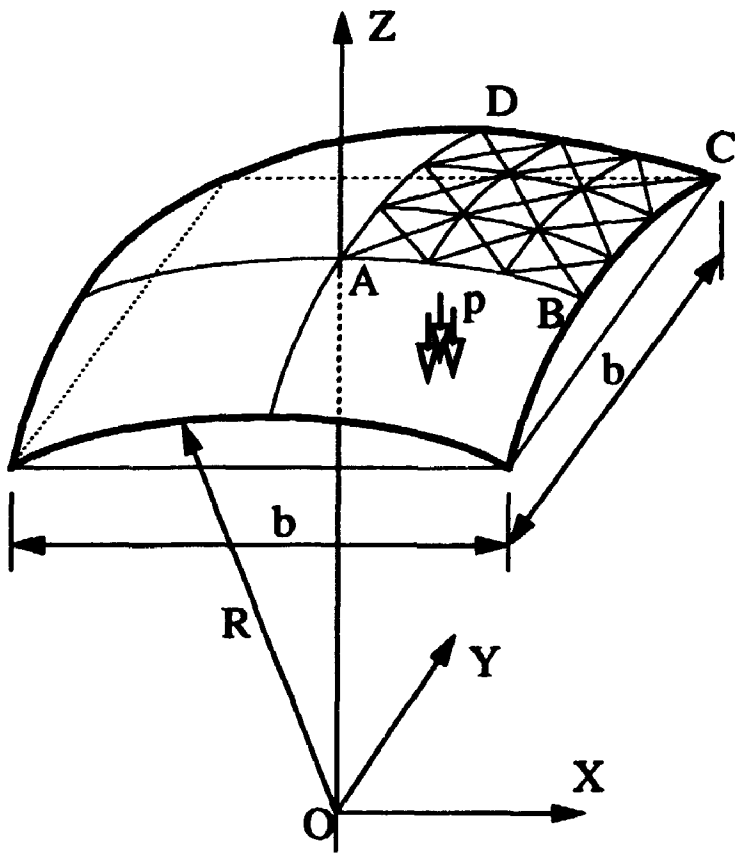

Figure 6.20 A laminated spherical shell segment under pressure load

(0/90/0/90/0/90/0/90/0). The total thickness of the shell is h = 0.01 m (0.3937 in). The thickness of 0° layers is h/10 and 90° layers is h/8. The projected side length of the shell is b = 1.0 m (39.37 in). The radius, R, is 10 m (393.7 in). The layer material properties of the spherical shell segment are:

$$E_1 = 2.0685\times10^{11}\ \text{N/m}^2\ (3.0\times10^7\ \text{psi});$$

$$E_2 = 5.1713\times10^{9}\ \text{N/m}^2\ (0.75\times10^6\ \text{psi});$$

$$G_{12} = 3.1028\times10^{9}\ \text{N/m}^2\ (0.45\times10^6\ \text{psi});$$

$$G_{13} = G_{23} = 2.5856\times10^{9}\ \text{N/m}^2\ (0.375\times10^6\ \text{psi});$$

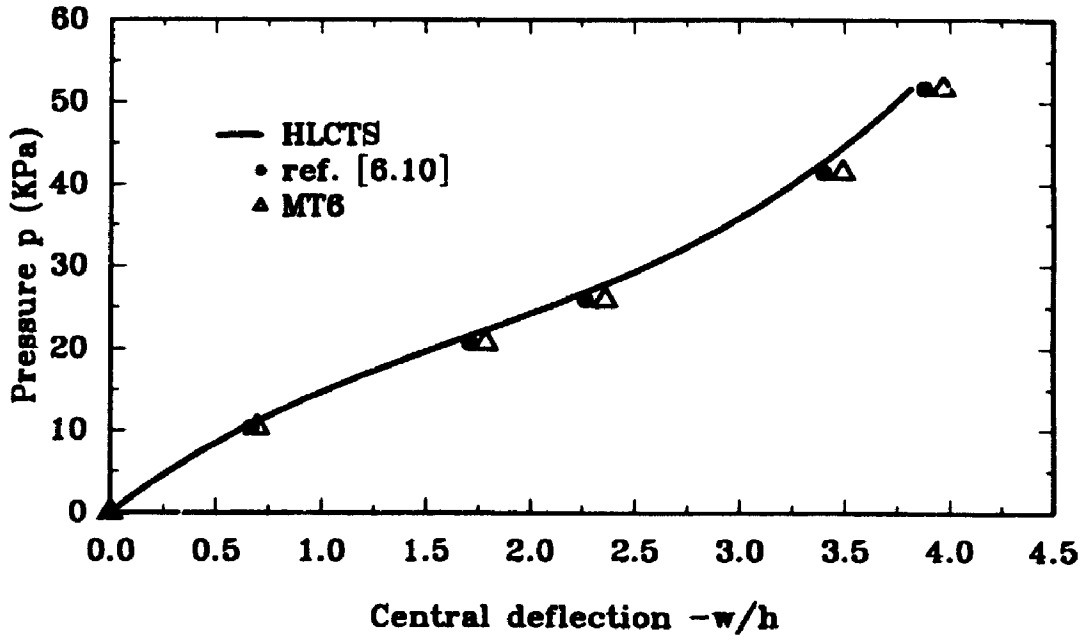

Figure 6.21 Load-displacement curve for the spherical shell under pressure load

and Poisson's ratio $\nu_{12} = 0.25$.

It is simply supported at four curved edges. A uniformly distributed pressure load p is applied. The latter is always normal and pointing to the outer surface of the shell. One quarter of the shell is modeled by using a 3 × 3 D mesh. The boundary conditions applied to the finite element model are: $V = \Theta_x = \Theta_z = 0.0$ at line AB, $V = W = \Theta_x = 0.0$ at BC, $U = W = \Theta_y = 0.0$ at DC and $U = \Theta_y = \Theta_z = 0.0$ at AD. After applying the boundary conditions, the total number of equations to be solved are 107. The shear correction factors are $\kappa_4 = \kappa_5 = (5/6)^{1/2}$.

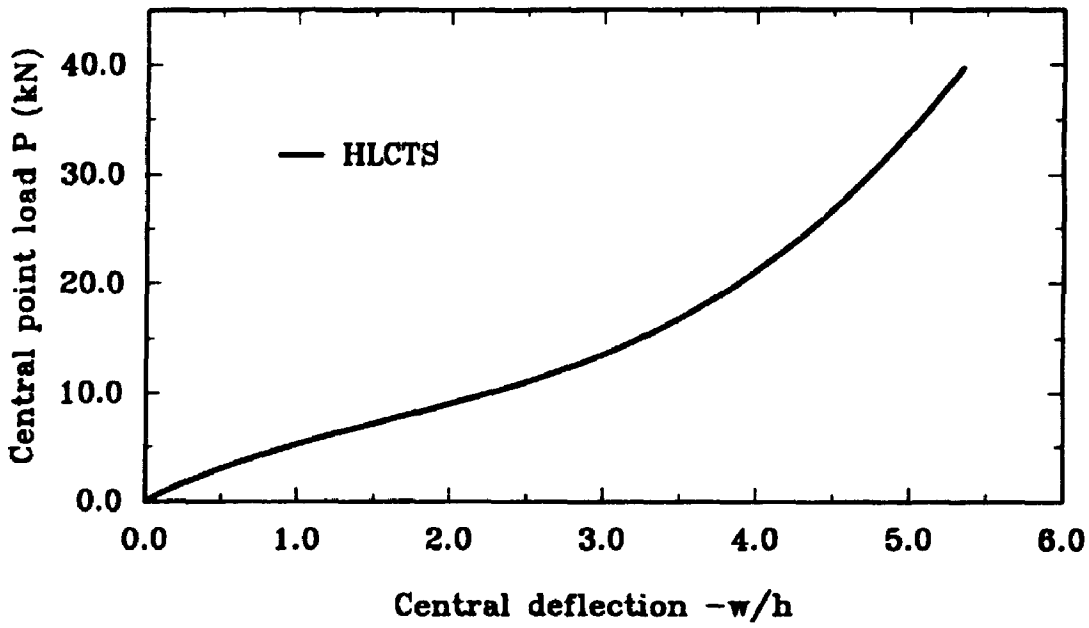

Figure 6.22 Load-displacement curve for the spherical shell subjected to point load

The finite element results obtained by employing the HLCTS element and those from reference [6.10] are given in Figure 6.21. In this figure, the HLCTS results are from a solution process using 150 load increments without iterations. The results denoted by ref. [6.10] are the converged finite element solutions from reference [6.10]. The finite elements used for these solutions are of mixed type. They were designated by MT6, MQ8 and MQ9 in this reference. The MT6 element is triangular and has six nodes. The MQ8 and MQ9 elements are quadrilateral and have eight and nine nodes, respectively. The respective number of DOF per element for MT6, MQ8 and MQ9 are 78, 104 and 117.

The results denoted by MT6 in Figure 6.21 are the MT6 element solutions from a 2 × 2 mesh for one quarter of the shell segment.

The same nine layer cross-ply laminated composite spherical shell segment is then subjected to a concentrated load at its central point A. The load is applied in the negative Z direction. The results are obtained by applying 120 load increments without iteration. Figure 6.22 shows the results. For this case there is no solution in the literature for comparison.

6.3 Dynamic Analysis of Structures of Isotropic Materials

Static analysis of geometrically nonlinear plate and shell structures of isotropic materials has been performed in section 6.1 and laminated composite materials in section 6.2. This and next sections are concentrated on dynamic analysis of such structures. In this section, two cases of single layer structures made of homogeneous isotropic materials are studied. They are a rectangular plate and a spherical cap subjected to step loadings. In both cases, the shear correction factor is $\kappa = 5/6$. The analysis is aimed at providing a concrete proof of the validity and accuracy of the HLCTS element in dealing with isotropic plate and shell structures.

6.3.1 Rectangular plate subjected to a step load

A rectangular plate shown in Figure 6.23 is considered here. The plate has been analyzed in references [6.2]. The geometrical and material properties are: side length a = 1.016 m (40 in), b = 1.524 m (60 in), thickness h = 0.0254 m (1 in), Young's modulus $E = 2.0685 \times 10^8$ N/m^2 (3×10^4 psi), Poisson's ratio $\nu = 0.25$ and density

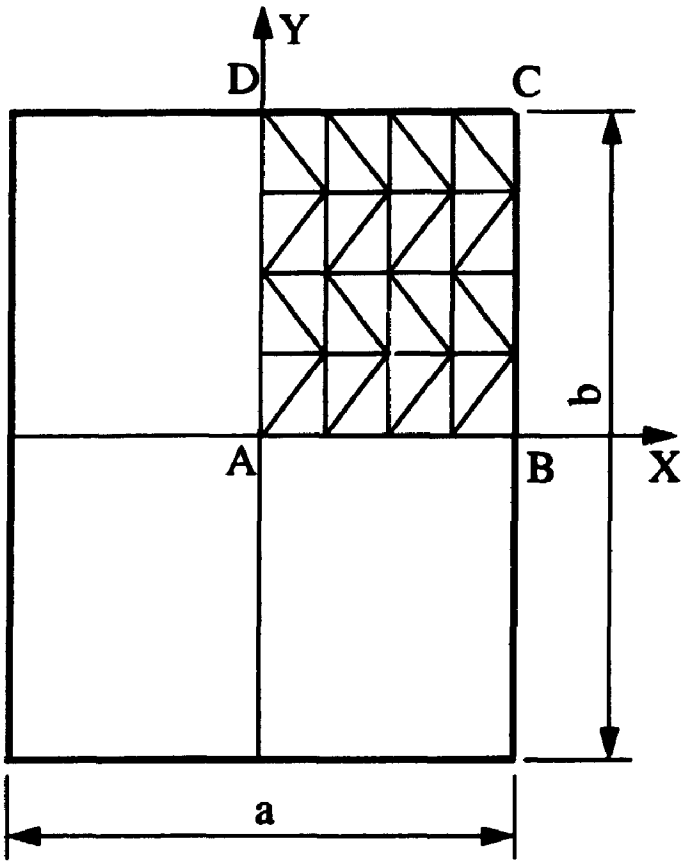

Figure 6.23 A 4×4 C mesh for a quarter of the rectangular plate

ρ = 3204.0 kg/m^3 (0.0003 lb-sec^2/in^4).

It is simply supported at four edges. One quarter of the plate is modeled by a 4 × 4 C mesh depicted in Figure 6.23. In this analysis, the membrane part of the element is ignored. That is, all V, U and Θ_z DOF are set to zero. In addition, the boundary conditions imposed on other DOF are: Θ_x = 0.0 at AB, W = Θ_x = 0.0 at BC, W = Θ_y = 0.0 at CD and Θ_y = 0.0 at AD. The total number of unknowns to be solved in this case are 48.

A ramp with the amplitude P_0 = 177.92 N (40 lb) is applied at the centroid of the

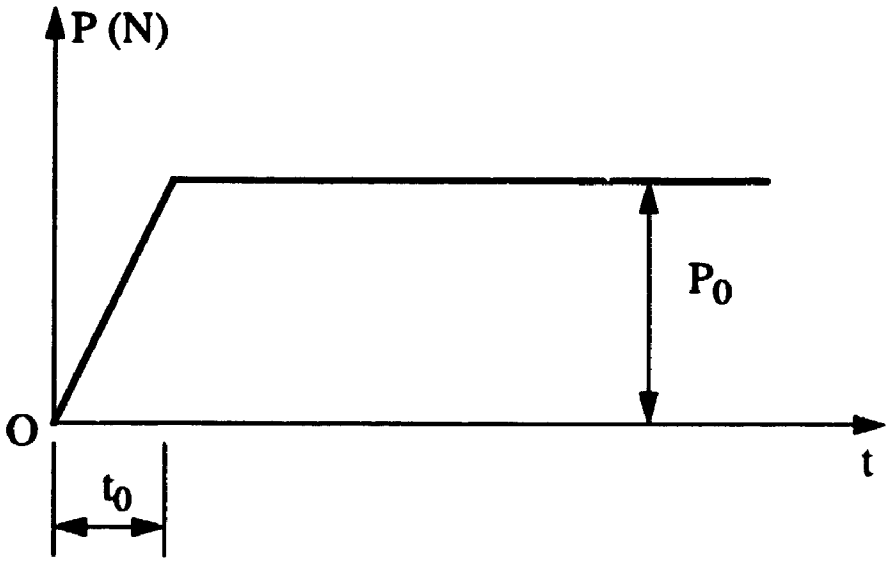

(a)

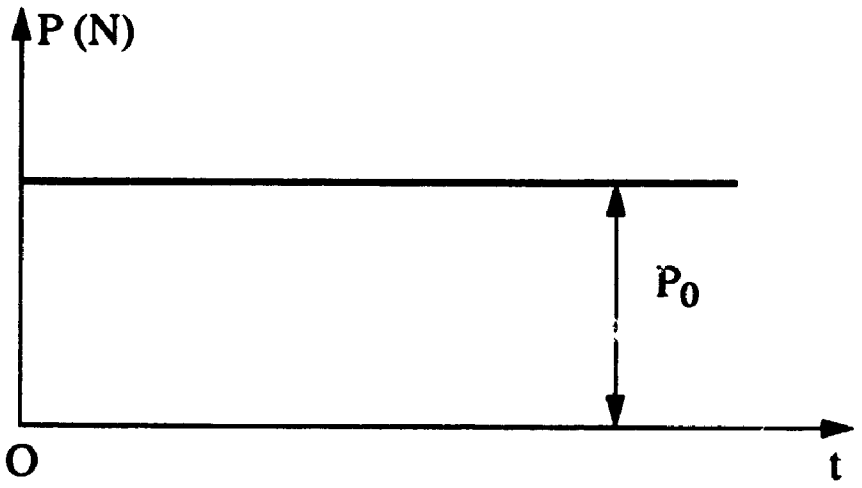

(b)

Figure 6.24 Time history of step loadings

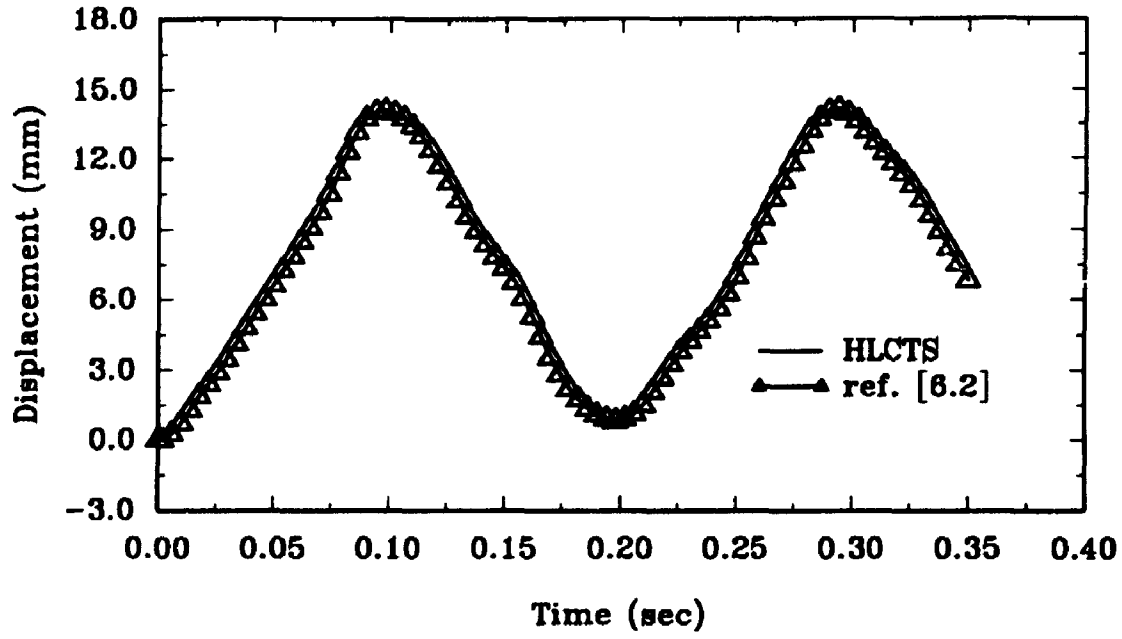

Figure 6.25 Time history of centre displacement of the rectangular plate

plate. As depicted in Figure 6.24(a), the acceleration time t_0 = 0.006 second. In the solution process, the trapezoidal direct integration scheme is adopted and the time step size is Δt = 0.002 seconds.

The HLCTS element results obtained with the options of large strain and updated thickness are included in Figure 6.25 together with those from reference [6.2]. These results are identical. A comparison between the geometrically nonlinear and linear solutions of the same plate is given in Figure 6.26. The geometrically nonlinear results have a shorter period and smaller amplitude. This phenomenon indicates stiffness hardening effects.

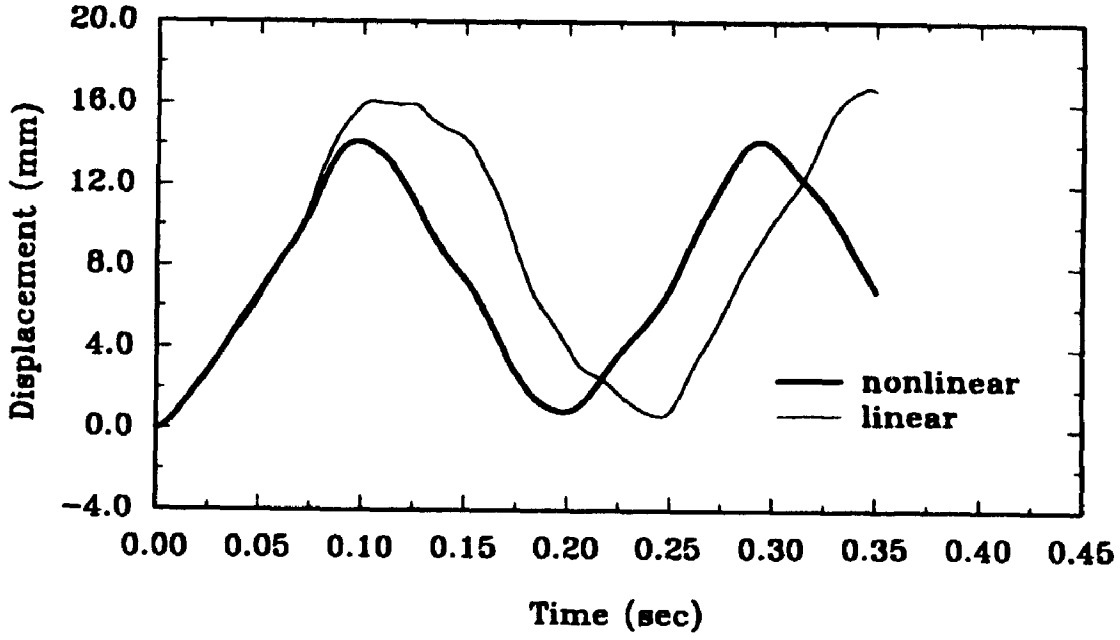

Figure 6.26 Comparison of nonlinear and linear analysis of the rectangular plate

6.3.2 Spherical cap subjected to a step load

The spherical cap analyzed in subsection 6.1.3 is now subjected to a step load applied at its apex. The step load function is give in Figure 6.24(b) and P_0 = 155.68 N (35 lb). The density of the shell is ρ = 2617.0 kg/m^3 (0.000245 lb-sec^2/in^4). Other pertinent data and boundary conditions have been given in subsection 6.1.3.

A relatively coarse mesh is used to model one quarter of the spherical shell. As shown in Figure 6.27, there are 46 nodes and 72 elements in this mesh. The mesh also has finer grid at its apex area and where is near the clamped circumference. The

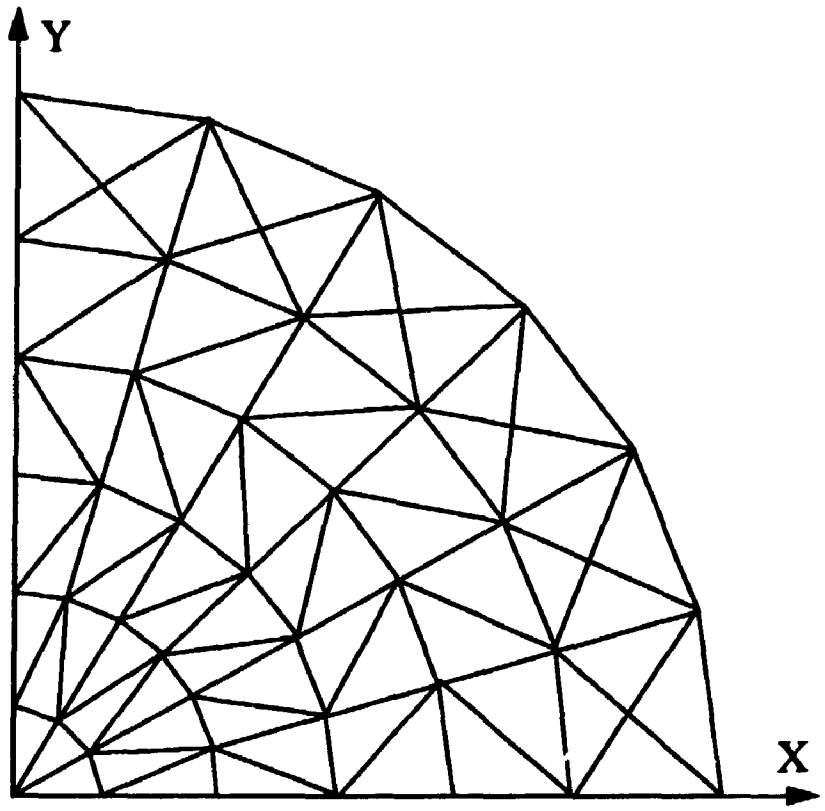

Figure 6.27 A 46 node, 72 element mesh for a quarter of the spherical cap

constrained computational model has 199 unknowns.

The same trapezoidal rule is employed in the integration and time step size is $\Delta t = 0.22 \times 10^{-5}$ sec. This Δt is about one-fiftieth of the fundamental period of the spherical cap. With the options of finite strain, excluding directors and constant consistent mass matrix, the results obtained by using the HLCTS element and those from reference [6.2] are plotted in Figure 6.28. To illustrate the effect of geometrical nonlinearity, the HLCTS element results are compared with those from linear analysis in Figure 6.29. It can be seen that the linear analysis predicts about four times smaller vibration amplitude

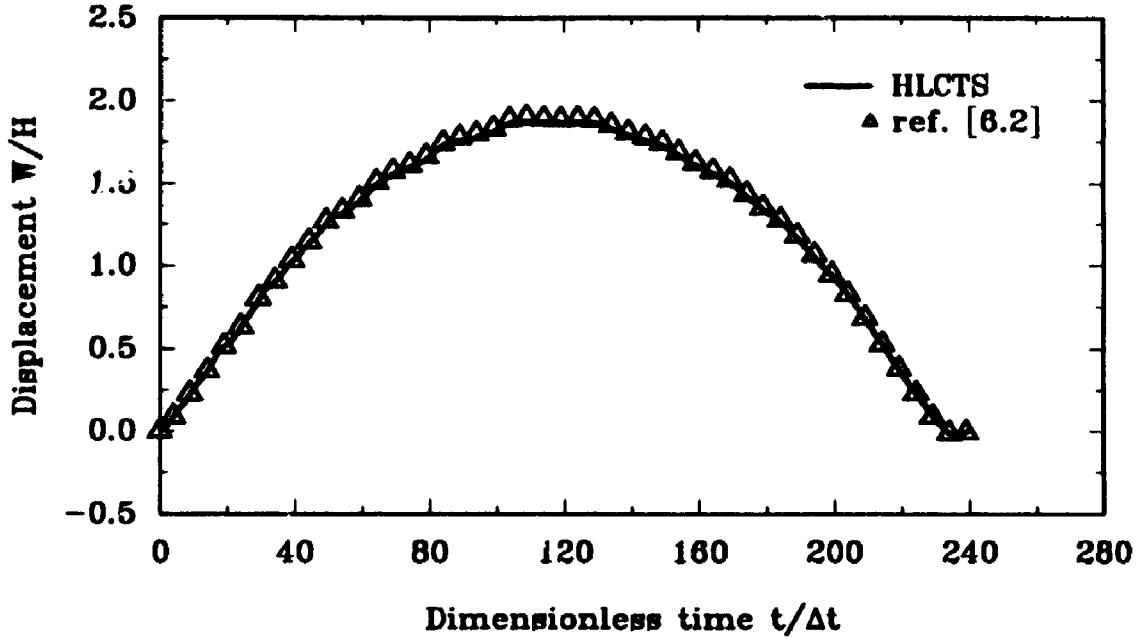

Figure 6.28 Time history of apex displacement of the clamped spherical cap

and five times higher oscillation frequency. The results of geometrical nonlinear analysis indicate stiffness softening effects, which agree with the observation in subsection 6.1.3.

6.4 Dynamic Analysis of Structures of Laminated Composite Materials

To demonstrate the attractive features of the HLCTS elements in predicting dynamic responses of structures of laminated composite materials, several plate and shell structures are analyzed in this section. These cases are the transient responses of a square plate, a cylindrical shell panel, a spherical shell segments and a cantilever panel. The

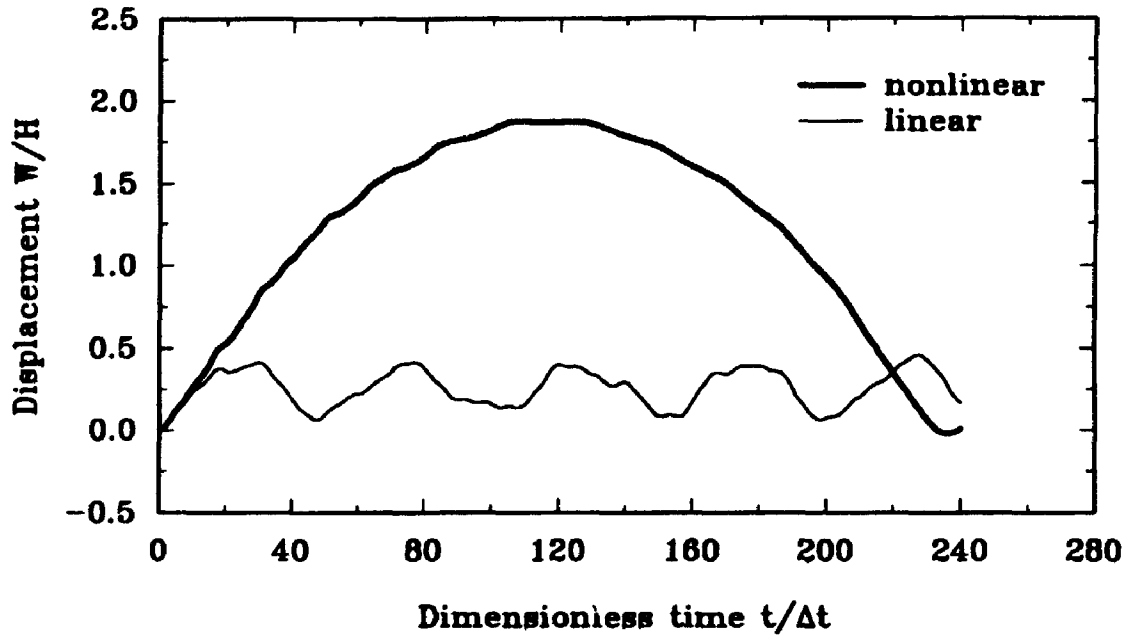

Figure 6.29 Comparison of nonlinear and linear analysis of the spherical cap

plates and shells are constructed with different numbers of layers and lamination schemes. For the first three cases the applied load are either concentrated load or uniformly distributed load which is a step function of time. For the cantilever panel a step moment is applied at the free end. Though the current HLCTS element formulation allows updating the consistent mass matrix in each time step, it is kept constant for the purpose of comparison with results available in the literature. Other options that the HLCTS element has in the static analysis remain valid in the dynamic analysis. The shear correction factors for these cases are $\kappa_4 = \kappa_5 = (5/6)^{1/2}$.

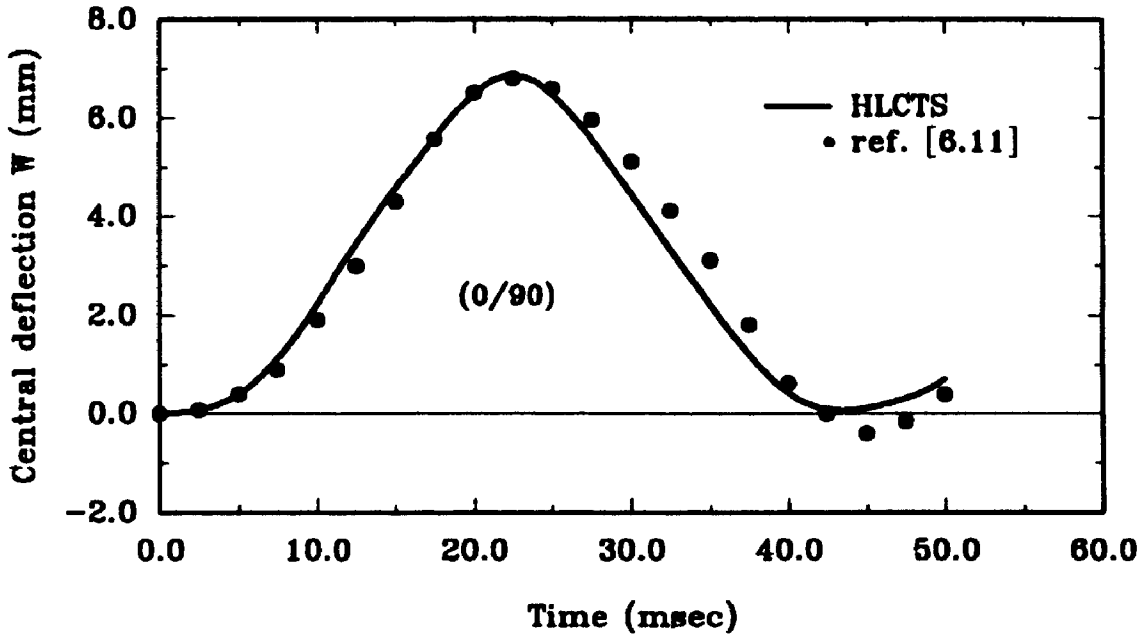

Figure 6.30 Transient response of a cross-ply plate under suddenly applied uniform load

6.4.1 Plates under uniformly distributed load

The square plate considered has two layers. Its geometrical dimensions are: side length a = 2.438 m and total thickness h = 0.00635 m. Each layer of the laminate has equal thickness. The plate stacking schemes are cross-ply (0/90) and angle-ply (45/-45). The layer material properties are: $E_2 = 6.8974 \times 10^{10}$ N/m^2, $E_1 = 25\ E_2$, $G_{12} = G_{13} = 0.5\ E_2$, $G_{23} = 0.2\ E_2$, $\nu_{12} = 0.25$ and density $\rho = 2498.61$ kg/m^3.

It is supported by hinges at its four edges. At these edges U or V parallel to the

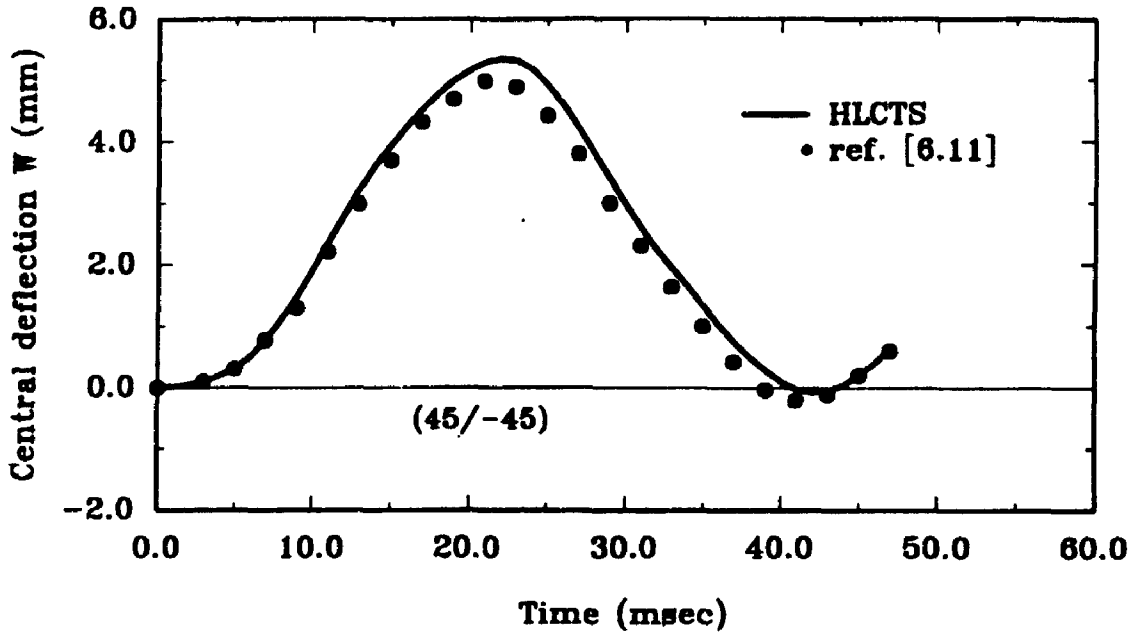

Figure 6.31 Transient response of a angle-ply plate under suddenly applied uniform load

edges are not constrained. These boundary conditions are denoted as BC1 in reference [6.11]. For the purpose of direct comparison with the results reported in the latter reference, one quarter of the plate is modeled by a 4 × 4 D mesh (see Figure 6.13 for the plate and Figure 3.7 for 4 × 4 D mesh). Thus, the boundary conditions applied are: $V = \Theta_x = 0.0$ at AB, $U = W = \Theta_x = 0.0$ at BC, $V = W = \Theta_y = 0.0$ at CD and $U = \Theta_y = 0.0$ at AD. In addition, all Θ_z are constrained. There are 158 unknowns in this case.

The uniformly distributed transversal step load with intensity $p_0 = 490.5$ N/m^2

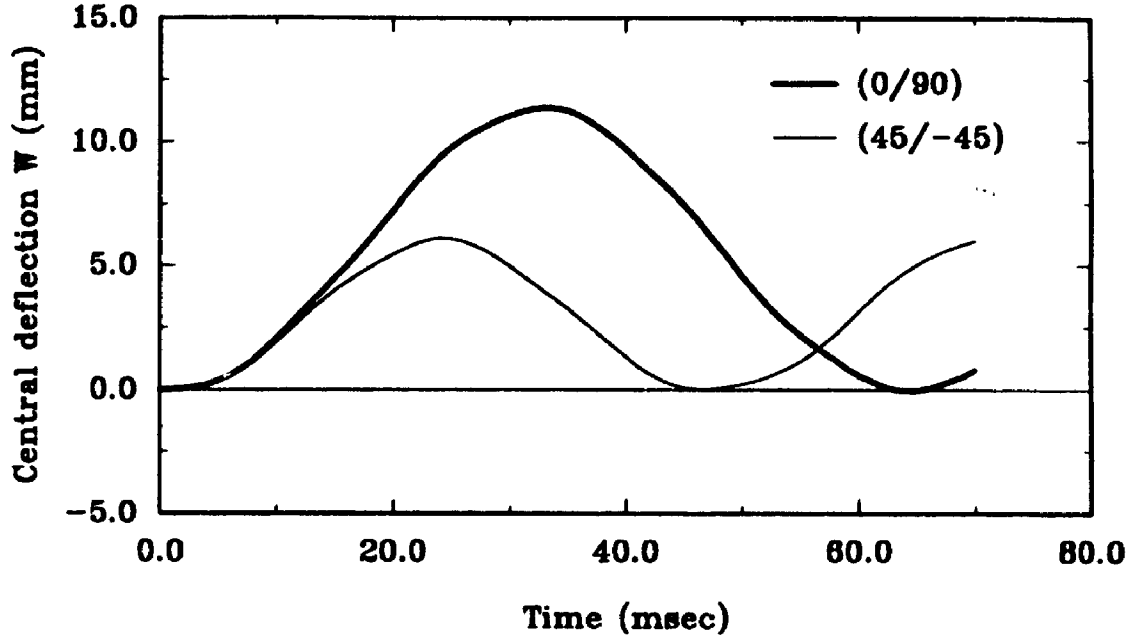

Figure 6.32 Comparison of the responses of cross-ply and angle-ply plates

is applied to the plate. Firstly, the (0/90) cross-ply plate is analyzed. In the analysis, the option of inclusion of directors and small strain are selected. The time step size is Δt = 0.001 seconds. The responses at the centroid obtained by using the HLCTS element are plotted in Figure 6.30. They are compared with those reported in reference [6.11]. In the latter the element adopted is a nine-node rectangular isoparametric element, which considers transverse shear and large rotations. Secondly, the (45/-45) angle-ply plate is solved with the same boundary and loading conditions, but using just the bending part of the HLCTS element. That is, all U, V and Θ_z are ignored. This choice is also made in

reference [6.11]. Thus, the results obtained with the proposed element can be compared with those taken from the latter reference. They are presented in Figure 6.31. The results from reference [6.11] were also obtained by using just the bending part of the element.

The two layers cross-ply and angle-ply plates are also considered under simply supported boundary conditions. These boundary conditions have been described in subsection 6.2.2. Here, all Θ_z are constrained. The number of unknowns are 160. With the 4 × 4 D mesh and uniformly distributed transversal step load described in the foregoing, the problems are solved. The HLCTS element results are given in Figure 6.32.

6.4.2 Cylindrical panels under internal pressure

A laminated cylindrical panel is shown in Figure 6.33. Two ply arrangements for the panel are considered. The first is the eight layers symmetrically laminated $(0/-45/90/45)_{sym}$ panel and the second is the two layers cross-ply (0/90) panel. Equal layer thickness is assumed. The pertinent geometrical data are: radius R = 2.54 m (100 in), arc length a = 0.508 m (20 in), length b = 0.508 m (20 in) and total thickness h = 0.00127 m (0.05 in) while φ = 0.1 rad. The material selected is graphite-epoxy. The material properties are:

$E_1 = 1.3790\times10^{11}$ N/m^2 (2.0×10^7 psi);

$E_2 = 9.8599\times10^9$ N/m^2 ($1.43\cdot10^6$ psi);

$G_{12} = G_{13} = G_{23} = 5.2402\times10^9$ N/m^2 (0.76×10^6 psi);

Poisson's ratio $\nu_{12} = 0.3$; and

density ρ = 1562.2 kg/m^3 (0.146×10^{-3} lb-sec^2/in^4).

The cylindrical shell panel is clamped at its curved and straight edges. One quarter

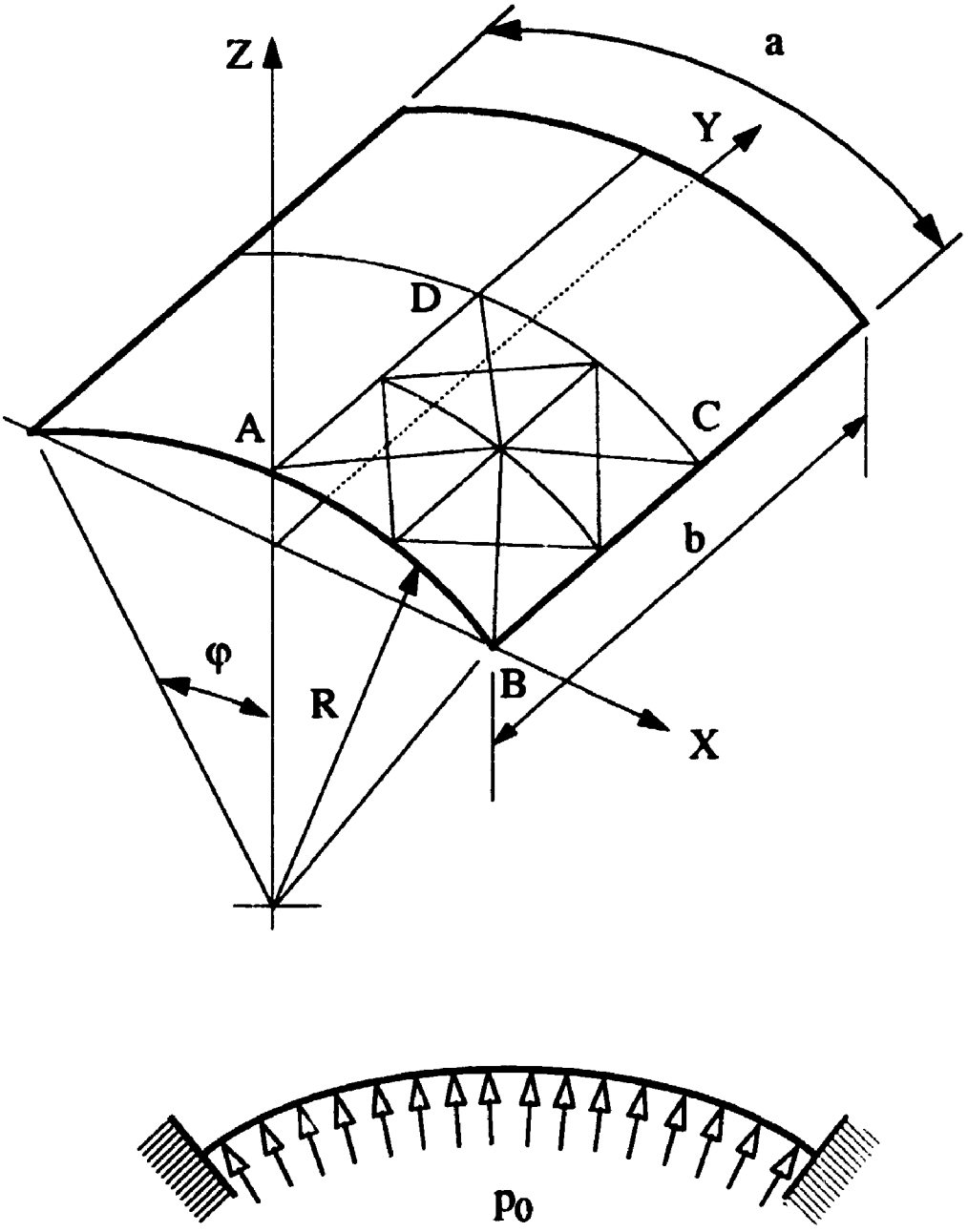

Figure 6.33 A clamped cylindrical panel under internal pressure

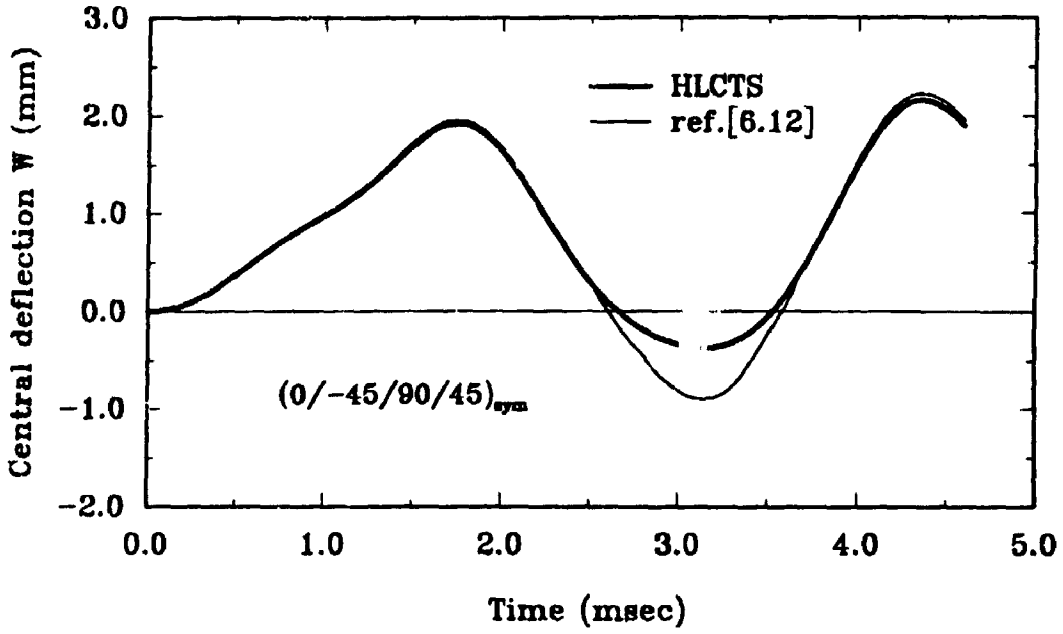

Figure 6.34 Transient response of a eight layers cylindrical panel under suddenly applied step internal pressure

of the panel is modeled by a 4 × 4 D mesh. The boundary conditions imposed on the finite element model are : $V = \Theta_x = 0.0$ at CD, $U = \Theta_y = 0.0$ at AD and all DOF are constrained at AB and BC. In this case, all Θ_z are also constrained. The total unknowns are 144. An internal step pressure with intensity $p_0 = 6895.0$ N/m^2 (1.0 psi) is applied to the panel.

The results shown in Figure 6.34 are transient responses at the centre of the eight layers cylindrical shell panel. In the figure, HLCTS denotes the results obtained by

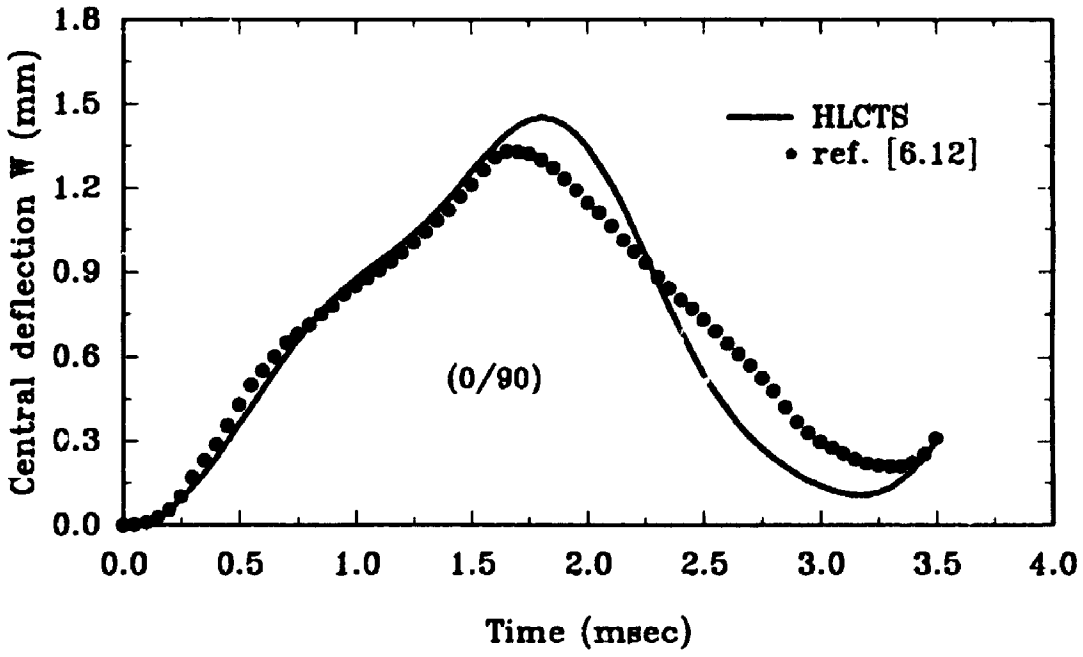

Figure 6.35 Transient response of a two layers cross-ply cylindrical panel under suddenly applied step internal pressure

employing the HLCTS element with the options of directors and large strain. The result from reference [6.12] were obtained with a curved high-order quadrilateral shell element and one quarter of the shell panel with a 2 × 2 mesh was considered. This element has 48 DOF and was developed based on the classical lamination theory. The present results are all obtained by using the trapezoidal integration scheme with a time step $\Delta t = 0.05$ msec. Both sets of results in the figure show excellent agreement. For the two layers cross-ply shell panel, the HLCTS element results are compared in Figure 6.35 with those

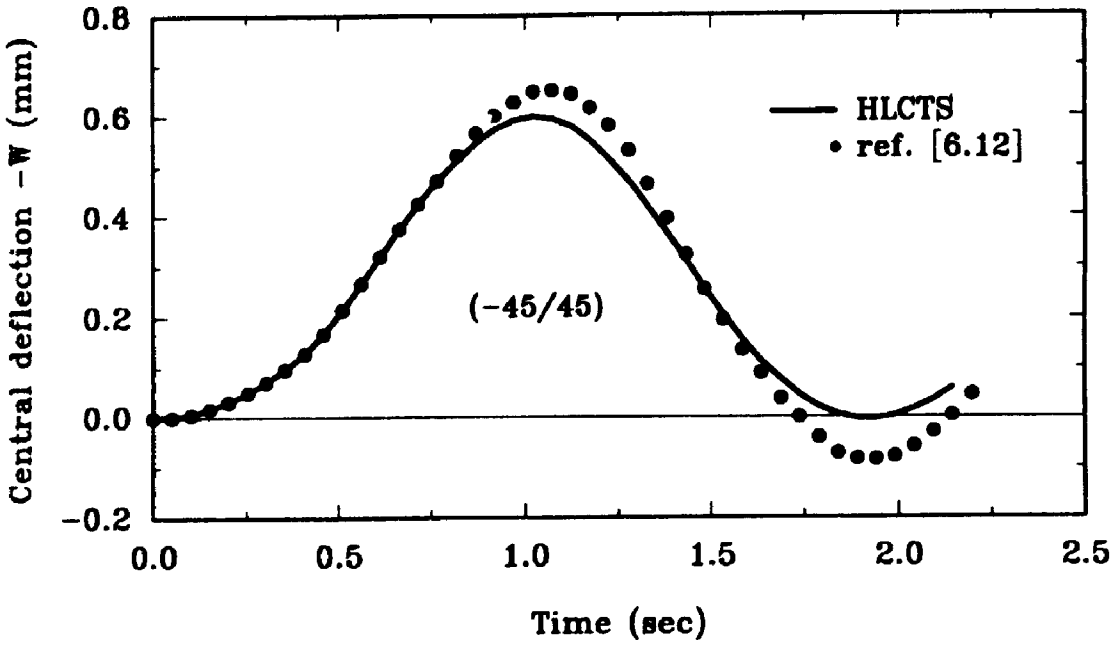

Figure 6.36 Transient response of a two layers angle-ply spherical shell segment under suddenly applied pressure load

from reference [6.12].

6.4.3 Spherical shell segments subjected to step loads

Two laminated spherical shell segments are considered. Their geometries are similar and both are simply supported. However, they are constructed with different materials and lamination schemes. Figure 6.20 shows the geometry of the laminated spherical shell segments. The geometrical properties are: radius R = 10.0 m, the side

length of the projected plane is b = 0.9996 m and the total thickness is h = 0.01 m.

The spherical shell segment is first considered having two equal thickness layers and they have the (-45/45) lamination scheme. The pertinent material properties are: $E_1 = 2.5\times10^{11}$ N/m^2, $E_2 = 1.0\times10^{10}$ N/m^2, $G_{12} = G_{13} = 0.5\times10^{10}$ N/m^2, $G_{23} = 0.2\times10^{10}$ N/m^2, Poisson's ratio $\nu_{12} = 0.25$ and density $\rho = 1.0\times10^{8}$ kg/m^3. One quarter of the shell is modeled by the HLCTS element with the 4 × 4 D mesh. The boundary conditions have been explained in subsection 6.2.4. The number of equations to be solved is 189. A distributed step pressure is applied to its outer surface (pointing toward the outer surface). It has an intensity $p_0 = 2000.0$ N/m^2. The time step used is 0.03 seconds. By using the same options as for the cylindrical panel, the nonlinear transient response at the apex (central point A of the shell segment) is obtained and plotted in Figure 6.36. The problem has been solved in reference [6.12] by utilizing the same curved high-order quadrilateral shell element quoted in last subsection. The results from reference [6.12] are reproduced in Figure 6.36 for comparison. It is observed that there is a discrepancy of about 8%, with respect to the HLCTS element results, for the amplitudes between the two set of results. However, they have the same vibration period.

The second spherical shell segment has the stacking sequence (0/90/0/90/0/90/0 /90/0). The thickness of the 0 degree layers is h/10 and of the 90 degree layers is h/8. The layer material properties for this shell are the same as those used in subsection 6.2.4. Two different step loadings are considered for this case. One is similar to the two layers angle-ply spherical shell segment described above. The another is a concentrated step load with $P_0 = 2000.0$ N applied at the apex and pointed downwards. In the trapezoidal direct integration process, a time step of 0.0004 seconds is used. The nonlinear transient

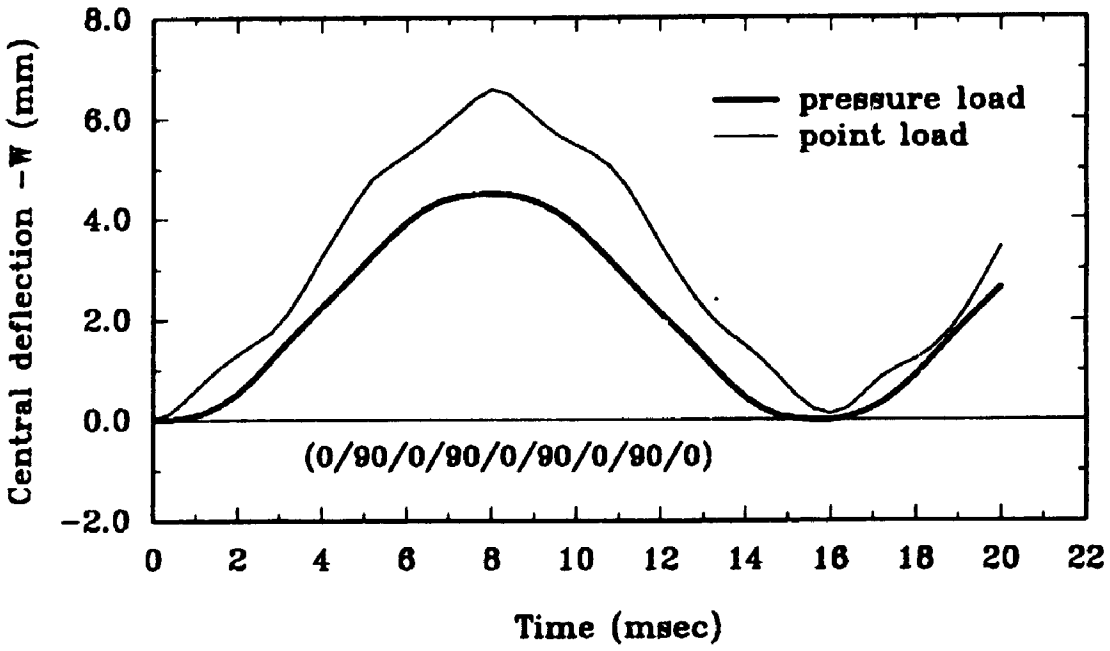

Figure 6.37 Comparison of the transient responses of a nine layers cross-ply spherical shell segment under different loadings

responses calculated for the central point A are given in Figure 6.37. It is seen that the vibration amplitudes are much higher than those of the two layer angle-ply shell segment. The concentrated step load causes even larger vibration amplitude at the central point A than that due to the distributed pressure.

6.4.4 Cantilever panel with a step moment applied to the free end

The finial case considered is a four layer cross-ply cantilever panel. It is

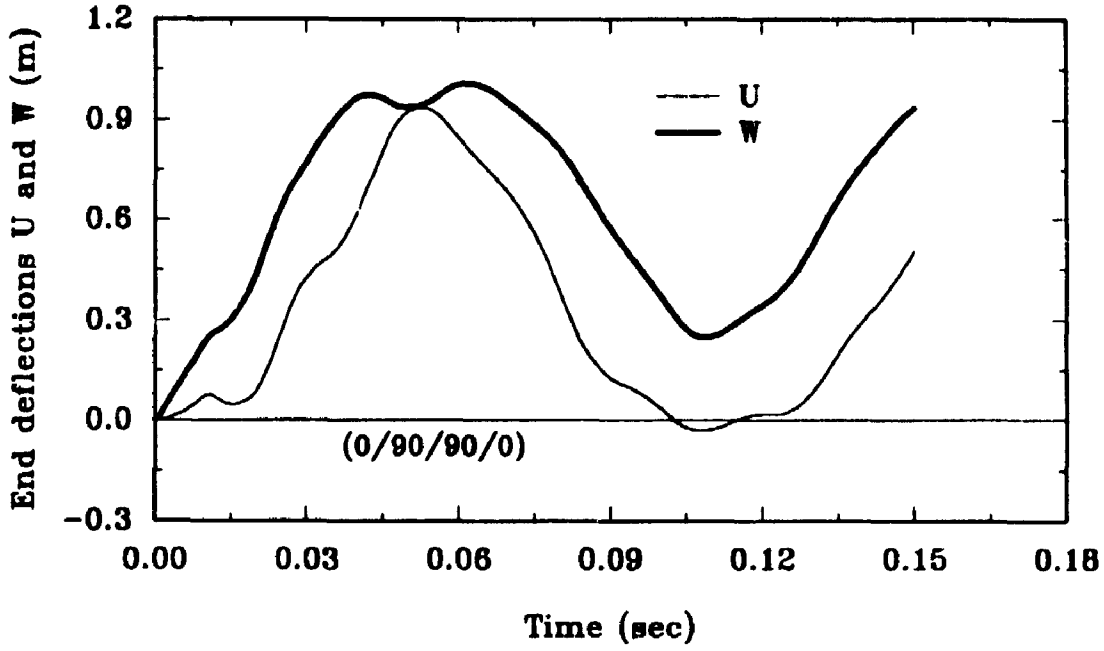

Figure 6.38 Transient response of a cross-ply cantilever beam with a step moment applied at the free end

symmetrically laminated with the stacking scheme (0/90/90/0). Its geometries have been depicted in Figure 6.1(a). They are: L = 1.2 m, b = 0.1 m and h = 0.01 m. The material used for this cantilever is the high modulus graphite/epoxy composite. Its material properties are: $E_1 = 2.0685\times10^{11}$ N/m^2, $E_2 = 5.1713\times10^{9}$ N/m^2, $G_{12} = 3.1028\times10^{9}$ N/m^2, $G_{13} = G_{23} = 2.5856\times10^{9}$ N/m^2, $\rho = 1605$ kg/m^3 and Poisson's ratio $\nu_{12} = 0.25$. A step moment M about an axis parallel to the width of the panel is applied to the free end. The amplitude of this moment is $m_0 = 1000.00$ N-m.

As shown in Figure 6.1(b), the panel is discretized by a 12 × 1 A mesh. At the fixed end, all DOF are constrained. The remaining nodes are constrained in two different ways. Firstly, $V = \Theta_x = \Theta_z = 0.0$ are imposed and secondly all DOF are free. These two finite element models have 72 (denoted as model 1) and 144 (denoted as model 2) unknowns, respectively.

For model 1, the time step $\Delta t = 0.001$ sec is employed in the trapezoidal direct integration. The nonlinear transient responses at the end of the cantilever are solved by selecting the options of director included, small strain and constant thickness. The total numbers of iterations are 15. The computed end deflections are plotted in Figure 6.38. When iterations are suppressed, the HLCTS element predicts a slightly smaller period for the nonlinear responses and encountered some numerical difficultic after the first period. These results are included in Figure 6.39. From Figures 6.38 and 6.39 one can see that the peak values of W have reached about 1.0 m which is 100 times of the thickness of the cantilever panel. The deflections and rotations are considerably large. In this case, the inclusion of directors in the formulation is crucial as the direc'ors are important parameters that constitute the so-called "exact geometry" for large rotation problems. Figure 6.40 shows the effects, with or without directors, on the responses in addiuon to small strain and constant thickness options. Without the directors, the solution process fails at t = 0.08 sec. While the displacements and rotations are very large, the strain level of this problem is still within the "small strain" range. Figure 6.41 reveals that the options of small strain and finite strain formulations lead to almost identical solutions. In these strain formulations the directors are included and thicknesses are kept constant. The deflection W in Figure 6.38 is compared with the linear solution in Figure 6.42. The

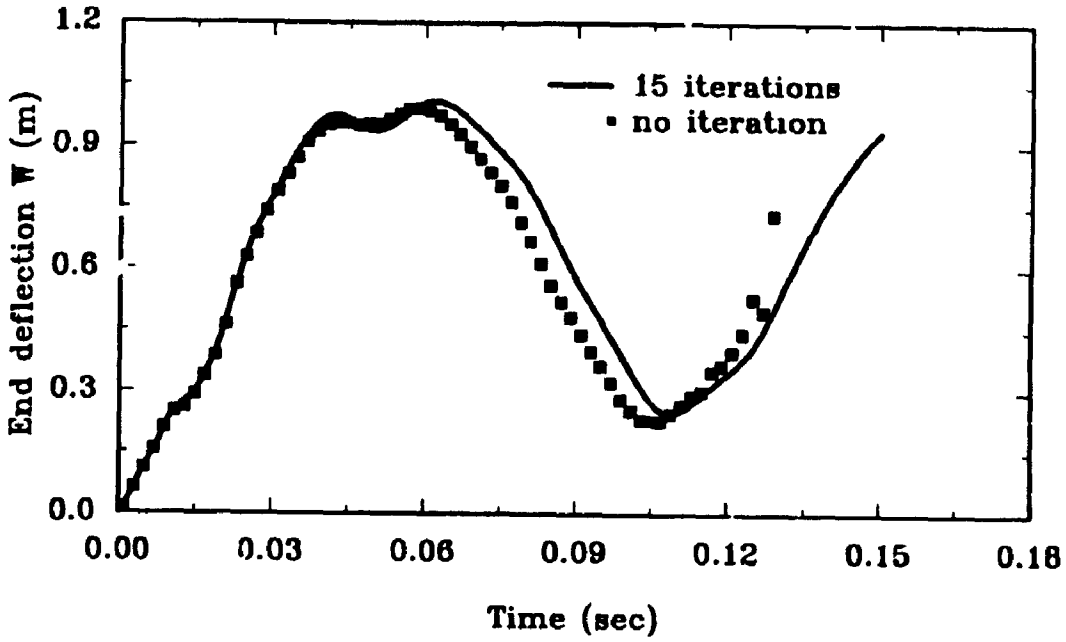

Figure 6.39 Comparison of the results obtained with and without iterations

peak value of the linear solution with the same free end moment for the nonlinear solution is much larger than the length of the panel. Theoretically, the linear solution is valid if it peak value is within 5% of the length of the panel. Clearly, this is not the case.

For model 2, the time step $\Delta t = 0.0005$ sec is used. There is one iteration for every ten steps. To compare with the results presented in Figure 6.38, the same options as for Figure 6.38 are selected. The results obtained by using model 2 are plotted in Figure 6.43 together with those from Figure 6.38. Since in model 1, the stretching in the Y direction has been constrained, that is $V = 0.0$, it is more stiff than model 2.

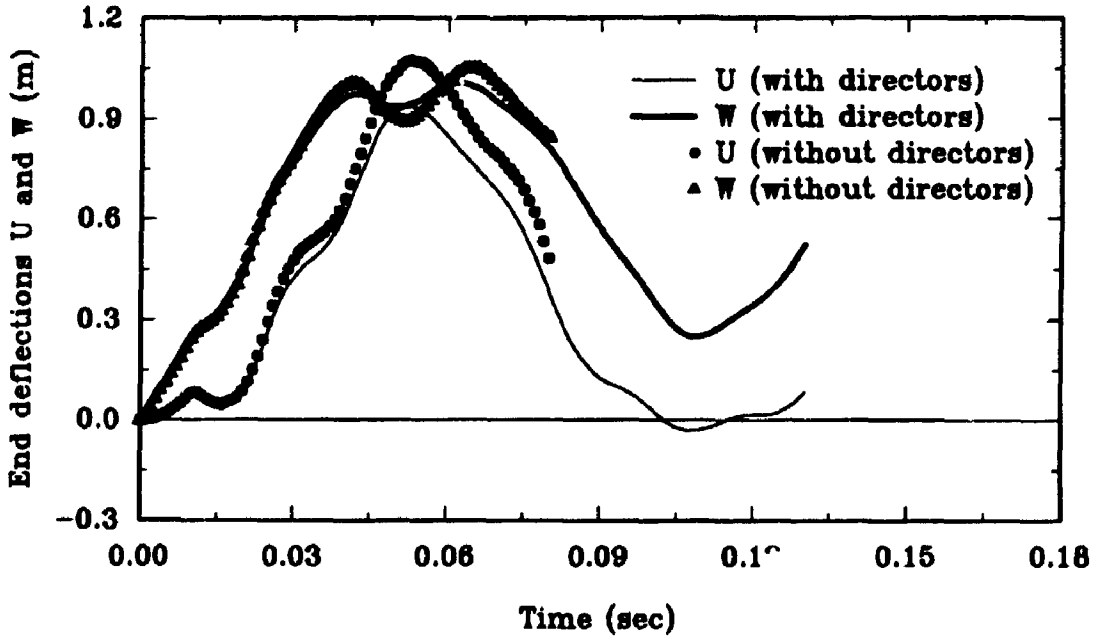

Figure 6.40 Comparison of the results obtained with and without including directors

However, the difference is not very significant. The small and finite strain options are also tested for model 2. The results are given in Figure 6.44. The same finding as for Figure 6.41 has been confirmed.

In addition to the inclusion of directors and small strain options, the updated thickness option is adopted for the calculation by using model 2. The results are shown in Figure 6.45. Owing to the thinning effect, the panel appears to be softer and larger deflections have been predicted. This is clearly illustrated in Figure 6.45.

Apparently, model 2 is more realistic. However, the number of unknowns is

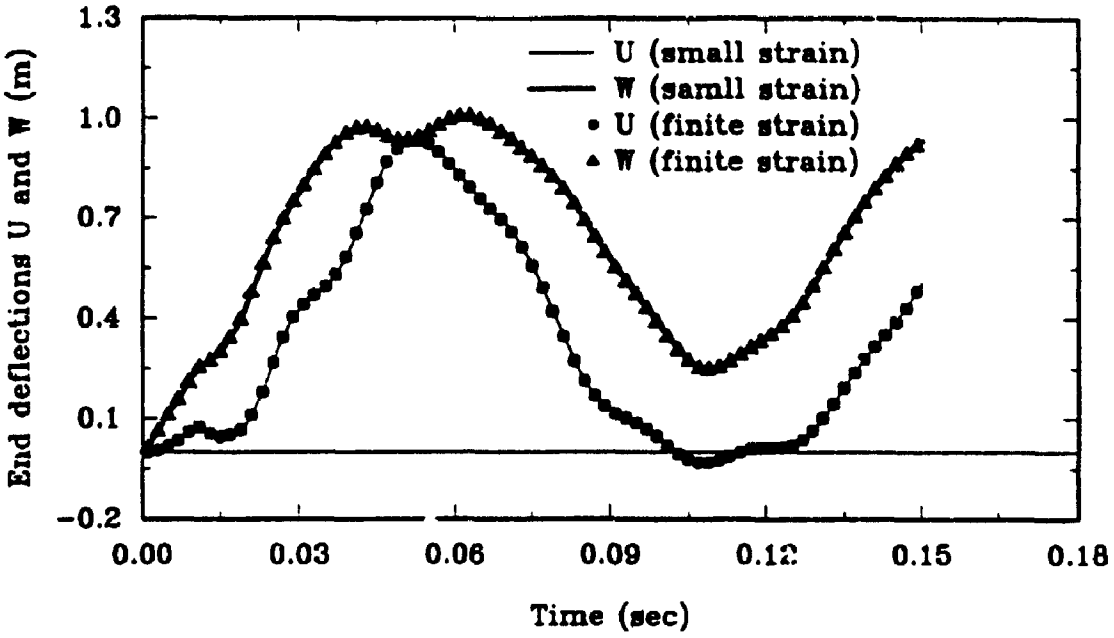

Figure 6.41 Comparison of the results obtained with small and finite strain options

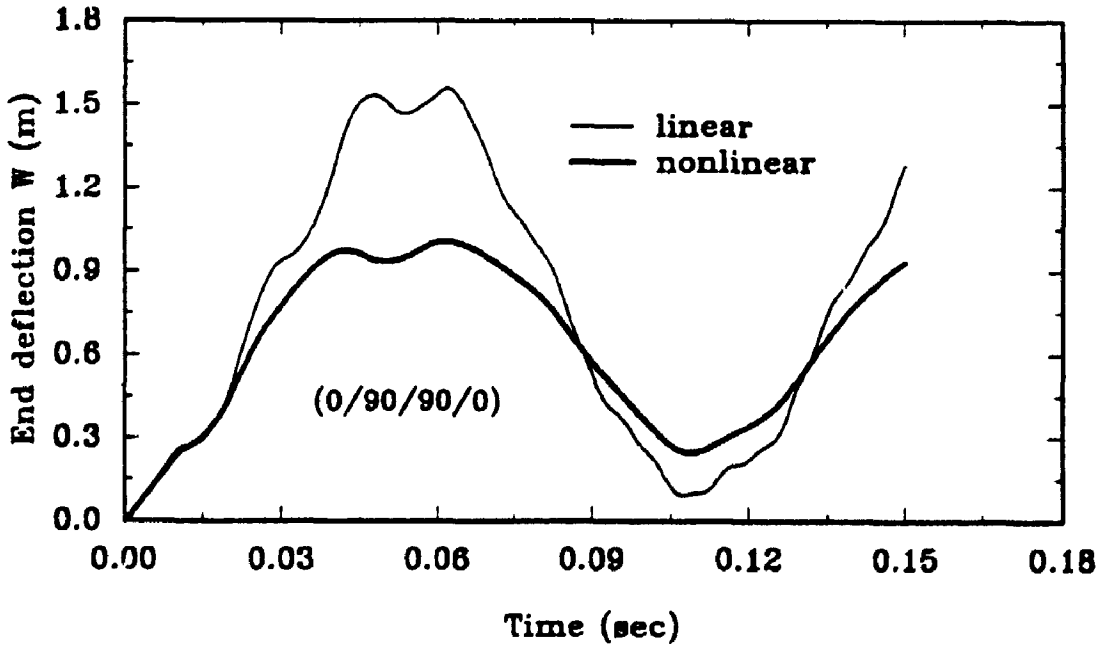

Figure 6.42 Comparison of the results obtained by linear and nonlinear analysis

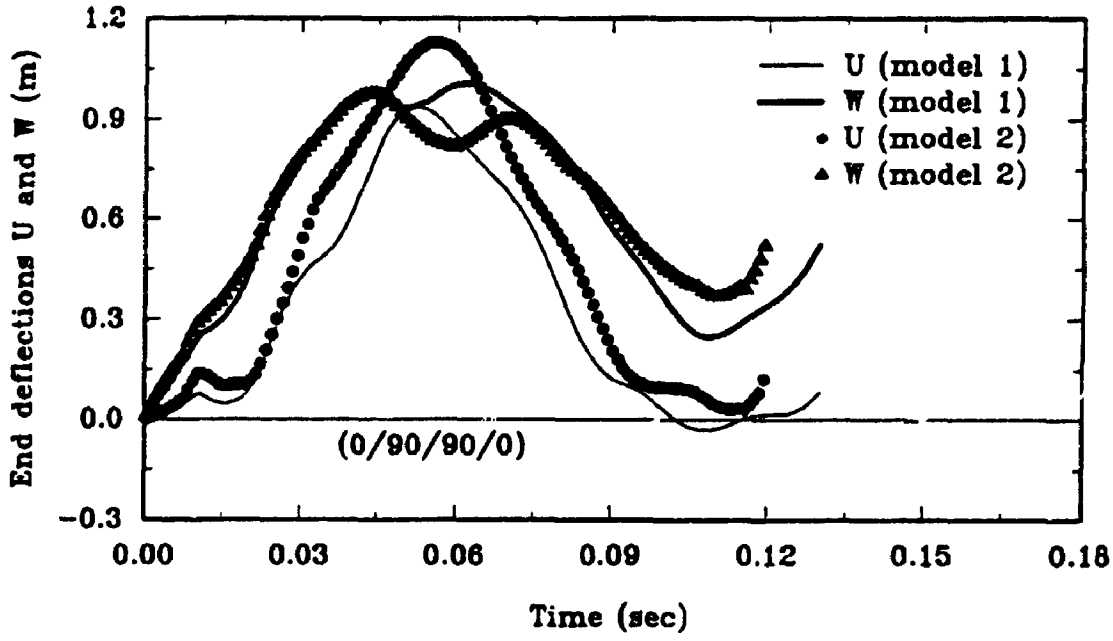

Figure 6.43 Comparison of the results from model 1 and model 2

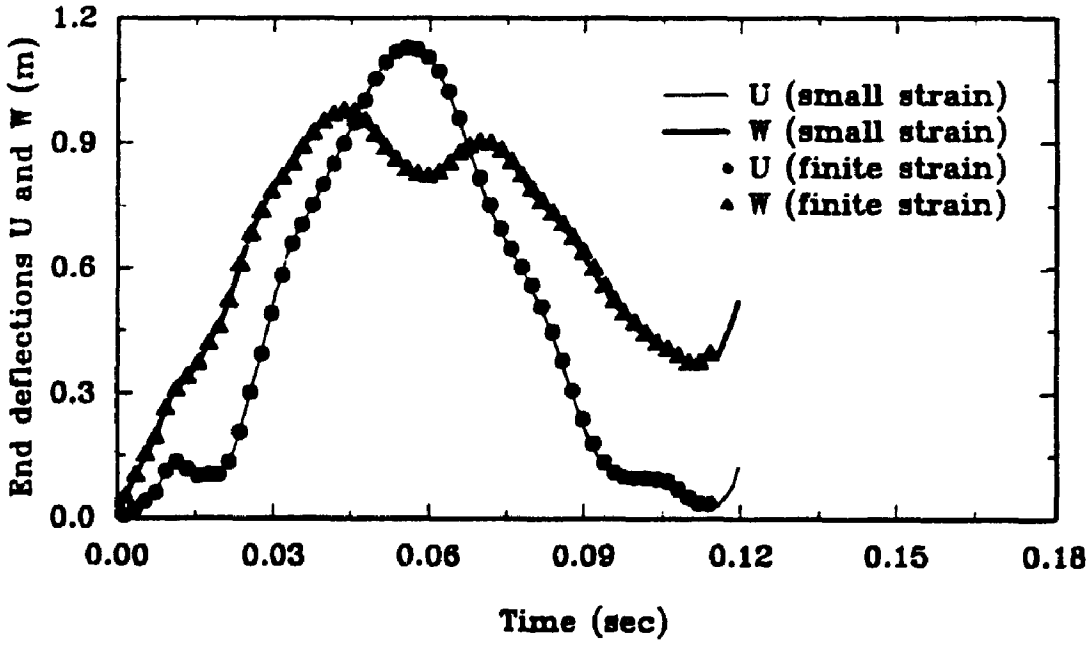

Figure 6.44 Comparison of the results obtained by using model 2 with small and finite strain options

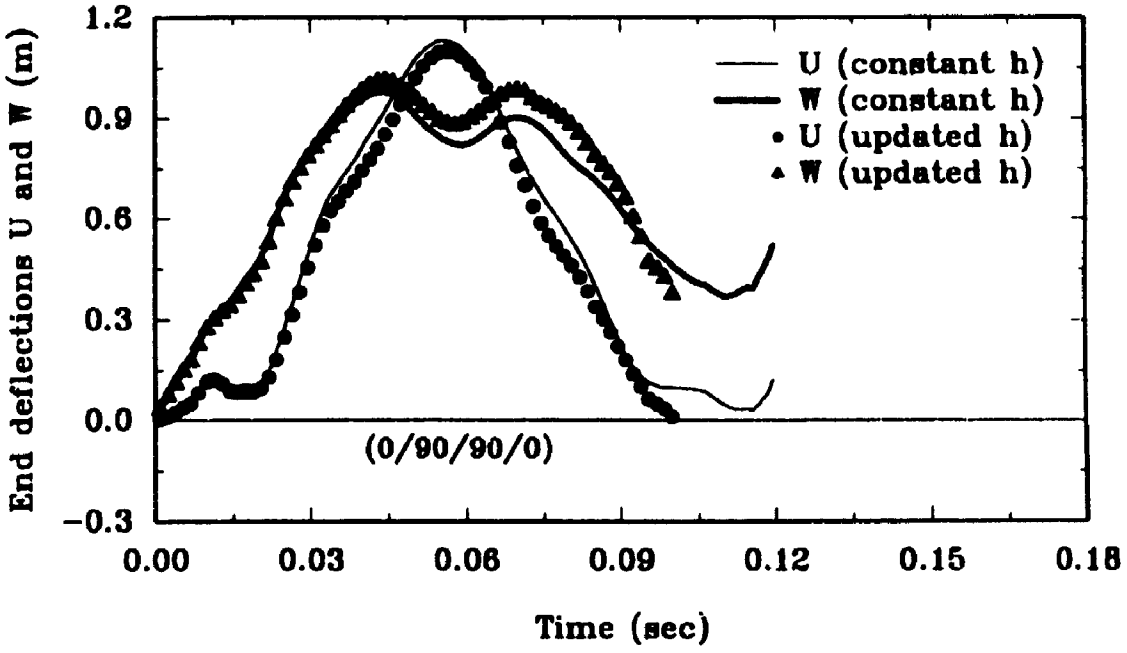

Figure 6.45 Comparison of the results obtained with constant and updated thickness options

doubled. Thus, the computational time required for their solutions is longer. Furthermore, unknowns along the Y axis are much smaller than those along the X and Z axes in this case. Therefore, the equations to be solved may be ill-conditioned. To circumvent this problem smaller time steps are required for the numerical integration. Therefore, from the computational efficiency point of view, model 1 seems to be a better choice. Of course, if the axis of applied step moment is not parallel to the width of the panel model 2 should be be used in order to provide realistic and accurate solutions.

Finally, a pictorial description of the evolution of the deformed panel is presented, for clarity, in Figures 6.46(a) and 6.46(b). Figure 6.46(a) depicts the evolution from t = 0.0 to t = 0.05 sec. At t = 0.0, the panel is undeformed and at t = 0.05 the deflection approaches the peak value. The configurations presented in Figure 6.46(b) are from t = 0.06 to 0.11 sec, which show the deformed panel bouncing back from its peak value.

6.5 Remarks

The HLCTS elements for the analysis of geometrically nonlinear laminated composite plates and shells have been employed to solve various static and dynamic problems. Before leaving this chapter, the following main observations and remarks should be noted:

(1) The HLCTS elements have been employed to solve various static and dynamic problems. These geometrically nonlinear problems include single layer isotropic plate and shell structures and multilayer laminated composite plates and shells. Relatively comprehensive case studies have been performed. The majority of results obtained by using the HLCTS elements have been compared with those available in the literature. The comparisons have validated the correctness of the results obtained and shown the accuracy and efficiency of the proposed elements.

(2) In the case of large rotations (see for examples, the cantilever panel subjected to an end moment in subsections 6.1.1 and 6.4.4) the option of including directors in the formulation gives better results in terms of faster convergence and higher accuracy. In some cases the incorporation of directors is critical. See for example, the case studied in subsection 6.4.4. In the large deformation problems with small rotations, the computed

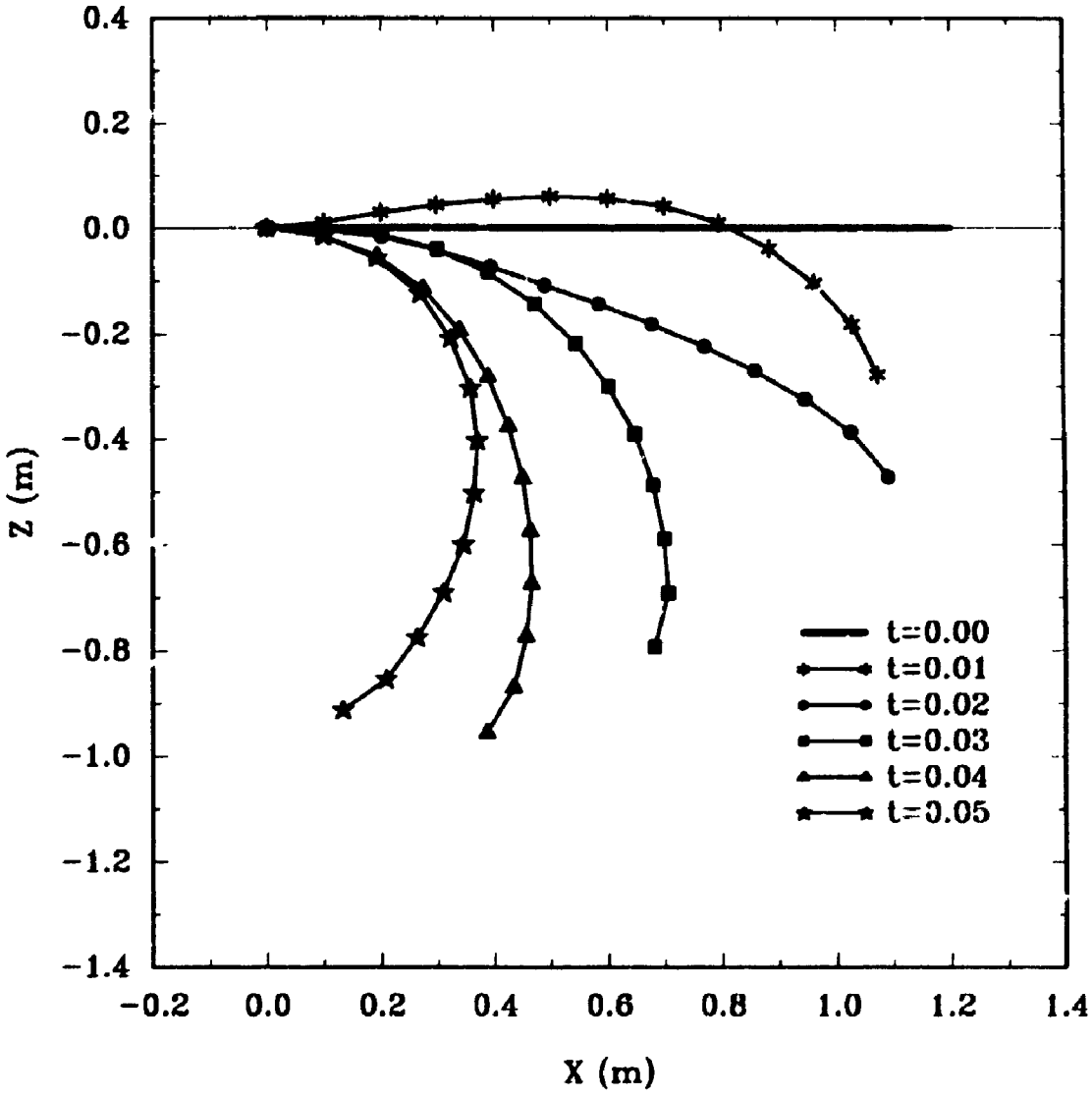

Figure 6.46(a) Deformed configurations of the cantilever panel during the evolution of nonlinear transient response

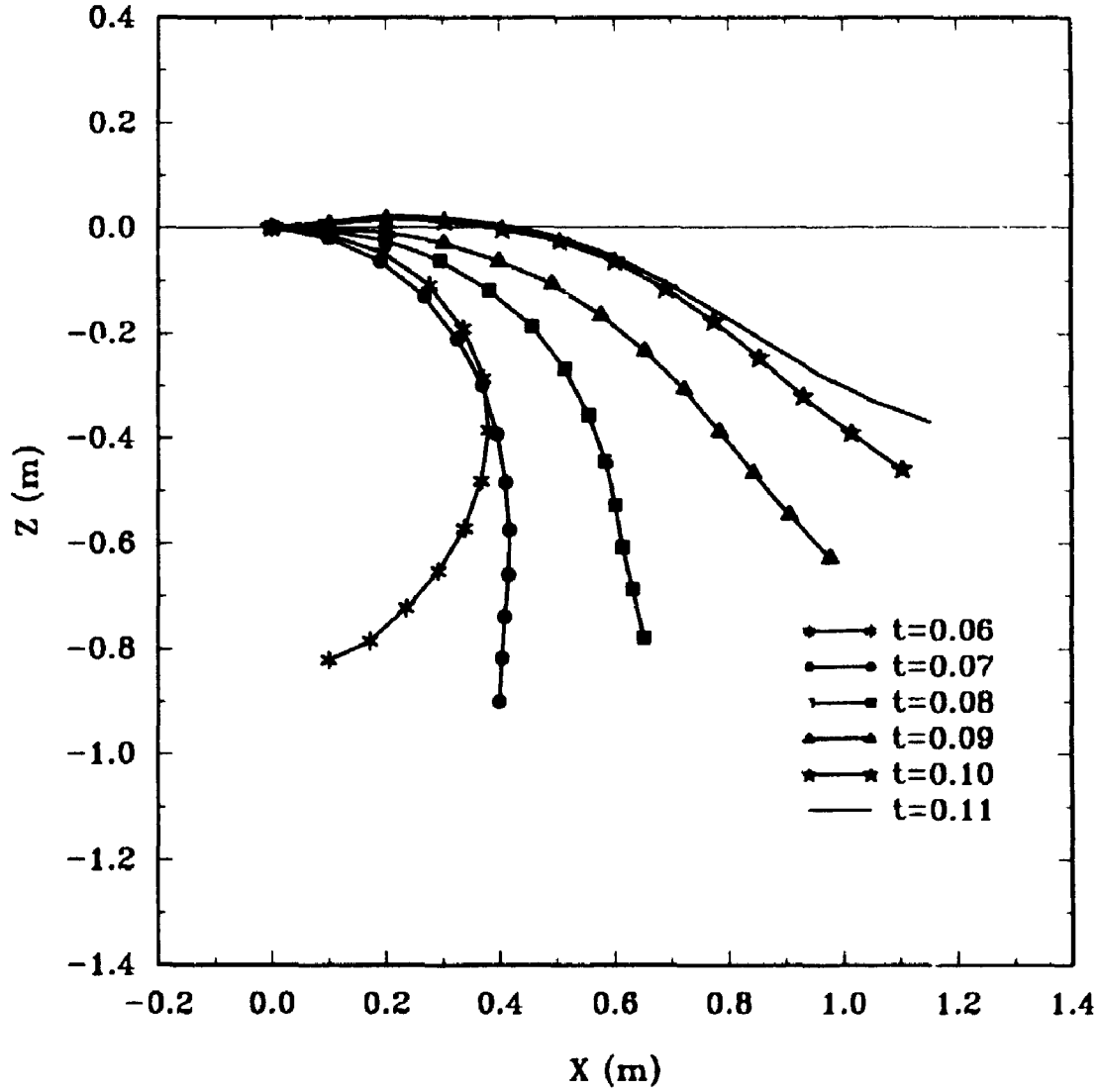

Figure 6.46(b) Deformed configurations of the cantilever panel during the evolution of nonlinear transient response

results predicted by using the elements with or without directors have no significant differences. Thus, problems in this category can disregard directors such that computational time can be saved.

(3) The computed results seem to suggest that all geometrically nonlinear problems studied in the literature and quoted in the present investigation are within the range of small strains. However, the incorporation of finite strain deformation in the HLCTS element formulation can be included in cases with deformations in the plastic range. Therefore, the HLCTS elements can be extended and modified to analyze problems with elastic-plastic deformations.

(4) Shear locking has not appeared in the results obtained thus far. This is a further proof of the excellent performance capability of the HLCTS elements developed.

(5) As the improved DDOF formulation has been considered, there is no zero energy mode detected in the problems studied in this chapter that employs the particular member of the HLCTS elements.

CHAPTER 7

CONCLUSIONS AND RECOMMENDATIONS

This chapter concludes the current investigation. It is divided into three sections. The first section summarizes the development and studies performed on the finite element analysis of linear and geometrically nonlinear laminated composite plate and shell structures. The second presents the conclusions of this investigation. The third section proposes the recommendations for further investigations.

7.1 Summary

In this investigation, the review shows that the understanding of mechanical and structural behaviours of laminated composite plate and shell structures and developing of simple, accurate and efficient finite elements for analyzing such structures is far from adequate. The complexity in the linear and nonlinear analysis of laminated composite shell structures requires more efforts in developing efficient computing strategies. To keep up with the booming applications of laminated composite materials for shell structures in modern industries, theories and computational models for finite element analysis of linear and geometrically nonlinear laminated composite plate and shell structures were studied and developed. This development had led to the derivation of new elements. Consequently, linear and geometrically nonlinear laminate composite plate and shell structures were analyzed. The considerations of large deformations of large rotations and finite strains were emphasized throughout the investigation. Static and dynamic responses

of such structures under various lamination schemes, boundary and loading conditions were evaluated. The investigation consisted of two phases. The first phase focused on linear analysis and the second concentrated on nonlinear analysis.

In the linear analysis, a series of simple three-node, six DOF per node, hybrid strain based flat laminated composite triangular shell finite elements were developed. They were based on the degenerated three dimensional solid concept. The first order shear deformation theory was adopted. The element matrices were obtained explicitly by using a combination of manual and computer assisted algebraic manipulations. Among these elements, the hybrid strain based BT derived in Section 2.5 has six fundamental DOF at each of its nodes. These six DOF include the DDOF. Because of the absence of the in-plane shear strain energy due to the skew symmetric part of the in-plane shear strain from the total potential energy equation, the DDOF formulation in the BT is not complete. To enhance the DDOF in the BT elements, the skew symmetric part of the in-plane torsional shear strain was considered. This accounted for the contribution from θ_t. The resulting element stiffness matrices k_{dh} and k_{dd} in Section 2.6 are thus hinged on a more sound theoretical basis. The numerical studies in Chapter 3 and 4, had shown that the proposed laminated composite shell elements with enhanced DDOF gave the best performance. The HLCTS elements developed for the linear static analysis are summarized and identified as follows:

(1) HLCTS^{lh} $k_e^{lh} = k_e^{l} + k_{dh}$, linear w in BT + hybrid DDOF;

(2) HLCTS^{qh} $k_e^{qh} = k_e^{q} + k_{dh}$, quadratic w in BT + hybrid DDOF;

(3) HLCTS^{ld} $k_e^{ld} = k_e^{l} + k_{dd}$, linear w in BT + displacement DDOF;

(4) HLCTS^{qd} $k_e^{qd} = k_e^{q} + k_{dd}$, quadratic w in BT + displacement DDOF.

Each of the element stiffness matrices consists of two parts. One is from the BT, and the other is the independently formulated DDOF. Comparing the four elements, $HLCTS^{qd}$ is the most favourable element with respect to accuracy and rank sufficiency. $HLCTS^{ld}$ and $HLCTS^{qd}$ are rank sufficient since the displacement formulation of DDOF is equivalent to employing three strain parameters in the strain field if the hybrid formulation is performed. In this sense, $HLCTS^{ld}$ and $HLCTS^{qd}$ provide no inconsistency to the hybrid formulation though the displacement type DDOF was adopted. As $HLCTS^{qd}$ was formulated by assuming a quadratic fi d for w, it improved the accuracy over the $HLCTS^{ld}$.

For the linear dynamic analysis, element consistent mass matrices were developed. These element mass matrices were formulated with the options of considering or not considering moment of inertia and the polar moment of inertia. Using these element mass matrices and the element stiffness matrices derived in Chapter 2, six elements for vibration analysis of laminated composite plate and shell structures were formed. These elements are denoted by $HLCTS_r^{qd}$, $HLCTS_r^{ld}$, $HLCTS_r^{qh}$, $HLCTS_r^{lh}$, $HLCTS_t^{qd}$ and $HLCTS_t^{qh}$. Together with the element stiffness matrices developed in Chapter 2, the HLCTS elements are all in explicit expressions. There is no numeric' inversion and integration involved.

The HLCTS elements developed in Chapter 2 have been used to study an extensive collection of single layer, multilayer plate and shell structures in Chapters 3 and 4. The structures analyzed were considered under different types of loadings with various boundary conditions and lamination schemes. In the linear dynamic analysis, the study was concerned with free vibrations. The results obtained in the analysis were compared

with those analytical and numerical solutions whenever they are available in the literature so as to ensure the validity of the HLCTS element results. Detailed information on geometrical and material properties of the structures, loadings and boundary conditions were given in every example.

In the second phase, geometrically nonlinear problems were investigated. Theories and the finite element formulations for the analysis of geometrically nonlinear laminated composite shell structures were presented in Chapter 5. The emphasis has been on establishing a sound theoretical basis for the formulation of simple and efficient finite elements for large scale geometrically nonlinear analysis of laminated composite shell structures. In the finite element formulations, the updated Lagrangian description has been adopted. The consideration of reducing the algebraic manipulations in obtaining element matrices to a minimum was one of the major reasons for using updated Lagrangian description. Consequently, the element linear and nonlinear stiffness matrices, the element consistent mass matrix and the pseudo-load vector have all been obtained explicitly. In particular, the element developed for the analysis of geometrically nonlinear laminated composite plate and shell structures was based on the $HLCTS_r^{9d}$ element proposed in Chapter 2 and Chapter 4 for linear analysis. It is an extension of the work in reference [5.1] which is for the analysis of isotropic shell structures. The element has independently assumed incremental strain and displacement fields. The formulation has considered many important aspects of geometrical nonlinear analysis of laminated composite structures, such as, transverse shear deformation, large deflection of finite strain and large rotation. The finite element procedure developed here is also capable of dealing with the "thinning" effect and handling cases in which the directors are not unique or difficult to evaluate.

To verify the effectiveness and simplicity of using the element proposed, applications of the element for various geometrically nonlinear static and dynamic problems were made and presented in Chapter 6.

7.2 Conclusions

The investigation has explored the theories, computational models and strategies for static and dynamic analysis of linear and geometrically nonlinear laminated composite plate and shell structures. A series of simple three-node, six DOF per node, hybrid strain based laminated composite triangular shell finite elements have been developed. The followings are the conclusions drawn from the investigation.

(1) The HLCTS elements are more accurate and converge faster when compared with other low-order finite elements. In some cases they can even be compared favourably with high-order elements. A relatively large collection of linear and geometrically nonlinear problems were solved. Static and dynamic responses of such structures under various lamination schemes, boundary and loading conditions were evaluated. In the nonlinear analysis, structures were analyzed under the considerations of large deformations of large rotations and finite strains. "Thinning effects" were also examined. The results obtained in the analysis were compared with analytical or numerical solutions whenever they are available in the literature. The numerical results have demonstrated the excellent performance of the HLCTS elements in both linear and nonlinear analysis.

(2) The numerical studies confirmed that the HLCTS elements with quadratic displacement field for w are more accurate and converge faster than those with linear

field. Whether the moment of inertia is included or not it seems to have no significant effect on results of thin plate and shell structures studied in this investigation.

(3) The investigation showed that the presence of DDOF, the sound theoretical basis and straightforward approach in deriving DDOF are absolutely important in formulating low-order flat shell elements. The improved formulation of DDOF has eliminated the zero energy modes from the HLCTS elements. With the displacement formulation of DDOF, all three zero energy modes are eliminated from the HLCTS elements, while the hybrid formulation of DDOF eliminates one.

(4) No shear-locking phenomenon was detected in using the HLCTS elements. The hybrid strain formulation seems to be effective in eliminating shear locking which is problematic in lower-order finite elements derived from employing displacement formulation. However, inferior mesh design, topology or severely distorted meshes may induce shear-locking [3.18, 3.22]. The studies in the investigation also showed that mesh topology affected the accuracy of triangular finite element results. The consistent use of D type mesh in this investigation had proved that such mesh can provide excellent results.

(5) In the l ıear static analysis, among the four HLCTS elements, $HLCTS^{qd}$, $HLCTS^{ld}$, $HLCTS^{qh}$ and $HLCTS^{lh}$, and the two basic triangles, BT^{q} and BT^{l}, $HLCTS^{qd}$ and $HLCTS^{ld}$ are the most favourite ones in terms of both accuracy and rank sufficiency. However, this does not exclude the use of $HLCTS^{qh}$, $HLCTS^{lh}$, BT^{q} and BT^{l}. The results from free vibration analysis showed that $HLCTS_r^{qd}$ converges faster than $HLCTS_r^{ld}$. Therefore, the $HLCTS_r^{qd}$ element was further developed for geometrically nonlinear analysis of laminated composite shell structures.

(6) Each of the $HLCTS_r^{qd}$, $HLCTS_r^{ld}$ and $HLCTS_t^{qd}$ elements has six rigid-body

modes and have no zero energy modes. The $HLCTS_r^{qh}$, $HLCTS_r^{lh}$ and $HLCTS_t^{qh}$ elements have six rigid-body modes and two zero energy modes, while the BT^q and BT^l elements have six rigid-body modes and three zero energy modes. The zero energy modes are all associated with the in-plane torsional rotations. In other words, the BT elements developed in Chapter 2 have three zero energy modes, whereas the $HLCTS^{qh}$ and $HLCTS^{lh}$ elements have two zero energy modes. The $HLCTS^{qd}$ and $HLCTS^{ld}$ elements do not have any zero energy mode. Thus, the improved formulation of DDOF by the displacement approach introduced in subsection 2.6 has eliminated the spurious modes from the elements.

(7) All the linear and nonlinear elements proposed in this investigation were derived explicitly by using a combination of manual and symbolic computer algebra manipulations. The explicit expressions eliminate the error introduced by employing numerical inversion and integration. For brevity, these explicit expressions are not included in the thesis. However, they are documented in references [7.1, 2].

(8) In the case of large rotations (see for examples, the cantilever panel subjected to an end moment in subsections 6.1.1 and 6.4.4) the option of including directors in the formulation gives superior results in terms of faster convergence and higher accuracy. This is due to the "exact" geometrical description of a body undergoing large rotations. The latter have been realized by using exponential mapping. In the large deformation of finite rotation cases the incorporation of directors is crucial. See for example, the case studied in subsection 6.4.4. In the large deformation problems with small rotations, the computed results predicted by using the elements with or without directors have no significant differences. Thus, problems in this category can disregard the directors so that

computational time can be saved.

(9) The computed results seem to suggest that all geometrically nonlinear problems studied in the literature and quoted in the present investigation are within the range of small strains. However, the incorporation of finite strain deformation in the HLCTS element formulation has been a focus of the investigation. The obtained element can be modified to cases with deformations in the plastic range.

(10) Finally, it should be emphasized that the investigation reported in this thesis is believed to be the only relatively comprehensive work that incorporates linear and geometrically nonlinear static and dynamic analysis of laminated composite shell structures. It is also believed to be the first one that considers large deformations of finite strains as well as large rotations for the static and dynamic analysis of laminated composite shell structures by the hybrid strain based finite element method.

7.3 Recommendations

This investigation has covered a relatively wide range of problems on static and dynamic analysis of laminated composite plates and shell structures. However, the limited time has not allowed the study to be extended to other interesting aspects. The latter can be performed in the future and are listed here.

Firstly, to further improve and develop the computational procedure and enable it for solving snap-through, snap-back buckling, and post buckling problems, the developed digital computer program can be expanded. This is a very important aspect in the study of behaviours of laminated composite shell structures and programming techniques are currently available in the literature. Therefore, it is achievable and

deserves immediate attention.

Secondly, as the HLCTS element developed accounts for large deformations of large rotations and finite strains it can be extended to analysis of elasto-plastic problems.

Finally, large deformations of finite strains and plastic deformations of laminated composite shell structures frequently accompanied by very complicated local stress distributions and delaminations. To provide a means for their examinations layerwise theories and associated finite elements are required.

REFERENCES

1.1 I.Y. Shtayerman, *On the Theory of Symmetrical Deformation of Anisotropic Elastic Shells*, Izvestia Kievsk. Politekh. i Sel. Khoz. Inst. (in Russian), Book 1, Vol. 1, 54-72 (1924).

1.2 C.W. Bert, Research on dynamic behaviour of composite and sandwich plates -- V: Part I, *Shock Vib. Dig.* **23**(6), 3-14 (1991).

1.3 C.W. Bert, Research on dynamic behaviour of composite and sandwich plates -- V: Part II, *Shock Vib. Dig.* **23**(7), 9-21 (1991).

1.4 C.Y. Chia, Geometrically nonlinear behavior of composite plates: A review, *Appl. Mech. Rev.* **41**, 439-451 (1988).

1.5 R.K. Kapania, A review on the analysis of laminated shells, *J. Pressure Vessel Tech.*, ASME, **111**, 88-96 (1989).

1.6 A.K. Noor and W.S. Burton, Assessment of shear deformation theories for multilayered composite plates, *Appl. Mech. Rev.* **42**, 1-12 (1989).

1.7 A.K. Noor and W.S. Burton, Assessment of computational models for multilayered composite shells, *Appl. Mech. Rev.* **43**, 67-96 (1990).

1.8 A.K. Noor, Mechanics of anisotropic plates and shells--a new lool. at an old subject, *Comput. Struct.* **44**, 499-514 (1992).

1.9 J.N. Reddy, A review of the literature on finite-element modelling of laminated composite plates, *Shock Vib. Dig.* **17**(4), 3-8 (1985).

1.10 J.N Reddy, On refined theories of composite laminates. *Mechanica* **25**, 230-238 (1990).

1.11 J.N. Reddy, A review of refined theories of laminated composite plates, *Shock Vib. Dig.* **22**(7), 3-17 (1990).

1.12 J.N. Reddy and D.H. Robbins Jr, Theories and computational models for composite laminates, *Appl. Mech. Rev.* **47**(6), Part 1, 147-169 (1994).

1.13 C.Y. Chia, *Nonlinear Analysis of Plates*, McGraw-Hill, New York (1980).

1.14 R.M. Jones, *Mechanics of Composite Material*, Hemisphere Publishing Co., New York (1975).

1.15 S. W. Tsai and H.T. Hahn, *Introduction to Composite Materials*, Technomic Pub. Co., Westport, CT, USA (1980).

1.16 J.R. Vinson and R.L. Sierakowski, *The behavior of Structures Composed of Composite Materials*, Martinus Nijhoff Publishers, Boston (1986).

1.17 K.J. Bathe, *Finite Element Procedures in Engineering Analysis*, Prentice-Hall, New York (1982).

1.18 M.A. Crisfield, *Nonlinear Finite Element Analysis of Solids and Structures*, Vol. 1, John Wiley & Sons, New York (1991).

1.19 M. Kleiber, *Incremental Finite Element Modelling in Nonlinear Solid Mechanics*, Ellis Horwood Ltd, New York (1989).

1.20 J.T. Oden, *Finite Elements of Nonlinear Continua*, McGraw-Hill, New York, (1972).

1.21 D.R.J. Owen and E. Hinton, *Finite Elements in Plasticity: Theory and Practice*, Pineridge Press, Swansea, U.K. (1980).

2.1 B.E. Greene, D.R. Strome and R.C. Weikel, Application of the stiffness method to the analysis of shell structures. In *Proc. Aviation Conference of ASME*, Los Angeles, CA, March (1961).

2.2 H.T.Y. Yang, S. Saigal and D.G. Liaw, Advances of thin shell finite elements and some applications -- Version I, *Comput. Struct.* **35**, 481-504 (1990).

2.3 C.S. Gran and T.Y. Yang, NASTRAN and SAP IV. Application of the seismic response of column-supported cooling towers. *Comput. Struct.* **8**, 761-768 (1978).

2.4 P.L. Gould, S.K. Sen and H. Suryoutomo, Dynamic analysis of column supported hyperboloidal shells. *Earthquake Engng Struct. Dynam.* **2**, 269-279 (1974).

2.5 R.H. Gallagher, R.A. Gellatly, J. Padlog and R.H. Mallett, A discrete element procedure for thin shell instability analysis. *AIAA J.* **5**, 138-145 (1967).

2.6 H.D. Hibbitt, B. Karlsson and E.P. Sorensen, *ABAQUS Theory Manual*. HKS, Inc., Providence, RI (1988).

2.7 ADINA Engineering, Inc., ADINA -- a fine element program for automatic dynamic incremental non-linear analysis -- user's manual. Report AE-81-1, Watertown, MA (1981).

2.8 P.C. Kohnke, ANSYS theoretical manual. Swanson Analysis Systems, Inc.,

Houston, PA (1987).

2.9 MARC Analysis Research Corporation, MARC general purpose finite element program, Vol. A-E. Palo Alto, CA (1981).

2.10 The NASTRAN theoretical manual. NASA SP-221(05), COSMIC (1978).

2.11 SAP7 -- A structural analysis program for static and dynamic problems -- user's manual. University of Southern California, CA (1981).

2.12 O.C. Zienkiewicz, C.J. Parikh and I.P. King, Arch dam analysis by a linear finite element shell solution program. In *Proc. Symposium on Arch Dams*, 19-22. I.C.E., London (1968).

2.13 R.W. Clough and C.P. Johnson, A finite element approximation for the analysis of thin shells. *Int. J. Solids Struct.* **4**, 43-60 (1968).

2.14 D.J. Dawe, Shell analysis using a simple facet element. *J. Strain Anal.* **7**, 266-270 (1972).

2.15 J.H. Argyris, P.C. Dunne, G.A. Malejannakis and E. Schelke, A simple triangular facet shell element with application to linear and nonlinear equilibrium and elastic stability problems. *Comput. Meth. Appl. Mech. Engng* **10**, 371-403; **11**, 97-131 (1977).

2.16 J.L. Batoz, K.J. Bathe and L.W. Ho, A study of three-node triangular plate bending elements, *Int. J. Numer. Meth. Engng* **15**, 1771-1812 (1980).

2.17 J.A. Stricklin, W.E. Haisler, P.R. Tisdale and R. Gunderson, A rapidly converging triangular plate element, *AIAA J.* **7**, 180-181 (1969).

2.18 K.J. Bathe and L.W. Ho, A simple and effective element for analysis of general shell structures, *Comput. Struct.* **13**, 673-618 (1981).

2.19 J.L. Batoz and G. Dhatt, Development of two simple shell elements, *AIAA J.* **10**, 237-248 (1972).

2.20 A.K. Noor, Multifield (mixed and hybrid) finite element models, A.K. Noor and D. Pilkey (eds.), in *State-of-the-Art Surveys on Finite Element Technology*, ASME, 127-162 (1983).

2.21 A.F. Saleeb, T.Y. Chang and S. Yingyeunyong, A mixed formulation of C^0-linear triangular element -- the role of edge shear constraints, *Int. J. Numer. Meth. Engng* **26**, 1101-1128 (1988).

2.22 D.J. Allman, A compatible triangular element including vertex rotations for plane

elasticity analysis, *Comput. Struct.* **19**, 1-8 (1984).

2.23 R.D. Cook, On the Allman triangle and related quadrilateral element, *Comput. Struct.* **22**, 1065-1067 (1986).

2.24 N. Carpenter, H. Stolarski and T. Belytschko, A flat triangular shell element with improved membrane interpolation, *Communications in Applied Numer. Meth.* **1**, 161-168 (1985).

2.25 P.G. Bergan and C.A. Felippa, A triangular membrane element with rotational degrees of freedom, *Comput. Meth. Appl. Mech. Engng* **50**, 25-69 (1985).

2.26 P.G. Bergan and M.K. Nygard, Finite elements with increased freedom in choosing shape functions, *Int. J. Numer. Meth. Engng* **20**, 643-664 (1984).

2.27 R.D. Cook, A plane hybrid element with rotational d.o.f. and adjustable stiffness, *Int. J. Numer. Meth. Engng* **24**, 1499-1508 (1987).

2.28 R.D. Cook, Modified formulations for nine-d.o.f. plane triangles that include vertex rotations, *Int. J. Numer. Meth. Engng* **31**, 825-835 (1991).

2.29 N. Carpenter, H. Stolarski and T. Belytschko, Improvements in 3-node triangular shell elements, *Int. J. Numer. Meth. Engng* **23**, 1643-1667 (1986).

2.30 O.C. Zienkiewicz and R.L. Taylor, *The Finite Element Method, Vol. 2*, McGraw-Hill, New York, 1991.

2.31 S. Ahmad, B. Irons and O.C. Zienkiewicz, Analysis of thick and thin shell structures by curved finite elements, *Int. J. Numer. Meth. Engng* **2**, 419-451 (1970).

2.32 B. Irons and S. Ahmad, *Techniques of Finite Elements*, Ellis Horwood Limited, Chichester, 1980.

2.33 C.W.S. To and M.L. Liu, Hybrid strain based three-node flat triangular shell elements, *Fin. Elem. Anal. Design* **17**, 169-203 (1994).

2.34 A.K. Noor and W.S. Burton, Assessment of computational models for multilayered composite shells, *Appl. Mech. Rev.* **43**, 67-96 (1990).

2.35 A.K. Noor and W.S. Burton, Assessment of shear deformation theories for multilayered composite plates, *Appl. Mech. Rev.* **42**, 1-12 (1989).

2.36 J.N. Reddy, A review of refined theories of laminated composite plates, *Shock Vib. Dig.* **22**(7), 3-17 (1990).

2.37 A.K. Noor, Mechanics of anisotropic plates and shells--a new look at an old subject, *Comput. Struct.* **44**, 499-514 (1992).

2.38 S.A. Ambartsumian, Some current aspects of the theory of anisotropic layered shells, in *Applied Mechanics Surveys*, edited by H.N. Abramson *et al.*, Spartan Books, Washington, DC, 301-314 (1966).

2.39 C.W. Bert, Analysis of shells, In *Composite Materials--Structural Design and Analysis, Part I*, **7**, edited by C.C. Chamis, Academic, NY, 207-258 (1975).

2.40 S. Dharmarajian and L.E. Penzes, Dynamic analysis of composite structures, *Composites* **8**, 27-32 (1977).

2.41 S.B. Dong, K.S. Pister and R.L. Taylor, On the theory of laminated anisotropic shells and plates, *J. Aerospace Sci.* **29**, 969-975 (1962).

2.42 O.A. Fettahlioglu and C.R. Steele, Asymptotic solutions for orthotropic nonhomogeneous shells of revolutions, *J. Appl. Mech.* **41**, 753-758 (1974).

2.43 P.C. Yang, C.H. Norris and Y. Stavsky, Elastic wave propagation in heterogeneous plates, *Int. J. Solids Struct.* **2**, 665-684 (1966).

2.44 S.B. Dong and F.K.W. Tso, On a laminated orthotropic shell theory including transverse shear deformation, *J. Appl. Mech.* **39**, 1091-1096 (1972).

2.45 J.B. Greenberg and Y. Stavsky, Vibration of axially compressed laminated orthotropic cylindrical shells, including transverse shear deformation, *Acta Mechanica* **37**(1-2), 13-28 (1980).

2.46 C.W. Bert and M. Kumar, Vibration of cylindrical shells of bimodulus composite materials, *J. Sound Vib.* **81**, 107-121 (1982).

2.47 Ya M. Grigorenko, E.I. Bespalova, A.B. Kitaigorodskii and A.I. Shinkar, One approach to numerical analysis of free vibration of thin walled structures, *Prikladnaya Mekhanika* **18** (11), 40-48 (1982).

2.48 Y.S. Hsu, J.N. Reddy and C.W. Bert, Thermoelasticity of circular cylindrical shells laminated of bimodulus composite materials, *J. Thermal Stresses* **4**, 155-177 (1981).

2.49 J.N. Reddy, Exact solutions of moderately thick laminated shells, *J. Eng. Mech.* **110**(5), 794-809 (1984).

2.50 C.W. Bert and V. Birman, Parametric instability of thick, orthotropic circular cylindrical shells, *Acta Mechanica* **71**, 61-76 (1988).

2.51 A.K. Noor and J.M. Peters, A posteriori estimates for shear correction factors in multilayered composite cylinders, *J. Eng. Mech.* **115**(6), 1225-1244 (1989).

2.52 A.V. Krishna Murthy and T.S.R. Reddy, A high order theory of laminated composite cylindrical shells, *J. Aeronaut Soc of India* **38**, 161-171 (1986).

2.53 M. Stein, Nonlinear theory for plates and shells including the effects of transverse shearing, *AIAA J.* **24**, 1537-1544 (1986).

2.54 J.N. Reddy and C.F. Liu, A high-order shear deformation theory of laminated elastic shells, *Int. J. Engng. Sci.* **23**, 319-330 (1985).

2.55 A. Bhimaraddi, Dynamic response of orthotropic, homogeneous and laminated cylindrical shells, *AIAA J.* **23**, 1834-1837 (1985).

2.56 A.A. Khdeir, L. Librescu and D. Frederick, A shear deformable theory of laminated composite shallow shell-type panels and their response analysis II: static response, *Acta Mechanica* **77**, 1-12 (1989).

2.57 S.B. Dong, Analysis of laminated shells of revolution, *J. Engng Mech. Div., ASCE* **92(6)**, 135-155 (1966).

2.58 E.A. Wilson and B. Parsons, The finite element analysis of filament reinforced axisymmetric bodies, *Fibre Sci. Technol.* **2**, 155-156 (1969).

2.59 L.A. Schmit and G.R. Monforton, Finite element analysis of sandwich plates and cylindrical shells with laminated faces, *AIAA J.* **8**, 1454-1461 (1970).

2.60 S.B. Dong and L.G. Selna, Natural vibrations of laminated orthotropic shells of revoiution, *J. Comp. Mater.* **4**, 2-19 (1970).

2.61 G.L. Thompson, Finite element analysis for free vibration of general anisotropic laminated thin shells, in *Proc. 6th St Louis Symposium, American Society for Composite Materials in Engineering Design* (edited by B.R. Norton), Metals Park, OH, 11-12, May 1972.

2.62 S.C. Panda and R. Natarajan, Finite element analysis of laminated shells of revolution, *Comput. Struct.* **6**, 61-64 (1976).

2.63 K.N. Shivakumar and A.V.K. Murthy, A high precision ring element for vibrations of laminated shells, *J. Sound Vib.* **58**, 311-318 (1978).

2.64 H.V. Lakshminarayana and S. Viswanath, A high precision triangular laminated anisotropic cylindrical shell finite element, *Comput. Struct.* **8**, 633-640 (1978).

2.65 K.P. Rao, A rectangular laminated anisotropic shallow thin shell finite element,

Comput. Meth. Appl. Mech. Engng **15**, 13-33 (1978).

2.66 P. Siede and P.H.H. Chang, Finite element analysis of laminated plates and shells, Report NASA CR-157106 (1078).

2.67 C. Jeyachandrabose and J. Kirkhope, A high precision triangular laminated anisotropic shallow thin shell finite element, *Comput. Struct.* **21**, 701-723 (1985).

2.68 S.C. Panda and R. Natarajan, Finite element analysis of laminated composite plates, *Int. J. Numer. Meth. Engng* **14**, 69-79 (1979).

2.69 S.C. Panda and R. Natarajan, Analysis of laminated composite shell structures by finite element method, *Comput. Struct.* **14**, 225-230 (1981).

2.70 R. Natarajan and G.E.O. Widera, Computer aided analysis of filament wound pressure vessels, University Program in Computer Aided Engineering Design and Manufacturing (UPCAEDM), 89-92 (1985).

2.71 R.V. Milford and W.C. Schnobrich, Degenerated isoparametric finite elements using explicit integration, *Int. J. Numer. Meth. Engng* **23**, 133-154 (1986).

2.72 S.M. Yunus, P.C. Kohnke and S. Saigal, An efficient through-thickness integration scheme in an unlimited layer doubly curved isoparametric composite shell element, *Int. J. Numer. Meth. Engng* **28**, 2777-2793 (1989).

2.73 J.N. Reddy, Bending of laminated anisotropic shells by a shear deformable finite element, *Fibre Sci. Technol.* **17**, 9-24 (1982).

2.74 H.V. Lakshminarayana and S.S. Murthy, A shear-flexible triangular finite element model for laminated composite plates, *Int. J. Numer. Meth. Engng* **20**, 591-623 (1984).

2.75 P. Siede and R.A. Chaudhuri, Triangular finite element for analysis of thick laminated pl. tes and shells, *Int. J. Numer. Meth. Engng* **24**, 1563-1579 (1987).

2.76 J.B. Kosmatka, ' reliable six-node triangular plate/shell element for the analysis of laminated composite structures, In *Proc. 29th AIAA/ASME/ASCE/AHS Structures, Structural Dynamics and Materials Conference, Part II*, 911-920, Williamsburg, Va., April 18-20, (1988).

2.77 P. Lardeur and J.L. Batoz, Composite plate analysis using a new discrete shear triangular finite element, *Int. J. Numer. Meth. Engng* **27**, 343-359 (1989).

2.78 J.B. Kosmatka, An accurate shear-deformable six-node triangular plate element for laminated composite structures, *Int. J. Numer. Meth. Engng* **37**, 431-455 (1994).

2.79 J.N. Reddy, On mixed finite element formulations of a higher order theory of composite laminates, In *Finite Element Methods for Plate and Shell Structures*, Vol. 2, *Formulations and Algorithms* (Edited by T.J.R. Hughes and E. Hinton), 31-57. Pineridge Press, Swansea, U.K. (1986).

2.80 C.P. Wu and C.B. Yen, Interlaminar stress mixed finite element analysis of unsymmetrically laminated composite plates, *Comput. Struct.* **49**, 411-419 (1993).

2.81 D.H. Robbins, Jr. and J.N. Reddy, Modelling of thick composites using a layerwise laminated theory, *Int. J. Numer. Meth. Engng* **36**, 655-677 (1993).

2.82 Y.K. Cheung and J. Kong, Approximate three-dimensional analysis of rectangular thick laminated plates: bending, vibration and buckling, *Comput. Struct.* **47**, 193-199 (1993).

2.83 J. Argyris and L. Tenek, A natural triangular layered element for bending analysis of isotropic, sandwich, laminated composite and hybrid plates, *Comput. Meth. Appl. Mech. Engng* **109**, 197-218 (1993).

2.84 J. Argyris and L. Tenek, Buckling of multilayered composite plates by natural shear deformation matrix theory, *Appl. Mech. Engng* **111**, 37-59 (1994).

2.85 S.T. Mau, P. Tong and T.H.H. Pian, Finite element solutions for laminated thick plates, *J. Comp. Mater.* **6**, 304-311 (1972).

2.86 A.K. Noor and C.M. Andersen, Mixed isoparametric finite element models of laminated composite shells, *Comput. Meth. Appl. Mech. Engng* **11**, 255-280 (1977).

2.87 R.L. Spilker, Hybrid-stress eight-node elements for thin and thick multilayer laminate plates, *Int. J. Numer. Meth. Engng* **18**, 801-828 (1982).

2.88 W.J. Liou and C.T. Sun, A three-dimensional hybrid stress isoparametric element for the analysis of laminated composite plates, *Comput. Struct.* **25**, 241-249 (1987).

2.89 D.J. Haas and S.W. Lee, A nine-node assumed-strain finite element for composite plates and shells, *Comput. Struct.* **26**, 445-452 (1987).

2.90 D.S. Kang, Present finite element technology from a hybrid formulation perspective, *Comput. Struct.* **35**, 321-327 (1990).

2.91 J.R. Vinson and R.L. Sierakowski, *The Behaviours of Structures composed of Composite Materials*, Martinus Nijhoff Publishers, Dordrecht/Boston/Lancaster, 1986.

2.92 J.M. Whitney, Shear correction factors for orthotropic laminates under static load, *J. Appl. Mech.* ASME, **40**, 302-304 (1973).

2.93 T.S. Chow, On the propagation of flexural waves in an orthotropic laminated plate and its response to an impulsive load, *J. Comp. Mater.* **5**, 306-319 (1971).

2.94 A.F. Saleeb, T.Y. Chang and W. Graf, A quadrilateral shell element using a mixed formulation, *Comput. Struct.* **26**, 787-803 (1987).

2.95 Symbolics, Inc., *VAX UNIX MACSYMA* Reference Manual, (1985).

2.96 B.W. Char, K.O. Geddes, G.H. Gonnet, B.L. Leong, M.B. Monagan and S.M. Watt, *MAPLE Language Reference Manual*, Waterloo Maple Publishing, Canada, (1991).

2.97 K.J. Bathe and L.W. Ho, A simple and effective element for analysis of general shell structures, *Comput. Struct.* **13**, 673-681 (1981).

2.98 R.D. Cook, D.S. Malkus and M.E. Plesha, *Concepts and Applications of Finite Element Analysis*, John Wiley & Sons, New York, 1989.

2.99 T.J.R. Hughes and F. Brezzi, On drilling degrees of freedom, *Comput. Meth. Appl. Mech. Engng* **72**, 105-121 (1989).

2.100 A. Ibrahimbegovic, R.L. Taylor and E.L. Wilson, A robust quadrilateral membrane finite element with drilling degrees of freedom, *Int. J. Numer. Meth. Engng* **30**, 445-457 (1990).

2.101 E. Reissner, A note on variational principles in elasticity, *Int. J. Solids Struct.* **1**, 93-95 (1965).

2.102 W. Kanok-Nukulchai, A simple and efficient finite element for general shell analysis, *Int. J. Numer. Meth. Engng* **14**, 179-200 (1979).

3.1 M.D. Olson and T.W. Bearden, A simple flat triangular shell element revisited, *Int. J. Numer. Meth. Engng* **14**, 51-68 (1979).

3.2 P.G. Bergan and C.A. Felippa, A triangular membrane element with rotational degrees of freedom, *Comput. Meth. Appl. Mech. Engng* **50**, 25-69 (1985).

3.3 N. Carpenter, H. Stolarski and T. Belytschko, Improvements in 3-node triangular shell elements, *Int. J. Numer. Meth. Engng* **23**, 1643-1667 (1986).

3.4 D.J. Allman, A compatible triangular element including vertex rotations for plane elasticity analysis, *Comput. Struct.* **19**, 1-8 (1984).

3.5 D.J. Allman, Evaluation of the constant strain triangle with drilling rotations, *Int. J. Numer. Meth. Engng* **26**, 2645-2655 (1988).

3.6 J.H. Argyris, Triangular elements with linear varying strain for the matrix displacement method. *J. Royal Areo. Soc*, **69, 711-713 (1965).**

3.7 S. Timoshenko and S. Woinowsky-Krieger, *Theory of Plates and Shells*, 2nd Edition, McGraw-Hill, New York, 1959.

3.8 H.V. Lakshminarayana and S.S. Murthy, A shear-flexible triangular finite element model for laminated composite plates, *Int. J. Numer. Meth. Engng* **20**, 591-623 (1984).

3.9 A.K. Noor and M.D. Mathers, Shear-flexible finite element models of laminated composite plates and shells, *NASA TN D*-8044 (1975).

3.10 J.D. Chieslar and A. Ghali, A hybrid strain technique for finite element analysis of plates and shells, *Comput. Struct.* **24**, 749-765 (1986).

3.11 Z. Xu, A thick-thin triangular plate element, *Int. J. Numer. Meth. Engng* **33**, 963-973 (1992).

3.12 J. Argyris and L. Tenek, A natural triangular layered element for bending analysis of isotropic, sandwich, laminated composite and hybrid plates, *Comput. Meth. Appl. Mech. Engng* **109**, 197-218 (1993).

3.13 F.G. Yuan and R.E. Miller, A cubic triangular finite element for flat plates with shear, *Int. J. Numer. Meth. Engng* **28**, 109-126 (1989).

3.14 D.J. Dawe, Parallelogramic elements in the solution of rhombic cantilever plate problems, *J. Strain Anal.* **1**, 223-230 (1966).

3.15 G.R. Monforton and L.A. Schmit Jr., Finite element analysis of skew plates in bending, *AIAA J.* **6**, 1150-1152 (1968).

3.16 L.L.D. Morley, Bending of clamped rectilinear plates, *Quart. J. Mech. Appl. Math.* **17**, 293-317 (1964).

3.17 E. Reissner and M. Stein, Torsion and transverse bending of cantilever plates, *NACA, TN* 2369 (1951).

3.18 A.F. Saleeb, T.Y. Chang and S. Yingyeunyong, A mixed formulation of C^0-linear triangular element -- the role of edge shear constraints, *Int. J. Numer. Meth. Engng* **26**, 1101-1128 (1988).

3.19 H. Tingyong, Y. Xuewu, S. Kang and W. Renjie, A study on CALL with CCVC

interfacial layer, *Report of the Institute of Composite Materials*, Shanghai Jiao Tong University, Shanghai, (1992).

3.20 W. Kanok-Nukulchai, A simple and efficient finite element for general shell analysis, *Int. J. Numer. Meth. Engng* **14**, 179-200 (1979).

3.21 H. Parisch, A critical survey of the 9-node degenerated shell element with special emphasis on thin shell application and reduced integration, *Comput. Meth. Appl. Mech. Engng* **20**, 323-350 (1979).

3.22 C.W.S. To and M.L. Liu, Hybrid strain based three-node flat triangular shell elements, *Fin. Elem. Anal. Design* **17**, 169-203 (1994).

3.23 G.R. Cowper, G.M. Lindberg and M.D. Olson, A shallow shell finite element of triangular shape, *Int. J. Solids Struct.* **6**, 1133-1156 (1970).

3.24 K. Forsberg and K. Hartung, An evaluation of finite difference and finite element techniques for analysis of general shells, *Symposium on High Speed Computation of Elastic Structures*, I.U.T.A.M., Liege, 837-859 (1970).

3.25 R.H. MacNeal and R.L. Harder, A proposed standard set of problems to test finite element accuracy, *Fin. Elem. Anal. Design* **1**, 3-20 (1985).

3.26 G. Horrigmoe and P.G. Bergan, Nonlinear analysis of free-form shells by flat finite elements, *Comput. Meth. Appl. Mech. Engng* **16**, 11-35 (1978).

3.27 L. Jiang and M.W. Chernuka, A simple four-noded corotational shell element for arbitrarily large rotations, *Comput. Struct.* **53**, 1123-1132 (1994).

3.28 R.H. Leicester, Finite deformations of shallow shells, *J. Eng. Mech. Div. ASCE* **94**, 1409-1423 (1968).

3.29 D.J. Haas and S.W. Lee, A nine-node assumed-strain finite element for composite plates and shells, *Comput. Struct.* **26**, 445-452 (1987).

4.1 A.W. Leissa, Recent studies in plate vibrations, 1973-1976: Classical theory, *Shock Vib. Dig.* **9**(10), 13-24 (1977).

4.2 A.W. Leissa, Plate vibration research, 1976-1980: Classical theory, *Shock Vib. Dig.* **13**(9), 11-22 (1981).

4.3 A.W. Leissa, Recent studies in plate vibrations, 1981-1985: Part I, Classical theory, *Shock Vib. Dig.* **19**(2), 11-18 (1987).

4.4 A.W. Leissa, Recent studies in plate vibrations, 1981-1985: Part II, Complicating

effects, *Shock Vib. Dig.* **19**(3), 10-24 (1987).

4.5 A.W. Leissa, *Vibration of Plates*, Washington, D.C.: US Government Printing Office, (1969).

4.6 A.W. Leissa, *Vibration of Shells*, Washington, D.C.: US Government Printing Office, (1973).

4.7 M.S. Qatu, Review of shallow shell vibration research, *Shock Vib. Dig.* **24**(9), 3-15 (1992).

4.8 C.W. Bert, Research on dynamic behaviour of composite and sandwich plates -- IV, *Shock Vib. Dig.* **17**(11), 3-25 (1985).

4.9 C.W. Bert, Recent advances in dynamics of composite structures, (Plenary Lecture), *Composite Structures 4, Proc. 4th Int. Conf. Comp. Struc.*, Paisley, Scotland, I.H. Marshall (Ed.), Elsevier Appl. Sci., London, 2, 2.1-2.17 (1987).

4.10 C.W. Bert, Research on dynamic behaviour of composite and sandwich plates -- V: Part I, *Shock Vib. Dig.* **23**(6), 3-14 (1991).

4.11 C.W. Bert, Research on dynamic behaviour of composite and sandwich plates -- V: Part II, *Shock Vib. Dig.* **23**(7), 9-21 (1991).

4.12 R.K. Kapania and S. Raciti, Recent advances in vibration and buckling of laminated beams and plates, *Design and Analysis of Composite Material Vessels*, D. Hui and T.J. Kozik (Eds.), ASME, New York, PVP-**121**, 43-54 (1987).

4.13 R.K. Kapania and S. Raciti, Recent advances in analysis of laminated beams and plates, Part II: Vibration and wave propagation, *AIAA J.*, **27**, 935-946 (1989).

4.14 J.G. Ren, Bending, vibration and buckling of laminated plates, *Handbook of Ceramics and Composites*, N.P. Cheremisinoff(Ed.), Dekker, New York, **1**, 413-450 (1990).

4.15 J.N. Reddy, A review of the literature on finite-element modelling of laminated composite plates, *Shock Vib. Dig.* **17**(4), 3-8 (1985).

4.16 J.N. Reddy, A review of refined theories of laminated composite plates, *Shock Vib. Dig.* **22**(7), 3-17 (1990).

4.17 R.K. Kapania, A review on the analysis of laminated shells, *J. Pressure Vessel Tech.*, ASME, **111**, 88-96 (1989).

4.18 H.T.Y. Yang, S. Saigal and D.G. Liaw, Advances of thin shell finite elements and some applications -- version I, *Comput. Struct.* **35**, 481-504 (1990).

4.19 A.K. Noor and W.S. Burton, Assessment of computational models for multilayered composite shells, *Appl. Mech. Rev.* **43**, 67-96 (1990).

4.20 K. Kamal and S. Durvasula, Some studies of free vibration of composite laminates, *Comp. Struc.* **5**(3), 177-202 (1986).

4.21 T.J. Craig and D.J. Dawe, Flexural vibration of symmetrically laminated composite rectangular plates including transverse shear effects, *Int. J. Solids Struct.* **22**, 155-169 (1986).

4.22 R.L. Ramkumar, P.C. Chen and W.J. Sanders, Free vibration solution for clamped orthotropic plates using Lagrangian multiplier technique, *AIAA J.*, **25**, 146-151 (1987).

4.23 J.A. Bowlus, A.N. Palazotto and J.M. Whitney, Vibration of symmetrically laminated rectangular plates considering deformation and rotatory inertia, *AIAA J.*, **25**, 1500-1511 (1987).

4.24 A.A. Khdeir, Free vibration of antisymmetric angle-ply laminated plates including various boundary conditions, *J. Sound Vib.* **122**, 377-388 (1988).

4.25 A.T. Chen and T.Y. Yang, A 36 DOF symmetrically laminated triangular element with shear deformation and rotatory inertia, *J. Comp. Materials* **22**, 341-359 (1988).

4.26 H.P. Huttelmaier and M. Epstein, Multi-layered finite element formulation for vibration and stability analysis of plates, *J. Engrg. Mech.* **115**, 315-325 (1989).

4.27 P. Lardeur and J.L. Batoz, Composite plate analysis using a new discrete shear triangular finite element, *Int. J. Numer. Meth. Engng* **27**, 343-359 (1989).

4.28 R.R. Kumar and Y.V.K.S. Rao, Free vibrations of multilayered thick composite shells, *Comput. Struct.* **28**, 717-722 (1988).

4.29 A.K. Noor and J.M. Peters, A posteriori estimates for shear correction factors in multilayered composite cylinders, *J. Eng. Mech.* **115**(6), 1225-1244 (1989).

4.30 A.K. Noor and M.D. Mathers, Shear-flexible finite element models of laminated composite plates and shells, *NASA TN D*-8044 (1975).

4.31 A.K. Noor and W.S. Burton, Assessment of shear deformation theories for multilayered composite plates, *Appl. Mech. Rev.* **42**, 1-12 (1989).

4.32 R.D. Cook, D.S. Malkus and M.E. Plesha, *Concepts and Applications of Finite Element Analysis*, 3rd edn., John Wiley & Sons, Inc. (1989).

4.33 M.L. Liu and C.W.S. To, Vibration analysis of structures by hybrid strain based three-node flat triangular shell elements, *J. Sound Vib.* (in press) (1995).

4.34 Symbolics, Inc., *VAX UNIX MACSYMA* Reference Manual, (1985).

4.35 A.W. Leissa, The free vibration of rectangular plates, *J. Sound Vib.* **31**, 257-293 (1973).

4.36 R.D. Blevins, *Formulas for Natural Frequency and Mode Shape*, Van Nostrand Reinhold Co., New York, (1979).

4.37 J.N. Reddy and N.D. Phan, Stability and vibration of isotropic, orthotropic and laminated plates according to a high-order shear deformation theory, *J. Sound Vib.* **98**, 157-170 (1985).

4.38 C.W. Bert and T.L.C. Chen, Effect of shear deformation on vibration analysis of antisymmetric angle-ply laminated composite plates, *Int. J. Solids Struct.* **14**, 465-473 (1978).

4.39 J.N. Reddy, Free vibration of antisymmetric, angle-ply laminated plates including transverse shear deformation by the finite element method, *J. Sound Vib.* **66**, 565-576 (1979).

4.40 K.P. Soldatos, Influence of thickness shear deformation on free vibrations of rectangular plates, cylindrical panels and cylinders of antisymmetric angle-ply construction, *J. Sound Vib.* **119**, 111-137 (1987).

4.41 J.N. Reddy and C.F. Liu, A higher-order shear deformation theory of laminated elastic shells, *Int. J. Engng Sci.* **23**, 319-330 (1985).

5.1 M.L. Liu and C.W.S. To, Hybrid strain based three node flat triangular shell elements - I. Nonlinear theory and incremental formulation, *Comput. Struct.* **54**, 1031-1056 (1995).

5.2 C.W.S. To and M.L. Liu, Hybrid strain based three node flat triangular shell elements - II. Numerical investigation of nonlinear problems, *Comput. Struct.* **54**, 1057-1076 (1995).

5.3 A.K. Noor and M.D. Mathers, Nonlinear finite element analysis of laminated composite shells, In *Computational Methods in Nonlinear Mechanics* (Ed. by J.T. Oden, E.B. Becker, R.R. Craig, R.S. Dunham, C.P. Johnson and W.L. Oberkampf). Proc. International Conference on Computational Methods in Nonlinear Mechanics, Austin, TX (1974).

5.4 A.K. Noor and S.J. Hartley, Nonlinear shell analysis via mixed isoparametric

elements, *Comput. Struct.* **7**, 615-626 (1977).

5.5 A.K. Noor and C.M. Anderson, Mixed models and reduced/selective integration displacement models for nonlinear shell analysis, *Int. J. Numer. Meth. Engng* **18**, 1429-1454 (1982).

5.6 T.Y. Chang and K. Sawamiphakdi, Large deformation analysis of laminated shells by finite element method, *Comput. Struct.* **13**, 331-340 (1981).

5.7 J.N. Reddy, A finite element analysis of large deflection bending of anisotropic shells, In *Nonlinear Finite Element Analysis of Plate and Shells* (Ed. by R.J.R. Hughes, A. Pifko and A. Jay), ASME AMD, **48**, 249-264 (1981).

5.8 W.C. Chao and J.N. Reddy, Analysis of laminated composite shells using a degenerated 3-D element, *Int. J. Numer. Meth. Engng* **?** , 1991-2007 (1984).

5.9 J.N. Reddy and K. Chandrashekhara, Nonlinear analysis of laminated shells including transverse shear strains, *AIAA J.*, **23**, 440-441 (1985).

5.10 J.N. Reddy and K. Chandrashekhara, Geometrically nonlinear transient analysis of laminated, doubly curved shells, *Int. J. Nonlin. Mech.* **20**, 79-90 (1985).

5.11 S. Saigal, R.K. Kapania and T.Y. Yang, Geometrically nonlinear finite element analysis of imperfect laminated shells, *J. Comp. Materials* **20**, 197--214 (1986).

5.12 H. Rothert and W. Dehmel, Nonlinear analysis of isotropic orthotropic and laminated plates and shells, *Comput. Meth. Appl. Mech. Engng* **64**, 429-446 (1987).

5.13 C.Y. Wu, T.Y. Yang and S. Saigal, Free and forced nonlinear dynamics of composite shell structures, *J. Comp. Materials* **21**, 898-909 (1987).

5.14 C.H. Yeom and S.W. Lee, An assumed strain finite element model for large deflection composite shells, *Int. J. Numer. Meth. Engng* **28**, 1749-1768 (1989).

5.15 C.L. Liao and J.N. Reddy, Analysis of anisotropic, stiffened composite laminates using a continuum-based shell element, *Comput. Struct.* **34**, 805-815 (1990).

5.16 A.F. Palmerio, J.N. Reddy and R. Schmidt, On a moderate rotation theory of laminated anisotropic shells-Part 1, Theory, *Int. J. Nonlin. Mech.* **25**, 687-700 (1990).

5.17 A.F. Palmerio, J.N. Reddy and R. Schmidt, On a moderate rotation theory of laminated anisotropic shells-Part 2, Finite element analysis, *Int. J. Nonlin. Mech.* **25**, 701-714 (1990).

5.18 H. Rothert and S. Di, Geometrically nonlinear analysis of laminated shells by hybrid formulation and higher-order theory, *Bulletin of IASS*, **35**, 15-32 (1994).

5.19 J.J. Lin, M. Fafard, D. Beaulieu and B. Massicotte, Nonlinear analysis of composite bridges by the finite element method, *Comput. Struct.* **40**, 1151-1167 (1991).

5.20 E. Madenci and A. Barut, A free-formulation-based flat shell element for nonlinear analysis of thin composite structures, *Int. J. Numer. Meth. Engng* **37**, 3825-3842 (1994).

5.21 J. Zhu, Application of natural approach to nonlinear analysis of sandwich and composite plates and shells, *Comput. Meth. Appl. Mech. Engng* **120**, 355-388 (1995).

5.22 Symbolics, Inc., *VAX UNIX MACSYMA* Reference Manual, (1985).

5.23 A.F. Saleeb, T.Y. Chang, W. Graf and S. Yingyeunyong, A hybrid/mixed model for nonlinear shell analysis and its applications to large-rotation problems, *Int. J. Numer. Meth. Engng* **29**, 407-446 (1990).

5.24 J.J. Rhiu, *A New and Efficient Formulation for Finite Element Analysis of Thin Shell Structures Undergoing Small and Large Deflection*, Ph.D. Thesis, University of Maryland (1985).

5.25 J.C. Simo and D.D. Fox, On a stress resultant geometrically exact shell model. Part I: Formulation and optimal parametrization, *Comput. Meth. Appl. Mech. Engng* **72**, 267-304 (1989).

5.26 J.C. Simo, D.D. Fox and M.S. Rifai, On a stress resultant geometrically exact shell model. Part II: The linear theory; Computational aspects, *Comput. Meth. Appl. Mech. Engng* **73**, 53-92 (1989).

5.27 J.C. Simo, D.D. Fox and M.S. Rifai, On a stress resultant geometrically exact shell model. Part III: Computational aspects of the nonlinear theory, *Comput. Meth. Appl. Mech. Engng* **79**, 21-70 (1990).

5.28 J.C. Simo, M.S. Rifai and D.D. Fox, On a stress resultant geometrically exact shell model. Part IV: Variable thickness shells with through-the-thickness stretching, *Comput. Meth. Appl. Mech. Engng* **81**, 91-126 (1990).

5.29 J.C. Simo and J.G. Kennedy, On a stress resultant geometrically exact shell model. Part V: Nonlinear plasticity; Formulation and integration algorithms, *Comput. Meth. Appl. Mech. Engng* **96**, 133-171 (1992).

5.30 J.C. Simo, M.S. Rifai and D.D. Fox, On a stress resultant geometrically exact

shell model. Part VI: Conserving algorithms for nonlinear dynamics, *Int. J. Numer. Meth. Engng* **34**, 117-164 (1992).

5.31 K.J. Bathe, *Finite Element Procedures in Engineering Analysis*, Prentice-Hall, New York (1982).

5.32 T.J.R. Hughes and W.K. Liu, Nonlinear finite element analysis of shells, Part I: Three dimensional shells, *Comput. Meth. Appl. Mech. Engng* **26**, 331-362 (1981).

5.33 T.J.R. Hughes and J. Winget, Finite rotation effects in numerical integration of rate type constitutive equations arising in large deformation analysis, *Int. J. Numer. Meth. Engng* **15**, 1862-1867 (1980).

5.34 M. Kleiber, *Incremental Finite Element Modelling in Nonlinear Solid Mechanics*, Ellis Horwood Ltd (1989).

5.35 J.W. Hutchinson, Finite strain analysis of elasto-plastic solids and structures, in *Numerical Solution of Nonlinear Structural* Problems (ed. R.F. Hartung), ASME, Detroit, 17-19 (1975).

5.36 J.C. Nagtegaal and J.E. de Jong, Some computational aspects of elastic-plastic large strain analysis, *Int. J. Numer. Meth. Engng* **17**, 15-41 (1981).

6.1 M.L. Liu and C.W.S. To, Hybrid strain based three node flat triangular shell elements - I. Nonlinear theory and incremental formulation, *Comput. Struct.* **54**, 1031-1056 (1995).

6.2 C.W.S. To and M.L. Liu, Hybrid strain based three node flat triangular shell elements - II. Numerical investigation of nonlinear problems, *Comput. Struct.* **54**, 1057-1076 (1995).

6.3 A.F. Saleeb, T.Y. Chang, W. Graf and S. Yingyeunyong, A hybrid/mixed model for nonlinear shell analysis and its applications to large-rotation problems, *Int. J. Numer. Meth. Engng* **29**, 407-446 (1990).

6.4 G. Horrigmoe and P.G. Bergan, Nonlinear analysis of free-form shells by flat finite elements, *Comput. Meth. Appl. Mech. Engng* **16**, 11-35 (1978).

6.5 K.K. Chen, Evaluation of a finite element for binder wrap calculation. General Motors Research Publication GMR-5209 (1985).

6.6 K.J. Bathe, E.L. Wilson and R.H. Iding, NOSAP, a structural analysis program for static and dynamic response of nonlinear systems, Report No. UC SESM 74-3, Structural Engineering Laboratory, University of California, Berkeley, CA (1974).

6.7 H. Rothert and W. Dehmel, Nonlinear analysis of isotropic orthotropic and laminated plates and shells, *Comput. Meth. Appl. Mech. Engng* **64**, 429-446 (1987).

6.8 C.H. Yoom and S.W. Lee, An assumed strain finite element model for large deflection composite shells, *Int. J. Numer. Meth. Engng* **28**, 1749-1768 (1989).

6.9 C.T. Sun and H. Chin, On the analysis of asymmetric composite laminates, *Proc. of the AIAA/ASME/ASCE/AHS 28th Structures*, Structural Dynamics and Materials Conference, 289-294 (1987).

6.10 A.K. Noor and S.J. Hartley, Nonlinear shell analysis via mixed isoparametric elements, *Comput. Struct.* **7**, 615-626 (1977).

6.11 J.N. Reddy, Geometrically nonlinear transient analysis of laminated composite plates, *AIAA J.*, **21**, 621-629 (1983).

6.12 Y.C. Wu and T.Y. Yang, Free and forced nonlinear dynamics of composite shell structures, *J. Comp. Materials* **21**, 898-909 (1987).

6.13 C.W.S. To and M.L. Liu, Private communication, Department of Mechanical Engineering, The University of Western Ontario (1995).

7.1 B. Wang and C.W.S. To, *Explicit Expressions for Linear Hybrid Strain Based Laminated Composite Triangular Shell Elements*, NDRL TR9501, Department of Mechanical Engineering, The University of Western Ontario (1995).

7.2 B. Wang and C.W.S. To, *Explicit Expressions for a Geometrically nonlinear Hybrid Strain Based Laminated Composite Triangular Shell Elements*, NDRL TR9502, Department of Mechanical Engineering, The University of Western Ontario (1995).